THE STUDY OF CRYSTALLIZATION AND INTERFACIAL MORPHOLOGY IN POLYMER/CARBON NANOTUBE COMPOSITES

A Dissertation
Presented to
The Academic Faculty

by

Marilyn Lillith Minus

In Partial Fulfillment
of the Requirements for the Degree
Doctor of Philosophy in the
School of Polymer, Textile, and Fiber Engineering

Georgia Institute of Technology
August 2008

THE STUDY OF CRYSTALLIZATION AND INTERACIAL MORPHOLOGY IN POLYMER/CARBON NANOTUBE COMPOSITES

Approved by:

Dr. Satish Kumar, Advisor
School of Polymer, Textile, and Fiber Engineering
Georgia Institute of Technology

Dr. Dr. Samuel Graham
School of Mechanical Engineering
Georgia Institute of Technology

Dr. Anselm Griffin
School of Polymer, Textile, and Fiber Engineering
Georgia Institute of Technology

Dr. Meisha Shofner
School of Polymer, Textile, and Fiber Engineering
Georgia Institute of Technology

Dr. Hamid Garmestani
School of Materials Science and Engineering
Georgia Institute of Technology

Date Approved: April 28, 2008

To My Family

ACKNOWLEDGEMENTS

I would like to express my most sincere and deepest gratitude to my advisor, Dr. Satish Kumar, for his patience, guidance, and dedication to my intellectual and personal growth throughout the course of my study. I would also like to thank Dr. Anselm Griffin, Dr. Meisha Shofner, Dr. Samuel Graham, and Dr. Hamid Garmestani for providng their time to serve on my thesis committee, for their critical reading of my thesis and suggestions, and their encouragement.

In addition, I would like to sincerely thank Dr. Tetsuya Uchida for his exceptional talk on *Transmission Electron Microscopy in Polymer Composites* that inspired the bulk of my PhD work. I am also grateful to Dr. Yong Ding, and Yolande Berta for providing training and personal instruction for use of the transmission electron microscopes. I would also like to thank Dr. Xeifei Zhang and Dr. Tao Liu for providing me with initial training on poly(vinyl alcohol)/carbon nanotube composites.

I would also like to thank fellow group member Dr. Han Gi Chae for many invaluable discussions on various research topics and experimental help with fiber spinning. I would like to thank previous group members, Dr. Sreekumar Veedu, Dr. Young-Bin Park, Dr. Shanju Zhang, Dr. Hongming Ma, Dr. Chongfu Zhou, Dr. Jing Liu, Dr. Tong Wang, Dr. Huina Guo, and current group members, Mr. Sudhakar Jaganathan, Mr. Beom-Jin Yoon, Mr. Rahul Jain, Mr. Young Ho Choi, Mr. Yaodong Liu, Ms. Erika Johnson, and Mr. Ian Winters for their help and friendship.

Last but certainly not least, I would like to express my earnest gratitude and abundant love to my mother (Beverly) and father (Leslie) who tirelessly supported,

inspired, and trained me to push through with integrity to attain this goal. To my brother (Iain) and sisters (Indira, Ianthe, and Megan) for their love, support, and understanding, and for my sisters continual fight that gave me the resilience to press on. I am greatly appreciative to Brandi, Skylar, Gabby, and a host of friends for their patience, love, and encouragement.

TABLE OF CONTENTS

LIST OF TABLES

LIST OF FIGURES

LIST OF ABBREVIATIONS

CNT	Carbon nanotubes
SWNT	Single-walled carbon nanotubes
DWNT	Double-wall carbon nanotubes
MWNT	Multi-wall carbon nanotubes
VGCNF	Vapor grown carbon nanofiber
CNF	Carbon nanofiber
NHSK	Non hybrid shish-kebab
CNI	Carbon Nanotechnologies Incorporated
PVA	Polyvinyl alcohol
PAN	Polyacrylonitrile
PE	Polyethylene
PMMA	Poly(methyl methacrylate)
LLDPE	Linear low density polyethylene
HDPE	High density polyethylene
LMWPE	Low molecular weight polyethylene
PP	Polypropylene
PS	Polystryrene
PBO	Poly(p-phenylene benzobisoxazole)
PVP	Poly(vinyl pyrrolidone)
PPO	Poly(oxypropylene)
PEO	Poly(oxyethylene)
SDS	Sodium dodecyl sulfate

SDBS	Sodium dodecylbenzenesufonate
CTAB	Cetyltrimethyl ammonium bromide
DTAB	Dodecyltrimetyl ammonium bromide
DMSO	Dimethyl sulfoxide
DMF	N,N, dimethylformamide
RBM	Radial breathing mode
DOS	Density of States
TEM	Transmission Electron Microscope
HR-TEM	High-resolution transmission electron microscopy
SEM	Scanning Electron Microscope
TGA	Thermogravimetric Analyzer
DSC	Differential Scanning Calorimetry
DMA	Dynamic Mechanical Analyzer
TMA	Thermomechanical Analyzer
SAXS	Small-angle X-ray Scattering
WAXS	Wide-angle X-ray Scattering
XRD	X-ray Diffraction
FT-IR	Fourier Transform Infrared
UV-VIS-NIR	Ultraviolet-visible-near infrared region
ED	Electron Diffraction
DF	Dark Field
BF	Bright Field
DR	Draw ratio

LIST OF SYMBOLS

J/g	Joules per gram (unit of energy)
m/min	meters per minute (unit of linear speed)
ml/hr	milliliters per hour
S/m	Siemen's per meter (unit of electrical conductivity)
m^2/g	square meters per gram (unit of surface area)
kV	kilovolts
eV	electron volts
mA	milliamperes
MPa	megapascals
GPa	gigapascals
nm	nanometers
μm	micrometers
ΔH_m	Enthalpy of melting
ΔH_c	Enthalpy of crystallization
T_c	Temperature of crystallization
f_c	Hermann's Orientation Factor
T_g	Glass Transition Temperature
T_m	Melting Temperature
m_p	Melting point
Δ	Epitaxial disregistry
Ψ	Electron beam tilt angle

hkl	Miller indices
λ	wavelength
E_1	longitudinal/axial modulus
E_2	transverse modulus
ν_{12}	Poisson's ratio
G_{12}	shear modulus
d_t	nanotube diameter
d_i	nanotube inter-tube spacing
ν	wavenumber
τ	relaxation time
$\dot{\varepsilon}_{ii}$	elongation deformation flow field
t	flow field time

SUMMARY

This study illustrates the ability of SWNT to nucleate and template polymer crystallization and orientation, and produce materials with improved properties and unique polymer morphologies. This research work focuses primarily on the physical interaction between single-wall carbon nanotubes (SWNT) and the flexible polymer system polyvinyl alcohol (PVA). Polymer crystallization in the near vicinity of SWNT (interphase) has been studied to understand the capability of SWNT in influence polymer morphology in bulk films and fibers.

Fibrillar crystallization was achieved by shearing PVA/SWNT dispersions and resulted in the formation of oriented PVA/SWNT fibers or ribbons, while PVA solutions produce unoriented fibers. PVA single crystals were grown in PVA solutions as well as PVA/SWNT dispersions over a period of several months at room temperature (25 °C). PVA single crystal growth in PVA/SWNT dispersions is templated by SWNT, and these crystals show the presence of new morphologies for PVA. PVA single crystals of differing morphology were also grown at elevated temperatures, and show morphology dependant electron beam irradiation resistance. Gel-spinning was used to produce PVA, and PVA/SWNT fibers where, PVA crystallization in the bulk fiber was observed. With 1 wt% SWNT loading in PVA, the fiber tensile strength increased from 1.6 GPa for the control PVA to 2.6 GPa for PVA/SWNT. Analysis of this data suggests stress of up to ~120 GPa on the SWNT. This is the highest reported stress on the SWNT to date and confirm excellent reinforcement and load transfer of SWNT in the PVA matrix. Raman spectroscopy data show high SWNT alignment in the fiber where the I_{0°/I_{90° ratio is

measured to be 106. High-resolution transmission electron microscopy (HR-TEM) is used to characterize polymer morphology near the polymer-SWNT interface for PVA/SWNT fibers. HR-TEM studies of Polymer/CNT composites show distinct morphological differences at the polymer-SWNT interface/interphase for semi-crystalline and amorphous polymer systems which may be related to polymer-SWNT interaction in the composite.

Studies on polymer crystallization, carbon nanotube (CNT)/polymer composite, and polymer composite interfacial literature in summarized in Chapter 1. Fibrillar crystallization of PVA and PVA/SWNT is presented in Chapter 2. PVA single crystal grown at varying temperatures is discussed in Chapter 3, followed by single crystal growth studies in PVA/SWNT dispersions in Chapter 4. Chapter 5 summarizes the gel-spinning studies of PVA and PVA/SWNT fibers. Conclusions and recommendations for future work pertaining to this study are given in Chapter 6. Results of HR-TEM studies on other polymer/SWNT composites are given in Appendix A, Appendix B summarizes work on PE crystallization in the SWNT/DMF dispersions, and studies of PVA and PVA/SWNT gel films are summarized in Appendix C.

CHAPTER 1

INTRODUCTION

1.1. Polymer Crystallization

During the earlier part of the twentieth century a single polymers molecule of molecular weight higher than 5000 was not thought to exist, and the arrangement of monomers in these polymer molecules was not well understood. Growth of molecular crystals from these low molecular weight compounds had long since fascinated scientists because of their well-faceted and periodic shapes. Scientists learned early on that these shapes were in fact related to the internal morphology of the molecules comprising each crystal but could only make guesses about the internal arrangement of the molecules. The discovery of X-rays by Rontgen in 1895, subsequently led to Laue's discovery in 1912 that molecules arranged in a crystalline state and this crystalline arrangement would cause X-rays to diffract. X-ray diffraction provided a means of studying and understanding the internal structure of crystals and measuring distances between atoms in the crystalline state. It was these studies of low molecular weight crystalline materials that led to the development of the framework for crystal lattice calculations [1], which became very important for understanding the morphology of molecular crystals. Initially X-ray diffraction studies were only performed on inorganic as well as crystalline short chain organic compounds. Later, throughout the late 1920s and 1930s the work of Hermann Staudinger and later William Carothers led to the realization that chain-like polymer macromolecules with molecular weights exceeding tens of thousands did indeed exist [2, 3]. These discoveries revamped the scientific thinking about the size, shape, and

structure of polymer molecules. These large molecules were also able to crystallize under the right conditions, and the internal arrangement of these polymer macromolecules could be studied by X-ray diffraction. The discovery of these materials ignited research for the development of a wide array of materials with applications in every aspect of life.

Due to the demand for new materials, the in-depth scientific study of polymeric materials became very important. The detailed study of polymer morphology at the sub-microscopic level became possible with the invention and development of the electron microscope in the 1930s [4, 5]. Early microscopy studies on polymer single crystal morphology provided the framework for understanding how flexible polymer systems crystallize [6-9]. Studying polymer morphology is essential for understanding the behavior of polymeric materials at the sub-microscopic level under specific processing conditions, and this in turn can be translated to macroscopic properties in materials produced from these polymers.

The long-chain flexible structures of polymers consisting of regular repeating units do not typically form long-range order or periodic three-dimensional structures at the lowest energy states. It is more typical for polymeric materials to form localized domains of order intermingled with purely entangled regions. This type of structure was first conceptualized by the fringed-micelle model (Figure 1.1). For this reason, polymeric materials able to crystallize are externally manipulated by drawing or stretching to form large crystalline domains with long range order along the chain axis. Some polymeric materials are also found to form folded chain or lamellar crystals, where the long range order of the crystal is typically perpendicular to the polymer chain axis

(Figure 1.2a). An important area in the study of polymer morphology is this process of polymer crystallization. The growth of single crystals of polymeric materials provides an ideal way of studying polymer chain morphology. There has been a tremendous amount of work dedicated to understanding this transformation "crystallization" process in polymeric materials [10-13].

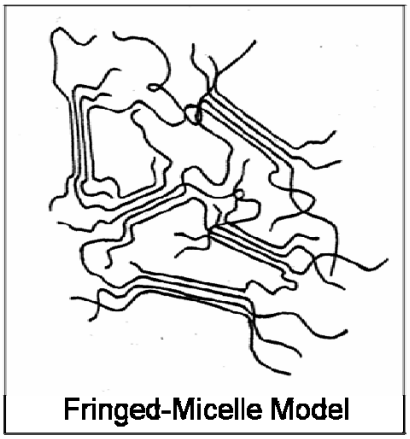

Figure 1.1. A schematic of the fringed-micelle model.

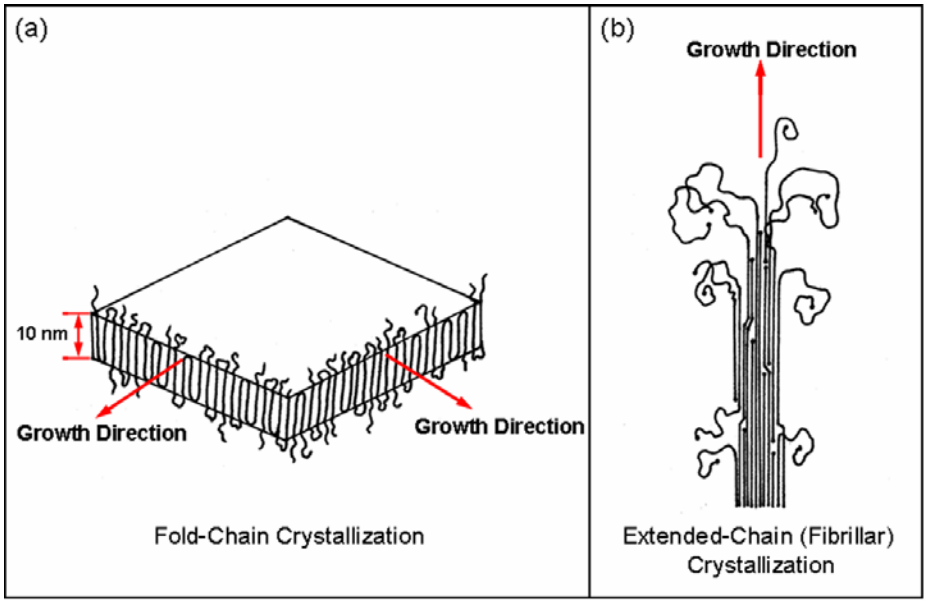

Figure 1.2. A schematic of (a) polymer lamellar crystal showing polymer chain folding where the chain axis is perpendicular to the lamellar surface, and (b) chain arrangement in a fibrillar crystal.

The idea that polymeric materials can go from a totally disordered state to an ordered state is quite amazing and not completely understood. The initiation process for polymer crystallization either in the melt or solution is called nucleation. In this process a 'nuclei' or 'crystal embryo' is formed and must reach a critical size [14], it is at this point that the polymer crystal can grow. Polymers which have significantly regular and periodic chain structure like polyethylene, polypropylene, and poly(vinyl alcohol) have been shown to crystallize. There are several chain irregularities that tend to retard polymer crystallization and these include branch points, bulky side-groups, chemically identical groups with different geometrical arrangements, as well as chemically different groups as in the case of copolymers. In the crystalline state, polymer molecules will adopt the same chain conformation which will be repeated to form long range 3-D order. The long –range 3-D order of polymers chains in the crystalline state can be described by a basic unit cell which is ultimately replicated.

1.1.1. Single Crystal Growth

Nucleation and growth of polymer single crystals can occur in one of the following two types of geometries, lamellar (folded-chain) or fibrillar. Although polymers do form single crystals, its formation is unlike low molecular weight compounds that can do so under almost any condition. Polymer single crystal growth has to occur under the right conditions, where the chains are given sufficient energy to rearrange themselves into highly periodic 3-D structures. The steric hindrances that need to be overcome for such a large macromolecule to form stable 3-D order are very large.

Both kinetics and thermodynamics contribute to the overall growth of the single crystal. Polymer single crystals grown at higher temperatures have higher internal energy along the crystal lattice because the chains are given more energy therefore, more rotational freedom. Polymer crystallization at low temperatures usually occurs where there is a minimum of internal energy along the crystal lattice, and this is typically the more favorable form of crystallization for the polymer chain.

1.1.2. Lamellar Single Crystals [11, 12]

Although polymer single crystals have been demonstrated to grow in the melt [15-19], it is very common to grow single crystals in dilute polymer solution, where polymer concentration is less than 1 wt %. Single crystals grown in dilute solutions are of the lamellar type where the growth direction if perpendicular to the chain axis, the lamellar thickness on the order of 10 nm, and the transverse direction of the crystals can be up to several microns (Figure 1.2a).

One of the first observations of polymer single crystals was in the 1930s of linear polyethylene [20]. This work sparked discussions which dealt mainly with possible growth models for crystals as well as the growth of short chain polymer (n-paraffins) single crystals [7, 21]. A short time later specific growth conditions were determined for growth of high molecular weight polyethylene single crystals [6]. Other high polymer single crystals were also reported including polyoxymethylene [8], nylon [22], nylon 66 [23], and polyacrylonitrile [24].

1.1.3. Fibrillar Crystallization [25]

Fibrillar-type crystallization from macromolecular materials was first recorded by Hermann Staudinger in the late 1920s [2]. Fibrillar crystals are initiated by small nuclei consisting of polymer chains aligned parallel to the chain direction. The subsequent growth front of these crystals continues along the chain direction (Figure 1.2b), and this is contrary to what is found in folded-chain crystals where the growth front is perpendicular to the chain direction (Figure 1.2a). Polymer chains in both the melt and solutions exist as intertwined coils therefore, in order for nuclei to form these chains must disentangle and undergo slow transitional diffusion [25]. Since this process is difficult for polymers, the use of external force is needed to facilitate the formation of nuclei for fibrillar crystallization. Subjecting a polymer solution or melt to flow fields has been shown successful for growth of fibrillar crystals. Crystallization of high molecular weight polymers from stirred/sheared polymer solutions was first reported in 1960s [26-31]. Morphological studies of fibrillar crystals show that the polymer molecules are extended along the length of the fibers. These materials can have high modulus and strength. Growth of fibrillar crystals from polyethylene lead to the first observation of the shish-kebab structure with extended-chain core and may be credited for the ultimate development, and commercialization of extended chain polyethylene fiber in 1980s [32-34] – an important milestone in the processing of high performance fibers from flexible polymers. After over 60 years of development in fiber processing technology, the basic morphological structure of commodity polymeric fibers such as nylon 6, nylon 66, polypropylene (PP), and polyethylene terephthalate (PET), has not changed significantly over the years. Typical polymer chain morphology for fiber produced by conventional

means consists of both crystalline and amorphous regions (Figure 1.3). Mechanical properties of fibers are significantly lower than predicted modulus and strength values for the extended polymer chain. Fibrillar crystallization has shown significant promise for producing extended chain polymeric materials. Fibrillar crystallization experiments performed using polyethylene produced macrofibers which consist of elementary fibrils or individual fibrillar crystals [29, 35] with significantly higher modulus and strength as compared to fibers produced using conventional means. The limiting step for performing fibrillar crystallization on a wide range of polymers is determining the right set of conditions for nuclei initiation. The discovery of single wall carbon nanotubes introduced a new material of nanoscale dimensions and needle- or fiber-like morphology that can be explored as an ideal nucleation candidate for fibrillar crystallization.

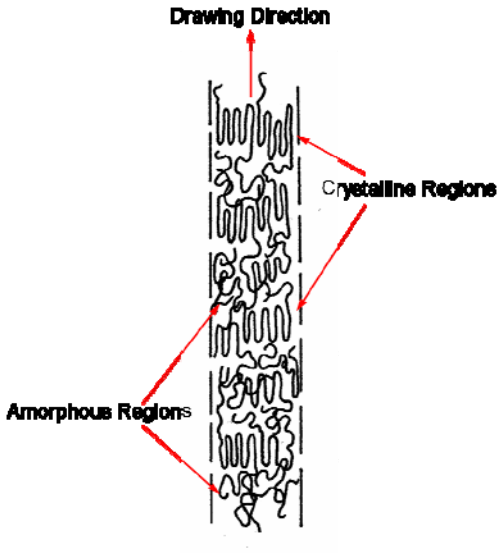

Figure 1.3. A schematic of the chain arrangement in drawn polymeric material with both amorphous and crystalline regions.

1.1.4. Characterization of Polymer Crystals

Electron microscopy as well as wide-angle and small-angle X-ray scattering (WAXS/SAXS) were and still are main characterization tools for studying the structure and morphology of lamellar and fibrillar polymer single crystals. Diffraction patterns obtained from electron microscopy can be related to the visual appearance of the single crystal. Electron diffraction from single crystals which show minimal to no presence of an amorphous halo in the diffraction pattern and only sharp diffraction spots are obtained from similarily-oriented crystallites. Destruction of the polymer lattice within the polymer single crystal by electron beam damage and cross-linking is instantaneous during imaging in the electron microscope. This result in the presence of amorphous regions/structures within the single crystal which can be detected in the electron diffraction pattern by the presence of an amorphous halo superimposed on the diffraction spots from the crystallites. It has been estimated that bombardment of electrons on the single crystals will result in disruption of the crystal lattice, and these disruptions result in diffusion of the crystallite diffraction spots [36]. The greater the distortion in the lattice the more diffused the diffraction spots become. Although the diffracting power of a polymer crystal is instantly destroyed in the electron microscope this is not the case for X-ray analysis. This is because the electrons in polymer crystal interact inelastically with the incident electron beam causing lattice vibrations and generation of thermal energy. For X-ray scattering which is non-destructive to the sample, X-ray photons interact elastically with the electrons in the sample. Although there are several disadvantages for using electron microscopy for studying polymer single crystals, it is still a very powerful tool. For this reason, polymer single crystal samples used in electron microscopy are

observed using different methods (e.g. metal shadowing, and use of low excitation voltage) to reduce electron beam damage.

1.2. Carbon Nanotubes

Several allotropes of carbon exist in nature. In 1985 a new allotrope of carbon was discovered by Harold Kroto, James Heath, Sean O'Brian, Richard Smalley, and Robert Curl who synthesized the Buckyminister fullerene "buckyball", C_{60}. Kroto, Smalley, and Curl subsequently won the Nobel Prize in Chemistry in 1996 for this discovery. This "buckyball" has a truncated icosahedron structure which resembles a soccer ball shape. The carbon nanotube structure, which is a cylindrical molecule of carbon is a part of the fullerene family. The discovery of carbon nanotubes (CNT) has been credited to Iijima for his 1991 transmission electron micrographs of MWNT, and his 1993 TEM of SWNT. CNT comprises a large field of study which may include carbon nanofibers (CNF), multi-walled carbon nanotubes (MWNT), double-walled carbon nanotubes (DWNT), and single-walled carbon nanotubes (SWNT). In this work CNF will not be included as part of the CNT family. The term CNT will only refer to structures consisting of concentric graphitic layers, and this includes SWNT, DWNT, and MWNT (Figure 1.4).

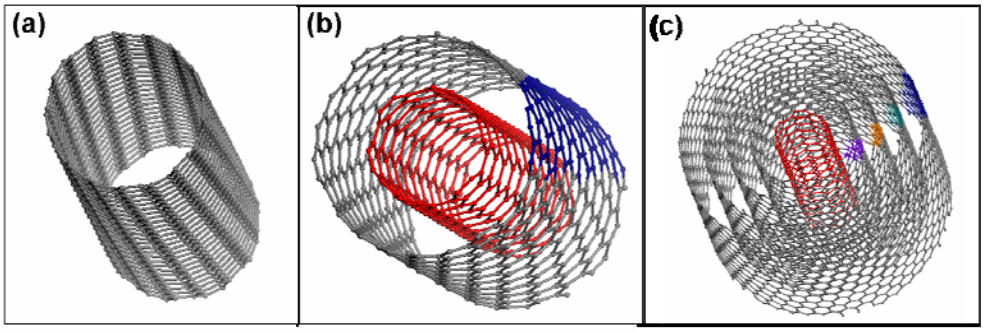

Figure 1.4. Molecular models for (a) single-wall carbon nanotube, (b) double-wall carbon nanotube, and (c) multi-wall carbon nanotube.

The existence of tubular carboneous nano-structures dates back to much earlier. In 1889 a French scientist first reported the formation of graphitic structure grown for the vaporization of hydrocarbons. After the development of the transmission electron microscope (TEM) in the 1930s, the ability to image these materials at the nanoscopic range became possible. The discovery of the TEM led to several publications showing the existence of tubular graphitic structures, although, it is not certain that these tubular graphite structures were CNT with concentric graphite layers. Tubular graphite structures have been around for some time, and it is possible that SWNT and MWNT may have existed long before Iijima's 1991 and 1993 publications [37, 38]. His work showed the observation of MWNT and SWNT with concentric layers which led to an incredible amount of interest in the field of CNT.

1.2.1 Synthesis of Carbon Nanotubes

Control of the synthesis process is very important for the production of CNT. MWNT tend to grow from a carbon cathode or on a substrate, whereas SWNT tend to grow in the gas phase. This may be one of the significant differences between the

synthesis process for SWNT and MWNT [38]. Recently vertically aligned SWNT forests have also been synthesized on substrates [39, 40]. SWNT self-organize into ropes which typically consists of anywhere from 100 to 500 SWNT. The formation of these "ropes" is due to the strong van der Waals forces between tubes. The tubes in these ropes can pack in either a 2-D hexagonal or trigonal crystal lattice [41]. Several production methods have been developed to produce SWNT. These include laser-ablation [41], arc-discharge [42], chemical vapor deposition (CVD)[43-45], and gas-phase chemical-vapor-deposition (HiPCO™) process [46]. A yield of over 70-90 % can be obtained when SWNT are synthesized by laser-vaporization of a carbon-nickel-cobalt mixture at 1200 °C [41]. SWNT produced in this method formed ropes that form a 2-D crystalline triangular lattice. Fullerene molecules were first generated using the arc-discharge method, and it was during the examination of fullerene soot produced by this method that CNT were observed [38]. In the arc-discharge process an electric arc-discharge is generated between two carbon electrodes in an inert environment at high temperatures until sublimation of carbon occurs. Well-packed bundles of SWNT were generated by arc-discharge [42]. This process was conducted in a helium atmosphere at 660 mbar pressure, and the arc-discharge was created using a 100 A current. Nickel-cobalt, cobalt-yttrium, and nickel-yttrium catalyst mixtures were all used in the process. The Ni-Y combination resulted in the best yield of SWNT. CCVD production of SWNT involves the decomposition of a hydrocarbon over supported metal catalyst nano-particles and as-grown SWNT is subsequently removed from the support. One such CCVD production method uses the decomposition of methane over metal particles on a MgO support at 1000 °C [47]. SWNT were later purified and removed from the support with an acid

treatment – the overall yield in this method was 70-80 %. For SWNT production using the HiPCO™ process CO pressure is maintained between 30 to 50 atm and the temperature ranges from 900 to 1100 °C. During the process gas phase CO is flowed over catalytic iron clusters $Fe(CO)_5$. At this temperature and pressure the flow of CO causes the thermal decomposition of $Fe(CO)_5$ which leads to the formation of SWNT. This production method can yield a production rate of 450 mg/h of SWNT, and each batch has a purity level of ~97 % [48]. While all these synthesis methods provide a way to produce sufficient batches of CNT, controlled synthesis of CNT is needed particularly for SWNT. Production of SWNT with specific chirality and diameter could have significant implications for materials produced using SWNT for electrical and optical applications since these parameters govern the semi-conducting and metallic properties of SWNT.

In all current production methods for SWNT a typical batch contains impurities that consist of metal catalyst [43], amorphous carbon, and other non-SWNT crystalline carboneous materials. For this reason, it is necessary to remove these impurities to make efficient use of SWNT material. There have been many methods used to purify as-produced SWNT. Most purification processes while they remove impurities also result in the destruction of SWNT. The preservation of SWNT yield during purification is important. Most purification processes for SWNT involve oxidation of the SWNT material in either liquid or gas phase. The liquid phase occurs in an acid. Examples of acids include nitric or sulfuric acid [49, 50]. The major function of this liquid-phase oxidation or refluxing process is to remove the metal catalyst however; it has been shown that this process can also lead to the introduction of functional carboxylic groups on the

SWNT as well as defect sites. The gas-phase oxidation process is also a necessary step for SWNT purification, and this typically occurs in an oxygen environment. During gas-phase oxidation, the temperature and pressure of the furnace is varied to change the oxidation levels. Similarily in the liquid-phase, reflux time, temperature, as well as the acid molarities can be changed to vary oxidation level. A purification process developed for HiPCO™ tubes involve oxidation in a wet Ar/O_2 environment followed by sonication in HCl [51] to remove iron oxide particles. SWNT produced by the arc-discharge method have been purified by first refluxing in 3M nitric acid for 16 h producing a yield of 82 % of the original carbonaceous material. This process is followed by oxidation in air at 550 °C for 30 min and the final yield is only 20% of the original material. This material is further annealed at 1500 °C in vacuum [52].

1.2.2. Characterization of Carbon Nanotubes

There are several tools used to characterize the properties of carbon nanotubes including Raman spectroscopy, UV-VIS-NIR spectroscopy, X-ray diffraction, as well as TEM. Raman spectroscopy is a powerful technique for characterization of SWNT because of the strong resonant behavior associated with the one-dimensional electronic properties of the SWNT. Raman bands associated with the radial breathing mode (RBM) or A_g active bands, which occur due to the collective motion of all the atoms moving along the radial or circumferential direction of the tube typically occur between 150 to 450 cm^{-1}. The RBM peak positions are strongly dependent upon the SWNT diameter. Peaks observed within this frequency range can be used to estimate the diameter distribution in a given SWNT batch. The relationship between frequency wavenumber

(ν) and diameter (d_t) is $\nu(cm^{-1}) = 223.8/d_t(nm)$ [53]. These Raman modes can also be assigned to (n,m) chiral vectors, which are also related to the tube diameter. Raman bands between 1400 and 1700 cm^{-1} are associated with the tangential vibration of the carbon atoms along the longitudinal axis of the tube or E_g active modes, and are dependent upon the excitation laser frequencies. Raman profiles can also give information about the electronic structure of SWNT [54].

Absorption spectroscopy in the ultraviolet to near infrared region (UV-VIS-NIR) can also be used to provide useful information about SWNT. The electronic properties of SWNT are dictated by their structure therefore, if (n-m) is a multiple of 3 the tubes are metallic else they are semi-conducting. The semi-conducting and metallic properties of SWNT are associated with a specific density of states (DOS) where, the band-gap is related to tube diameter [55]. Lower energy van Hove transitions (associated with the DOS of SWNT) for metallic tubes can be observed between ~400 to 600 nm while higher energy transitions of semi-conducting tubes can be observed between ~550 to 1600 nm in the absorption spectra. Broadened and red-shifted van Hove features in the absorption spectra are associated with the aggregation of SWNT into small bundles while sharper features are associated with isolated tubes [56]. This tool can be used to probe the exfoliation status of SWNT in a solution or solid-state material. It also provides a picture for the electronic diversity of the types of SWNT present in a given production batch.

X-ray diffraction is another method that can be used to characterize SWNT since SWNT bundles can pack into either a 2-D hexagonal or trigonal crystal lattice (Figure 1.5). Typical X-ray profiles for SWNT powder show the presence of *(hk)* reflections [41, 42]. Although higher order *(hk)* peaks have been observed for well crystallized SWNT

samples [41], this is not typical due to the high curvature and entanglement of SWNT bundles. For most SWNT samples, the *(10)* and *(11)* peaks are the predominant features in X-ray patterns and can be used to determine the average diameter and monitor changes in inter-tube spacing in the SWNT bundle using equations one to three below.

$$d_{10}\ (nm) = \frac{\sqrt{3}a_o\ (nm)}{2} \tag{1.1}$$

$$d_{11}\ (nm) = \frac{a_o\ (nm)}{2} \tag{1.2}$$

$$a_o\ (nm) = d_t\ (nm) + d_i\ (nm) \tag{1.3}$$

Where d_t is SWNT diameter, and d_i is inter-tube spacing typically taken as 0.32 nm[57] for SWNT powder. Both *(10)* and *(11)* peaks show up as broad peaks except for well crystallized samples [41, 42].

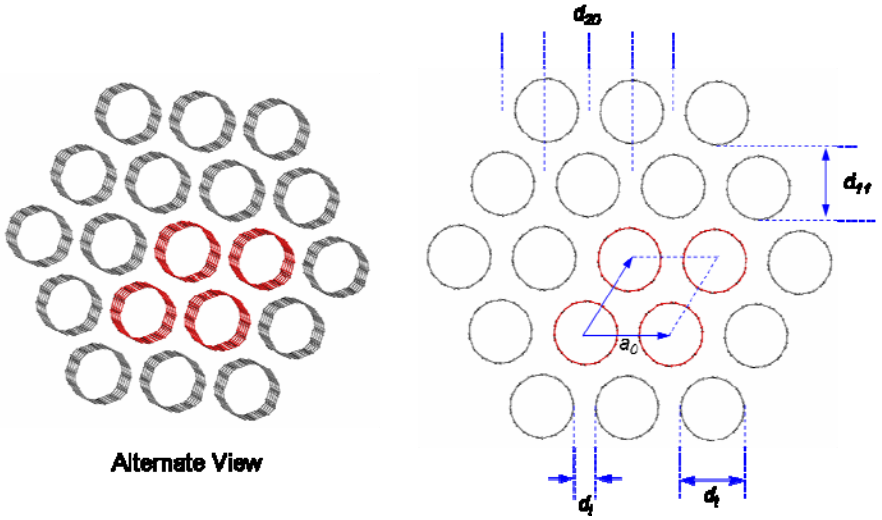

Figure 1.5. A schematic of the hexagonal crystal arrangement of SWNT in a bundle/rope.

Electron microscopy also provides a direct way for imaging SWNT. The first images of SWNT were obtained by TEM. SEM typically does not have the resolution to

image individual SWNT however; it can be used to observe SWNT ropes. Direct lattice imaging of CNT can be obtained by TEM. SWNT, DWNT, and MWNT can be distinguished clearly based on the number of sidewalls. TEM is also used to observe SWNT before and after purification procedures to see whether metallic nano-particles have been removed. Electron diffraction has also been used to measure the chiral distribution of tubes in a SWNT bundle [58] as well as the walls in MWNT [59]. Both SEM and TEM only provide small snapshots of the entire sample. Electron microscopy is a complimentary characterization tool along with spectroscopy and thermal characterization.

1.2.3. Properties of CNT

CNT have been shown to possess a unique combination of exceptional properties making them useful for mechanical, thermal, optical, electrical, and biomedical [60, 61] applications. Young's modulus for a (10,10) tube has been calculated to be 0.64 TPa [62]. Other calculated properties include E_1, E_2, and G_{12} which are the axial, transverse, and shear moduli while ν_{12} is the Poisson's ratio. The parameter values are 640 GPa for axial modulus [63]; 15 GPa for transverse modulus [64]; 19.5 GPa (1 nm), 6 GPa (5 nm bundle), and 1 GPa (20 nm bundle) for shear modulus [64-66]; and 0.17 for the Poisson's ratio [64]. Electrical conductivity for SWNT along the longitudinal direction can reach up to 10^6 S/m at 300 K [41]. Longitudinal electrical conductivity for MWNT has been measured to be 5000 S/m [67]. Although CNT are currently used for a wide variety of applications the commercialization of most materials especially those made using SWNT is limited because of high CNT cost (SWNT ~ $300 to 2000/g [68]).

1.2.4. SWNT-Polymer Composites

The production of polymer composites using a variety of fillers is not a new field. No material combining the dimensional and mechanical properties of SWNT has ever been available until recently. Their small dimensions mean a large surface area (~1300 m^2/g) which allows for much more surface interaction with the polymer matrix compared to conventional fillers like carbon fibers which have microscopic dimensions. The idea behind polymer/SWNT composites is to produce materials that will utilize the properties of both the polymer and the SWNT whether it is for mechanical, electrical, thermal, or optical applications. In this section the focus will be limited to the mechanical reinforcement in polymer/SWNT composites.

Most of the exceptional properties associated with SWNT are predicted for individual SWNT. Difficultly lies in the processing path for SWNT/polymer composites because of the existence of SWNT bundles due to strong van der Waals forces, and weaker interfacial interaction between SWNT and polymer. It is desirable to process composites that can take advantage of the properties of individual SWNT to obtain the maximum effect of SWNT in the composite. For this reason, dispersion and exfoliation of SWNT in the polymer matrix are key issues in polymer/SWNT composite processing. The initial work on polymer/SWNT composite materials has hinted at the evidence of interaction between the polymer matrix and SWNT. Composite fibers produced from polyacrylonitrile (PAN) [69], and poly(p-phenylene benzobisoxazole) (PBO) [70] have shown a reduction in thermal shrinkage. Since the shrinkage occurring in polymers are of an entropic nature the presence of SWNT act as a barrier to these actions, and the

polymer is not free to move about easily which indicates good polymer-SWNT interaction. Recent work on PAN/SWNT gel-spun fibers has shown that during fiber drawing the SWNT bundles are exfoliated [71]. During the drawing process, the PAN molecules are extended, and due to good PAN-SWNT interaction the SWNT bundles are dragged along and subsequently exfoliated.

1.2.5. Dispersion Methods

Dispersion and exfoliation are key issues in polymer-SWNT composite processing. As-produced SWNT materials are insoluble in organic solvents, making it difficult to process. Stable SWNT solutions have been obtained in strong acids where the acid protonates the SWNT therefore counteracting van der Waals forces between SWNT. The use of strong acids for materials processing is rather limited. This problem has been addressed in several ways which include chemical attachment of functional groups to SWNT, surfactant treatments, and sonication.

Chemical functionalization of SWNT is typically achieved by oxidation of SWNT[72]. This method leads to the shortening of SWNT [72], introduction of defects, and sometimes the large destruction of the graphitic structure of SWNT [73]. Further functionalization of SWNT with a polymers and proteins like DNA [74] can also be achieved by several methods. Functionalization of SWNT with proteins have been shown to improve the load transfer and cohesion between PVA matrix and the SWNT [75, 76].

Several surfactants have also been used to disperse SWNT, and these include sodium dodecyl sulfate (SDS), sodium dodecylbenzenesufonate (SDBS), Triton X-100,

cetyltrimethylammonium bromide (CTAB), dodecyltrimethyl ammonium bromide (DTAB), Tween, polystyrene sulfonate, and PEO-PPO-PEO triblock polymer [77-79]. The idea behind the use of surfactants as a dispersing agent for SWNT is to form a coating on the SWNT which will subsequently induce electrostatic repulsions between the tubes. The use of surfactants can become a problem since complete removal of the surfactant for later processing is very difficult and in most cases not possible. Phase diagrams produced for SDS/SWNT/water system shows that there is an optimal range for the SDS to SWNT concentration in order to obtain a homogeneously dispersed system [80]. The use of SDS has been very successful for producing SWNT dispersion where SWNT are exfoliated to individual SWNT. Absorbance spectra for SDS treated SWNT further stabilized with poly(vinyl pyrrolidone) (PVP) have been obtained and show the presence of individual SWNT[55]. SDS/SWNT/PVP systems have also been used with PVA to produce composite films at SWNT loading of 1 and 5 wt%, and these films show evidence of good load transfer between SWNT and matrix [81]. PVA/SDS/SWNT/collagen films produced with 4 wt % SWNT show an increase of 170 % in tensile strength and a 167 % increase in modulus as compared to PVA/SDS/SWNT (4 wt%) films [82]. Although the structure is not known for certain, experimental evidence suggests that surfactants like SDS form ordered domains on the surface of SWNT [83].

Sonication of SWNT in a variety of organic solvents is often preformed before processing with polymer. Debundling of SWNT can be achieved by sonication. This process can break the SWNT down to shorter lengths which is undesirable for processing

composites with high mechanical properties. In recent work, SWNT have been dispersed with little to no sonication with the use of ionic liquids [84].

1.3. PVA/SWNT Composites

Poly(vinyl alcohol) (PVA) has played a critical role in single wall carbon nanotube processing [75, 81, 85-88]. Macroscopic fibers from SWNT were for the first time processed in PVA solutions [80]. Super tough fibers have also been processed from PVA/SWNT composites [89, 90]. SWNT dispersed in polyvinyl alcohol (PVA) were used to make films at concentrations of 0.1 and 1 wt%. DSC studies of these PVA/SWNT films show the evidence of increase PVA degradation during second heating cycles as compared to control PVA films[91]. Increased toughness of polymer soaked SWNT buckypaper has been attributed to the load transfer between SWNT and polymer. Interfacial interaction between SWNT and polymer is expected from the knowledge that the polymer can crystallize on the surface of SWNT bundles [92]. The morphology study using SEM shows a sheath core structure, where the sheath is composed of densely aligned nanotubes bundles (caused by the flow of PVA), and the core consists of a loosely packed nanotubes (less aligned) bundles called “nanofelt”. The bundle size range is 10-30 nm. Absorption was studied using capillary condensation, and wetting was studied using droplet absorption. The pore size distribution of the fiber is 0.3 to 50 nm. The absorption isotherms of the fibers are comparable to buckypaper, there are both mesopores (hysteresis loops form which are typical of mesoporous solids) and micropores [93].

1.3.1. SWNT as a Nucleating Agent

Although both MWNT and SWNT have been used as reinforcement agents in the polymer matrix this work will primarily focus on the work of SWNT/polymer composites. Studies of SWNTs and MWNTs in polymer matrices are shown to nucleate crystallization. Multi-walled carbon nanotubes (MWNT) have been shown to improve polymer crystallinity in poly(ethylene terephthalate)[94], poly(ε-caprolactone) [95], poly(m-phenylenevinylene-co-2,5 dioctyloxy-p-phenylenevinylene) [96] composites. MWNT was also shown to nucleate alternate crystal structure growth in nylon 1010 [97], and polypropylene [98] composites. A number of recent studies demonstrate that single wall carbon nanotubes act as a nucleating agent for polymer crystallization [88, 99-108] including poly(vinyl alcohol) [109, 110], polypropylene [111], and polyethylene [112]. Polymer/SWNT studies show that a smaller crystallite size is found in the case of the composite versus the pure polymer [99, 106, 112], and this is indicative of the increased number of nucleation sites due to SWNT. Isothermal crystallization studies of polyethylene (PE)/SWNT composites show that onset of crystallization can occur earlier in the composites than the neat polymer, and the crystallization rate is faster in the composite [113]. In-situ polymerization of ε-caprolactone in the presence of SWNT leads to the formation of film nanocomposites containing ε-caprolactone functionalized SWNT in the polymer matrix with concentrations from 0.5 to 4.6 wt %. DSC results implied that the presence of SWNT in the ε-caprolatone matrix increased crystallinity, but crystal growth was much faster – possibly due to the increase of nucleation density because of SWNT [102]. Comparison studies on each nanocomposite as a function of SWNT concentration show little differences. In PVA/MWNT composites increased

sonication time provides more time for the entire MWNT free surface to be exposed to the free polymer allowing PVA to form surface layer [114]. Increased mechanical strength in Polymer/CNT composites can be expected in a nanocomposite when the polymer crystallization is readily promoted by the presence of CNT. This type of interaction will positively affect the mechanical properties of the nanocomposite [110].

1.3.2. SWNT Templated Crystallization and Orientation

Due to the high curvature of SWNT, it is unexpected for SWNT to template crystallization at the molecular level. When the SWNT and surrounding material have high interaction templating behavior is observed. Small molecules such as H_2SO_4 have been shown to form ordered structures induced by SWNT [115]. X-ray diffraction gives evidence of orientation. Proteins have been shown to crystallize in an ordered helical fashion on the surfaces of MWNT [116]. The MWNT that induces protein crystallization are of a specific size, and protein crystallization occurred consistently throughout the system. SWNT has also been shown to induce crystallization and orientation in the sheared polymer melt [117], and polymer melt containing aligned SWNT [118]. Polyethylene (PE) and nylon 66 have been shown to crystallize on the surface of both SWNT and MWNT to form nano hybrid shish kebab (NHSK) structures [100]. Recently PE oligomers have been shown to decorate the surface of SWNT by a mechanism of "soft-epitaxy"[101].

1.4. Interface/Interphase [119]

Studying the nature and morphology of interfaces/interphases is important for understanding adhesion, composites, blends, and dispersions. The interface can be defined as the boundary between the reinforcement component and the matrix, or the boundary between two matrices in a blend. The interphase also termed the interfacial layer or interfacial region is define as the inhomogenous region between two bulk phases where the properties do not match those of the bulk phase in a composite or blend. These property changes include compositional changes, molecular density, orientation, charge density, or electron density. Variations in the interphase occur in the direction normal to the bulk phases. Figure 1.6 describes both the interface and interphase pictorially. The properties of a composite result from the combined behavior of the reinforcement component (filler), matrix, and filler/matrix interface.

The types of interfacial bonding between reinforcement materials and matrix fall into three main categories: mechanical bonding, physical bonding, and chemical bonding. Mechanical bonding takes into account interlocking or gripping interactions between both materials. In the case of mechanical bonding, the presence of internal compressive forces on the reinforcement materials is usually detected [120, 121]. Physical bonding at the interface involves secondary, van der Waals, dipolar, or hydrogen bonding between the materials. Chemical bonding occurs when there is a reaction at the interface. Chemical bonding can be induced using coupling agents for glass fiber composites, or using surface treatments as in the case of carbon fibers. Test methods used to measure the degree of interfacial bonding in composites include flexural tests, bending tests, interlaminar shear

stress test (ASTM D2344), single fiber pullout tests, fragmentation tests [122], as well as indentation tests.

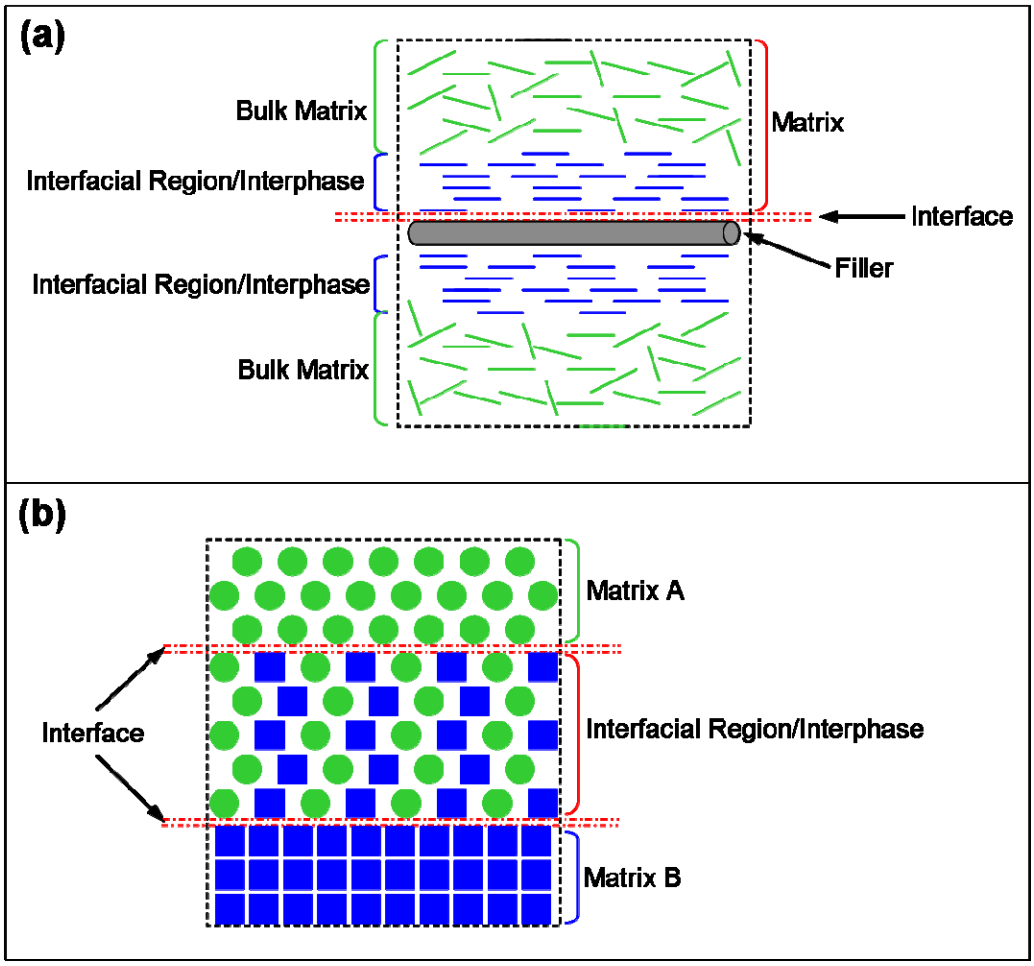

Figure 1.6. Schematic of (a) a composite, and (b) a blend showing both the interface and interfacial region/interphase.

1.4.1. Role of Interface/Interphase in Composites

Fabrication of composites has led to a class of materials with improved properties over conventional materials. Some of the common reinforcement materials used in composites are glass fibers, ceramic fibers, boron fibers, silicon carbide, carbon fibers, and organic fibers (oriented ultra-high molecular weight PE, and aramid fibers). Typical matrix materials include polymer, metals, and ceramic. It is important that the

components of the composite work together well. For this reason a well-bonded interface is desirable for composites. The composite will be weakened by flaws at the interface and will ultimately fail. A great deal of work has gone into studying the interface in composites and improving interfacial interactions. Most reinforcement fibers undergo some kind of surface treatment before being added to the matrix material in order to improve interfacial interactions.

To increase interfacial bonding in polymer/glass fiber composites, glass fibers are typically treated with silane molecules with the molecular formula R-SiX_3. The *R* group is usually compatible to the polymer and the *X* groups can be hydrolyzed in aqueous size solutions to form hydrogen bonds with the glass surface. Aramid fibers (e.g. Kevlar®), and high performance PE fibers (Dyneema®, and Spectra®) show poor adhesion to polymer matrices in composites. Hydrolysis of Kevlar can be carried out using acids (HCl, H_2SO_4) or a base (NaOH) to introduce functional groups on the surface for better matrix interactions [119]. Plasma treatment of PE fibers has been shown to increase surface roughness and add functional groups to the fiber surface to increase interfacial interactions [123, 124].

In order to increase bonding between the polymer matrix and carbon fibers oxidative treatment of the fibers with dilute nitric acid or dilute sodium hydroxide was performed to etch fiber surface and introduce surface groups [125]. Oxidative treatment of carbon fibers produce —CO_2H, —C-OH, and —C=O functional groups at the fiber surface. Surface treatment of carbon fibers has been shown to improve adhesion between the matrix and fiber due to the removal of the weak outer layer on the carbon fibers, and the introduction of functional groups which interact with the matrix [126]. Oxidation of

carbon fibers can be carried out in both the liquid [125, 127] and gas phase [128]. Another method used to increase interfacial interaction in carbon fiber composites is *whiskerization*. This involves the growth of silicon carbide single crystals on the surface of the fibers by chemical vapor deposition (CVD). Carbon fiber/epoxy composites which use whiskerized fibers show almost three times the interlamellar shear strength as compared to composites without whiskerized fibers[129]. The process of whiskerization is expensive and can also weaken the carbon fiber.

1.4.2. Role of Interface/Interphase in Nanocomposites

Nanocomposites are comprised of a field where the reinforcement material has at least one dimension in the range of few to tens of nanometers. Due to the size of nano materials composites can be reinforced with small amounts of these materials. Methods for synthesis of nanomaterials include hydrothermal synthesis, sol-gel synthesis, CVD, microwave synthesis, and high-energy ball mill processes [130]. The most widely investigated nanocomposites are layered silicate composites and CNT composites. Polymer/layered nanocomposites can be classified into three categories: intercalated, flocculated (aggregated), and exfoliated. For intercalated sample, the matrix material alternates almost periodically with the nano materials. For exfoliate nanocomposites the matrix is dispersed randomly around the nano material. In both theses cases the interaction between matrix and nanofiller is greatest and this translates to more interfacial regions.

Nylon-6/clay nanocomposites studied by X-ray and DSC show changes in crystallization and crystallinity in nanocomposites indicating some specific interaction at

the nylon-6/clay interface [131]. For a metal nanocomposite Al_2O_3/SiC and Al_2O_3/TiN interfaces were studied by measuring interfacial dihedral angles using TEM to determine the interfacial energy. It was found that SiC strength grain boundaries in the composites whereas TiN weakened grain boundaries and these properties were translated to the bulk composite properties [132]. TEM images PMMA/silica nanocomposites show that PMMA monomer forms a uniform coating on the silica particles and PMMA latex particles are formed during in-situ polymerization at the silica surface indicating good interfacial interaction between PMMA and silica [133]. Other nano materials have also been shown to interact near the interface with polymers that are able to intercalate into the material [134]. These materials include metal chalcogenides (e.g. $(PBS)_{1.18}$, and $(TiS_2)_2$), carbon oxides (e.g. graphite oxide), metal phosphates (e.g. $Zr(HPO_4)_2$), clays and layered silicates (e.g. montmorillonite, hectorite, saponite), and layered double hyroxides (e.g. $Mg_6Al_2(OH)_{12}CO_3\, nH_2O$).

1.4.3. Role of Interface/Interphase in Polymer/CNT Composites

Because of the perfect graphitic structure of CNT, they are atomically smooth. Surface roughness is introduced into CNT surface by the presence of defect sites, or attachment of functional groups to the surface. Unlike macroscopic composites the dimensions of CNT are so small that mechanical and physical bonding between the matrix and CNT is more likely. Chemical bonding can also occur when there are functional groups attached to the CNT surface that can interact with the matrix material. Single fiber pullout test performed using MWNT and polyethylene-butane show interfacial strength of 50 MPa [135]. Finite element simulation of functional-

MWNT/epoxy composite estimate that interfacial strengths as high as 5 GPa can be achieved when there is one chemical bond with the matrix per repeat unit of CNT [136]. Interfacial strength was shown to decrease to 500 MPa and 50 MPa when chemical bonding between the matrix and CNT was reduced to 5 bonds per 10 nm of CNT, and 3 bonds per 20 nm of CNT respectively [136]. Polymer molecules have been shown to wrap CNT leading to improved mechanical properties and crystallinity in the samples prepared [137, 138]. PAN/SWNT fiber prepared by gel-spinning show the presence of a well-crystallized interphase region [71]. Functionalization of MWNT with epoxide-based groups was performed in order to obtain entanglements and increase interaction between functional groups and epoxy at the epoxy/CNT interface [139]. Pull-out studies of MWNT and SWNT ropes in epoxy report interfacial strength of 35 to 376 MPa for MWNT and ~366 MPa for a 12 nm SWNT rope [140]. TEM image of these composites show a layer of epoxy coated on the CNT. In-situ studies of polystryrene (PS)/MWNT composites show that as the composite is fractured MWNT bridge the crack and do not break or pull out until the crack exceed ~800 nm. Improved mechanical properties of these composites show the evidence of good load transfer between PS and MWNT [141]. Understanding polymer properties near the polymer/CNT interface is important to address key issues about the optimization of mechanical properties in these composites.

There has been a tremendous amount of work in the literature dedicated to polymer/SWNT composites. A large percentage of this work reports about polymer/SWNT materials in which the SWNT are still in bundle form. Very little has been reported on polymer/SWNT nanocomposites where SWNT have been fully exfoliated [71]. The research challenge of dispersing and exfoliating SWNT is one that

requires much needed attention. Many have sought to answer this question by examining the solution properties of SWNT in different solvent systems, others use chemical methods to alter the surface structure of SWNT making them more compatible with solvents, and this process also alters the inherent properties of SWNT. Still others try to study the nature of interaction between different polymers and SWNT as a method for improving dispersion. In this work, we will focus on the third method of studying polymer-SWNT interaction by looking in detail at the nucleation capability of SWNT to crystallize polymers and change polymer morphology.

1.5. Thesis Objectives

The key objectives of this study are:

- To study carbon nanotube templated orientation and crystallization of poly(vinyl alcohol).
- To study the single crystal growth of polyvinyl alcohol under different growth conditions.
- To study the single crystal growth of poly(vinyl alcohol) in the presence of SWNT as a nucleating agent.
- To study the effect of carbon nanotubes on gelation, crystallization, and drawing behavior of poly(vinyl alcohol).
- To study the structure and properties of gel spun poly(vinyl alcohol)/carbon nanotube fibers.
- To study the interphase of polymer/carbon nanotube composites.

CHAPTER 2

CARBON NANOTUBE TEMPLATED ORIENTATION AND FIBRILLAR CRYSTALLIZATION OF POLY(VINYL ALCOHOL)

2.1. Introduction

Polymer orientation and crystallization are key steps needed to process polymeric fibers with modulus and tensile properties that approach theoretical values. CNT have been studied as reinforcement agents in polymer fibers, but their unique needle-like morphology has not yet been fully explored as a possible crystallization and orientation template for flexible polymers. As discussed in chapter 1 a number of recent studies demonstrate that SWNT act as a nucleating agent for polymer crystallization and the oriented template for small molecules. Also discussed, is the critical role of PVA in the processing of PVA/SWNT composite fibers and films. In this chapter, we report that stirred and sheared solutions of PVA result in the formation of isotropic fibers with low crystallinity, while under comparable conditions PVA/SWNT dispersions result in oriented fibers with high crystallinity.

2.2. Experimental

Atactic poly(vinyl alcohol) (PVA) (from Kuraray Co. Ltd., lot # 636837, degree of polymerization: 18,000, and 98.4 % hydrolyzed) was dissolved in an 80:20 volume ratio of dimethyl sulfoxide (DMSO) (from J.T Baker Cas. No. 67-68-5) and distilled water respectively in a 1 liter 3-necked round-bottomed flask equipped with a magnetic stir bar and Liebig condenser assembled for reflux and heated to 110 °C to obtain a 1

wt% PVA solution (80 ml DMSO, 20 ml water, and 1.1 g PVA). SWNT (obtained from CNI, lot# P-0247, purity > 98 %) (10mg/ml) dispersion was obtained in DMSO by sonicating (using a Fisher FS30 bath sonicator, frequency 43 kHz, power 150 W) for 12 h at 55 °C and subsequently added to the PVA solution to obtain PVA:SWNT weight ratio of 99:1. The mixture was stirred with an overhead mechanical stirrer (Caframo high shear mixer, model# BDC1850) at shear speeds between 500 RPM to 800 RPM continuously for 72 h. Dispersion was periodically sonicated for about ten minutes after every two hours while stirring. The same procedure was carried out for PVA solution without nanotubes. Macroscopic fibers formed in each solution within two hours of stirring, and no change was observed after about six hours. Continuous sonication results in dissolution of these fibers. Fibers were placed on a glass slide and dried in the hood for several days followed by drying under vacuum at 30 °C for 72-96 h.

2.2.1. Sample Characterization

Scanning electron microscopy (SEM) was done on LEO 1530 thermally assisted field emission microscope (accelerating voltage 10 kV) (manufactured by Carl Ziess Micro-Imaging Inc., Thornwood, NY, USA) on samples sputtered coated with gold. To reveal the internal fiber structure, both PVA and PVA/SWNT fibers were split using a needle for SEM observation. Transmission electron microscopy (TEM) was done using a Hitachi HF-2000 Field Emission Gun electron microscope (accelerating voltage 200 kV) (manufactured by Hitachi High Technologies America Inc., Pleasanton, CA, USA). TEM samples were prepared by taking a drop of fibril containing dispersion using a pipette and dropping it on lacey carbon coated 300 mesh copper grids (Electron Microscopy Sciences Cat. # 71140). Grids were dried in air under a hood for several

days. Raman spectroscopy was performed on a Holoprobe Raman microscope (manufactured by Kaiser Optical Systems Inc., Ann Arbor, MI, USA) at an excitation wavelength of 785 nm and 1.5 MW beam power. Leica DMRX Optical Microscope (manufactured by Leica Microsystems, Gemany) equipped with a Sony Digital Photo Camera DKC-5000 was used to image the fibers and study their birefringent behavior. Wide-angle X-ray scattering was done on the Rigaku Micro Max 002 X-ray generator operated at 45 kV and 0.66 mA and equipped with R-axis VI++ detector (manufactured by Rigaku/MSC, Inc., The Woodlands, TX, USA). For X-ray studies, single filaments were mounted on the tip of 0.3 mm diameter glass fibers (Hamilton Research Cat. # HR8-030). Crystallinity and orientation from wide angle X-ray diffraction were determined using the software MDI Jade 6.1. AreaMax software was used for background subtraction and integration. The area due to the crystalline and amorphous contribution of the polymer was determined by peak fitting analysis.

2.3. Results and Discussion

Diameter/width of both the PVA and PVA/SWNT self-assembled fibers/ribbons is in the range of 5 μm to 45 μm, and the length is typically from 0.5 mm to 3 mm. Both the PVA and PVA/SWNT fibers are composed of fibrils ranging from about 100 nm to 800 nm in diameter (Figure 2.1). The PVA/SWNT fibrils also appear to consist of nano fibrils ranging from 25 nm to about 100 nm in diameter, while the PVA fibrils did not show the obvious presence of nano fibrils. In the case of both PVA and PVA/SWNT fibers the fibril formation with respect to the macroscopic fiber demonstrate some degree of ordering, and this may be induced by the shear forces in the flow field (Figure 2.2).

Wide-angle x-ray scattering (Figure 2.3) and polarizing optical microscopy, both show that PVA fibers are isotropic, while PVA/SWNT fibers are oriented (Figure 2.4a and 2.5).

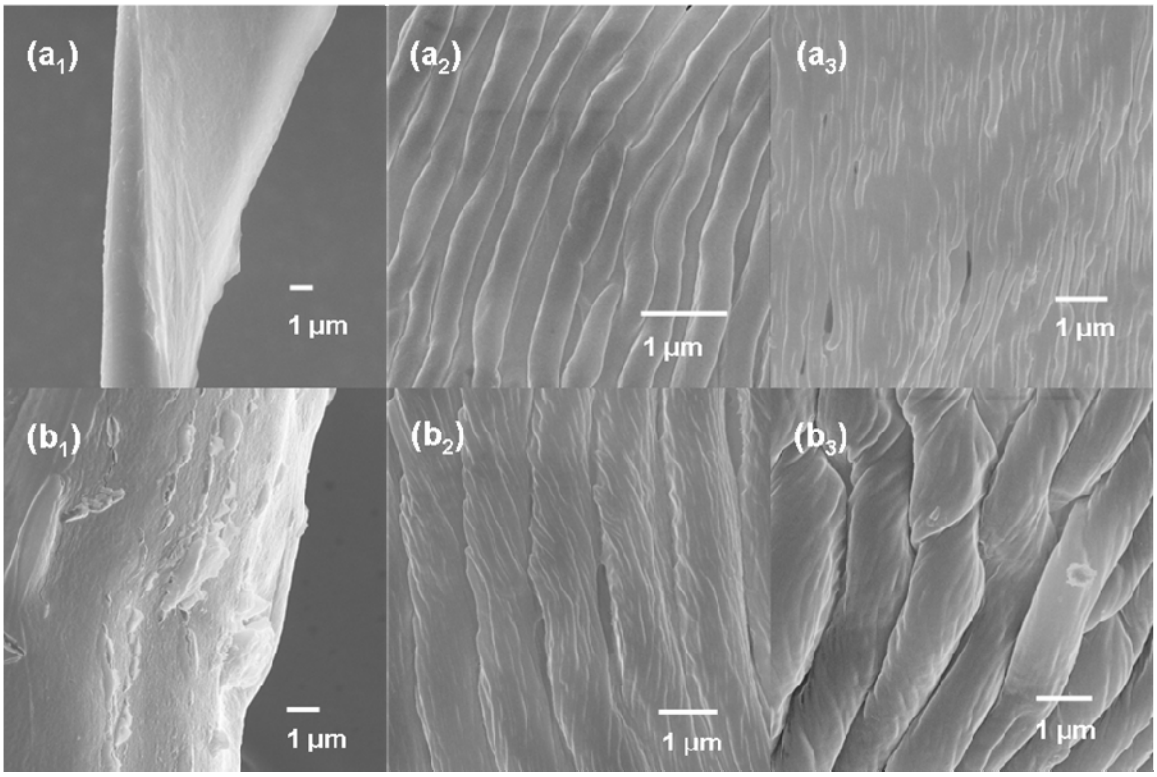

Figure 2.1. Scanning electron micrographs of self-assembled (a) PVA and (b) PVA/SWNT fibers. (a_1, b_1) fiber surface, (a_2, a_3) and (b_2, b_3) internal surface obtained by fiber splitting.

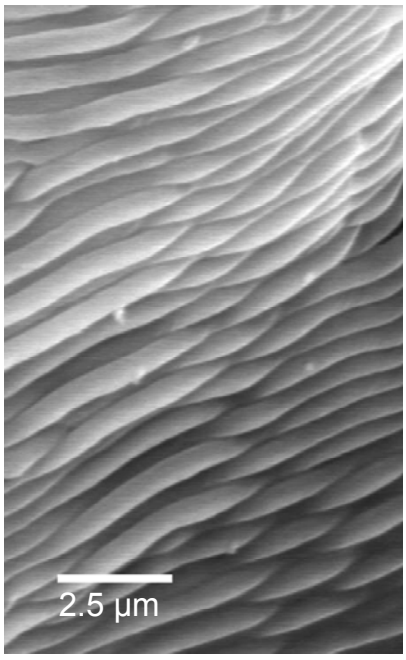

Figure 2.2. Scanning electron micrograph of patterned arrangement of fibrils in a PVA macroscopic fiber.

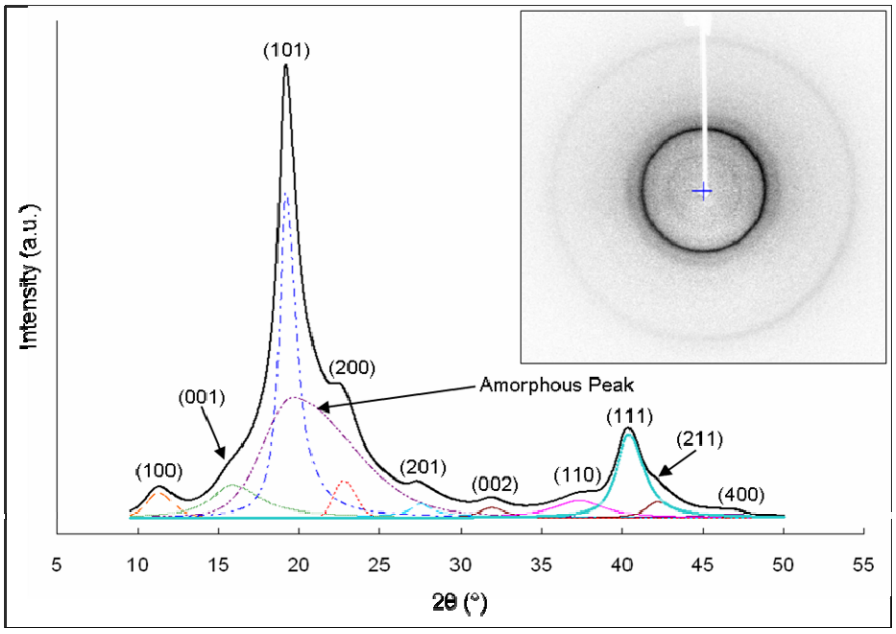

Figure 2.3. Peak fitted integrated X-ray diffraction intensity as a function of 2θ of self-assembled PVA fiber. Inset: wide-angle X-ray diffraction pattern with vertical fiber axis.

Wide-angle X-ray diffraction (WAXD) of the self-assembled PVA fibers show strong intensity (101) peak (Figure 2.3), which is also the case for solution spun and drawn PVA fibers [142, 143]. In the self-assembled PVA/SWNT fibers, medium intensity (101) reflection is observed as a four-point pattern at 32.2º off the meridian. Strong intensity (200) reflection is present on the equator, and the (102) plane is on the meridian (Figure 2.4b). Various crystal sizes determined from WAXD data using Scherrer equation [144] (using K= 0.9) as well as d-spacing values in both PVA and PVA/SWNT fibers are listed in Table 2.1. The crystallinity in self-assembled PVA and PVA/SWNT fibers, determined using crystalline and amorphous peak areas, was about 48 % and 84 %, respectively (Figures 2.3 and 2.4a). It is noted that crystallinity in gel spun PVA/SWNT fiber (draw ratio 6), containing 3 wt% SWNT was only ~53 % [88]. It is noteworthy that 84 % crystallinity in the current work is without annealing or drawing.

Table 2.1. Wide-angle X-ray determination of d-spacing and crystal size for predominant *(hkl)* planes in both self-assembled PVA and PVA/SWNT fiber diffraction patterns.

	PVA/SWNT Fiber			**PVA Fiber**		
Diffraction Plane	**2θ (°)**	**d-spacing (nm)**	**Crystal Size (nm)**	**2θ (°)**	**d-spacing (nm)**	**Crystal Size (nm)**
(100)	—	—	—	11.3	0.785	4.2
(001)	15.5	0.571	3.1	15.8	0.559	2.2
(101)	20.4	0.434	6.3	19.5	0.453	6.6
(200)	22.9	0.387	6.2	22.7	0.390	5.8
(102)	34.5	0.259	9.7	—	—	—
(111)	—	—	—	40.3	0.201	4.3

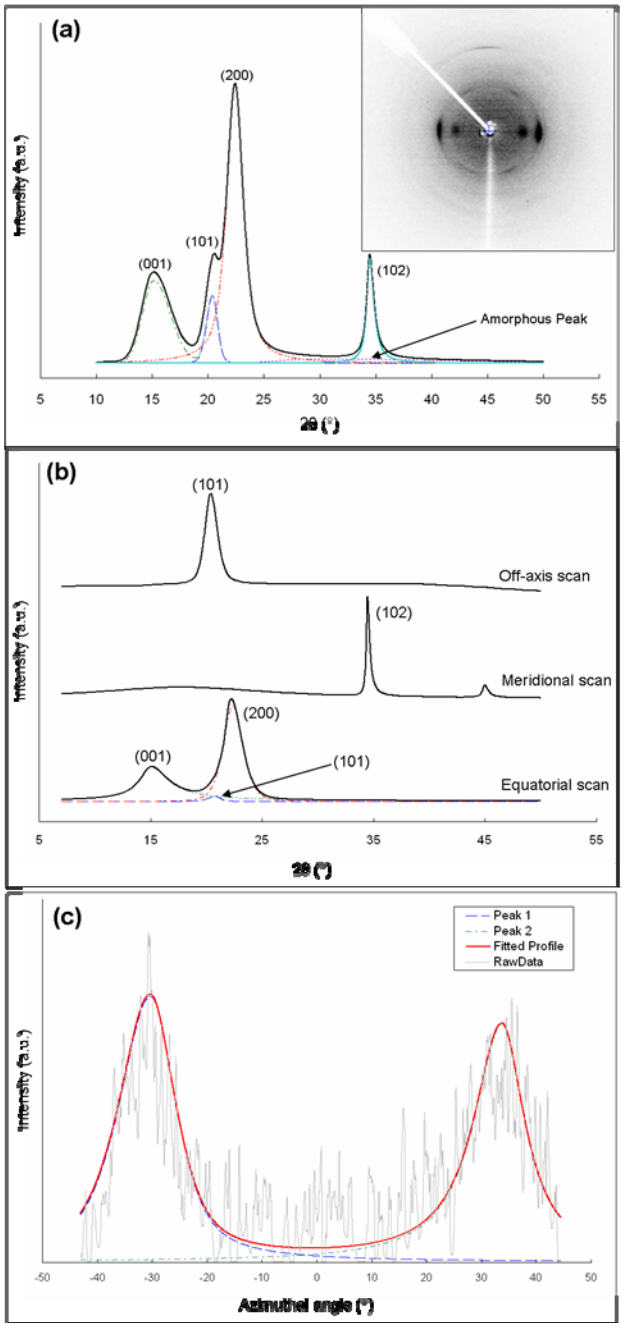

Figure 2.4. Wide-angle X-ray diffraction of self-assembled PVA/SWNT fiber. (a) Peak fitted integrated intensity as a function of 2θ. Inset: wide-angle X-ray pattern with vertical fiber axis. (b) Equatorial, meridional, and off-axis (32.2° from the meridian) intensity as a function of 2θ. (c) Azimuthal intensity plot for the (101) diffraction plane. 0° represents the meridional direction.

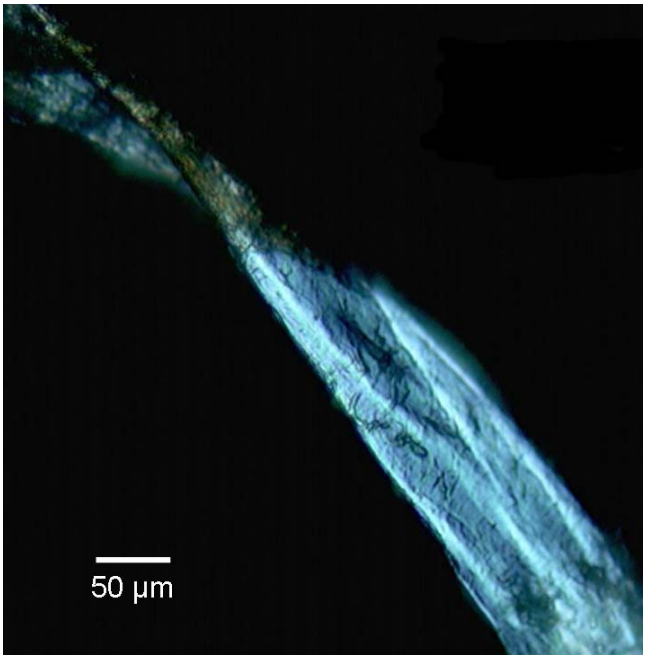

Figure 2.5. Optical micrograph of self-assembled PVA/SWNT fiber under cross polarizers. Fiber axis is at 45° to the polarization direction.

PVA orientation factor, f_b, was determined from (200) and (001) diffraction planes using Wilchinsky's equation [145]:

$$\overline{\cos^2\theta_{b-axis}} = 1 - \frac{(1-2\sin^2\rho_2)(\overline{\cos^2\phi_1}) - (1-2\sin^2\rho_1)(\overline{\cos^2\phi_2})}{\sin^2\rho_1 - \sin^2\rho_2} \tag{2.1}$$

Where,

$$f_b = \frac{3\left\langle\overline{\cos^2\theta_{b-axis}}\right\rangle - 1}{2} \tag{2.2}$$

The subscripts, 1 and 2 refer to the two planes, (200) and (001), used in the orientation characterization, and ρ is the angle between the given plane normal and the a- or c-axis. PVA unit cell parameters are [146]: a = 7.81 Å, b = 2.52 Å, c = 5.51 Å, β = 91.7°. Thus, ρ values for (200) and (001) are calculated with respect to the a-axis to be 0° and 88.3°, respectively. The (200) and (001) azimuthal intensity was used to calculate $\overline{\cos^2\phi_{h0l}}$ for

the two planes. Using this approach $\overline{\cos^2 \theta_{b-axis}}$, and f_b in the PVA/SWNT fiber was calculated to be 0.82, and 0.72, respectively giving PVA misorientation angle, θ_{b-axis} of about 26° with respect to the fiber axis.

Figure 2.4c shows the (101) intensity as a function of azimuthal angle. The angle between (101) plane normal and the self assembled fiber axis (α) was calculated using the following equation [147].

$$\cos\delta = \frac{\cos\alpha}{\cos\theta} \tag{2.3}$$

Where δ is the azimuthal angle between the diffraction maximum and the meridian direction as measured from the X-ray, and θ is the (101) Bragg angle. The values for δ and θ measured from WAXD were 32.2º and 10.2°. From these parameters, α was calculated to be 33.6°, while the theoretical value based on above listed unit cell parameters would be 35.2º. Peak-fitting analysis of the equatorial WAXD scan of the self-assembled PVA/SWNT fiber also shows a low intensity (101) peak on the equator (Figure 2.4b), suggesting two distinctly different orientations of the PVA molecules in the self-assembled fiber.

The presence of SWNT in fibers assembled from PVA/SWNT dispersion was confirmed by Raman spectroscopy (Figure 2.6a), where the Raman spectrum of the self-assembled fiber is compared to the spectrum of the SWNT powder. Due to resonance enhanced Raman scattering, SWNT intensity dominates and no PVA peaks were observed in the Raman spectra even at this low SWNT concentration. As can be seen in Figure 2.6, Raman spectrum of the PVA/SWNT fiber is nearly identical to the SWNT

powder spectra. Polarized G-band Raman intensity as a function of the angle between the polarization direction and fiber axis is given in figure 2.6c. The average SWNT orientation with respect to the fiber axis was calculated using a previously described method [65, 71] from the polarized Raman G-band intensity as a function of polarization angle. SWNT orientation factor was determined to be 0.44, which yields an approximate SWNT orientation angle of about 38° from the self-assembled fiber axis.

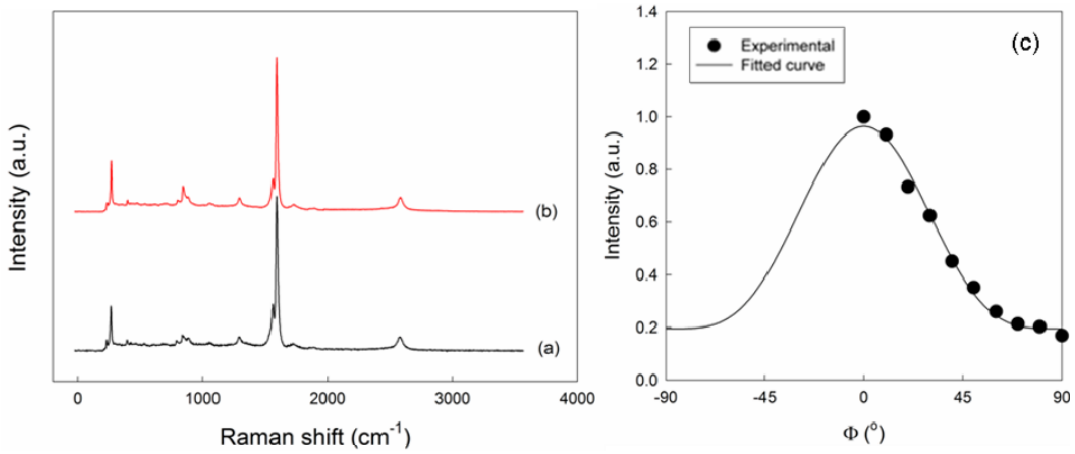

Figure 2.6. Raman spectra of (a) SWNT powder and (b) self-assembled PVA/SWNT fiber. (c) Polarized tangential mode (G-band) Raman intensity of the self-assembled PVA/SWNT fibers as a function of angle between polarization direction and the fiber axis.

High-resolution transmission electron micrograph (HR-TEM) in Figure 2.7a shows a PVA/SWNT nano fibril of about 120 nm diameter. Higher magnification lattice images of this nano fibrils (Figure 2.7b and 2.7c) show well resolved (200) lattice planes as well as the presence of SWNT. (200) plane and hence the b-axis (the PVA chain axis) is parallel to the SWNT axis and both are in turn perpendicular to the nano fibril axis. Moire [148] patterns can also be seen in Figure 2.7b (indicated by arrow). Figure 2.7 shows significantly larger crystal sizes, both along and perpendicular to the b-axis

direction, than the average crystal sizes observed from X-ray. It is also noted that PVA/SWNT fibrils were highly resistant to the electron beam. Under comparable electron beam irradiation conditions, PVA samples without nanotubes could not be lattice imaged. WAXD and Raman spectroscopy show PVA and SWNT orientation. However the two orientation values were somewhat different. HR-TEM (Figure 2.7) provides evidence that PVA molecules are oriented parallel to the nanotube axis.

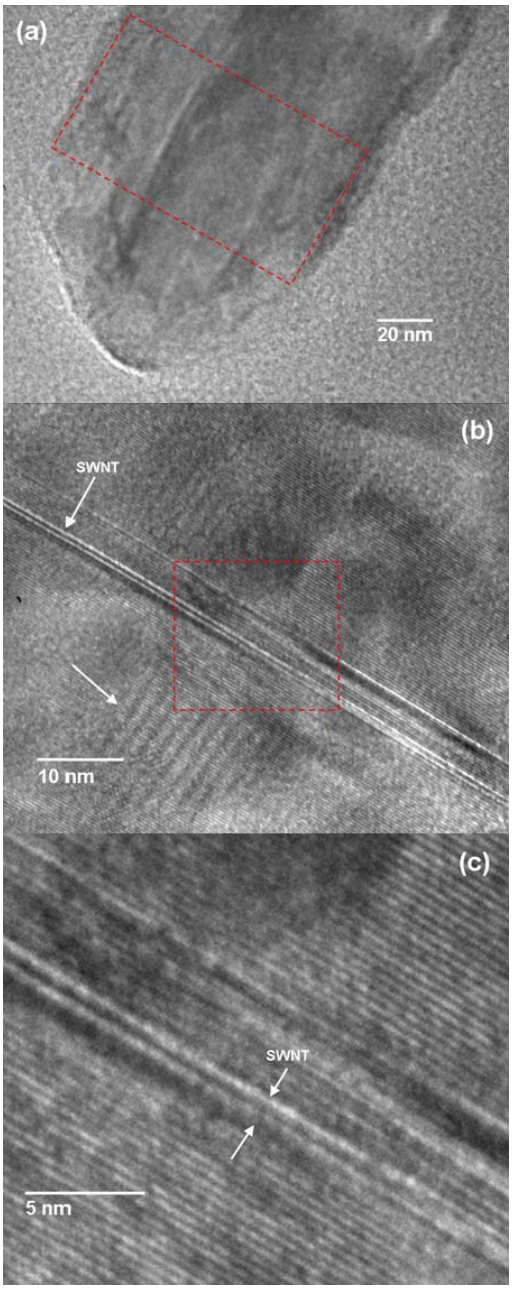

Figure 2.7. (a) High-resolution transmission electron micrographs of self-assembled PVA/SWNT nano fibril (b) is a higher magnification image of the boxed region in (a). (c) is a higher magnification image of the boxed region in (b). Nano fibril diameter is about 120 nm. SWNT and PVA (200) lattice planes (d-spacing ~0.385 nm) parallel to SWNT axis can clearly seen in (b) and (c).

2.4. Conclusions

In summary, we conclude that the presence of SWNT, results in significantly enhanced polymer crystallinity, and that SWNT act as a template for polymer orientation.

While there are a number of previous studies in the literature reporting enhanced crystallinity and crystallization rate [149] in polymers in the presence of carbon nanotubes and particularly single wall carbon nanotubes, here it is observed that SWNT templated polymer orientation occurs in solutions. SWNT templated polymer orientation has also been reported recently during melt processing [117]. Polymer orientation facilitated by the presence of fully exfoliated SWNT may have implications for polymer processing.

CHAPTER 3

SOLUTION GROWN SINGLE CRYSTALS OF POLY(VINYL ALCOHOL)

3.1. Introduction

PE and PVA share a similar planar zig-zag chain structure. However, from crystal lattice calculations the predicted modulus of PVA is higher than that for PE (~255 and ~240 GPa respectively) because of inter- and intra-chain hydrogen bonding in PVA [150]. Hydrogen bonding has been a drawback in PVA fiber processing and results in limitations in the drawing process. This reduces the chain orientation and the ultimate tensile properties [151, 152]. An in-depth study of PVA crystallization is therefore needed to understand chain-to-chain interactions during crystallization. Atactic PVA single crystals were first observed in the 1960s [153-155]. PVA single crystals were grown in several solvent systems including triethylene glycol, ethylene glycol, and 1,3-propanediol at elevated temperatures typically between 80 to 170 °C over a period of 1-3 days. These single crystals were parallelograms in shape due to directional growth along the (100) plane. Electron diffraction of these single crystals show predominant reflections for both the (101) and (200) peaks. Since 1960s, there has not been any significant body of literature focused on the single crystal growth of PVA [49, 146, 153-157]. To the best of our knowledge, there have been no attempts to grow PVA crystals in solution below 80 °C. Lowering the crystallization temperature can reduce thermal strain and dislocation density and therefore increase crystal perfection, and avoid polymorphic phase changes in the crystals [158]. In this chapter, we discuss PVA single

crystals grown at 25, 50, and 60 °C in H_2O: dimethyl sulfoxide (DMSO) mixtures over different time scales. These crystals exhibit several different morphologies and each distinct type of morphology is associated with differing amounts of crystal perfection and electron irradiation stability.

3.2. Experimental

3.2.1. Room Temperature (25 °C) Single Crystal Growth

Atactic poly(vinyl alcohol) (PVA) (from Kuraray Co. Ltd., lot # 636837, degree of polymerization 18,000, and 98.4 % hydrolyzed) was dissolved in 80:20 volume ratio of dimethyl sulfoxide (DMSO) (from J.T Baker Cas. No. 67-68-5) and distilled water at temperatures between 110 °C to 120 °C (flask equipped with condenser) to obtain a 1 wt% PVA solution (80 ml DMSO, 20 ml water, and 1.1 g of PVA). The PVA solution was stirred with an overhead mechanical stirrer (Caframo high shear mixer, model# BDC1850) at shear speeds between 500 RPM to 800 RPM continuously for 72 h. The solution was periodically sonicated for about ten minutes after every two hours while stirring. Macroscopic fibers formed in each solution within two hours of stirring, and no change was observed after about six hours. Continuous sonication results in dissolution of these fibers. Characterization of the self-assembled macroscopic fibers has been reported separately [159]. For crystallization at room temperature (25 °C) the polymer solution was diluted with distilled H_2O until the DMSO:H_2O volume ratio was 2:98. The polymer concentration for the solution used for room temperature crystallization was 0.02 wt%. The diluted PVA solution was allowed to stand in sealed flasks for months at room temperature. The diluted solution was periodically (about once a month) observed in the

transmission electron microscope, by placing a droplet on a Lacey carbon coated transmission electron microscope (TEM) grid (Electron Microscopy Sciences, HC200-Cu). Single crystals, were first observed after ~ 12 months of the initial dilution of the solution.

3.2.2. Elevated Temperature Single Crystal Growth

For PVA single crystal growth at elevated temperatures of 50 and 60 ºC a 0.4 wt% PVA solution was obtained by dissolving PVA in 80:20 ratio of DMSO and distilled H_2O at temperatures between 85 to 90 ºC. Isothermal crystallization occurred as the solution was kept constant at 50 and 60 ºC respectively. Precipitates were observed by eye after ten and seven days at 50 and 60 ºC respectively. PVA single crystals were collected on Lacey carbon coated TEM grids and on clean glass slides for further analysis.

3.2.3. Sample Characterization

Scanning electron microscopy (SEM) was performed on a LEO 1530 thermally assisted field emission microscope (at 10 kV) on samples sputtered coated with gold, and non-coated samples were observed using a Zeiss SEM ULTRA60 (manufactured by Carl Zeiss Inc., Thornwood, NY, USA) (at 5 kV) (single crystals samples collected on the TEM grids as described above were also used for SEM observation). Transmission electron microscopy (TEM) was performed using both JEOL 100CX II and JEOL 100C (accelerating voltage 100 kV), and JEOL 4000EX (accelerating voltage 400 kV) electron

microscopes. For electron diffraction, camera length was calibrated using evaporated aluminum standard (Electron Microscopy Sciences, Cat. # 80044).

3.3. Results and Discussion[†]

3.3.1. Room Temperature (25 °C) Single Crystal Growth

Polyvinyl alcohol (PVA) single crystals formed at room temperature (25 °C) in diluted PVA solutions over a period of several months, and showed several distinct morphological features (Figure 3.1). These PVA single crystals were slowly crystallized over long growth times (several months) at room temperature, rather than previously reported short time scales (1-3 days) at elevated temperatures (from 80 °C to 170 °C in solution) [154, 155]. These single crystals at low magnification in the electron microscope appear to be either thick agglomerations of well-formed PVA diamond-shaped platelets (Figure 3.1a) or irregularly shaped thin particles (Figure 3.1b). At higher magnification these irregular particles are shown to consist of many small diamond shaped platelets that have agglomerated into the larger irregular-shaped thin particles (Figure 3.1c).

[†] *Definition for crystallographic symbols used throughout discussion:* [ ] *refers to Miller indices of a lattice direction,* ⟨ ⟩ *refers to all symmetrically equivalent Miller indices of a lattice direction,* ( ) *refers to Miller indices representing a crystal face/plane, and* { } *refers to all symmetrically equivalent Miller indices representing crystal faces/planes.*

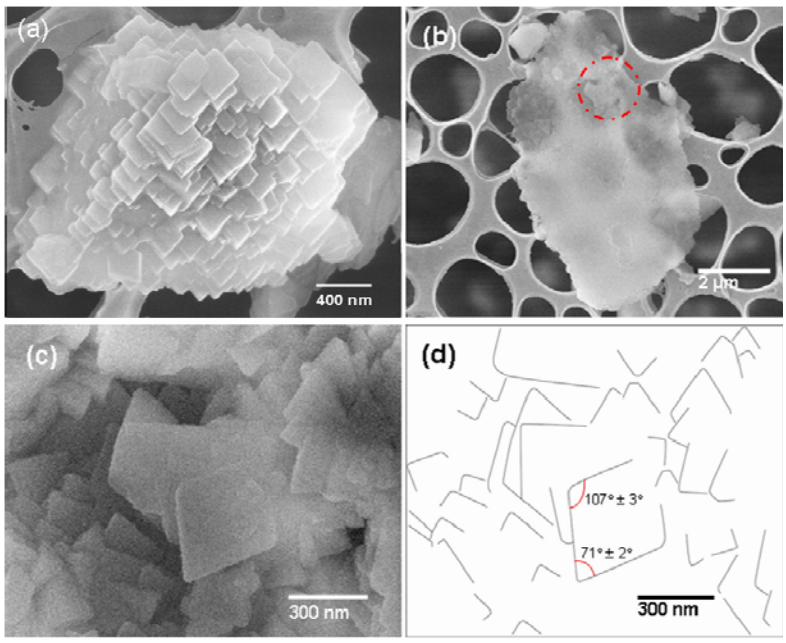

Figure 3.1. Scanning electron micrographs of PVA single crystals. (a) stacked diamond single crystals, (b) irregular agglomeration of diamond platelet single crystals, and (c) higher magnifications of diamond platelets. (d) Schematic of SEM image in (c).

The lamellar thickness for the individual diamond platelets has been estimated from electron microscope observations to range from ~ 15 to 20 nm. This thickness is consistent with the literature where it has been reported that PVA single crystal lamellar thickness ranges from 10 to 15 nm [49]. The geometry of the diamond platelets was examined, and from SEM, the obtuse and acute angles of the PVA diamond platelet crystals were measured to be 107° ± 3° and 71° ± 2° respectively (Figure 3.1d and Table 3.1). Based on the known monoclinic PVA unit cell parameters determined by Bunn [146] ($a = 0.781\,nm$, $b = 0.252\,nm$, $c = 0.551\,nm$, and $\beta = 91.7^{\circ}$), the obtuse and acute angles for (101) growth planes were calculated to be 107.3° and 69.3° respectively (Figure 3.2a). This agreement between experiment and theory suggests that the diamond shape of the platelets is the result of (101) growth facets. Electron diffraction of the

diamond platelets shows (*h0l)* reflections (Figure 3.3a), consistent with the (101) growth facets.

Table 3.1. Theoretical and observed angles for PVA crystals grown at 25, 50, and 60 °C. Theoretical values were calculated using Bunn's unit cell [146] for the given *(hkl)* planes.

Temperature (°C)	Schematic (Crystal shape observed)	Theoretical		Experimental	
		Obtuse	Acute	Obtuse	Acute
25	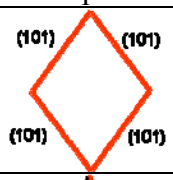	107.3°	69.3°	107 ± 3°	71 ± 2°
50	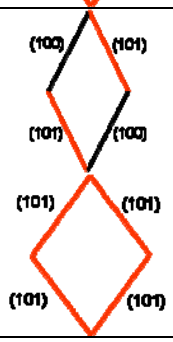	126.3° 107.3°	53.7° 69.3°	124 ± 1° 114 ± 5°	58 ± 2° 63 ± 2°
60	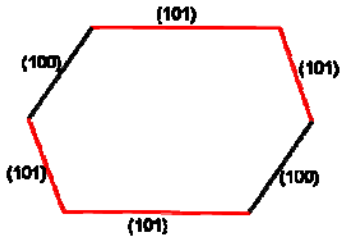	$(\bar{1}01) \angle (100) =$ 122.9° $(101) \angle (100) =$ 126.3° $(\bar{1}01) \angle (101) =$ 107.3		121 ± 2° 124 ± 2° 115 ± 5°	—

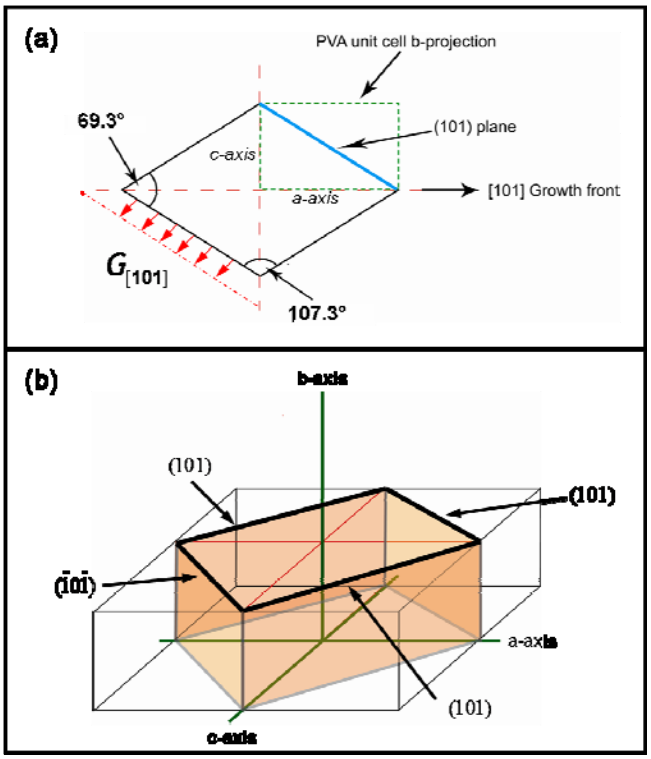

Figure 3.2. Schematic of (a) diamond-shaped PVA crystal showing crystal geometry and [101] growth front ($G_{[101]}$), and (b) (101) plane symmetry in four adjacent PVA unit cells.

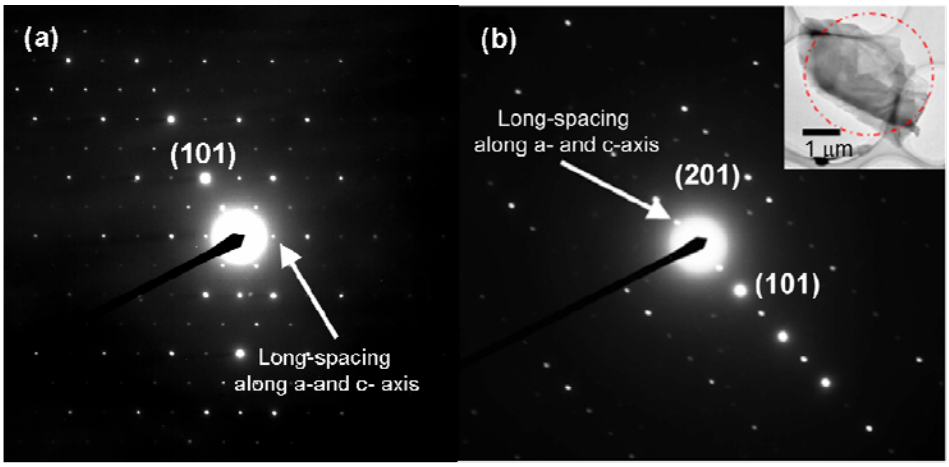

Figure 3.3. Electron diffraction of PVA single crystals showing (a) *(h0l)* reflection with (101) peak identified, and (b) 2-D symmetry after sample has been tilted in the electron microscope.

Table 3.2. List of *(h0l)* d-spacing's observed in electron diffraction pattern for PVA single crystal grown at 25 °C. Theoretical values are also listed.

(hkl)	$d_{spacing}$ **(nm)** *(theoretical)*	$d_{spacing}$ **(nm)** *(experimental)*
***(h0l)* reflections observed**		
(101)	0.449	0.451
(202)	0.224	0.223
(303)	0.151	0.146
(404)	0.111	0.109
(102)	0.257	0.254
(204)	0.128	0.127
(306)	0.085	0.084

Further evidence for the (101) growth facets is found in the electron diffraction patterns taken from the PVA diamond platelet agglomerates which show only the presence of (*h0l)* reflections (Figure 3.3a). By tilting the sample stage in the microscope slightly with respect to the electron beam an electron diffraction pattern with 2-D symmetry where *(h0l)* reflections can be observed (Figure 3.3b). Table 3.2 lists the main reflections and spacing's observed in the electron diffraction patterns as compared to their theoretical values calculated from Bunn's monoclinic PVA unit cell. Only reflections from planes parallel to the chain axis *(h00, 00l, h0l)* are expected when the molecular axes are normal to the crystal lamellar surface. The existence of only *(h0l)* reflections in the diffraction pattern observed implies that the b-axis or chain axis of the PVA molecule is normal to the crystal lamellar surface. The upper bound lamellae thickness (10 to 20 nm) is considerably shorter than the contour length of the PVA chains

(4536 nm)[‡], suggesting folded chain conformation. It has been shown that PVA molecules do have the flexibility to exist in the folded chain conformation [49].

In the literature, PVA single crystals are typically grown at temperatures between 80 to 170 °C over a period of 1 - 3 days [154, 155], while the crystals in the present work were grown at room temperature over a period of several months. Literature reported PVA single crystals grown at elevated temperatures exhibit low degree of perfection [153] and electron diffraction only show strong first order (101) and (200) reflections. Slow crystal growth is expected to result in an increase in crystal perfection. Electron diffraction of these room temperature PVA single crystals shows strong diffraction spots up to the eight orders for *(h0l)* reflections. Previous reports on well-formed polyethylene diamond-shaped single crystals show electron diffraction patterns which show up to seven orders for predominant *(hk0)* (i.e. (110) and (200)) reflections [160].

The electron diffraction pattern for these single crystals also show six symmetrical spots around the center spot (see arrow in Figure 3.3a). Further analysis of the electron diffraction patterns for these slowly grown single crystals show the existence of *extra spots* in the electron diffraction patterns (Figure 3.3a). The observance of *extra spots* otherwise known as *secondary spots* in an electron diffraction pattern is not uncommon [161]. This type of pattern has also been observed for polyethylene diamond-shaped crystals [6, 162]. The existence of *secondary spots* has previously been

---

[‡] *The contour length is taken as the maximum end-to-end distance of the chain in the all-trans conformation. The repeat unit length is 0.252 nm (calculated using the bond angle* $\angle C-C-C = 109.5^{\circ}$ *and bond length* $C-C = 0.154\ nm$*) and the degree of polymerization for the PVA molecule is 18,000, therefore the contour length,* l *is 4,536 nm.*

explained in terms of kinematic theory of diffraction for spots observed in polyethylene single crystals [163, 164]. Each *secondary spot* occurs at exactly double the d-spacing of a primary spot. For example, in the diffraction pattern the measured d-spacing of the (101) refection is 0.454 nm, and the d-spacing of the *secondary spot* occurs at 0.908 nm (Figure 3.3). A spacing of 0.908 nm is much larger than the longest axis for the PVA unit cell ($a = 0.781\,nm$), therefore it is not expected to observe such large spacings. These large spacings are all observed with respect to the *(h0l)* reflections, and are consistent with large crystalline growth and perfection along the *a*- and *c*- axes (Figure 3.3a). The *secondary spots* observed arise from rotational differences between individual lamellar layers in the single crystal platelets. This concept is described in the Figure 3.4.

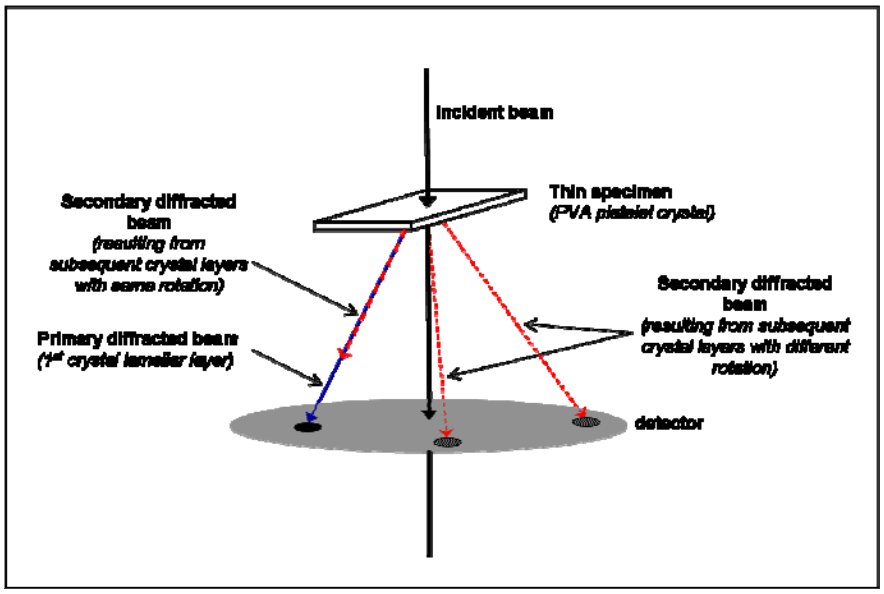

Figure 3.4. Schematic describing the primary and secondary diffraction of the incident electron beam from a layered specimen in the electron microscope.

Destruction of the polymer lattice within the polymer single crystal by electron beam damage and cross-linking is typically instantaneous during imaging in the electron

microscope. These results in the presence of amorphous regions/structures within the single crystal which can be detected in the electron diffraction pattern by the presence of an amorphous halo superimposed on the diffraction spots from the crystal. It has been estimated that bombardment of electrons on the single crystals will result in disruption of the crystal lattice, and these disruptions result in diffusion (azimuthal arching) of the crystal diffraction spots [36]. The greater the distortion in the lattice the more diffused the diffraction spots become. For this reason, polymer single crystal samples used in electron microscopy are observed using different methods (e.g. the use of low excitation voltage < 80 kV) to reduce electron beam damage [11].

In this work, PVA single crystals show strong electron irradiation resistance and maintain crystal structure and diffracting power beam strengths of 100 and 400 kV. Electron diffraction patterns of PVA single crystals show almost no change after 100 seconds at 100 kV (Figure 3.5) and diffracting power is maintained. At beam strength of 400 kV, crystal diffracting power lasts for up to 4 minutes (Figure 3.6). Figure 3.7 shows a schematic for the two types of arrangements of single crystal platelets in the agglomerations. The crystal in Figure 3.5 is of *type I* and after beam exposure the amorphous PVA was burned away (Figure 3.5b_2) leaving behind a polka-dot pattern. The crystal agglomeration shown in Figure 3.6 was of *type II*, and there is not change to the crystal shape after beam exposure. In addition, crystal lattice images can be taken during this time (Figure 3.8).

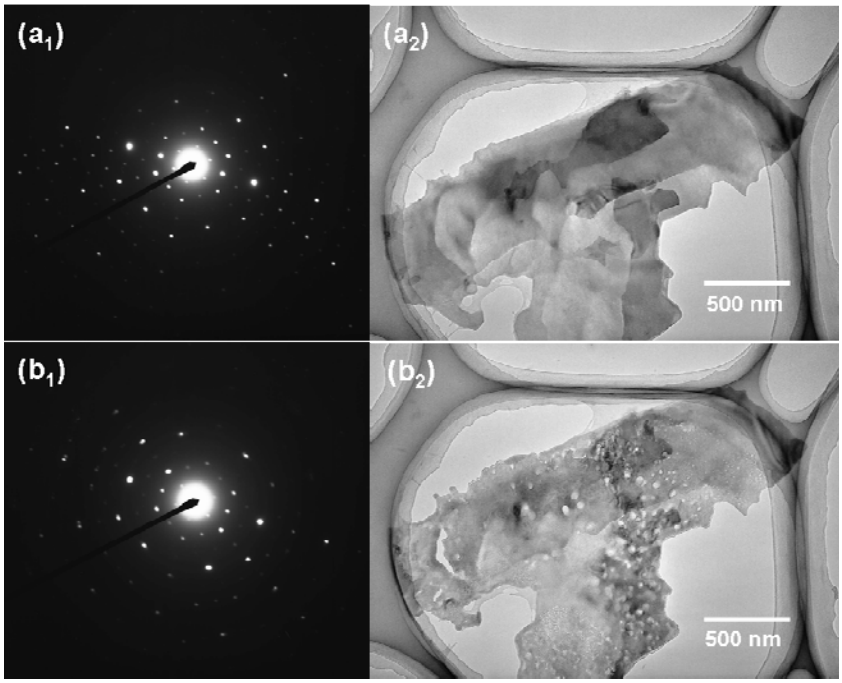

Figure 3.5. TEM micrographs and electron diffraction patterns taken at 100 kV for PVA single crystal grown at room temperature (25 °C) (a_1, a_2) with no electron beam irradiation damage, and (b_1, b_2) after being exposed to the electron beam for ~100 seconds showing very little electron beam damage.

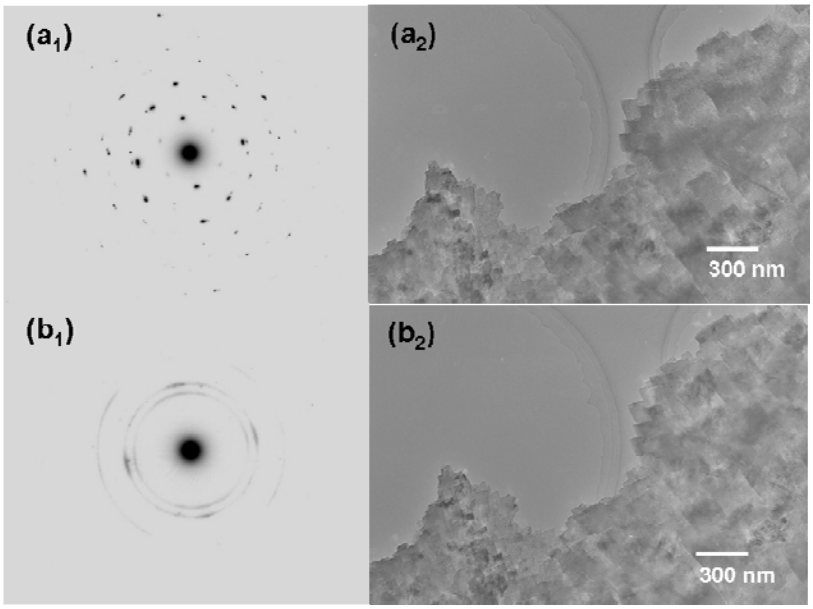

Figure 3.6. TEM micrographs and electron diffraction patterns taken at 400 kV for PVA single crystal grown at room temperature (25 °C) (a_1, a_2) with no electron beam irradiation damage, and (b_1, b_2) after being exposed to the electron beam for ~ 240 seconds showing electron beam damage.

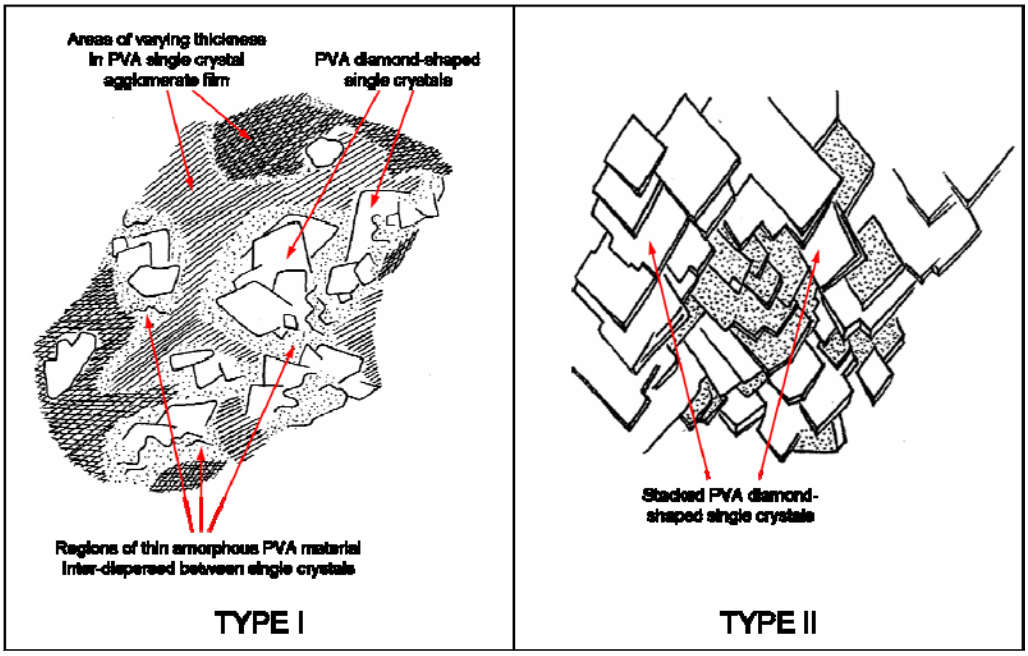

Figure 3.7. Schematic of arrangement of PVA single crystals in agglomerates.

Due to good radiation resistance at 400 kV, at magnifications of ×400,000 PVA lattice images were able to be obtained quite readily. By comparison, for radiation sensitive polymers, like isotactic-polystyrene [165] and polyethylene [166], special precautions must be taken to obtain high-resolution lattice images. These precautions include low-dose electron microscopy, low illumination, long exposure times, image filtering etc. Even then, images are typically very noisy. For polymers exhibiting higher radiation resistance, such as poly(p-pheylene benzobisthiazole) [167, 168] and poly(p-xylylene) [169, 170], lattice images can be obtained under normal operating conditions. We previously obtained clear PVA lattice image in the vicinity of single-wall carbon nanotubes [159]. To the best of our knowledge, Figure 3.8 represents the first example of clear PVA lattice image (from the neat polymer without carbon nanotube) obtained under normal electron microscopy conditions. It is noted that this Figure also shows

moiré fringes resulting from the mismatch between different lamellar layers. Previous studies show moiré fringes observed for polyethylene crystals however diffraction power of these crystal are not stable for long periods of time therefore the patterns are taken using weaker beam strengths and at much lower magnification [163]. Consequently, fine details of the polymer structure cannot be observed. Lattice imaging for more radiation resistant polymers like poly(p-phenylene benzobisoxazole) (PBO) [171] and poly(p-phenylene benzobisthiazole) (PBZT) [167] have also been observed using the electron microscopy at 200 kV and $\times$500,000 magnification. The moiré pattern observed here is also further evidence of the rotation between the lamellar layers which result in secondary electron diffraction spots.

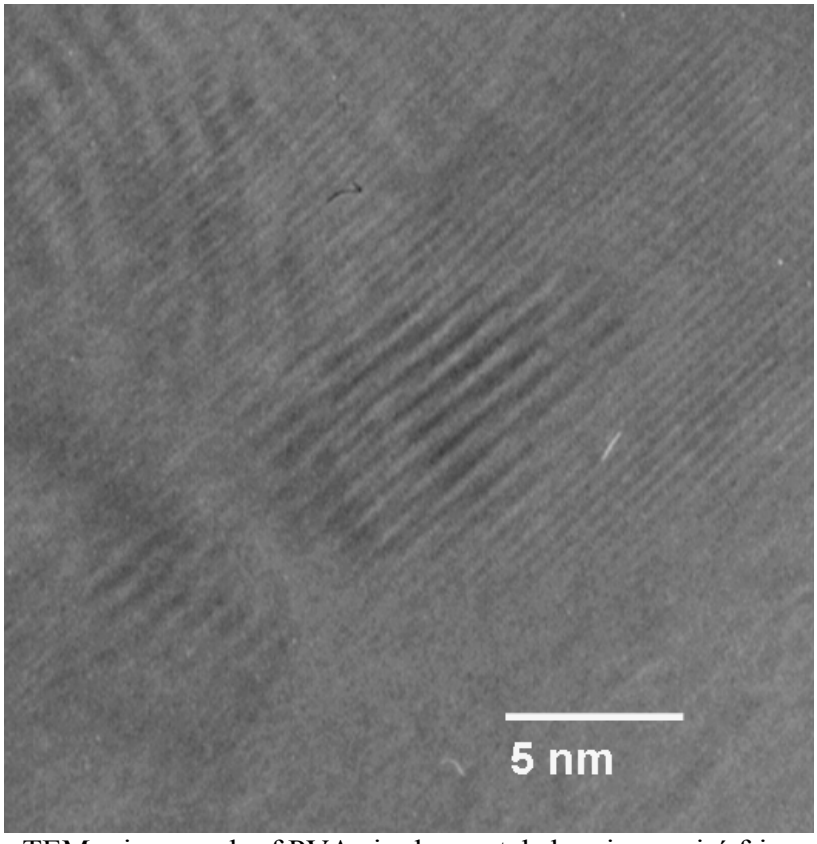

Figure 3.8. TEM micrograph of PVA single crystal showing moiré fringes taken at beam strength of 400 kV and ×500,000 magnifications.

3.3.2. Elevated Temperature Single Crystal Growth

By working with dilute solutions, individual polymer chains are less likely to become entangled with one another and more likely to participate in the formation of a crystal lattice. The growth of single crystals in dilute solutions has been well established [11]. In this work the growth of PVA single crystals at 0.4 wt % concentration in DMSO/H_2O mixtures has been very successful. Isothermal crystallization of PVA in DMSO/H_2O solutions yields several new morphologies. At 50 °C diamond-shaped lamellar single crystals were formed, and at 60 °C hexagonal-shaped lamellar crystals were formed. The lateral shaped/structure of the crystals at each given temperature is determined by the maximum growth rate of the crystallographic planes which are controlled by both lateral and fold surface energies. Polymer diffusion in solution and crystallization kinetics will depend on factors such as crystallization temperature (T_C), polymer concentration, polymer-solvent interaction, and polymer molecular weight. In the current study at 50 and 60 °C, all other factors remains the same except T_C. With all other factors being equal, temperature at which crystallization occurs dictates crystal geometry. Thickening of crystals during growth in isothermal conditions can also occur, and this may happen by two major methods (1) spiral growth or (2) addition of lamellae from a screw-type dislocation.

3.3.2.1. PVA Single Crystal Growth at 50 °C

At 50 °C, diamond shape individual crystals as well as polygonal crystals are obtained. Using both theoretical and experimental angular measurements (Table 3.1), it was determined that PVA crystals grown at 50 °C were primarily of two types C_1 and C_2.

For C_1, obtuse and acute angles of 114 ± 5° and 63.4 ± 2° were observed respectively. These measurements are consistent with a diamond-shaped crystal bound by (101) growth facets (Figure 3.2). C_2 crystals had obtuse and acute angles of 124 ± 1° and 58 ± 2° respectively consistent with a diamond-shaped platelets bounded by both (101) and (100) growth facets (Figure 3.9) (theoretical obtuse and acute angles between (100) and (101) growth facets were calculated to be 126.3° and 53.7°, respectively). Polygonal crystals are shown in Figure 3.10.

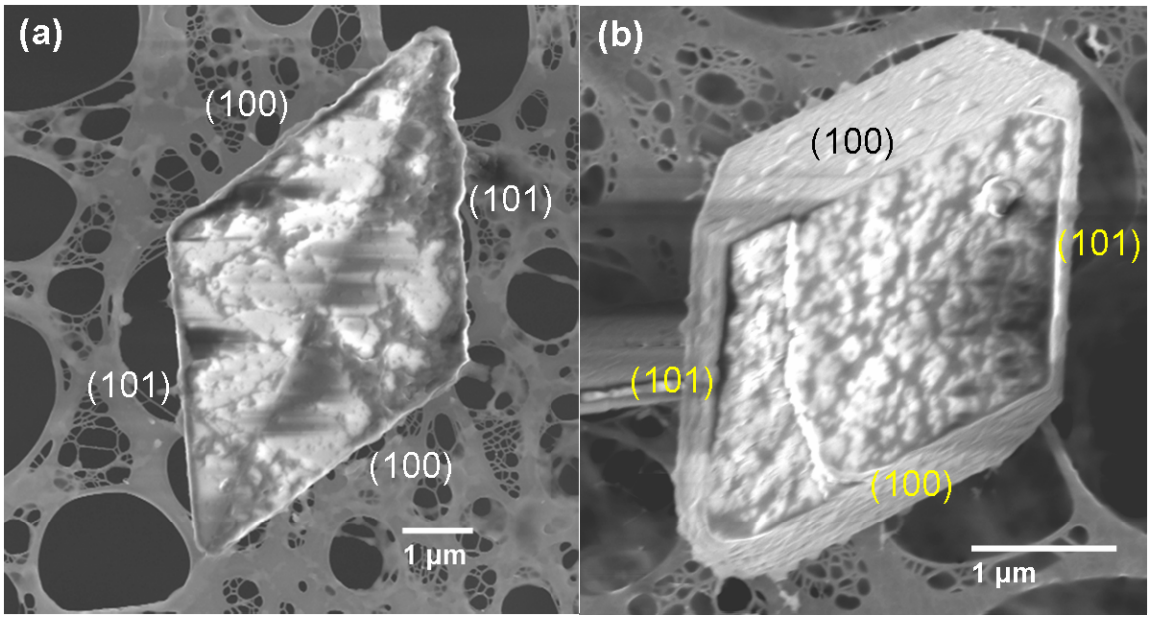

Figure 3.9. Scanning electron micrograph of PVA diamond-shaped single crystals grown at 50 °C of (a) C_1, growth planes (101) and (b) C_2, growth planes (101) and (100) types.

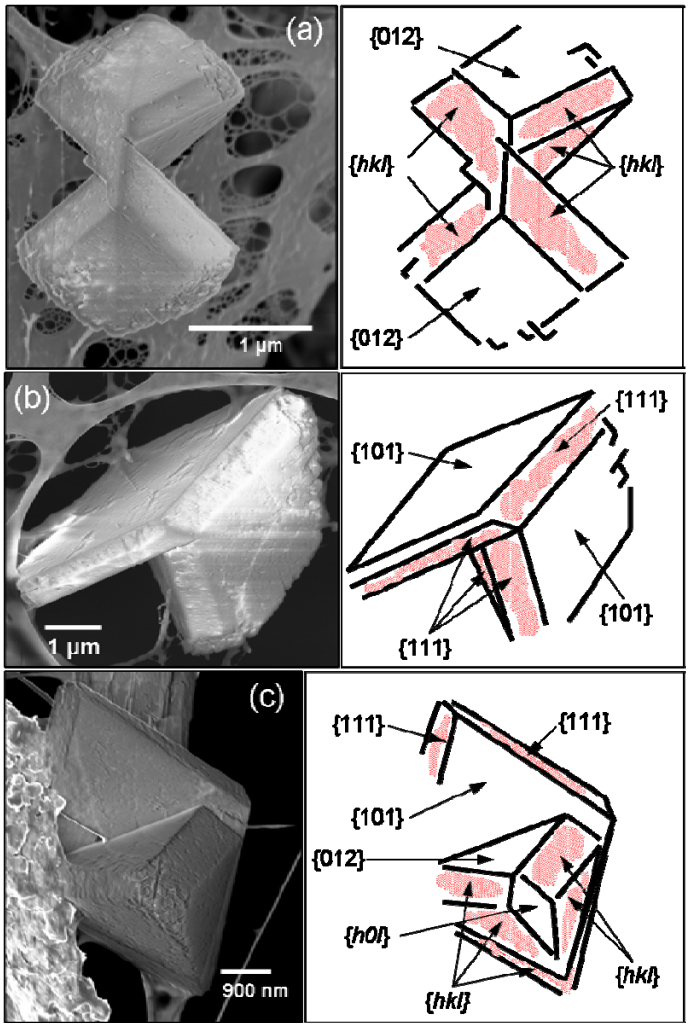

Figure 3.10. (a), (b), and (c) scanning electron micrographs of PVA polygonal crystals grown at 50 °C and their corresponding schematics with growth facets indicated.

The diamond shape crystals grown at 50 °C show rough growth edges (Figure 3.11). Secondary spots in the diffraction pattern are either very weak or not observed at all (Figure 3.11a_2). Radiation resistance of 50 °C crystals is substantially lower than that for the room temperature grown crystals. Diffracting power of these crystals can be readily destroyed at 100 kV (Figure 3.11) and images of these crystals could not be obtained at 400 kV. At comparable electron beam illumination after ~100 seconds, the crystal grown at 50 °C shows significant damage (Figure 3.11), while the crystal and its

diffracting power at 25 °C shows almost no change (Figure 3.5). Further evidence of radiation sensitivity of the 50 °C crystal is found when the electron beam in the SEM at 5 kV is focused on the PVA single crystal for one minute, resulting in significant radiation damage (Figure 3.12).

Diamond-shaped crystals grown at 50 °C are either bounded by (101) growth facets or both (101) and (100) growth facets (Figure 3.9). As mentioned earlier, literature reported PVA single crystals grown above 80 °C are parallelogram type. This work shows the first observation of diamond-shaped PVA single crystals. Polygonal PVA crystals are also observed at 50 °C bounded by (101), (111), and (012) growth facets (Figure 3.10). These growth facets were determined using the angular measurements between the planes. Polygonal crystals have been referred to as hedrites [11, 172]. Twinning has also been observed in polymer lamellar single crystals, where two or more crystal grow from a single nucleus at different degrees of orientation [173, 174]. Lath-like dendritic or star shaped twinned crystal structures have been observed for polyethylene and polyoxymethylene [160, 173]. In this work, we also observe PVA hedrites/polygons. In addition, it was found that in some cases twinning in PVA polygonal crystals form unique morphologies (Figure 3.10).

After growth time of approximately six months PVA rod crystals were observed (Figure 3.13), and exhibited twinning resulting in unique cross-shaped and star-like rod crystals. Figures 3.13d and 3.13e show these crystals after being damaged by the electron beam revealing the stacked PVA lamella layers along the lengths of the rods. End-on vies of these PVA rod crystals (Figure 3.13) show evidence of (101) growth

facets based of the angular measurements of the diamond shape (obtuse ~ 110° and acute ~70°).

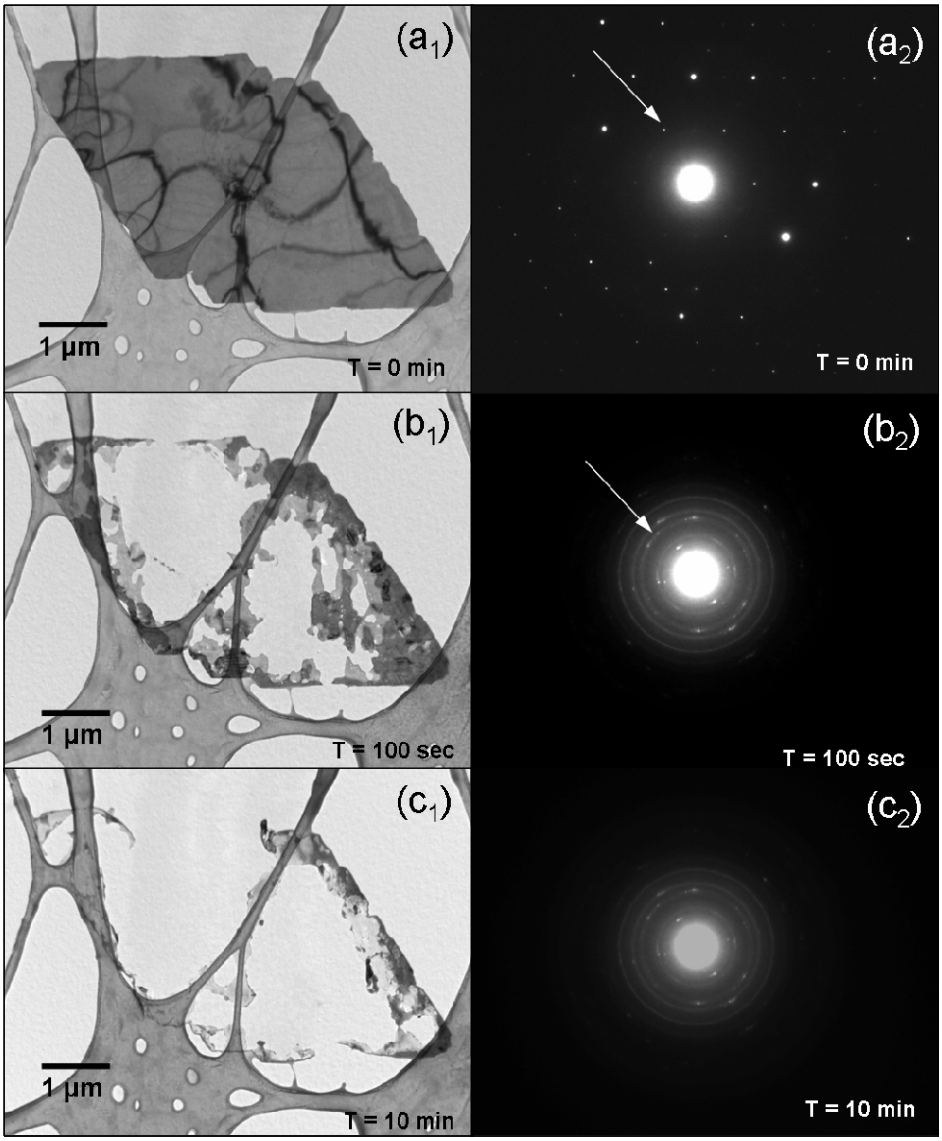

Figure 3.11. TEM micrographs and electron diffraction patterns taken at 100 kV for diamond-shaped PVA single crystal grown at 50 °C (a_1, a_2) with no electron beam irradiation damage, and (b_1, b_2) after being exposed to the electron beam for ~100 seconds showing significant electron beam damage, and (c_1,c_2) after ~10 minutes of beam exposure showing nearly total destruction of the crystal.

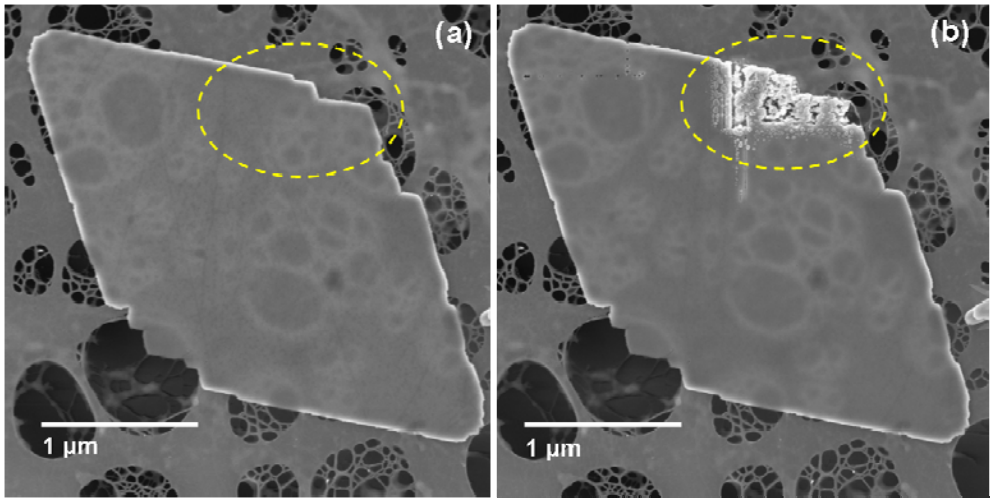

Figure 3.12. Scanning electron micrographs of PVA diamond-shaped crystal grown at 50 °C taken at 5 kV with no metallic coating circled area shows (a) no beam damage after initial, and (b) significant damage after one minute exposure by focused beam.

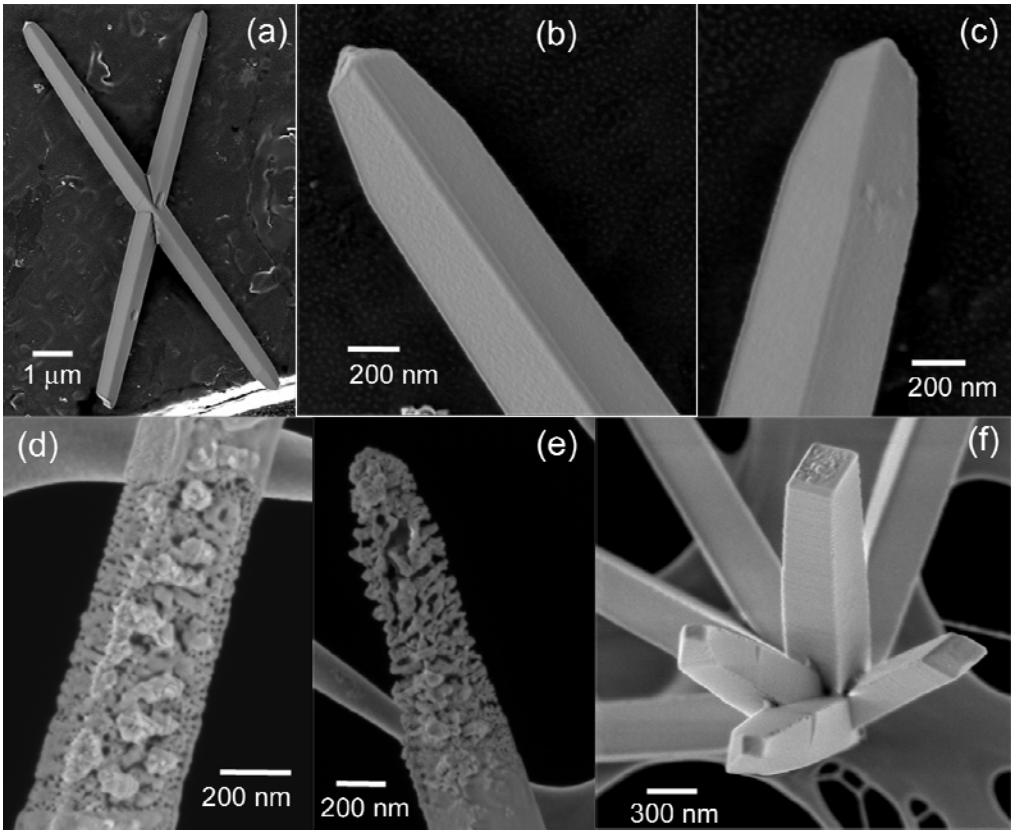

Figure 3.13. Scanning electron micrographs of (a to c) PVA rod crystals grown at 50 °C over six months. (d & e) shows rod crystals after electron beam damage (at 5 kV) revealing PVA lamellar layers stacked along the length of the rods. (f) end-on view of rod crystals showing diamond shape.

3.3.2.2. PVA Single Crystal Growth at 60 °C

At 60 °C, mostly hexagonal crystals (also first time for PVA) were observed with predominantly (100) and (101) growth facets (Figure 3.14). The crystal thickness was measured using SEM and ranged from ~20 to 150 nm. After long crystal growth times (three weeks), the lateral dimensions of these crystals become rather large, in some cases exceeding 100 μm (Figure 3.14c). In some cases the crystal shape changes and becomes more like a rounded quadrilateral for larger crystals (Figure 3.14f). In rarer instances parallelogram-shaped crystals were also observed (Figure 3.15). At broken points or tears in the crystals, and depending on the tear direction, either the chains are stretched for their folded state are observed (Figure 3.16).

Electron diffraction of the 60 °C hexagonal-shaped crystals shows the presence of strong secondary spots. High irradiation resistance is observed for these 60 °C crystals, and this is similar to the behavior of the 25 °C crystals. As compared to the crystals grown at 25 °C after ~100 sec of electron beam exposure in both cases almost no change in the electron diffraction pattern (Figures 3.5 and 3.17). The diffracting power at 100 kV does not change significantly even after 10 minutes (Figure 3.17) and very little amorphous halo or azimuthal arching is observed. Consistent with the previous data beam illumination was maintained so that photograph exposure time ranged from 0.25 to 0.5 sec. Relatively thin and large crystals will bend when deposited on the lacey carbon film of the TEM grid. As a result, bending contours arise when the specimen is not flat, and show up as dark lines in the bright-field image, or bright lines in the dark-field image. These are observed for the hexagonal crystals (Figure 3.18).

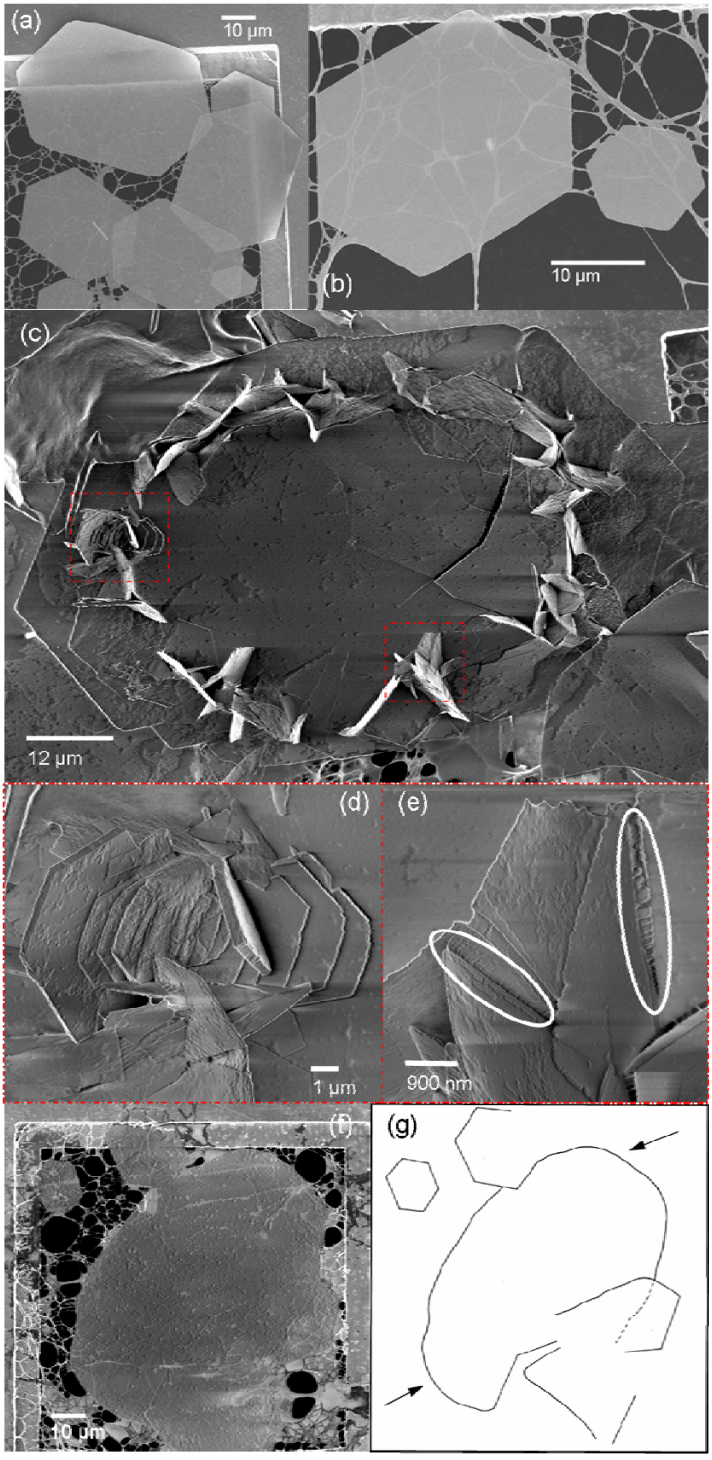

Figure 3.14. Scanning electron micrographs of hexagonal PVA single crystals grown at 60 °C showing (a) and (b) different sizes of hexagonal crystals, (c) large hexagonal crystal with cracks and growth of other hexagonal crystals in different directions, (d) and (e) magnified images of boxed regions in (c) showing lamellar thickness of hexagonal crystals (d) and crack regions where PVA lamellar pull-out is visible (e), (f) large hexagonal crystal with rounded edges, and (g) schematic of rounded crystal in (f).

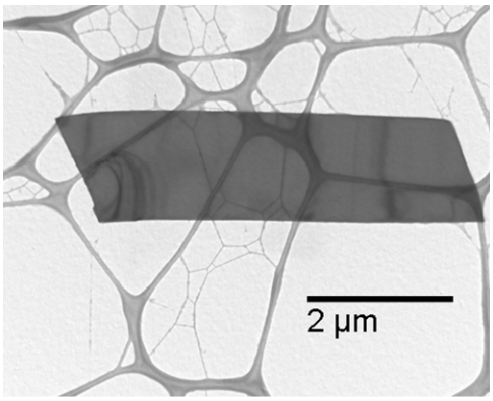

Figure 3.15. TEM micrograph of PVA parallelogram single crystal grown at 60 °C

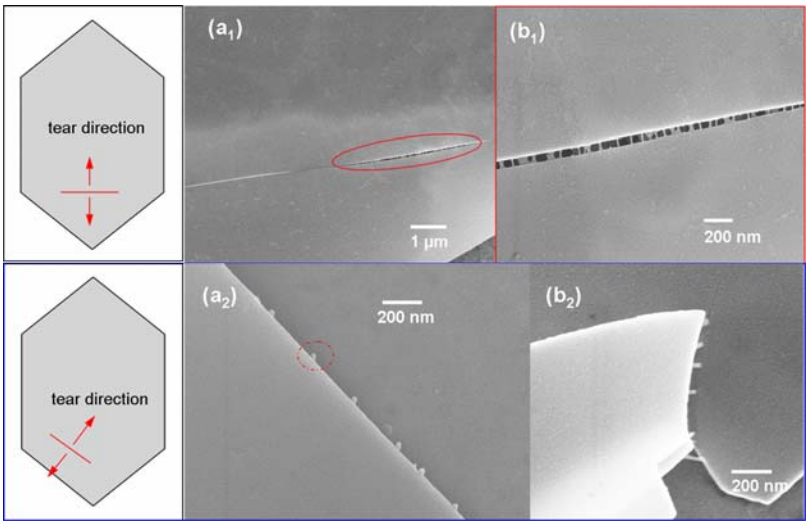

Figure 3.16. Scanning electron micrographs of a hexagonal PVA single crystal grown at 60 °C showing cross-hatched structure and crystal torn (a_1, a_2) perpendicular to the [100] growth front, and (b_1, b_2) parallel to the [101] growth front.

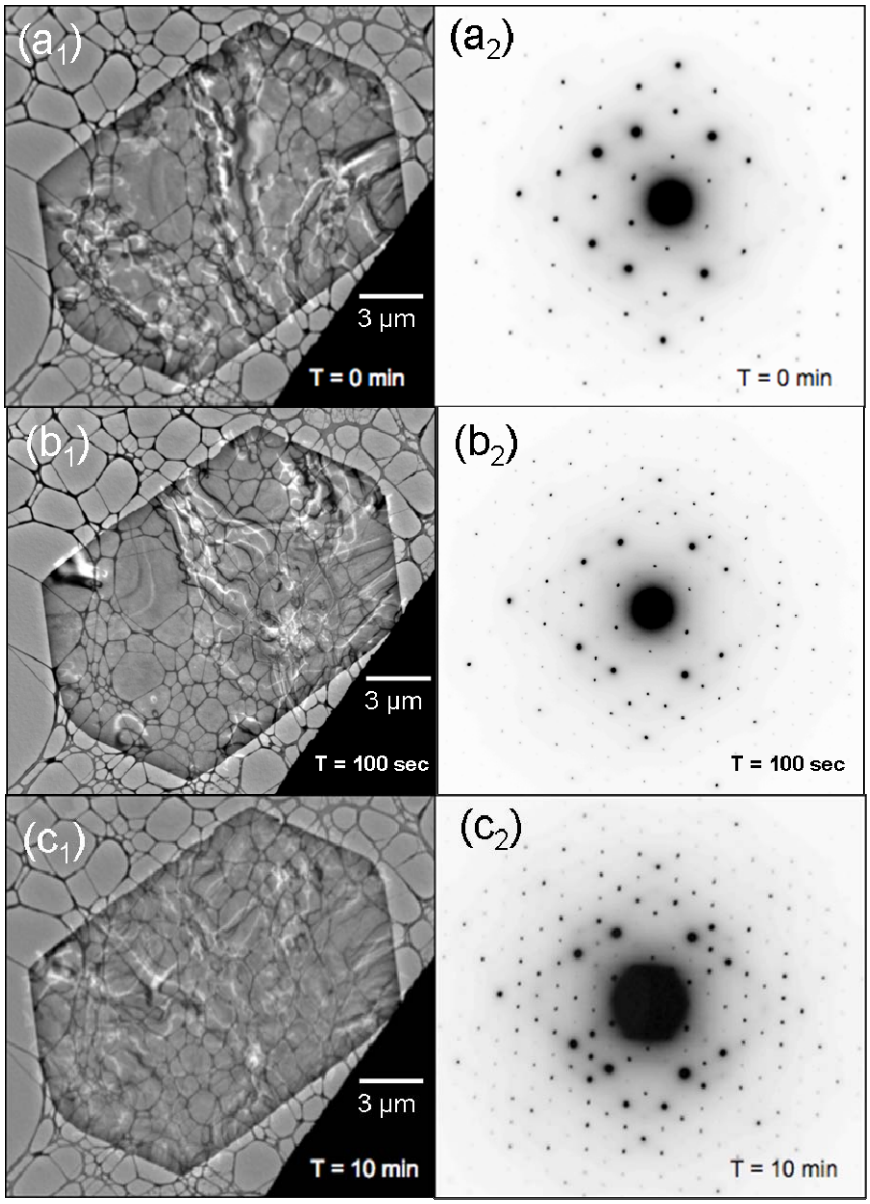

Figure 3.17. TEM micrographs and electron diffraction patterns taken at 100 kV for hexagonal-shaped PVA single crystal grown at 60 °C (a_1, a_2) with no electron beam irradiation damage, (b_1, b_2) hexagonal-shaped PVA single crystal after being exposed to the electron beam for ~100 seconds showing little electron beam damage, and (c_1,c_2) after beam exposure of ~10 minutes showing little damage.

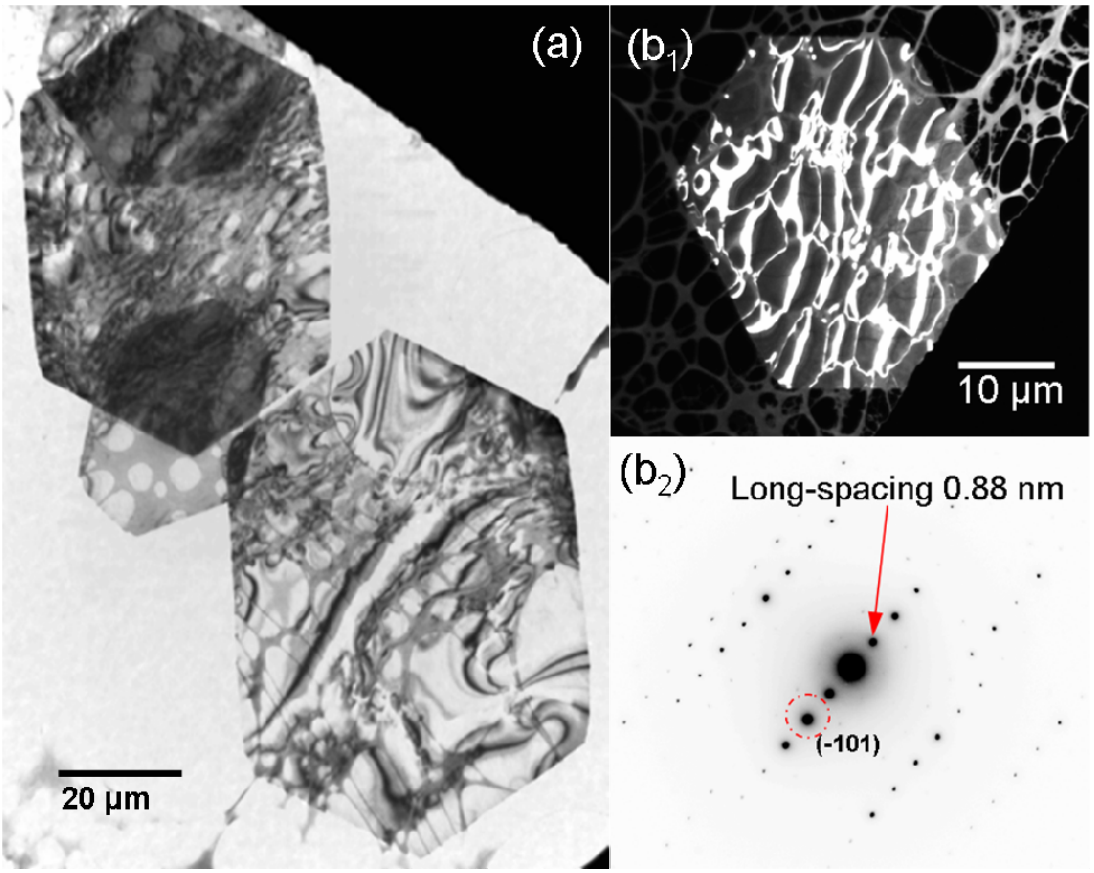

Figure 3.18. TEM bright-field micrographs of single crystals grown at 60 °C showing (a) bending contours and (b) dark-field image using (101) refection.

3.4. Conclusions

In summary, this work leads to several key conclusions. (1) Crystal growth has been observed in PVA solutions at room temperature (25 °C), where PVA single crystals have diamond-shaped platelet morphologies where both geometric, and electron diffraction gives evidence of a {101} growth facets. (2) PVA diamond platelets grown at room temperature agglomerate into thin films. (3) PVA room temperature single crystals show a high degree of crystal perfection and up to eight orders of *(h0l)* reflections can be observed in the electron diffraction patterns. (4) PVA room temperature single crystals show strong electron irradiation resistance at beam strengths of 100 kV and even at beam

strengths up to 400 kV, where diffracting power lasts for ~10 minutes and 4 minutes respectively. (5) PVA single crystals grown at 50 °C also show diamond-shape morphology with (101) or (100) and (101) growth facets, and exist as individual platelets, showing significant lamellar thickening. (6) Based on electron diffraction evidence crystals at 50 °C appear to be less perfect than the ones at 25 °C. (7) At 100 kV the diffracting power of 50 °C crystals begins to degrade significantly after one minute. (8) PVA polygonal crystals are also formed at 50 °C and display unique geometries bounded by (101), (111), and (012) growth planes. (9) PVA rod crystals showing twin morphology were observed after six months growth time at 50 °C. (10) PVA single crystals grown at 60 °C show hexagonal-shape morphology displaying predominant (100) and (101) growth facets. (11) At 60 °C crystals remain thin and do not show evidence of significant lamellar thickening as compared to the 50 °C crystals even after long growth times. However, lateral dimensions reach over 100 μm in some directions and in some cases the shape of the crystal change to a rounded quadrilateral. (12) 60 °C crystals similar to the 25 °C crystals show a high degree of irradiation resistance and diffracting power at 100 kV does not change even after ~10 minutes. (13) Bright-field and dark-field images of PVA bending contours are observed in the large thin hexagonal-shaped PVA platelets.

CHAPTER 4

SOLUTION GROWN SINGLE CRYSTALS OF POLY(VINYL ALCOHOL) IN POLY(VINYL ALCOHOL)/SINGLE WALL CARBON NANOTUBE DISPERSIONS

4.1. Introduction

Heterogeneous crystallization of polymer has been studied for a long time. Nucleated crystal growth has been studied for several flexible polymer systems [175-177] including polypropylene [178], and polyethylene [100, 101]. The ability of a substrate to nucleate crystal growth in a polymer depends on its nucleating activity [175-177]. A wide range of studies on crystallization show that polymer crystal growth nucleates quite readily on carbon fibers [178, 179], carbon black, and pyrolitic graphite[180-182].

Well-aligned graphitic structures have been shown to be highly active nucleating substrates for long chain polymers [178]. It is no surprise then that carbon nanotubes (CNT) have also been shown to induce crystal growth in long chain polymers [87, 104]. MWNT consist of concentric graphitic layers all aligned along the nanotube axis, while SWNT consist of one seamless tube of nearly perfect (depending on the processing conditions) graphite sheet elongated along the nanotube axis. CNT have also been shown to nucleate crystallization in polyvinyl alcohol (PVA) in bulk films and fibers [81, 88, 96, 103, 107-109, 159]. Until now single crystal growth of PVA in the presence of SWNT has not been reported. The study of single crystal growth of PVA by single-wall carbon nanotubes (SWNT) is discussed in this chapter.

4.2. Experimental

Atactic poly(vinyl alcohol) (PVA) (from Kuraray Co. Ltd., lot # 636837, degree of polymerization 18,000, and 98.4 % hydrolyzed) was dissolved in 80:20 volume ratio of dimethyl sulfoxide (DMSO) (from J.T Baker Cas. No. 67-68-5) and distilled water at temperatures between 110 to 120 °C (flask equipped with condenser) to obtain a 1 wt% PVA solution (80 ml DMSO, 20 ml water, and 1.1 g PVA). SWNT (obtained from CNI, lot# P-0247) (10 mg/ml) dispersion was obtained in DMSO by sonicating (using a Fisher FS30 bath sonicator, frequency 43 kHz, power 150 W) for 12 h at 55 °C and subsequently added to the PVA solution to obtain PVA:SWNT weight ratio of 99:1. The solution was stirred with an overhead mechanical stirrer (Caframo high shear mixer, model# BDC1850) at shear speeds between 500 RPM to 800 RPM continuously for 72 h. The solution was periodically sonicated for about ten minutes after every two hours while stirring. Macroscopic fibers formed in each solution within two hours of stirring, and no change was observed after about six hours. Continuous sonication results in dissolution of these fibers. The PVA/SWNT dispersion was quite inhomogeneous, where in addition to macroscopic fibers, SWNT particles could also be observed. Characterization of the self-assembled macroscopic fibers has been reported separately [159]. This inhomogeneous solution was further diluted to 50 times the original concentration with only distilled water at 25 °C. The diluted PVA/SWNT dispersion was allowed to stand in sealed flasks for months at room temperature (25 °C). The diluted solution was periodically (about once a month) observed in the transmission electron microscope, by placing a droplet on a Lacey carbon coated transmission electron microscope (TEM) grid

(Electron Microscopy Sciences, HC200-Cu). Single crystals, were first observed after ~ 9 months of the initial dilution of the solution.

4.2.1. Sample Characterization

Scanning electron microscopy (SEM) was performed on a LEO 1530 thermally assisted field emission microscope (at 10 kV) on samples sputtered coated with gold (single crystals samples collected on the TEM grids as described above were also used for SEM observation). Transmission electron microscopy (TEM) was performed using both JEOL 100CX II electron microscope (accelerating voltage 100 kV), and JEOL 4000EX electron microscope (accelerating voltage 400 kV). For electron diffraction, camera length was calibrated using evaporated aluminum standard (Electron Microscopy Sciences, Cat. # 80044). X-ray diffraction was performed using a Rigaku MicroMax-002 Microfocus X-ray Generator (operating voltage at 45 kV, current at 0.66 mA) equipped with an R-Axis++ SAXS/WAXS 2-D detector. Fourier transform infrared (FT-IR) spectra were obtained using a Perkin-Elmer AutoIMAGE Spectrum-One FT-IR spectrometer (Ser. # 50961).

4.3. Results and Discussion

PVA/SWNT *aloe plant* structures observed in a diluted PVA/SWNT dispersion after keeping it at room temperature (25 °C) for over eleven months are shown in Figure 4.1. The plant *root* contains both PVA and SWNT, while the *leaves* are only PVA single crystals without any SWNT (Figure 4.1). During growth, *leaf* crystals are attached to the *root* later as the crystals grow larger they (5 to 20 μm) will break away from the root, leaving a stump. TEM of the root/stump region for these crystals show the presence of individual and small bundles of SWNT ranging from 1 to 4 nm which are coated by PVA

(Figure 4.2). The PVA coating is well-crystallized and the PVA lattice can be observed by high-resolution transmission electron microscopy (HR-TEM) (Figure 4.3). PVA *leaf* single crystals have a well-defined near triangular shape with curved edges (Figure 4.4a) and upper bound crystal thickness in the range of 100 to 200 nm (Figure 4.4b). The crystal is thicker at the root and tapers off becoming thinner toward the crystal tip (30 to 50 nm) (Figures 4.4b and 4.4c).

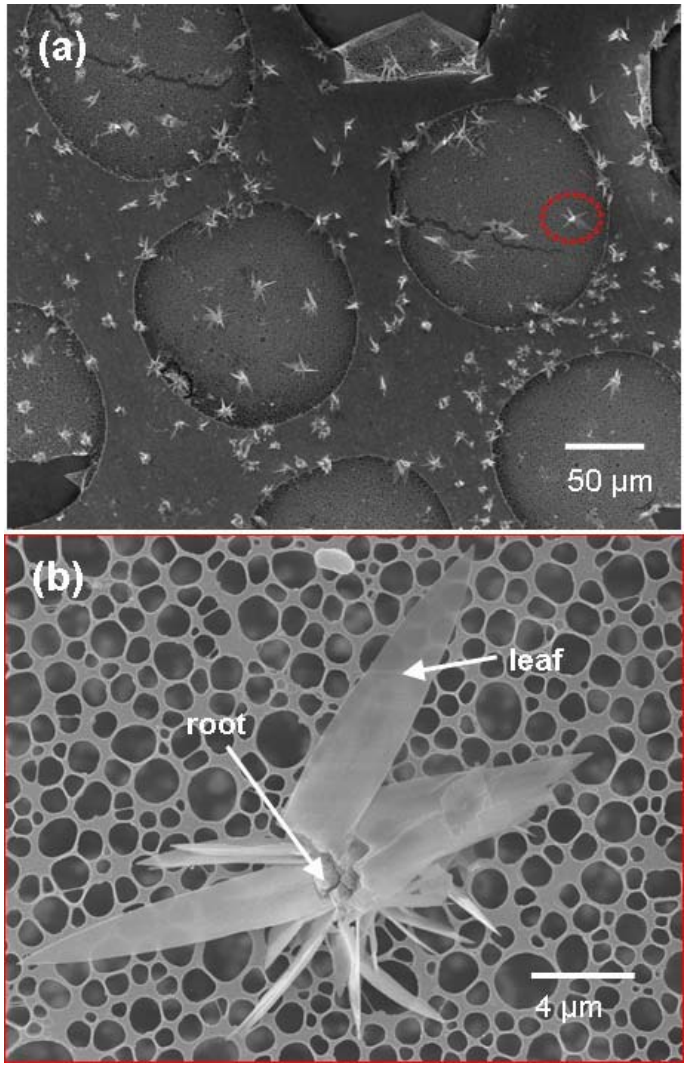

Figure 4.1. Scanning electron micrographs of PVA/SWNT aloe plant crystals. (a) and (b) are low and high magnification images, respectively.

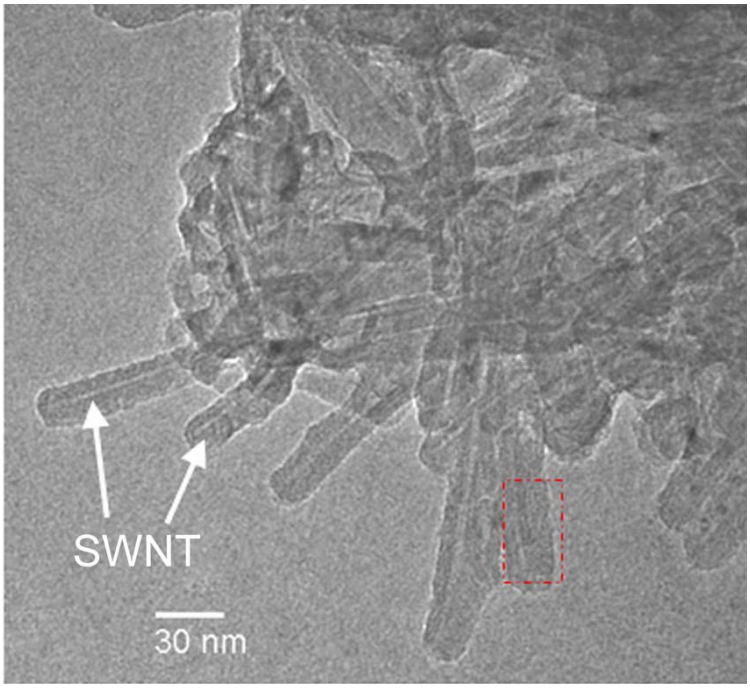

Figure 4.2. TEM micrograph of individual and small SWNT bundles coated with PVA.

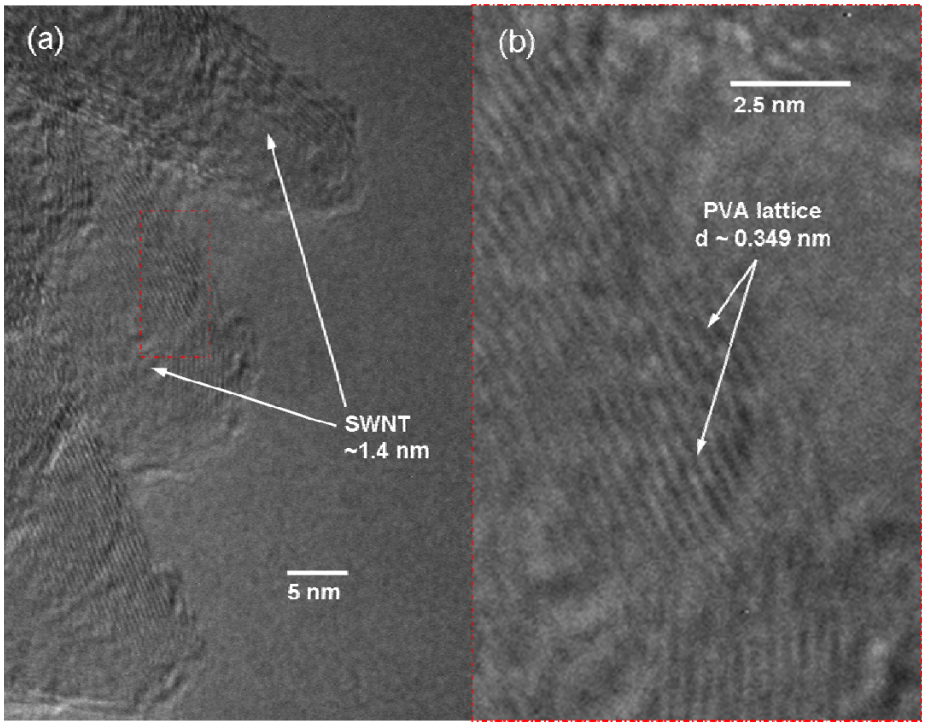

Figure 4.3. High-resolution TEM micrographs of (a) PVA coated SWNT showing PVA coating is crystalline and (b) higher magnification where PVA lattice is visible (lattice spacing ~ 0.349 nm).

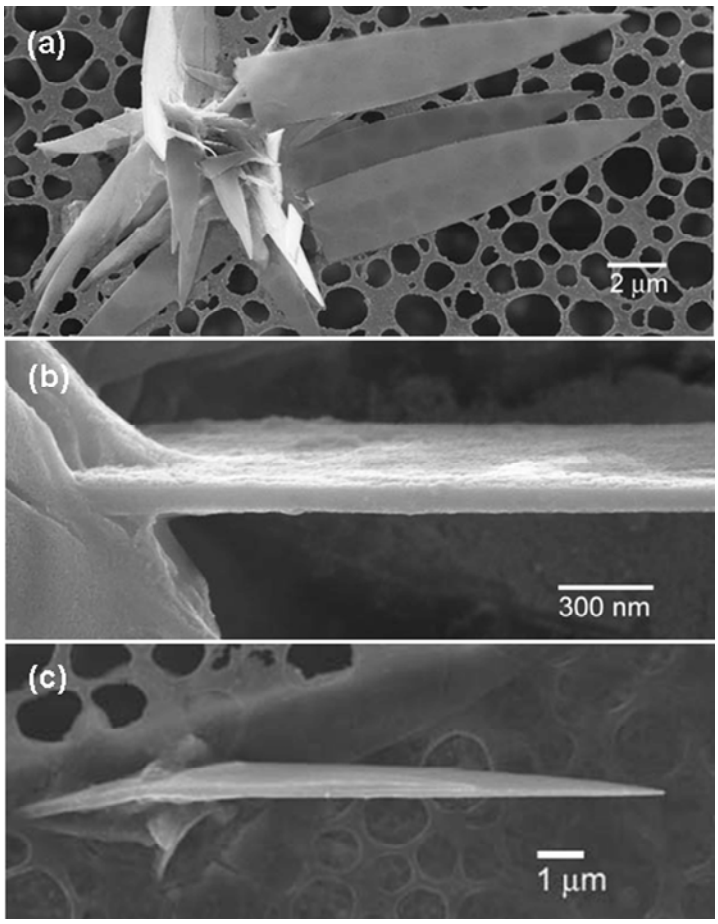

Figure 4.4. Scanning electron micrographs of PVA/SWNT aloe plant crystals showing (a) leaf crystal with triangular shape and curved edges, (b) edge of leaf crystal near aloe plant root showing smooth and large lamellar thickness, and (c) leaf crystal showing lamellar thickness tapering off toward the tip.

HR-TEM evidence of PVA molecules wrapped around individual and small SWNT bundles (Figure 4.2 and 4.3) suggests that there is an *epitaxial* interaction between PVA and SWNT. Figure 4.5a shows one epitaxial model for fully extended PVA chains with (010) plane direction parallel to graphite (1000) plane direction. This model can be extrapolated to arm-chair, zig-zag, and chiral SWNT (Figure 4.5b, 4.5c, and 4.5d). Equation (4.1) is used to calculate the epitaxial disregistry (Δ) between the two planes, and the resulting disregistery value of -2.35 %. This is well within the range

of epitaxial matching between polymer and substrate which typically has an upper bound limit of ~10 % [183, 184]. At the plant root, PVA molecules are templated onto the SWNT surface by epitaxial means to form the nucleus from which the single crystal grows. During crystallization, PVA molecules are continually added to this template to form leaf crystals, resulting in the formation of aloe plant structures. Epitaxial model suggests that PVA molecule will make an angle between 0° to 30° to the nanotube axis for the chiral tubes, 0° for the arm-chair tubes (Figure 4.5b), and 30° for the zig-zag tubes (Figure 4.5c).

$$\Delta = 100(d_{PVA} - d_{graphite}) / d_{graphite} \tag{4.1}$$

Where, d_{PVA} (010) and $d_{graphite}$ (1000) are the d-spacing's between two PVA ($d_{PVA(010)} = 0.252\ nm$) lattice planes and two graphite planes ($d_{graphite(1000)} = 0.246\ nm$) respectively.

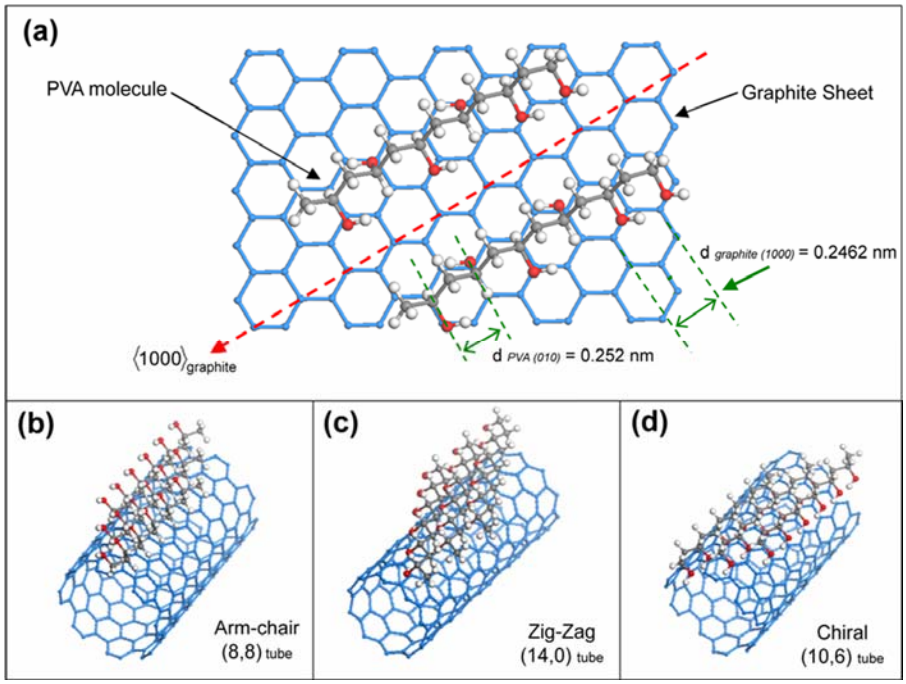

Figure 4.5. Molecular model of (a) possible [1000]//[010] epitaxial matching between PVA chain and graphite sheet, and arrangement of PVA chains with this epitaxial matching on (b) arm-chair SWNT, (c) zig-zag SWNT, and (d) chiral SWNT.

The total thickness of the PVA leaf crystals (30 to 200 nm) grown from PVA/SWNT dispersions is significantly larger than typical crystal lamellar thickness observed (~10 nm) for solution grown single crystals from most polymers. As mentioned in Chapter 3 as well as in the literature solution grown PVA single crystals are usually between 10 nm to 20 nm in thickness [153, 154]. The edges of these PVA *leaf* crystals are smooth, and SEM observations show no evidence of crystal thickening either by step or spiral growth. Electron diffraction of entire *leaf* crystals gives rise to a 2-D diffraction pattern and HR-TEM show moiré fringes which provide evidence of layered crystallites. Based on this evidence, the crystals are made up of many identical lamellar layers of the same orientation.

Thickness at the base of the leaf crystal (near the root) is 100 to 200 nm, while at the tip it is 30 to 50 nm. As mentioned above, epitaxial layering of PVA on SWNT occurs at the aloe plant root and forms a polymer-SWNT template which acts as the crystal nucleus. The cross-sectional areas of these templates are on the order of the critical nucleus size, and the lengths of these templates are several tens of nanometers. For this reason, multiple nucleation sites along the length of the template are available to the PVA molecules for crystals to grow. Figure 4.6 shows a SEM image of several layers protruding from the root which converge together to form a leaf crystal. Since each PVA crystal growth will match this template, each lamellar layer is formed at the template and continues to grow with respect to the other layers along the same direction. Consequently, the large crystal thickness observed in these PVA leaf single crystals is related to the length of the polymer-SWNT template protruding out of the root. As the PVA leaf single crystal continues to grow, and moves farther away from the template (at

the root) the PVA molecules tend to relax and adopt a more energetically favorable fold (geometrical shape of PVA leaf crystal shows evidence of small (101) growth sectors near the crystal tip).

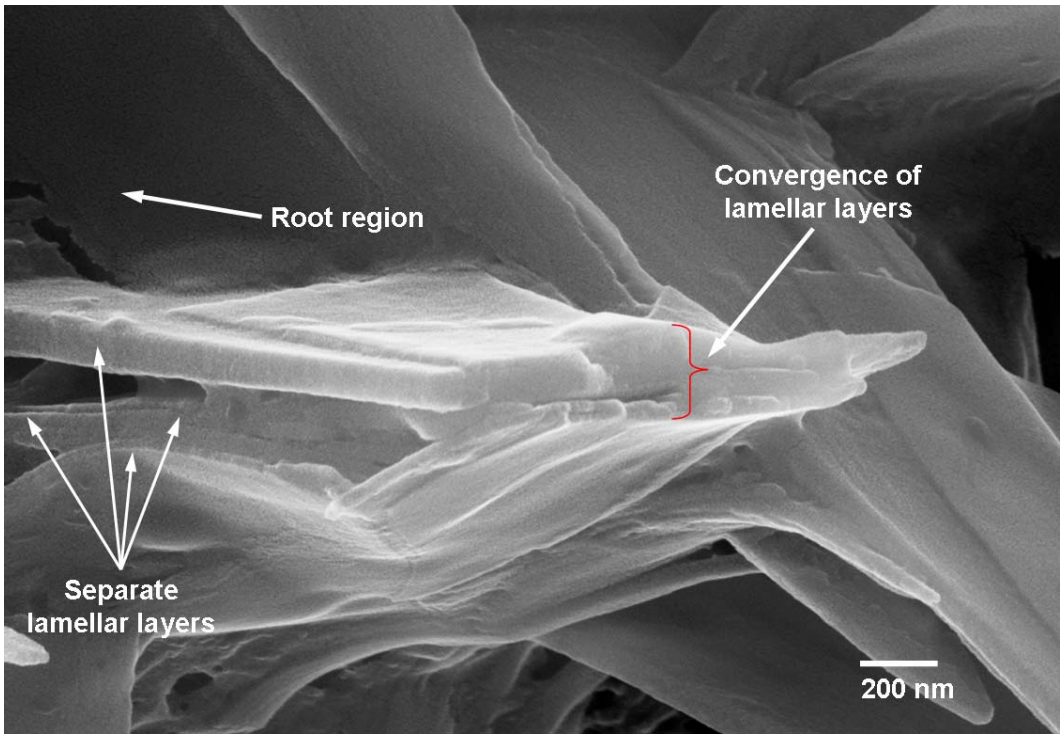

Figure 4.6. Scanning electron micrograph of thin leaf crystals growing from the aloe plant root and converging to form leaf crystal with large lamellar thickness.

With the electron beam parallel to the leaf thickness, crystals grown from PVA/SWNT dispersions show strong reflections at 0.352 nm and weak PVA (101) reflections (Figure 4.7b). The electron diffraction pattern was also taken from the edge-on direction of a PVA leaf crystal (Figure 4.7d). This pattern shows only two reflections at 0.707 nm and 0.352 nm, revealing that PVA chains are packed closely in these single crystals. The leaf dimensions suggest that growth along the one axis is about 3.5 times faster than along the other, indicating directional crystal growth. X-ray diffraction on a powder containing these aloe plant structures show a distinctly different pattern than what

is expected for monoclinic PVA unit cell (Bunn [146]) suggesting the formation of a new crystal structure for PVA (Figure 4.8 and 4.9).

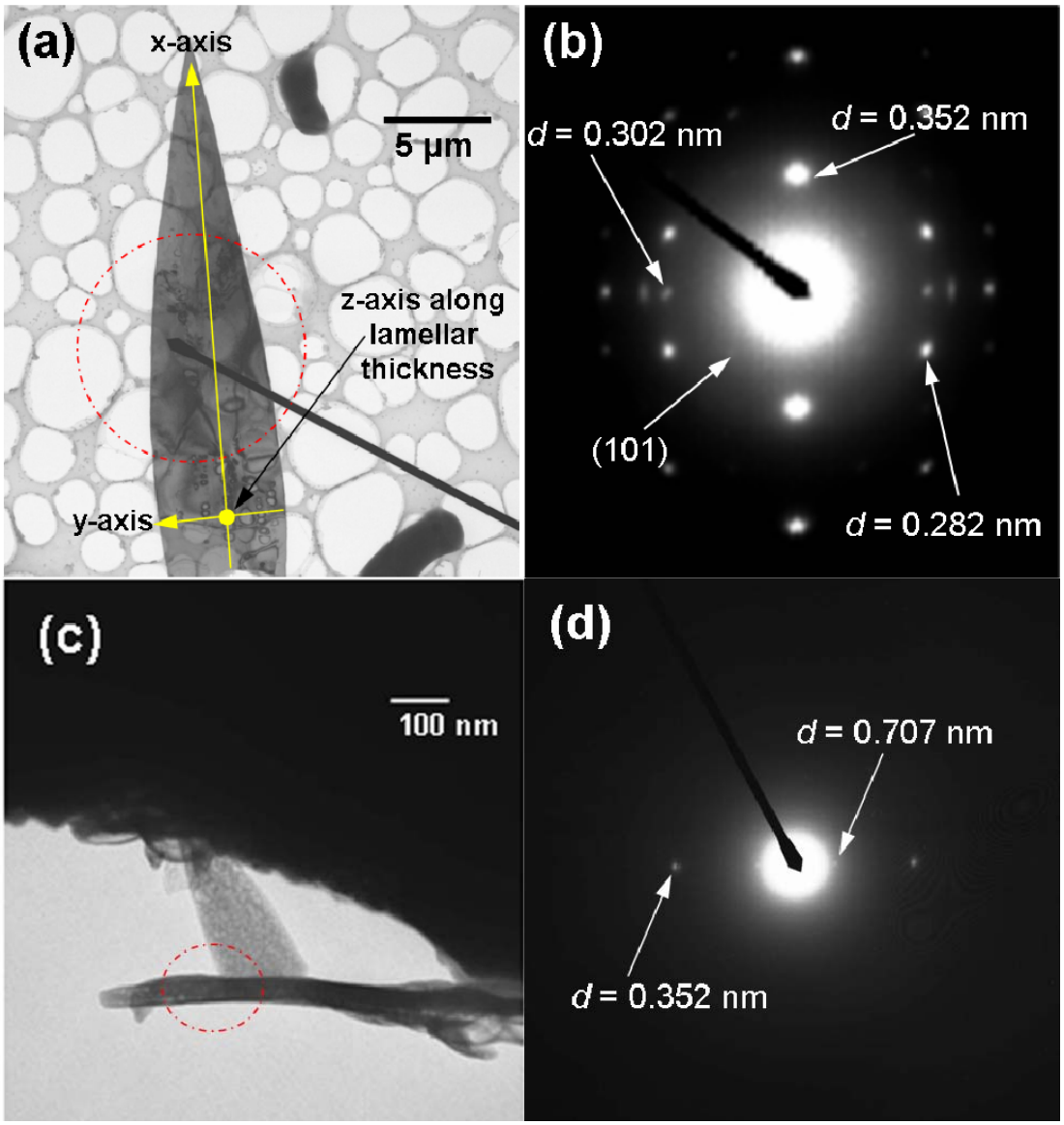

Figure 4.7. TEM bright-field image of PVA leaf single crystal (red circle represents selected area for electron diffraction), designated x,y,z axes shown. (b) Electron diffraction of PVA leaf crystal from selected area shown in (a). Electron diffraction shows predominant spots at 0.352 nm and 0.282 nm, and weak spots at 0.302 nm and (101) reflections. (c) TEM bright-field image of edge-on view of leaf single crystal (red circle represents selected area for electron diffraction). (d) Electron diffraction pattern from (c) showing only the spots present at 0.707 nm and 0.352 nm.

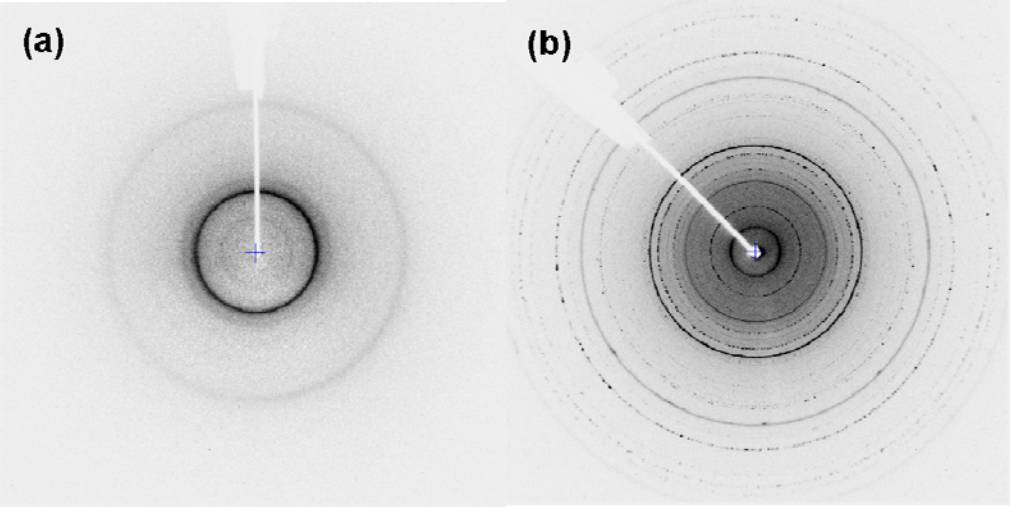

Figure 4.8. Wide-angle X-ray diffraction patterns of (a) PVA/SWNT film cast from original dispersion, and (b) PVA/SWNT aloe plant crystal powder grown in diluted PVA/SWNT dispersion.

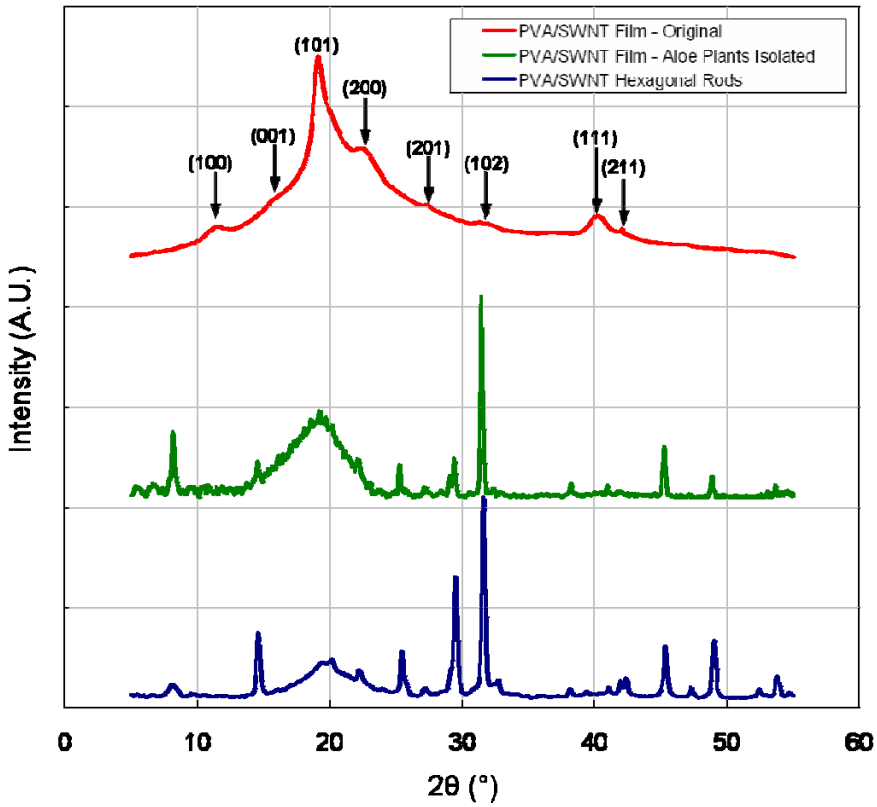

Figure 4.9. Wide-angle X-ray integrated scans of PVA/SWNT original solution cast film (red), PVA/SWNT aloe plants grown in original solution (green), and PVA/SWNT hexagonal rods (blue).

Electron diffraction data of the aloe leaves show a predominant diffraction spot at 0.352 nm, a less predominant spot at 0.282 nm, and a weak spot at 0.302 nm. X-ray diffraction of a powder containing these aloe plants is consistent with the electron diffraction showing similar diffraction spacing's. However, contrary to electron diffraction the intensities of these peaks differ for X-ray diffraction where, 0.282 nm is the most predominant peak, 0.302 nm is the second most predominant and 0.352 nm show medium intensity. Based on this information, it may be possible to postulate the crystal structure for a new PVA unit cell using the spacing's correlated between both X-ray and electron diffraction. Previous to this work there have been several other proposed crystal structures for PVA and they are listed in Table 4.1.

Table 4.1. List of different proposed crystal structures for PVA based on experimental results.

		PVA Crystal Structure		
Year	Group/ Author	Tacticity	Unit Cell Type	Unit Cell Dimensions
1941	R.C.L. Mooney [185]	atactic	Pseudo-orthorhombic	$a = 0.782\ nm, b = 0.252\ nm, c = 0.56\ nm, \beta = 90^{\circ}$
1948	C.W. Bunn† [146]	atactic	Monoclinic	$a = 0.781\ nm, b = 0.252\ nm, c = 0.551\ nm, \beta = 91.5^{\circ}$
1950	I. Sakurada, et.al. [186, 187]	atactic	Monoclinic	$a = 0.783\ nm, b = 0.252\ nm, c = 0.553\ nm, \beta = 93^{\circ}$
1960	T. Mochizuki [188]	atactic	Monoclinic	$a = 0.781\ nm, b = 0.2533\ nm, c = 0.551\ nm, \beta = 91^{\circ}$
1974	B.G. Colvin [189]	atactic	α-monoclinic	$a = 1.558\ nm, b = 0.759\ nm, c = 1.865\ nm, \beta = 96^{\circ}$
			β-orthorhombic	$a = 1.586\ nm, b = 0.595\ nm, c = 1.054\ nm$

† Predominantly PVA literature shows a crystal structure consistent with Bunn's model.

In this work, a new monoclinic crystal structure is proposed for these aloe plant crystals with unit cell dimensions $a = 1.07\ nm$, $b = 0.252\ nm$, $c = 0.613\ nm$, and $\beta = 98.9^{\circ}$. Figure 4.10a shows an X-ray pattern for a PVA crystalline film containing aloe plant crystals showing a composite diffraction pattern of both known PVA reflections from Bunn's unit cell and the newly proposed PVA crystal structure. Ironically, these d-spacing's observed from X-ray for the aloe plants can not only be indexed by this new monoclinic unit cell, they can also be indexed by a 2-D hexagonal unit cell with $a_0 = 1.212\ nm$ (Figure 4.10b). This would be the same crystal structure used to index well-organized SWNT bundles with $d_t \cong 1.0\ nm$. Theoretical calculations are listed in Table 4.2. The average nanotube diameter in the batch of SWNT (P-0247) used in this study is ~0.973 nm measured from Raman spectroscopy. Table 4.3 lists the experimental and theoretical d-spacing's and *(hkl)* indices for the aloe plants, and the proposed crystal structures. X-ray results provide compelling evidence of the epitaxial interaction between SWNT and PVA. Comparatively X-ray diffraction was also taken for films cast from the original undiluted PVA/SWNT dispersions. The patterns show only PVA Bunn's monoclinic unit cell reflections (Figure 4.9) suggesting that crystal growth only takes place over time and in the diluted PVA/SWNT dispersions.

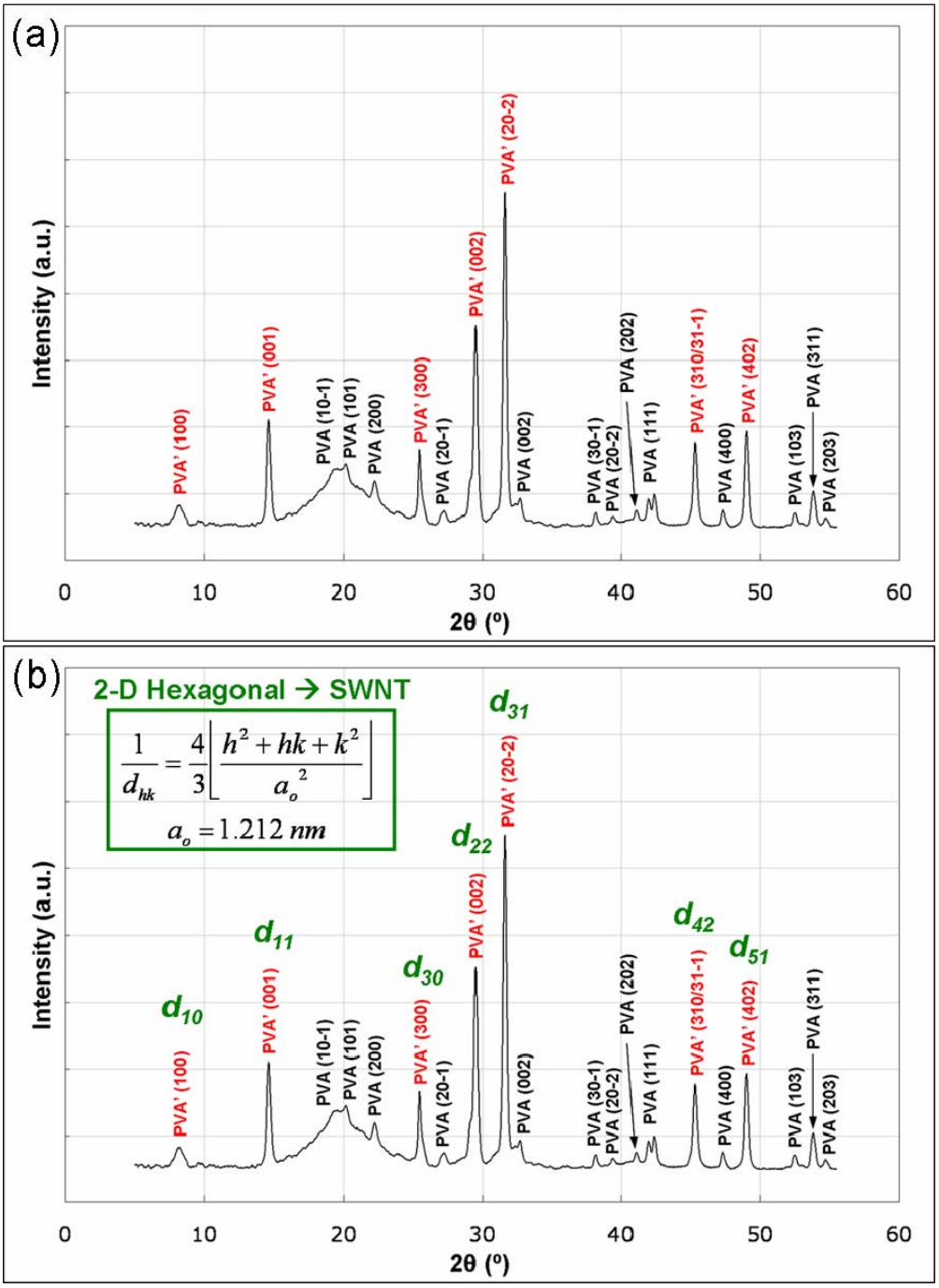

Figure 4.10. Wide-angle X-ray integrated scans of PVA/SWNT aloe plants and hexagonal rod crystals showing a composite diffraction pattern. (a) Both d-spacing from Bunn's [146] PVA crystal unit cell, and the new proposed unit cell can be indexed. (b) Calculated d-spacing for 2-D hexagonal unit cell (corresponding to SWNT) can also be used to index these new peaks.

Table 4.2. List of theoretical *(hkl)* d-spacing's observed in electron and X-ray diffraction patterns for PVA/SWNT aloe plant single crystal grown at 25 °C pertaining to 2-D hexagonal lattice for SWNT. Experimental values are also listed.

d_{hk}		$d_{theoretical}$ (nm) (2D Triangular Lattice)	$d_{experimental}$ (nm)
d_{10}	$\frac{\sqrt{3}a_o}{2}$	10.49	10.7997
d_{11}	$\frac{a_o}{2}$	6.06	6.0621
d_{30}	$\frac{\sqrt{3}a_o}{6}$	3.49	3.4982
d_{22}	$\frac{a_o}{4}$	3.03	3.0253
d_{31}	$\frac{\sqrt{3}a_o}{2\sqrt{13}}$	2.91	2.8273
d_{42}	$\frac{\sqrt{3}a_o}{4\sqrt{7}}$	1.98	1.9994
d_{51}	$\frac{\sqrt{3}a_o}{2\sqrt{31}}$	1.88	1.8575
d_{hk}		***Ratio***	***Theoretical***	***Experimental***
d_{10}	$\frac{\sqrt{3}a_o}{2}$	$\frac{d_{10}}{d_{11}}$	1.73	1.78
d_{11}	$\frac{a_o}{2}$			
d_{30}	$\frac{\sqrt{3}a_o}{6}$	$\frac{d_{30}}{d_{31}}$	1.201	1.237
d_{31}	$\frac{\sqrt{3}a_o}{2\sqrt{13}}$			
d_{22}	$\frac{a_o}{4}$	$\frac{d_{22}}{d_{42}}$	1.527	1.513
d_{42}	$\frac{\sqrt{3}a_o}{4\sqrt{7}}$			

Table 4.3. List of *(hkl)* d-spacing's observed in electron and X-ray diffraction patterns for PVA/SWNT aloe plant single crystal grown at 25 °C pertaining to both Bunn's PVA crystal unit cell and the proposed new crystal unit cell. Theoretical values are also listed.

PVA ***(Bunn's Unit Cell)***		***PVA'*** ***(Proposed New Unit Cell)***	
$d_{hkl} = \frac{b}{\sqrt{\frac{\left(h/a\right)^2 + \left(l/c\right)^2 - \frac{2hl}{ac}\cos\beta}{\sin^2\beta} + k^2}}, \alpha = \gamma = 90^\circ, \beta \neq 90^\circ$			
$a = 0.781\ nm$ $b = 0.252\ nm$ $c = 0.551\ nm$ $\beta = 91.7^\circ$		$a = 1.07\ nm$ $b = 0.252\ nm$ $c = 0.613\ nm$ $\beta = 98.9^\circ$	
(hkl)	***Theoretical*** $d_{spacing}$ ***(nm)***	***Experimental*** $d_{spacing}$ ***(nm)***	***Theoretical*** $d_{spacing}$ ***(nm)***	***Experimental*** $d_{spacing}$ ***(nm)***
(100)	0.781	0.775 *(x)*	1.06	1.07 *(x)*
(001)	0.551	0.556 *(x)*	0.606	0.606 *(x,e)*
$(10\bar{1})$	0.453	0.452 *(x,e)*		
(101)	0.446	0.439 *(x,e)*		
(200)	0.391	0.397 *(x)*		
(300)			0.352	0.351 *(x,e)*
$(20\bar{1})$	0.323	0.322 (x,e)		
(002)	0.275	0.273 *(x)*	0.302	0.302 *(x,e)*
$(30\bar{1})$	0.236	0.235 *(x)*		
$(20\bar{2})$			0.282	0.282 *(x,e)*
(202)	0.223	0.220 *(x)*		
(111)	0.219	0.217 *(x)*		
(310)			0.199	0.199 *(x,e)*
$(31\bar{1})$				
(400)	0.195	0.192 *(x)*		
(402)			0.185	0.185 *(x,e)*
(600)			0.176	0.174 *(x,e)*
(311)	0.171	0.170 *(x)*		
(203)	0.164	0.167 *(x)*		

x – represents reflection present in the X-ray diffraction pattern.
e – represents reflections present in the electron diffraction pattern.

FT-IR experiments were performed on these aloe plant crystals to confirm that they were in fact PVA. The FT-IR spectra were collected for these aloe plant crystals showing new X-ray behavior, a film cast from the original undiluted PVA/SWNT dispersions, and neat PVA films both showing X-ray patterns consistent with Bunn's crystal unit cell. All these FT-IR spectra are consistent (Figure 4.11) revealing that although crystallographically the material differs the chemical make-up is the same.

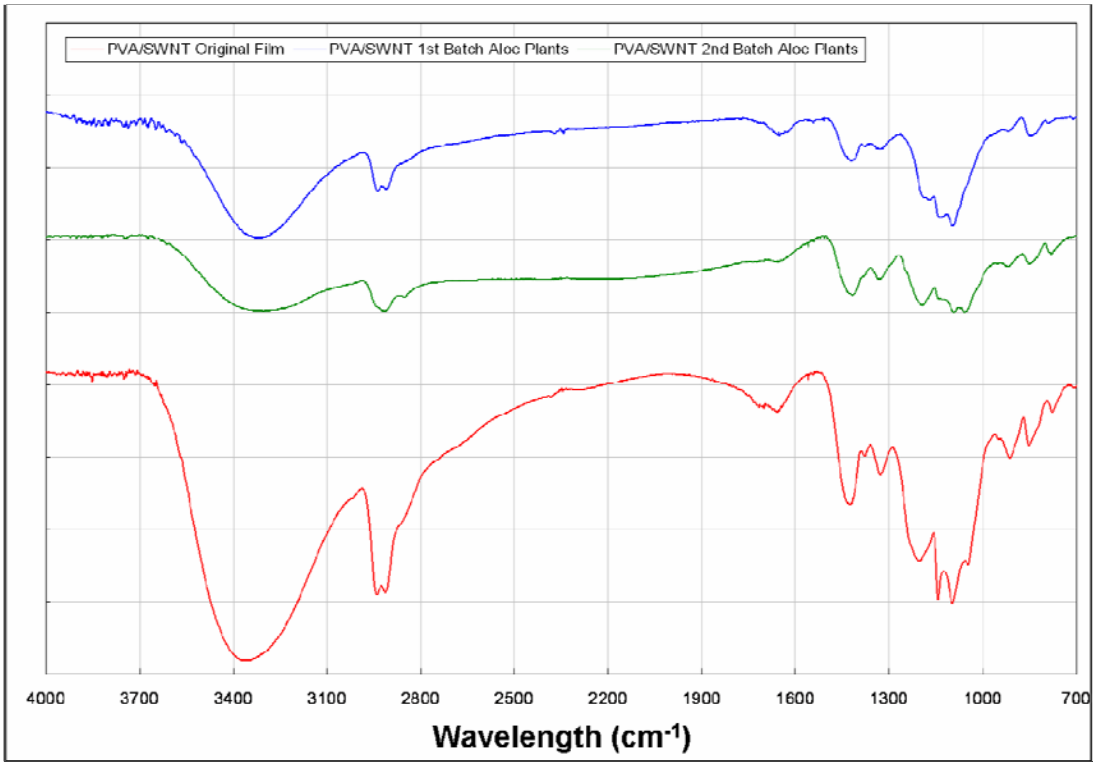

Figure 4.11. FT-IR spectra for PVA/SWNT original solution cast film (red), 1st batch of PVA/SWNT aloe plants (blue), and 2nd batch of PVA/SWNT aloe plants (green).

X-ray diffraction of lamellar polymer single crystals is usually difficult to obtain since for most crystals grown in dilute solutions large enough sample sizes are difficult to obtain. On average the crystal lamellar thickness is also of the order of ~10 nm, therefore the efficiency of X-ray scattering is not sufficient to produce meaningful patterns. The

electron microscope is heavily relied upon to analyze chain arrangement in polymer single crystals. In this work, PVA/SWNT aloe plant crystals can be obtained in sufficient quantities to obtain useful X-ray diffraction patterns. From X-ray diffraction peaks, crystal sizes is calculated for these leaf crystals and are in the range of 20 nm to 37 nm (Table 4.4). For drawn PVA and PVA/SWNT gel spun fibers crystal size determined by X-ray is on the order of 3 nm to 7 nm. Based on the crystal size for the *leaf* crystals and the proposed unit cell the crystal size along the *a*- and *c*- axes are 26 nm and 37 nm respectively. Such large crystal sizes are typically observed for inorganic materials which are typically comprised of short molecules. For high-molecular weight polymers this level of crystal perfection is typically prevented by chain entanglements.

Table 4.4. Crystal size values determined from wide-angle X-ray diffraction for the PVA/SWNT aloe plant single crystals.

PVA'		***Crystal size (nm) (measured by XRD)***
(hkl)' (Proposed unit cell)/SWNT(d_{hk})	***$d_{spacing}$ (nm) (measured by XRD)***	
(100)′/d_{10}	1.06	26
(001) ′/d_{11}	0.606	37
(300) ′/d_{30}	0.352	24
(002)′/d_{22}	0.302	30
$(20\bar{2})'/d_{31}$	0.282	35
$(310/31\bar{1})'/d_{42}$	0.199	30
(402)′/d_{51}	0.185	27

PVA *leaf* crystals radiation resistance is related of the leaf thickness. For thinner crystals (30 to 50 nm) the diffracting power at beam strengths of 100 kV lasts only ~100 seconds (Figure 4.12). Thicker crystals (>100 nm) can diffract up to 10 minutes at 100

kV. If beam illumination is kept to a minimum the crystal lattice remains uninterrupted and sharp diffraction patterns can be obtained (Figure 4.13a). Time elapsed diffraction patterns from the leaf crystals shows how electron beam damage begins in the crystal by distortion of the lamellar layers which results in azimuthal arching (Figure 4.13b), and later all of the lamellar layers are at random resulting in diffraction rings (Figure 4.13c). With continued beam exposure the crystal lattice will eventually be totally destroyed resulting in diminishment of the diffraction pattern. At 200 kV and 400 kV the crystals can be imaged readily at low illuminations, and crystallite and lattice images can be obtained up to $\times 500{,}000$ magnifications (Figure 4.14 and Figure 4.15). Although electron beam damage does occur, the existence of many layers lengthens the total time for complete beam damage so that HR-TEM images can be obtained. Figure 4.14 shows an *aloe plant* before and after lattice images were taken revealing the extent of electron beam damage.

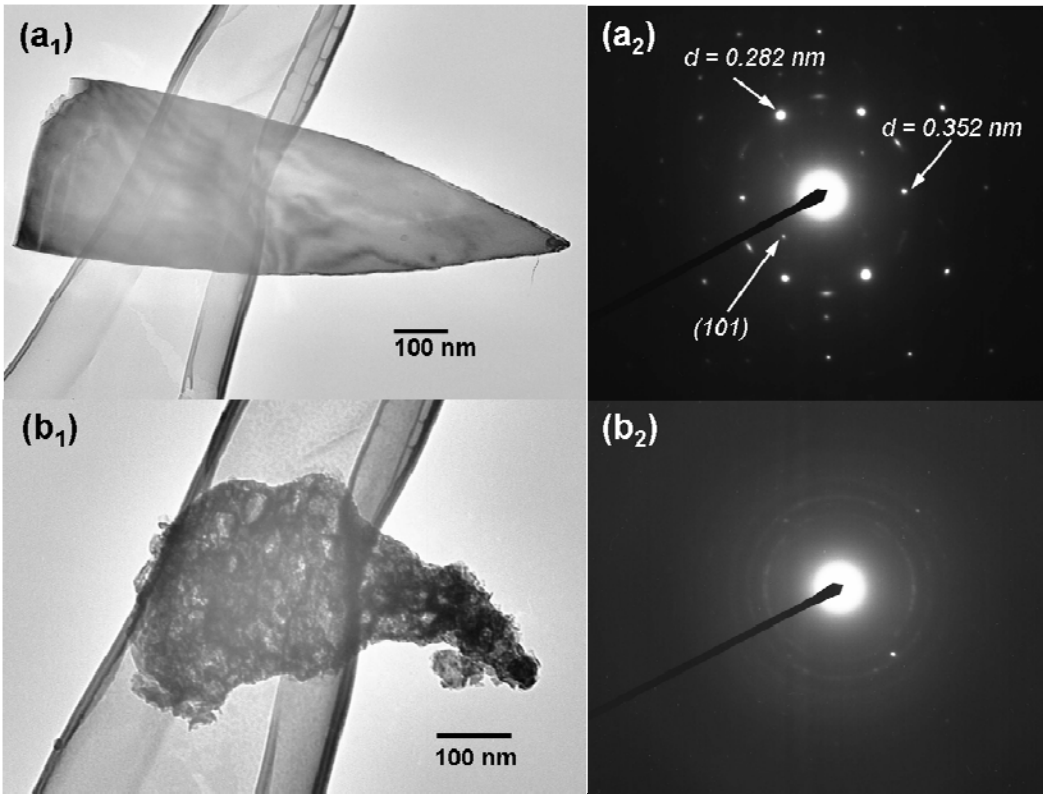

Figure 4.12. TEM images and electron diffraction patterns taken at 100 kV for (a_1, a_2) PVA/SWNT aloe plant single crystal with no electron beam irradiation damage, and (b_1, b_2) PVA/SWNT aloe plant single crystal after being exposed to the electron beam for ~100 seconds showing major electron beam damage.

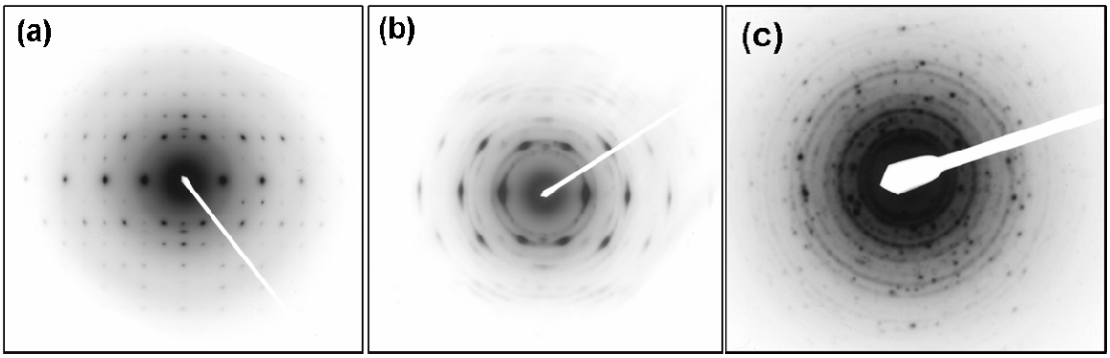

Figure 4.13. Electron diffraction patterns of (a) an undamaged leaf crystal, (b) a leaf crystal which sustained some damage and show azimuthal arching arising from the misalignment of lamellar layers, and (c) a severely damaged leaf crystal showing diffraction rings arising from total misalignment of lamellar layers.

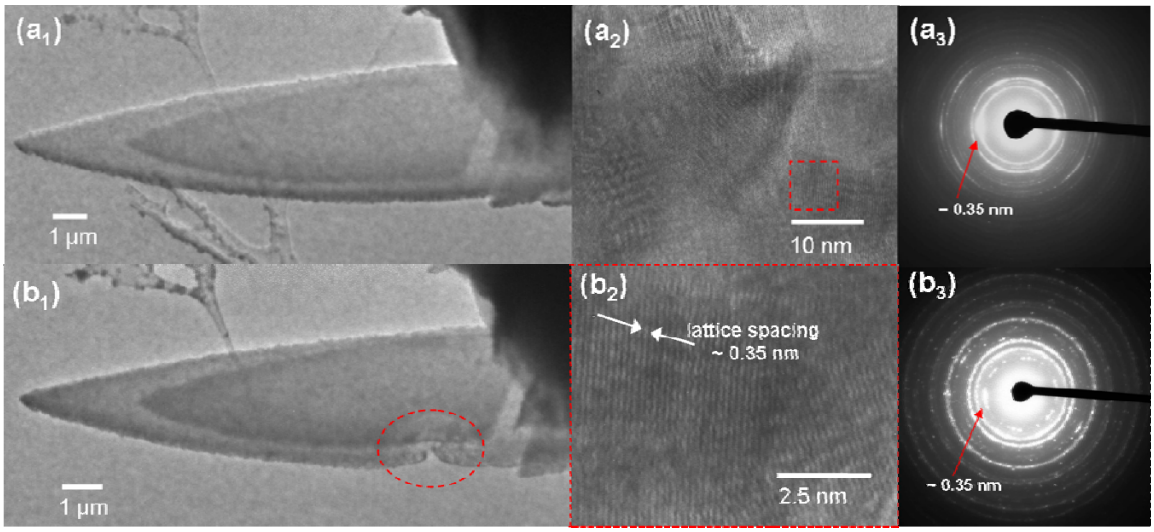

Figure 4.14. (a_1, b_1) TEM bright field images of leaf crystal before and after electron beam damage respectively. (a_2) TEM bright field images of PVA lattice and moiré fringes, and (a_3) electron diffraction pattern of the area in (a_2) where some electron beam damage has occurred. (b_2) TEM bright field images of PVA lattice with spacing (~ 0.35 nm), and (b_3) electron diffraction showing significant electron beam damage after long exposure time.

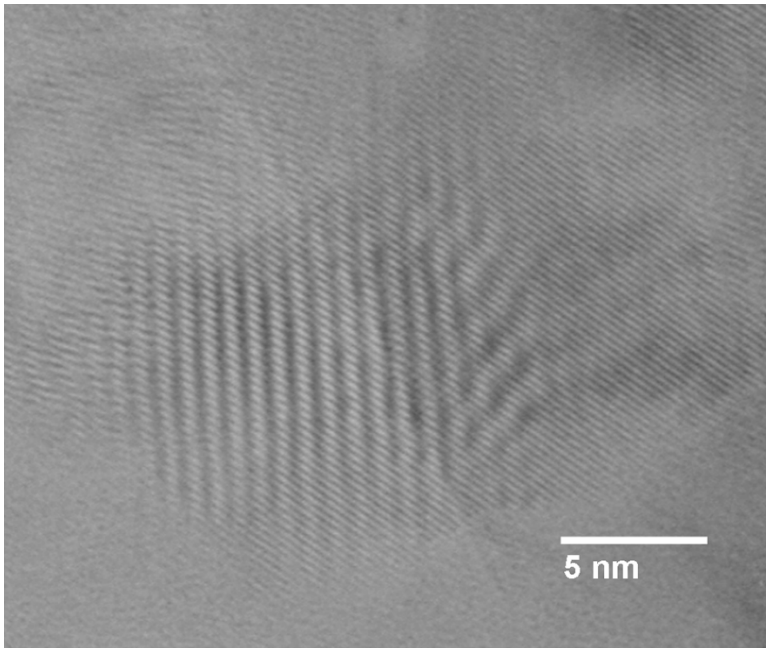

Figure 4.15. High-resolution TEM bright-field image of PVA/SWNT leaf single crystal showing moiré fringes taken at beam strength of 400 kV and ×500,000 magnifications.

After approximately 18 months, hexagon-shaped crystals were observed in this PVA/SWNT dispersion, and in some cases overgrowth of the aloe plant root structures were also hexagonal in shape (Figure 4.16). This ~18 month old PVA/SWNT dispersion was treated at slightly elevated temperature (~ 70 °C) and in this case hexagonal rods were also observed (Figure 4.17). Electron diffraction could not be obtained for these rods because their large size, therefore X-ray diffraction was performed on a powder containing hexagonal-rods and this pattern is almost identical to the X-ray pattern obtained for just aloe plant structures (Figure 4.9). Even at higher temperatures this new PVA crystal structure continues to dominate.

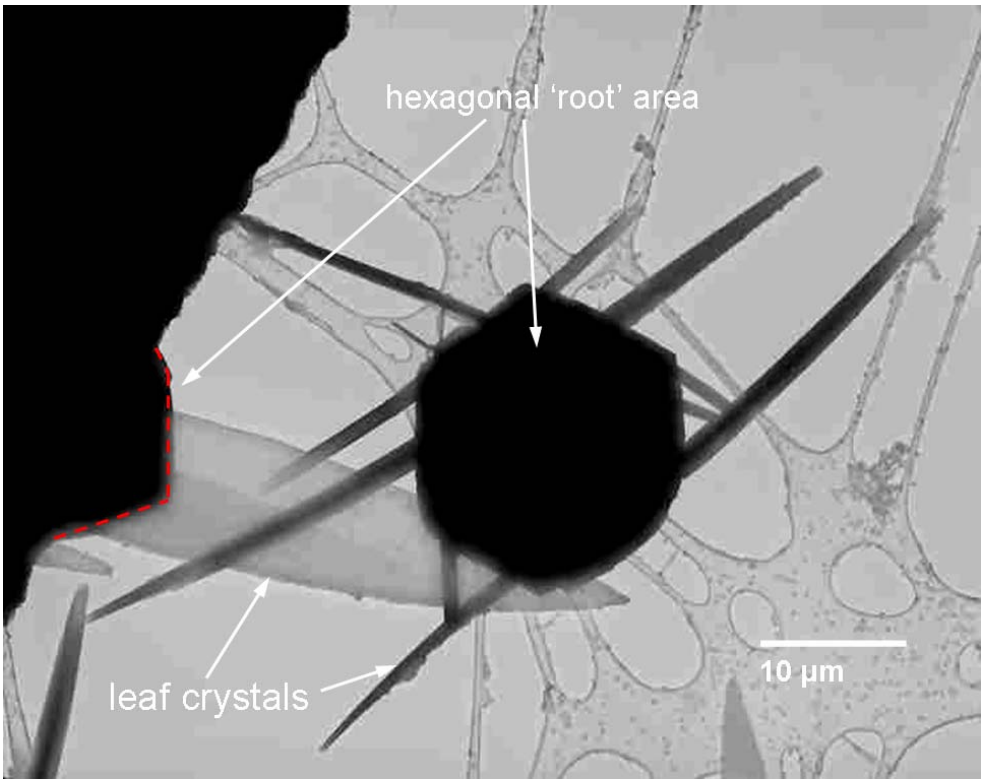

Figure 4.16. TEM bright field image of PVA/SWNT aloe plants with hexagonal-shaped root region.

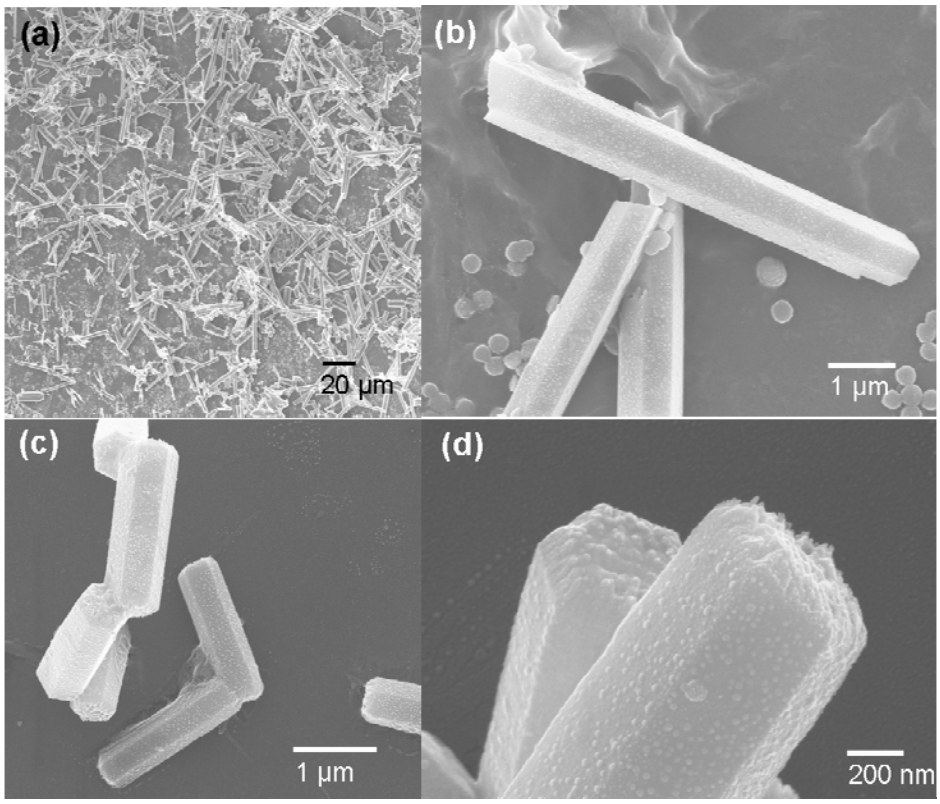

Figure 4.17. Scanning electron micrographs of (a) a large amount of hexagonal rods, and (b, c, and d) higher magnifications of hexagonal rods.

4.4. Conclusions

(1) PVA/SWNT dispersions yield aloe plant structures, where the *aloe leaves* are PVA single crystals templated by SWNT. (2) PVA molecules are aligned along SWNT surface by epitaxial means. (3) PVA leaf crystals are up to 200 nm thick near the root and taper off at the crystal tip, and related to the convergence of lamellar layers nucleated at the root. The thickness of the PVA leaf crystal at its base is therefore dictated by the PVA-SWNT template length protruding out of its root. (4) SWNT templating in single crystal growth lead to the formation of a new crystal structure for PVA and is evident in both X-ray and electron diffraction patterns. (5) FT-IR confirms that although this crystal structure differs, chemically this material is identical to PVA that crystallizes in the form

of Bunn's unit cell when not templated by SWNT. (6) Electron irradiation resistance is not particularly high in these leaf crystals, yet the thick stacking of individual lamellar prolongs the life of the crystal in the presence of the electron beam. (7) Up to five orders of reflections can be observed in diffraction patterns taken under minimal illumination conditions in the electron microscope. (8) PVA lattice images and moiré fringes can be obtained at beam strengths of 400 kV at $\times$500,000 magnifications. (9) After ~18 months of growth time hexagonal overgrowth on the aloe plants is observed, and at elevated temperature hexagonal rods are grown.

CHAPTER 5

POLY(VINYL ALCOHOL) AND POLY(VINYL ALCOHOL)/SINGLE-WALL CARBON NANOTUBE FIBERS GELATION AND COAGULATION STUDIES

5.1. Introduction

Similar to polyethylene (PE), PVA chain structure is planar zigzag. For this reason PVA is a candidate for high-strength fibers like polyethylene. The melting temperature of PVA is in the range of 230 to 250 °C, while PE only has a melting temperature in the range of 130 to 150 °C. It has been estimated that with perfect alignment of the polymer chains the lattice modulus of PVA could reach 250-300 GPa, where the lattice strains for PVA fibers under applied stress were measured by X-ray diffraction and used to calculate the elastic moduli of the crystalline regions of the polymer [150]. Therefore it has become desirable to obtain high-performance PVA fibers. To date the highest modulus attained for PVA fibers is 115 GPa [190], where as-spun fibers were obtained from Kurare Co. Ltd., and high modulus is attributed to a zone-drawing technique used to achieved high extension of the PVA molecules in the fiber, and X-ray diffraction show that crystal size along the chain axis (020) is ~16 nm [152, 190]. High-strength and high-modulus PVA fibers have also been produced using wet spinning, dry-jet wet spinning, gel spinning, dry spinning, and melt spinning methods [152].

The gel-spinning technique was originally developed by Smith and Lemstra, whose work led to the development and production of extended chain polyethylene fibers [32-34]. For PVA fiber, full extension of the chain is prohibited by the steric hinderances

to chain slippage caused by the presence of the —OH groups as well as intra- and inter-chain hydrogen bonding [151]. PVA is made by hydrolysis of polyvinyl acetate. The melting temperature increases as the degree of hydrolysis increases. The fully hydrolyzed PVA has a melting temperature in the range of 230 °C to 250 °C, while partially hydrolyzed PVA has a melting temperature in the range of 180 °C to 190 °C. Higher degree of hydrolysis leads to a higher degree of hydrogen bonding, resulting in higher melting temperature, lower draw ratio, and higher heat of fusion. Drawing PVA fibers near the melting temperature helps to loosen the hydrogen bonds and increase the draw ratio [190, 191]. PVA fibers drawn repeatedly at temperatures near the melt temperature have shown an increase in modulus. As mentioned above, PVA fibers had a modulus and strength of 115 and 3 GPa respectively [152, 190], however a zone-drawing technique which employed simultaneous vibration and heating of the fiber was used to minimize hydrogen bonding during fiber production to achieve such high properties. Typical modulus and strength of commercial PVA fibers ranges from 11 to 43 GPa and 0.9 to 1.9 GPa respectively (See Table 5.1).

Table 5.1. Typical mechanical property data for commercially produced PVA fibers.

Sample	Tensile Modulus (GPa)	Tensile Strength (GPa)	Elongation to Break (%)	Wet Shrinkage (%)†
Kuraray - Kuralon	25-41	0.88-1.6	6-10	—
Kuraray – Kuralon K-II	11-43	1.3-1.9	6-12	3.1-3.4

† Wet shrinkage data obtained by treating the yarn in water at 100 °C for 30 minutes.

The addition of CNT into the polymer matrix has been another effective way of improving the fiber mechanical properties. CNT act as a reinforcement agent for the polymer, and it has also been shown to nucleate polymer crystallization and enhance orientation. Work on the gel spinning of PVA, and PVA/SWNT fibers are discussed

here. Studies on the optimization of the spinning parameters such as spin bath temperature, as well as coagulation/gelation time are presented and discussed.

Objectives of this work:

Studies were performed on the gel spinning process for PVA and PVA/CNT fibers with the goal of improving mechanical properties of the fibers. Figure 5.1 shows a schematic of the gel-spinning set-up. The solution is pumped using a syringe pump through a needle at a controlled rate. A small gap ranging from 2 to 5 mm is maintained between the needle tip and the solvent in the gelation bath. Gelation bath temperature is maintained so that the solution extruded for the needle tip becomes a gel fiber once it is immersed in the gelation bath. The gelation bath is cooled using dry ice and temperature of the bath is maintained within ±1 °C for the duration of the spinning process. The gel fibers are subsequently collected on a take-up roller. The speed of this take-up roller is varied to ensure that the as-spun fiber is uniform, and to vary the duration of the as-spun fiber in the gelation bath. The collected drawn/undrawn as-spun fibers are immediately immersed in a second coagulation bath maintained at low temperatures for variable time periods. Previous work performed in this group on the PVA and PVA/SWNT (3 wt%) gel-spun fibers showed some improvement in the mechanical properties of the fiber with the addition of SWNT [88]. This work provided the basis to further explore PVA and PVA/CNT gel fiber spinning. In the present study only 1 wt % SWNT, and MWNT were used.

For discussion proposes, this study is separated into four major parts. Part I (Section 3.1) describes the initial spinning of PVA, PVA/SWNT, and PVA/MWNT fibers, where the spinning conditions were maintained similar to those used for spinning the PVA and PVA/SWNT (3 wt%) fibers [88]. Although the details of this study will be discussed later, it was found that under the spinning conditions used, the PVA/MWNT fibers showed a decrease in properties as compared to the PVA fiber. For this reason,

only PVA and PVA/SWNT fibers were used for the subsequent studies. Part II (Section 3.2) is a study of how the gelation bath temperature affects the drawability of the as-spun fibers, and what effect this drawing has on the mechanical properties of the final fiber. Part III (Section 3.3) describes how the length of time for the as-spun fibers in the coagulation bath affects the final fiber properties. Finally, in Part IV (Section 3.4) effect of low gelation temperature and time final fiber properties has been studied.

5.2. Experimental

Sample Preparation and Characterization: Atactic poly(vinyl alcohol) (PVA) (from Kuraray Co. Ltd. Tokyo, Japan; lot # 636837, DP: 18,000, and 98.4 % hydrolyzed) was dissolved in an 80:20 volume ratio of dimethyl sulfoxide (DMSO) (from Fisher Chemicals Cas. No. 67-68-5), and distilled water in a 400 ml Erlenmeyer flask equipped with a magnetic stir bar and heated to temperatures between 85 °C to 95 °C to obtain a 3 wt% PVA solution (80 ml DMSO, 20 ml water, and 3.4 g PVA). SWNT (obtained from CNI, Houston, TX, USA, lot# P-0247, metallic impurity ~2 wt%), dispersions were obtained in DMSO (0.4 mg of SWNT/ml of DMSO) by sonicating (using a Branson 3520 bath sonicator manufactured by Branson Instruments, Danbury, CT, USA; frequency 42 kHz, power 100 W) for 24 h at 33 °C. The mixture was continuously stirred for 72 hours with an overhead mechanical stirrer (Caframo high shear mixer, model# BDC1850 manufactured by Caframo Ltd., Wiarton, Ontario, Canada) at shear speeds between 600 RPM to 700 RPM.

Gel spinning was performed using a syringe pump (Fisher Scientific Co.). The polymer solution was placed into a syringe (B-D glass syringe) and spun through a needle (Popper 18-gauge blunt tip pipeting needle). The polymer solution was maintained at ~60 °C during spinning. The air gap between needle tip and spin bath was varied between 2 to 5 mm. The solution was pumped at a linear speed of 2.5 m/min into a methanol spin bath maintained at temperatures ranging from -70 °C to 0 °C for PVA, and

PVA/SWNT fiber spinning. This methanol spin-bath also acted as the first gelation bath. The take-up roller speed was varied to produce as-spun fibers with different draw ratios. These as-spun fibers were further coagulated in a second methanol bath for varying amounts of time and the bath was maintained at temperatures between -30 °C to -78 °C. Fibers were subsequently drawn in a three-stage process at temperatures of 100 °C, 160 °C, and 200 °C respectively on a fiber drawing hot plate manufactured by Bradford University Research Ltd. In some cases the fibers were also drawn for a fourth stage on a hot plate at 290 °C. This temperature exceeds the melting temperature of PVA. Therefore to accomplish this, fibers were only in contact with the hot plate for ~ 300 ms (times exceeding 1 s resulted in the fiber melting/degrading and drawing was not possible). All gel-spun fibers were taken through several heat-drawing stages before vacuum drying for one to three days at 60 °C for testing.

5.2.1. Sample Characterization

Scanning electron microscopy (SEM) was done on LEO 1530 thermally assisted field emission microscope (at 10 kV) on samples sputtered coated with gold, and a Zeiss Ultra60 SEM at operating voltages of 1-5 kV on uncoated samples. Fibers broken in tensile tests were used for SEM observation. Transmission electron microscopy (TEM) studies were carried out on Hitachi HF-2000 Field Emission Gun electron microscope (accelerating voltage 200 kV) (manufactured by Hitachi High Technologies America Inc., Pleasanton, CA, USA). TEM samples were prepared on Lacey carbon coated TEM grids (Electron Microscopy Sciences, Hatfield, PA, USA; Cat.# HC200-Cu). Raman spectroscopy was performed on a Holoprobe Raman microscope (manufactured by Kaiser Optical Systems Inc., Ann Arbor, MI, USA) at an excitation wavelength of 785 nm and 1.5 MW beam power. Wide-angle X-ray scattering was done on the Rigaku Micro Max 002 X-ray generator operated at 45 kV and 0.66 mA and equipped with R-axis VI++ detector. For X-ray studies of fibers, 10-20 filaments were mounted in a fiber

frame. Crystallinity, crystal size, and orientation from wide-angle X-ray diffraction were determined using the software MDI Jade 6.1. AreaMax software was used for background subtraction and integration. The area due to the crystalline and amorphous contribution of the polymer was determined by peak fitting analysis. Thermal shrinkage measurements were performed on Thermal mechanical analyzer (TMA) (manufactured by TA Instruments, New Castle, DE, USA). Tensile properties of these fibers were measured using a RSA III solids analyzer (manufactured by Rheometrics Scientific Co., Piscataway, NJ, USA) at a gauge length and crosshead speeds of 25 mm and 0.25 mm/s respectively. For tensile test measurements a circular diameter is assumed to calculate cross-sectional area. Fiber diameter was calculated using a weight method, where the weight of a specific length of fiber was divided by the fiber density (determined experimentally from crystallinity measurements – PVA amorphous density (ρ_a) and crystalline density (ρ_c) are 1.269 and 1.345 g/cm^3 respectively). The volume is evaluated from the previous calculation, and a circular cross-section is assumed to determine the fiber diameter.

5.3. Results and Discussion

Table 5.2 summarizes the processing parameters for various fibers. It should be noted that a higher as-spun ratio is coupled with shorter duration in the gelation bath (T_{gel}) (Table 5.2 and Figure 5.2). Figure 3 plots the relationship between the modulus of both PVA and PVA/SWNT fibers to the hot-stretch draw ratio. Table 5.3 lists the mechanical property data for the fibers produced in each study. Wide-angle X-ray diffraction (WAXD) analysis was performed on all the fibers in this work. Crystallinity and orientation data are listed in Table 5.4, while crystal size data are listed in Table 5.5. Figure 5.4 shows the integrated intensity versus 2θ scans for both PVA and PVA/SWNT fibers. Crystallinity values for the fibers were calculated by fitting both crystal and amorphous peaks (Figure 5.4).

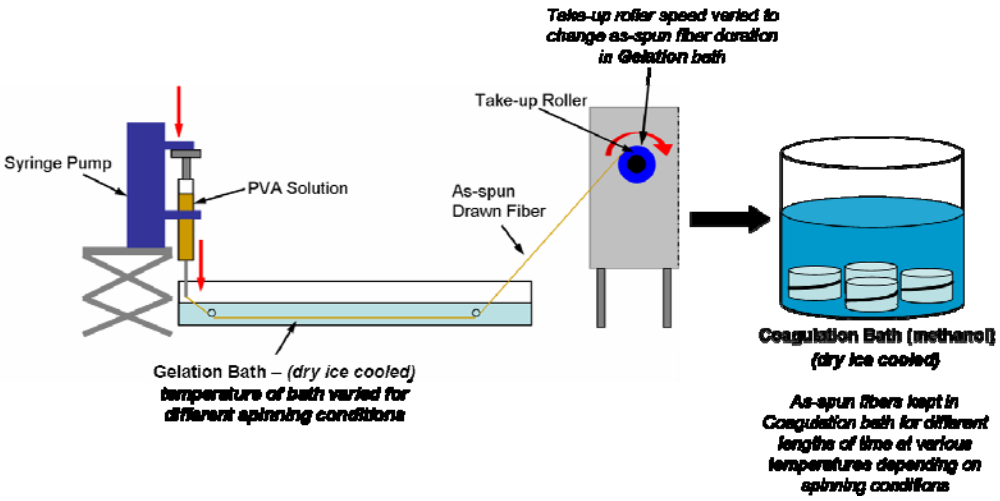

Figure 5.1. Schematic of the gel spinning set-up.

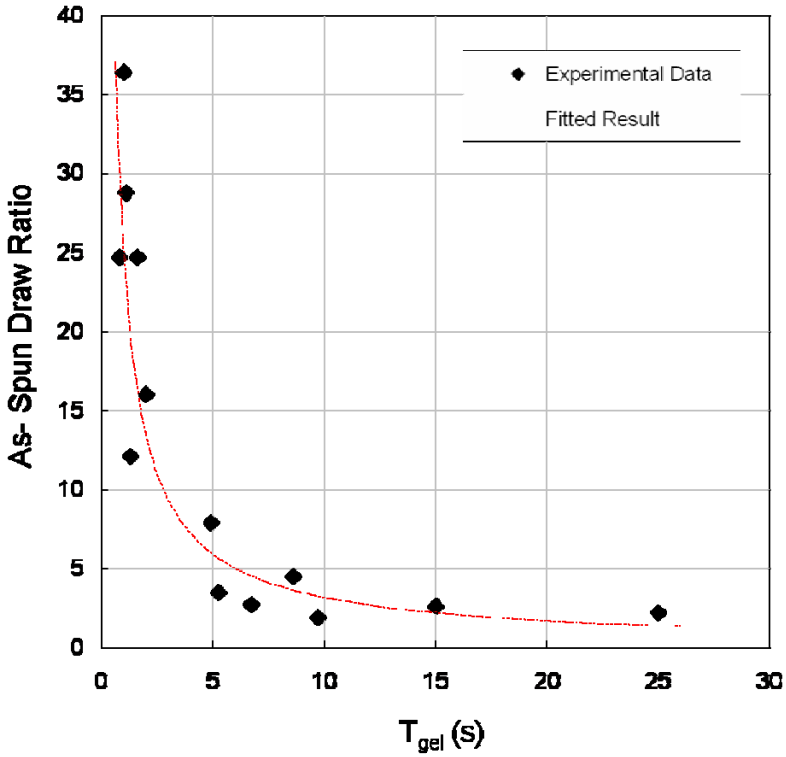

Figure 5.2. Experimental and fitted data for all fiber showing the relationship between as-spun draw ratio and gelation time (T_{gel}).

Table 5.2. Summary of drawing procedure for both PVA and PVA/CNT gel-spun fibers.

Study	Sample		As-Spun Conditions			Coagulation Time (Days)/ Temperature (°C)♦	Draw Ratio†					
			Gelation -Bath Temp. (°C)♦	As-Spun DR‡	t_{gel}* (s)		Stage 1 100 °C	Stage 2 160 °C	Stage 3 200 °C	Stage 4 290 °C	Total DR	Hot Stretch DR
Initial Study	A1	PVA/SWNT	-10	16	2	1/-30	2.0	1.8	1.4	—	79.8	5.0
	B1	PVA	-10	16	2	1/-30	2.0	1.6	1.2	—	57.1	3.8
	C1	PVA/ MWNT	-25	28.8	1.1	1/-30	1.6	1.6	1.9	—	138.3	4.7
Draw Ratio Optimization	A2	PVA/SWNT	-12	36.4	1	1/-30	1.5	1.9	1.4	—	136.4	4.0
	B2	PVA	-30	24.7	1.6	1/-30	1.8	1.8	1.4	—	85.5	4.5
Coagulation Study	$A3_1$	PVA/SWNT	-20	24.7	0.8	1/-30	2.0	1.5	1.4	—	101.4	4.1
	$A3_2$	PVA/SWNT	-20	24.7	0.8	4/-30	1.7	1.1	1.3	—	60.5	2.5
	$A3_3$	PVA/SWNT	-20	24.7	0.8	8/-30	1.7	1.1	1.2	—	57.0	2.3
	$B3_1$	PVA	-25	12.1	1.3	1/-30	1.6	2.0	1.5	—	59.4	5.0
	$B3_2$	PVA	-25	12.1	1.3	4/-30	1.6	2.3	1.3	—	54.8	4.7
	$B3_3$	PVA	-25	12.1	1.3	8/-30	1.6	2.0	1.2	—	47.5	3.9
Gelation Study	A4	PVA/SWNT	-78	2.61	15	1/-78	3.2	1.8	1.4	1.8	42.2	14.1
	B4	PVA	-78	2.68	15	1/-78	2.0	2.1	1.2	1.8	24.8	9.1

* t_{gel} *refers to time as-spun fibers spend immersed in the gelation bath before collection on the take-up roller.*

♦ *Methanol was used for both gelation- and coagulation-baths.*
‡ *As-spun draw pertains to the amount fiber is stretched between extrusion into the gelation bath and collection on the take-up roller.*
† *Draw ratios at each heat-drawing stage was maximized.*

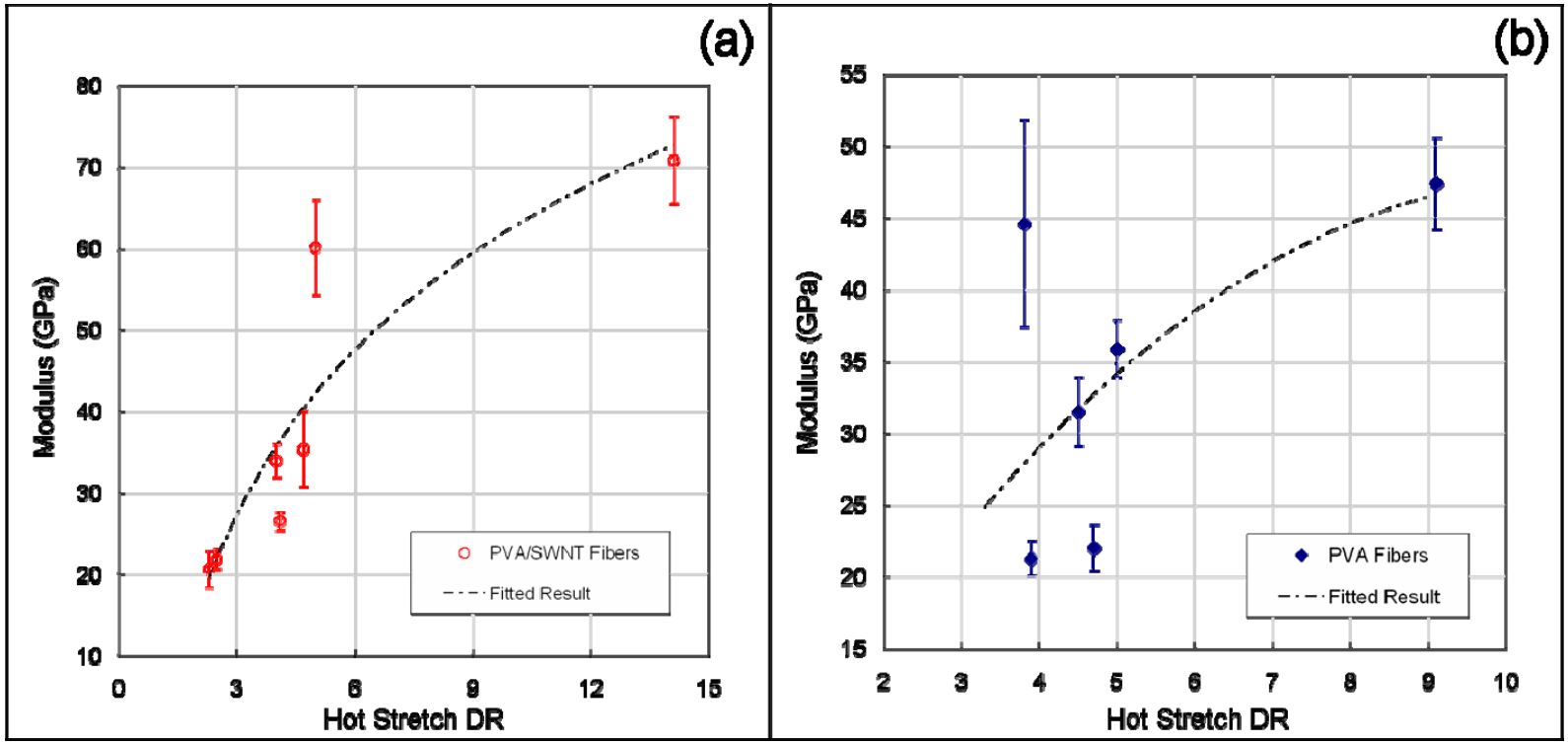

Figure 5.3. Experimental and fitted data for (a) PVA/SWNT and (b) PVA fibers showing the relationship between modulus and hot-stretch draw ratio.

Table 5.3. Summary of mechanical property data for both PVA and PVA/CNT gel-spun fibers.

Study	Sample	Effective Fiber Diameter (μm)†	Tensile Modulus (GPa)	Tensile Strength (GPa)	Elongation to Break (%)	Toughness (J/g)
Initial Study	A1	11.5	60.1 ± 5.8	1.4 ± 0.1	4.9 ± 0.5	28.9 ± 6.1
	B1	13.1	44.6 ± 7.2	1.0 ± 0.1	5.3 ± 0.3	21.9 ± 3.5
	C1	9.5	35.4 ± 4.6	0.9 ± 0.1	4.5 ± 0.4	17.5 ± 3.5
Draw Ratio Optimization	A2	10.8	34.0 ± 2.0	0.94 ± 0.1	5.7 ± 0.8	21.7 ± 2.4
	B2	13.1	31.5 ± 2.4	1.1 ± 0.1	5.4 ± 0.3	21.2 ± 2.2
Coagulation Study	$A3_1$	14.5	26.6 ± 1.1	0.66 ± 0.03	5.4 ± 0.3	14.5 ± 1.4
	$A3_2$	18.8	21.9 ± 1.2	0.42 ± 0.07	8.6 ± 1.9	18.0 ± 6.1
	$A3_3$	22.6	20.7 ± 2.2	0.42 ± 0.04	10.1 ± 2.4	21.0 ± 7.8
	$B3_1$	14.4	35.9 ± 2.0	0.88 ± 0.14	4.1 ± 0.7	14.9 ± 4.5
	$B3_2$	17.3	22.0 ± 1.6	0.59 ± 0.03	5.2 ± 0.2	12.1 ± 1.1
	$B3_3$	18.1	21.3 ± 1.2	0.51 ± 0.02	5.4 ± 0.2	11.6 ± 0.5
Gelation Study	A4	22.6	70.8 ± 5.4	2.6 ± 0.2	6.2 ± 0.7	58.4 ± 6.8
	B4	25.1	47.4 ± 3.2	1.6 ± 0.1	6.5 ± 1.4	40.1 ± 5.9

† Effective fiber diameter was calculated using a weight method, where the weight of a specific length of fiber was divided by the fiber density (determined experimentally from crystallinity measurements – PVA amorphous density (ρ_a) and crystalline density (ρ_c) are 1.269 and 1.345 g/cm^3 respectively). The volume is evaluated from the previous calculation, and a circular cross-section is assumed to determine the fiber diameter. For tensile test measurements a circular diameter is also assumed to calculate cross-sectional area.

Table 5.4. Orientation and crystallinity data for PVA, and PVA/CNT gel spun fibers

Study	Sample	$\overline{\cos^2 \phi_{200}}$	$\overline{\cos^2 \phi_{101}}$	$\overline{\cos^2 \theta_{b-axis,\,PVA}}$	$f_{b-axis,\,PVA}$	f_{SWNT}	Crystallinity (%)
Initial Study	A1	0.113	0.063	0.930	0.895	0.91	63
	B1	0.145	0.062	0.967	0.951	—	63
	C1	0.071	0.068	0.869	0.803	—	61
Draw Ratio Optimization	A2	0.169	0.085	0.924	0.886	—	61
	B2	0.163	0.077	0.939	0.909	—	63
Coagulation Study	$A3_1$	0.208	0.120	0.855	0.783	—	56
	$A3_2$	0.186	0.110	0.862	0.794	—	52
	$A3_3$	0.165	0.097	0.879	0.819	—	51
	$B3_1$	0.158	0.077	0.934	0.901	—	52
	$B3_2$	0.169	0.082	0.930	0.895	—	55
	$B3_3$	0.181	0.101	0.887	0.829	—	55
Gelation Study	A4	0.172	0.072	0.965	0.948	0.84	58
	B4	0.186	0.99	0.896	0.843	—	60

Table 5.5. Crystal size data for PVA, and PVA/CNT gel-spun fibers

	(hkl)	Samples											
		Initial Study		Optimization Study		Coagulation Study						Gelation Study	
		A1	B1	A2	B2	$A3_1$	$A3_2$	$A3_3$	$B3_1$	$B3_2$	$B3_3$	A4	B4
Crystal Size	(100)	6	7	5	6	5	7	8	6	6	6	4	5
	(101)	4	5	6	6	5	6	6	6	6	6	6	5
	(200)	4	5	6	7	5	8	7	5	6	6	4	6
	(010)	11	8	6	5	6	6	6	9	8	9	11	—
	(111)	8	7	6	6	3	7	7	8	7	8	8	9
	(211)	6	6	7	7	7	8	7	6	6	6	6	7

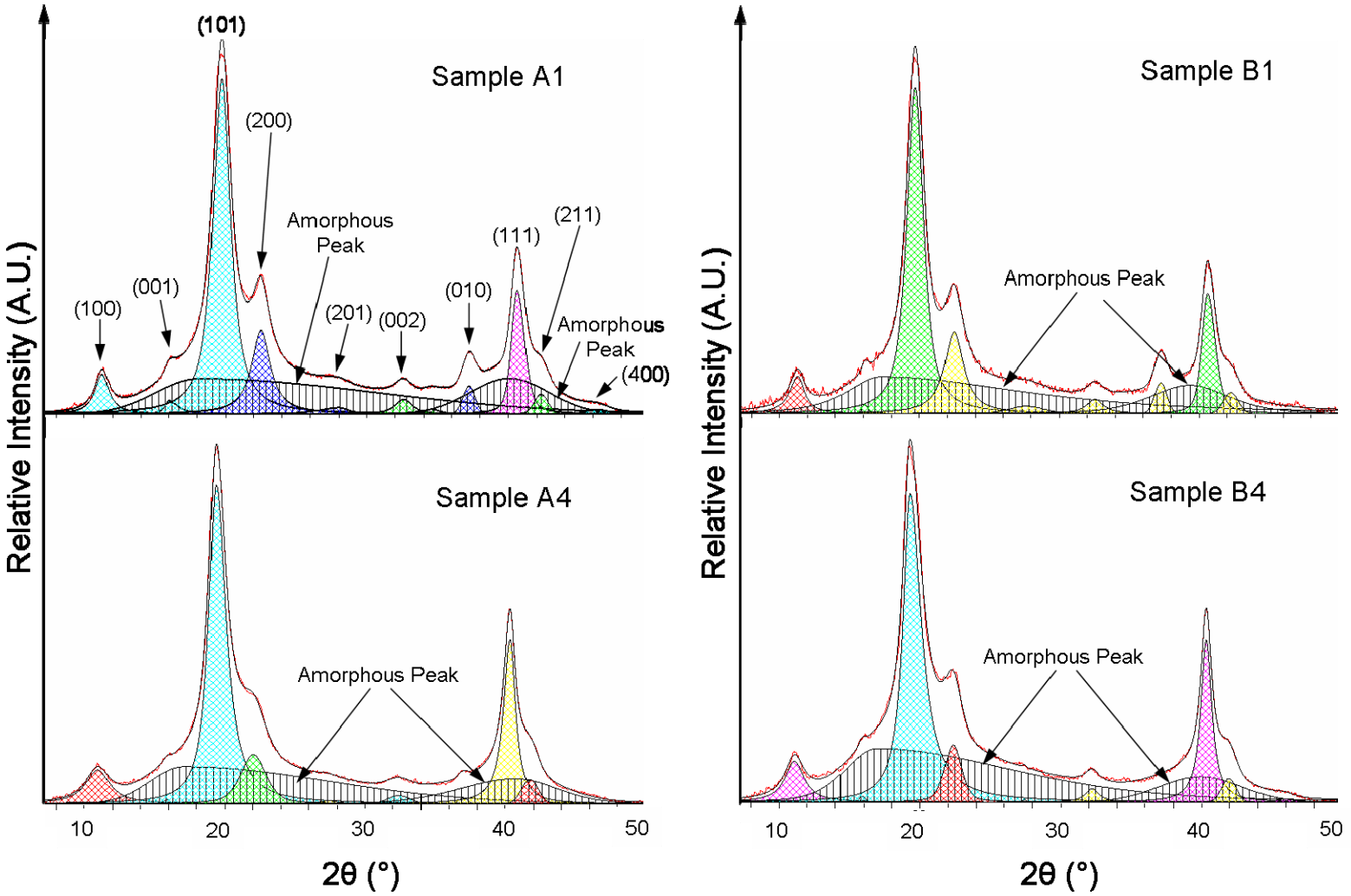

Figure 5.4. Sample peak fitted integrated wide-angle X-ray intensity vs. 2θ scans shown for samples, A1, B1, A4, and B4. This method was used to calculate fiber crystallinity by X-ray.

5.3.1. Initial Gel-Spinning of PVA, PVA/SWNT, and PVA/MWNT Fibers (Samples A1, B1, and C1)

The gelation and coagulation conditions of PVA, PVA/SWNT, and PVA/MWNT dispersions play an important role in the spinning process for PVA, PVA/SWNT, and PVA/MWNT fibers. PVA solutions must be cooled below the critical gelation point to form gel fibers. In the literature, PVA solutions in DMSO/H_2O mixtures have been spun into gelation baths maintained at temperatures between -20 °C to 20 °C. At all temperatures a gel fiber could be obtained, however fibers with the highest mechanical properties were found for fibers spun at -20 °C [143]. For this reason it was desirable to spin PVA, PVA/SWNT, and PVA/MWNT fibers at low gelation temperatures. In this work, it was found that the gelation of PVA/SWNT and PVA/MWNT fibers differed from neat PVA fibers. Lower gelation temperature (below -25 °C) led to freezing of the PVA/SWNT fiber, while the PVA and PVA/MWNT fibers were still flexible and gel-like. Frozen fibers exhibit brittle behavior. Figure 5.5 shows the PVA/SWNT fiber after immersion in a gelation bath at -40 °C (we begin to observe this freezing behavior below -25 °C). Figure 5.4 shows photographs of PVA/SWNT and PVA/MWNT fibers during drawing in methanol at -30 °C. Figure 6a shows that PVA/SWNT fibers do not draw easily and exhibit brittle failure, while PVA/MWNT fibers (Figure 5.6b) are flexible and can be drawn easily at this temperature. PVA fibers behave similar to PVA/MWNT fibers but are not shown because for their transparency. Figure 5.6 shows PVA fibers of different diameters, however this behavior is observed independent of fiber diameter. The gelation temperature for the fiber spinning process was controlled so that pliable gel fibers could be obtained. For this reason, a range of gelation/coagulation temperatures were used to ensure all solutions/dispersions could be spun into gel fibers.

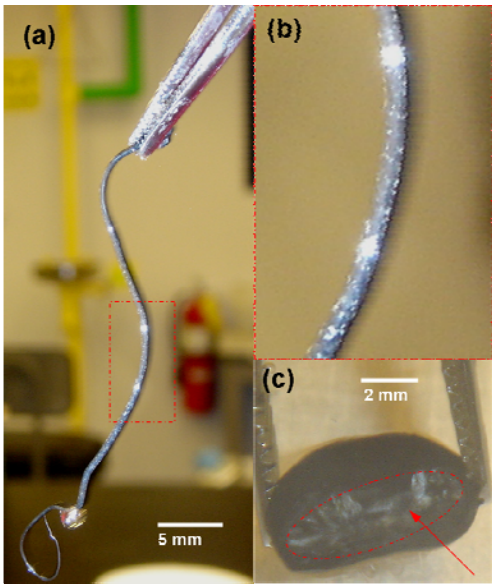

Figure 5.5. Photographs of (a) PVA/SWNT gel fiber after immediately being immersed in -40 °C methanol – the fiber is completely frozen. (b) A magnified image of the boxed region in (a). (c) A frozen cross section of PVA/SWNT material showing that the freezing is throughout.

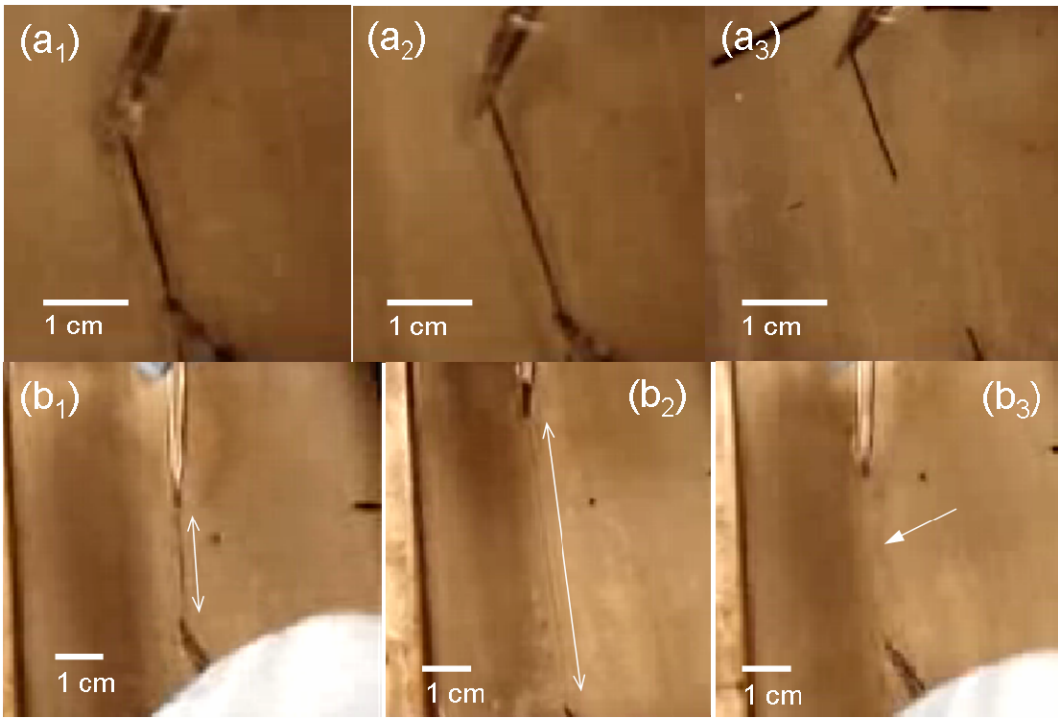

Figure 5.6. Photographs of (a) PVA/SWNT fibers showing brittle-like behavior when drawn in methanol at -30 °C, and (b) PVA/MWNT fiber showing flexible behavior when drawn in methanol at -30 °C (PVA fibers behaved similar to PVA/MWNT but could not be photographed because fibers were transparent). (b_3) arrow points to flexible PVA/MWNT fiber after drawing.

As-spun fibers were collected on a take-up roller at a speed of 40 m/min, therefore PVA and PVA/SWNT fibers were stretched and the as-spun draw ratio was 16. Figure 5.1 shows a schematic for the fiber spinning set-up. The as-spun fibers were heat drawn at 100 °C, 160 °C, and 200 °C on a hot plate. The total draw ratio for PVA, and PVA/SWNT fibers was 57, and 80 respectively. Draw ratios obtained during each stage of the hot-stage drawing process was comparable for the two fibers (Table 5.2). The mechanical properties for the fibers are listed in Table 5.3. PVA/SWNT fibers show an increase of 35 % and 40 % in modulus and tensile strength as compared to the control PVA fibers. Polarized G-band intensity data were also used to determine the orientation of the SWNT and X-ray azimuthal data to determine orientation of PVA molecules in the fibers, and these orientation values are listed in Table 5.4. Crystal size values are listed in Table 5.5. Overall the control PVA fiber had higher molecular orientation and crystallinity than the composite fibers. Fitted X-ray profiles for samples A1 and B1 are shown in Figure 5.4. Polarized Raman G-band intensity as a function of angle (Ψ) between fiber axis and the polarization direction is plotted in Figure 5.7, and Raman spectra as a function of fiber orientation is shown in Figure 5.8. The I_{0°/I_{90° ratio for the PVA/SWNT fiber was 100 revealing high SWNT orientation.

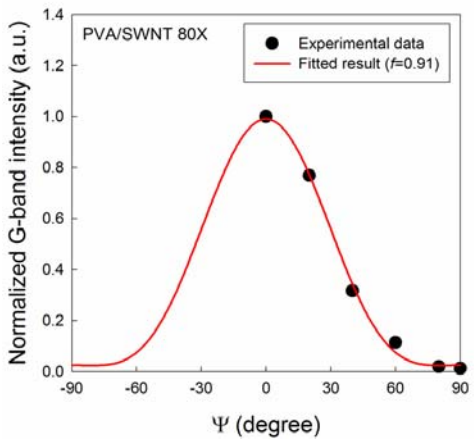

Figure 5.7. Polarized Raman G-band intensity profile as a function of fiber orientation angle, Ψ for PVA/SWNT (A1) fiber.

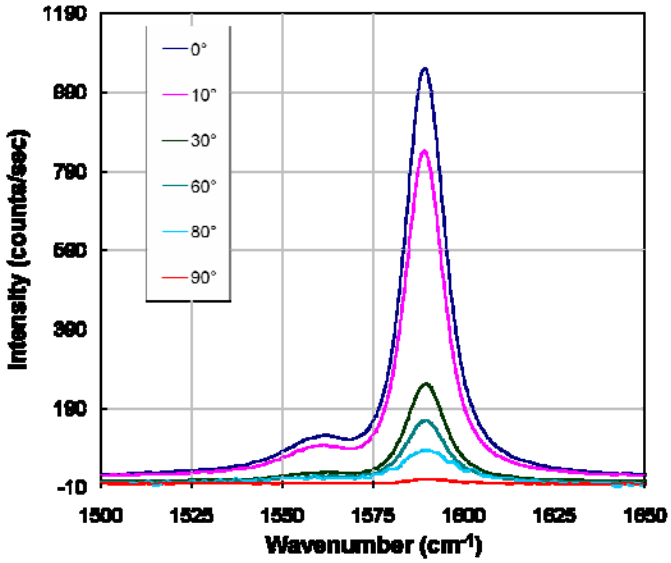

Figure 5.8. Polarized Raman spectra plotted as a function of fiber orientation angle, Ψ for PVA/SWNT fiber (A1).

The effective modulus contributions of the SWNT in the PVA composite fibers can be determined using the rule of mixture for uniaxial composites [192] in Equation 5.1.

$$E_c = V_{SWNT} E_{SWNT} + (1 - V_{SWNT}) E_m \tag{5.1}$$

Where, E_c, E_m, and E_{SWNT} are Young's modulus of the composite, matrix, and SWNT respectively and V_{SWNT} is the volume fraction of the SWNT. This can be extended to determine the effective strength contribution (Equation 5.2).

$$\sigma_c = V_{SWNT} \sigma_{SWNT} + (1 - V_{SWNT}) \sigma_m \tag{5.2}$$

Since SWNT have defined length they are discontinuous throughout the matrix and also not perfectly aligned in the composite. Therefore, both length and orientation factors η_L and η_o are incorporated in to the rule of mixture (Equation 5.3 and 5.4) to take account to for this [192, 193].

$$E_c = \eta_L \eta_o V_{SWNT} E_{SWNT} + (1 - V_{SWNT}) E_m \tag{5.3}$$

$$\sigma_c = \eta_L \eta_o V_{SWNT} \sigma_{SWNT} + (1 - V_{SWNT}) \sigma_m \tag{5.4}$$

The SWNT orientation in the composite is measured using Raman spectroscopy. The calculate effective Young's modulus and strength integrate the effective length factor ($E_{eff} = \eta_L E_{SWNT}$ and $\sigma_{eff} = \eta_L \sigma_{SWNT}$). Using equations 5.3 and 5.4 the average effective Young's modulus and strength contributions of the SWNT are determined for the gel-spun PVA/SWNT fibers and found to be 1.70 TPa and 44 GPa respectively. Theoretically the Young's modulus of SWNT has been predicated to range from 1 to 5.5 TPa [63, 194-197], while experimentally measured to be around 1 TPa [198, 199]. The exceptionally high effective Young's modulus and strength calculated here for the SWNT in the PVA/SWNT fibers shows its ability to provided excellent reinforcement at low weight concentrations. It also suggests good load transfer between the SWNT and PVA matrix.

Figures 5.4 and 5.9 show X-ray diffraction fitted integrated 2θ profiles and pattern for the fibers respectively. The predominant *(hkl)* reflections present in all fibers produced in this gel-spinning process are identified in Figure 5.4. Significant difference in crystal size (Table 5.5) for the PVA fiber as compared to the PVA/SWNT fiber is observed along the (001) and (002) planes, but is comparable along other crystallographic planes. This would imply that from a morphological standpoint, most of the changes in the composite fiber mechanical properties as compared to the control fiber may be related to SWNT orientation as well as to the physical PVA-SWNT reinforcement interactions. The spinning parameters also affect the final fiber properties. Therefore, further optimization studies of the spinning process are performed.

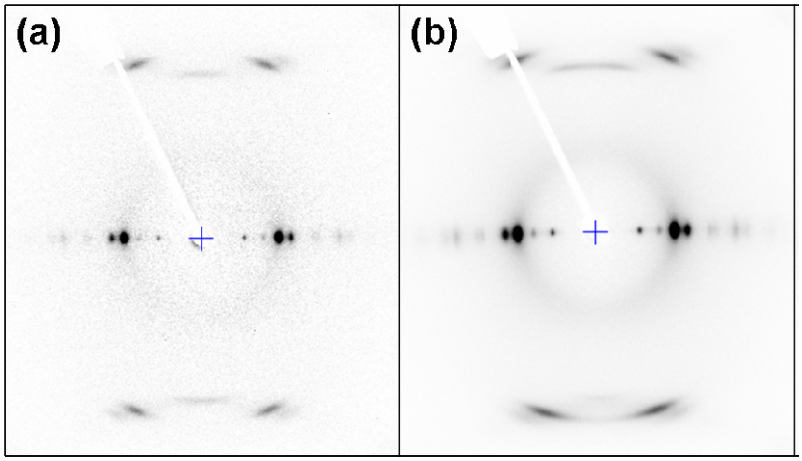

Figure 5.9. Wide-angle X-ray diffraction patterns for (a) PVA (B1) and (b) PVA/SWNT (A1) fibers spun in initial study.

5.3.2. Draw Ratio Optimization Study (Samples A2 and B2)

Methanol is typically used in PVA gel and dry-jet wet spinning as both a gelation and coagulation bath [88, 143, 191, 200-202]. PVA fiber drawing is limited by inter- and intra-chain hydrogen bonding. Studies show that an increase of draw ratio has been shown to improve tensile strength and modulus [190, 202]. The advantage of the gel-spinning process is to produce gel fibers where the polymer molecules are inter-dispersed with solvent molecules and bonded together by physical crosslinks and microcrystalline regions. High alignment of the polymer molecules is also possible since the chains can slide more easily with respect to each other due to the presence of solvent molecules. In this section the effect of the gelation bath temperature is discussed for its effect on the drawability of the PVA and PVA/SWNT fibers. As the PVA solution and PVA/SWNT dispersion is extruded into the methanol spin bath, gel fibers form and these fibers are drawn immediately.

As mentioned in the previous section, depending on the gelation bath temperature, the PVA and PVA/SWNT gel fiber formation differs. Below -25 °C PVA/SWNT fibers freeze and are very difficult to handle as they become brittle. As the temperature is increased (> -20 °C) the fiber is gel-like but becomes more pliable making fiber drawing

possible. The schematic for this spinning set-up is shown in Figure 5.1. The PVA solutions and PVA/SWNT dispersions are extruded into the methanol bath at temperatures ranging from -70 to 10 °C and take-up roller speed is varied to pull the fiber to the maximum extension rate without breaking the fiber. This data is represented in Figure 5.10. PVA fibers showing freezing behavior below temperature of -45 °C, while PVA/SWNT fiber freeze below -25 °C. The frozen fibers show brittle failure and can only be drawn to low extensions (DR < 20).

The drawing of PVA fiber was performed over the temperatures ranging from -40 to -10 °C. PVA drawing goes through a maximum at ~ -28 °C (Figure 5.10). Below this temperature the fiber consistently exhibits gel-like behavior, and above this temperature the gel-fiber becomes sticky suggesting that it is not completely gelled. PVA/SWNT dispersions extruded into cooled methanol were found to freeze at temperatures where PVA fiber would be gel-like. For this reason, the temperature ranges over which drawing experiments were conducted for PVA/SWNT is much higher than for PVA fibers. For PVA/SWNT, spin bath temperatures ranged from -30 to 0 °C. PVA/SWNT fiber continued to exhibit freezing behavior up to about -20 °C. These partially frozen fibers could be drawn therefore data was obtained. PVA/SWNT drawing was maximized at ~ -7 °C (Figure 5.9), and the fiber maintained its gel-like consistency as opposed to PVA fibers which were sticky at similar temperatures. PVA/SWNT fiber could also be drawn to 2× the draw ratio of PVA fibers.

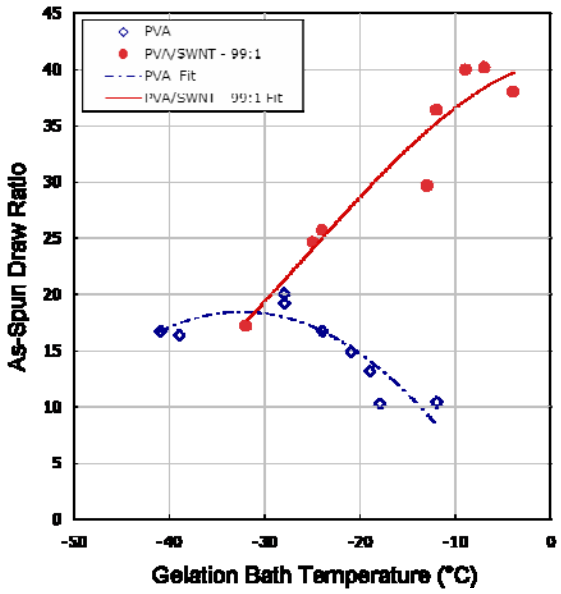

Figure 5.10. Draw ratio optimization data showing the as-spun draw ratio for PVA (B2) (diamonds) and PVA/SWNT (A2) (circles) fibers as a function of gelation (spin bath) temperature.

To understand why PVA and PVA/SWNT fibers exhibit freezing behavior at different temperatures the solution composition is examined. PVA solutions and PVA/SWNT dispersion in this work are made in 80:20 ratio of DMSO:H_2O mixtures. At this ratio DMSO:H_2O mixture will exhibit liquid-like behavior down to ~ -40 °C [203]. Separately, H_2O freezes at 0 °C and DMSO at ~ 15 °C [203]. From this information the freezing behavior of the PVA fiber at -45 °C is understood. PVA/SWNT exhibit freezing even up to -25 °C where DMSO:H_2O mixture should be in the liquid state. One possible explanation is that phase separation of the solvent occurs in the PVA/SWNT dispersions at low temperatures, where the solvent interaction with PVA and SWNT may differ leading to phase separation of either H_2O and DMSO solvent within the spun fiber that ultimately freeze. Further study is required to understand this behavior.

Both PVA and PVA/SWNT fiber with the highest as-spun draw ratios were subsequently heat drawn at 100 °C, 160 °C, and 200 °C on a hot plate to final draw ratios of 85 and 137 respectively (Table 5.2). In both cases the draw ratio at each heat stage was comparable. The fibers were subsequently dried in vacuum for mechanical and

wide-angle X-ray analysis. Although the overall draw ratios of these fibers were much higher than the previous study, both the PVA mechanical and orientation properties of these fibers are lower (Table 5.3 and 5.4). This was unexpected since previous studies on PVA fiber spinning have shown an increase in orientation and mechanical properties with overall draw ratio [202, 204]. However, for previous work [88, 143, 202, 204] there is very little to no elongation of the as-spun PVA fiber, and hot-drawing is used instead to maximize the draw ratio, therefore the increase in mechanical properties may be related to hot-drawing of the PVA fibers. For the conditions used in this study the as-spun draw is maximized.

For a similar study on polyethylene where different elongation rates (1 m/min to 500 m/min) (see Table 5.6) were used during the spinning process, a similar drop in orientation and mechanical properties with higher elongation is observed [205, 206]. It was found that flow instabilities result in fiber defects at high extension rates which would ultimately lower the mechanical properties. Also, competition between the polymer chain relaxation (τ) and elongational deformation ($\dot{\varepsilon}_{ii}$) by the flow field, as well as time in the orientation flow field (t) would determine whether the polymer molecules would actually become oriented during extension [205, 207]. Two conditions $\dot{\varepsilon}_{ii} t >> 1$ and $\dot{\varepsilon}_{ii} \tau > 1$ must be satisfied for orientation to occur. For the PVA and PVA/SWNT fibers in this work the fibers appear uniform from SEM observations (Figure 5.11), therefore flow instabilities may not play a large factor in the decrease of mechanical properties. In these fibers the decrease in orientation of the PVA molecules may be the main reason for the reduction in mechanical properties which may be related to the polymer deformations in the flow. At high extension rates both PVA and PVA/SWNT fibers are subjected to the orientation flow field and gelation bath for less than one second therefore the polymer chain mechanics conditions $\dot{\varepsilon}_{ii} t >> 1$ and $\dot{\varepsilon}_{ii} \tau > 1$

may not be satisfied and orientation is lowered. Based on the conditions for this study, although maximizing the as-spun draw ratio was effective for the overall increase in the draw ratio it has a negative effect on the overall mechanical properties of the fiber.

Table 5.6. Experimental data for polyethylene, PVA, and PVA/SWNT fibers showing a decrease in tensile properties with an increase in as-spun drawing of the fibers.

Sample		Extrusion Speed (m/min)	Take-up speed (m/min)	Tensile Strength (GPa)
High molecular weight PE gel-fibers [205, 206]		1 100 100	1 250 500	7.2 3.2 0.3
PVA	B2 B4	2.5 2.5	62 6.5	0.94 1.6
PVA/SWNT	A2 A4	2.5 2.5	91 6.5	1.1 2.6

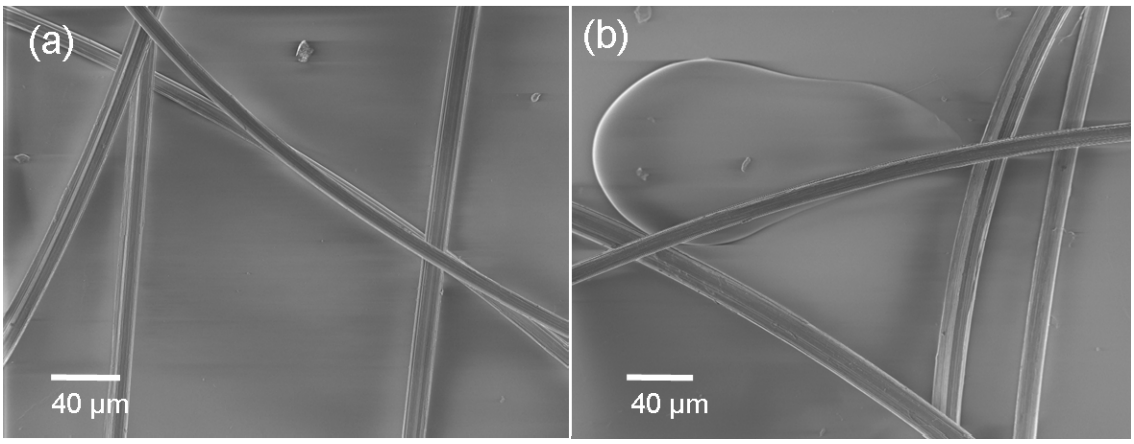

Figure 5.11. Scanning electron micrograph of PVA/SWNT fibers drawn at maximum extension rate (as-spun draw ratio of 40) showing smooth surface.

3.3. Coagulation Study (Samples A3 and B3)

Methanol is also used as a coagulation medium for PVA fiber spinning [88, 143, 202]. In this section the PVA and PVA/SWNT fiber were studied as a function of coagulation time. The coagulation period was varied from one to eight days and methanol bath was maintained at -30 °C. During coagulation, solvent exchange is

expected to occur. Therefore methanol will exchange with DMSO and H_2O over time. H_2O and DMSO have a boiling point at100 °C and ~185 °C respectively. TGA experiments were run in air up to 400 °C. The residual weight loss was measured at 200 °C to determine the amount of weight loss of solvent from the fiber. These measurements gave some indication of the remaining amount of solvent in the fiber for each coagulation period. TGA results show that with longer coagulation time the overall % weight of DMSO and H_2O decreased (Figure 5.12 and 5.13). The fibers were also drawn at 100 °C, 160 °C, and 200 °C on a hot plate. The overall draw ratio decreased slightly as the coagulation time increased (Table 5.2). PVA orientation in the PVA/SWNT fibers ($A3_1$, $A3_2$, and $A3_3$) was comparable, while in the PVA fiber ($B3_1$, $B3_2$, and $B3_3$) decreased with increasing coagulation time (Table 5.4). However, crystallinity and crystal size remained about the same throughout all the fibers (Table 5.4 and 5.5). This suggests that the presence of DMSO and H_2O in the fiber aids in chain slippage and reduces inter-chain hydrogen bonding resulting in higher draw ratio. With subsequent removal of solvent the drawability is reduced. This phenomenon was observed for both PVA and PVA/SWNT fibers. The mechanical properties for both PVA and PVA/SWNT fibers also decreased with increasing coagulation time (Figure 5.14 and Table 5.3).

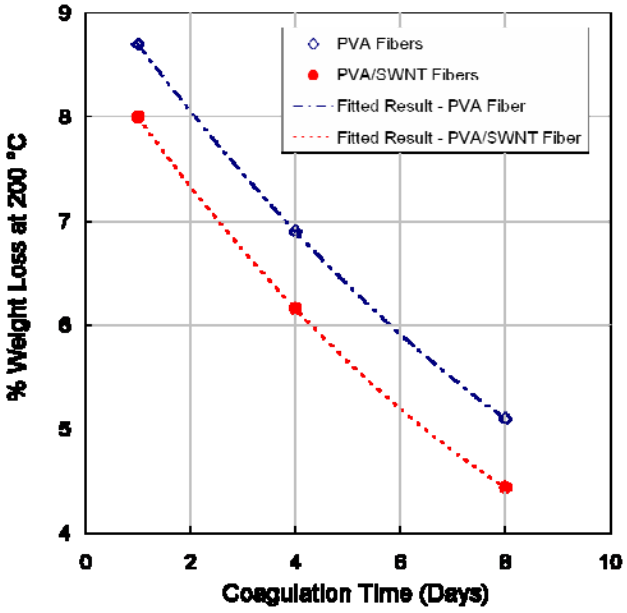

Figure 5.12. TGA data for residual solvent weight in both PVA (B3) and PVA/SWNT (A3) as a function of coagulation time.

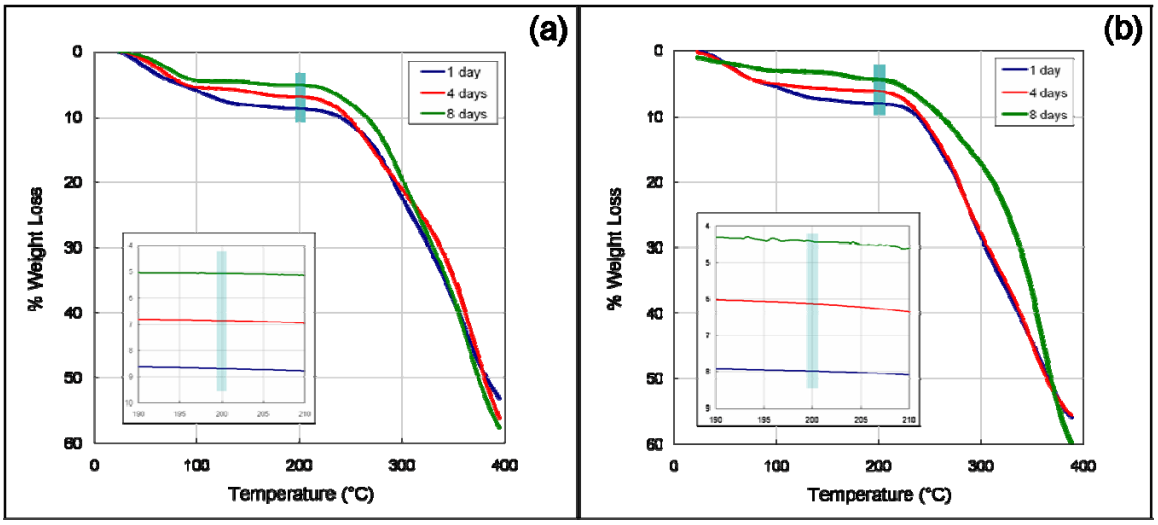

Figure 5.13. TGA curves for (a) PVA and (b) PVA/SWNT fibers showing increase in weight loss at 200 °C with increasing coagulation time. Insets show magnification of TGA curves near 200 °C. (Samples heated in nitrogen atmosphere at 10 °C /min)

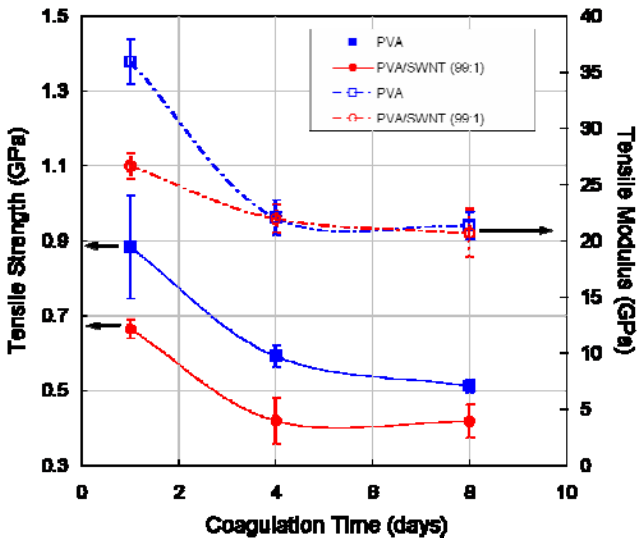

Figure 5.14. Tensile strength and modulus data for both PVA (B3) and PVA/SWNT (A3) fibers as a function of coagulation time.

3.4. Gelation Study (Samples A4 and B4)

In this last section, the gelation behavior of both PVA and PVA/SWNT fiber is studied for its effect on the final fiber properties. As mentioned previously, the gelation behavior of PVA/SWNT fiber differs from PVA and exhibits freezing behavior at higher temperatures than PVA fibers. For this study, the temperature for both the methanol spin/gelation bath and coagulation bath were chosen so that the freezing behavior of both the PVA and PVA/SWNT fibers would be similar. Therefore, the entire spinning process for both fibers would remain consistent. The PVA solution and PVA/SWNT dispersion were spun into a methanol bath maintained at -78 °C (freezing point of methanol is ~ -98 °C) to form both PVA and PVA/SWNT frozen/gel fibers. Mechanical properties have been shown to increase as the spin/gelation bath temperature is lowered [143, 201, 202]. The lowest gelation temperature used in these previous studies is -30 °C. In this study, at such low temperatures both sets of fiber were frozen and exhibited brittle fracture. The fibers were collected on a take-up roller and the take-up roller speed was varied to

increase the duration time of the spun fibers in the gelation bath. As-spun gel fibers were coagulated for one day in methanol maintained at -78 °C. All fibers were drawn in a four-stage process at 100, 160, 200, and 290 °C respectively on a fiber drawing plate. As mentioned earlier, for drawing at 290 °C, the fiber duration on the hot plate at this temperature was ~ 300 ms to prevent melting/degradation of the fiber. Drawing conditions are summarized in Table 5.2.

Both the tensile strength and modulus increased with increasing gelation time (Figures 5.15). A similar increasing trend in tensile strength and modulus is observed with increasing hot-stretch draw ratio (Figure 5.16). Mechanical data is summarized in Table 5.3. The gelation time was varied from 0.5 to 25 seconds. At gelation times > 15 s (low take-up speeds) the spinning process was unstable and as-spun fibers were not uniform under these conditions. For PVA fibers the tensile strength and modulus properties were increased from 0.5 to 1.6 GPa and 30 to 47 GPa respectively. For PVA/SWNT fibers the tensile strength and modulus properties were increased from 0.5 to 2.6 GPa and 25 to 70 GPa respectively.

Tan δ curves obtained from dynamic mechanical analysis show two transitions (Figure 5.17). The transition at higher temperature corresponds to the T_g for PVA. This transition is broadened for PVA/SWNT fibers as compared to the PVA fiber, and the T_g is increased from ~ 86 °C in the PVA fiber to ~93 °C in the PVA/SWNT fiber. Table 5.7 lists the best tensile strength, modulus, and toughness values for the PVA and PVA/SWNT fibers and compares these to the current commercial high-performance fibers. Fracture energy of these fibers is substantially higher than those of the best commercial fibers. In this section subsequent analysis is performed on samples with the

highest strength and modulus. X-ray analysis was performed on the best PVA and PVA/SWNT fibers, and crystallinity and orientation data is summarized in Table 5.4. Crystal size data is shown in Table 5.5. X-ray diffraction patterns and fitted intensity versus 2θ profiles are shown in Figures 5.18 and 5.4.

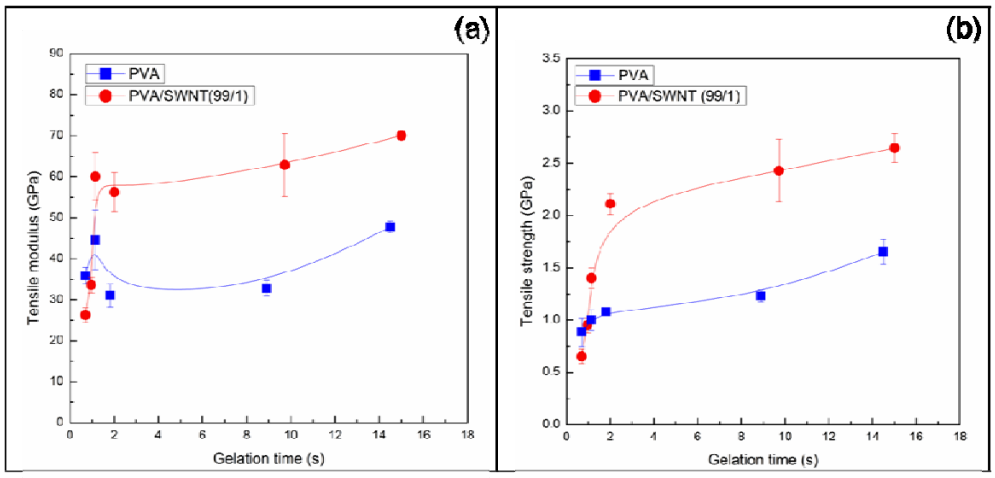

Figure 5.15. Plots for (a) tensile modulus of PVA (B4) and PVA/SWNT (A4) fibers, and (b) tensile strength of B4 and A4 fibers as a function of gelation time.

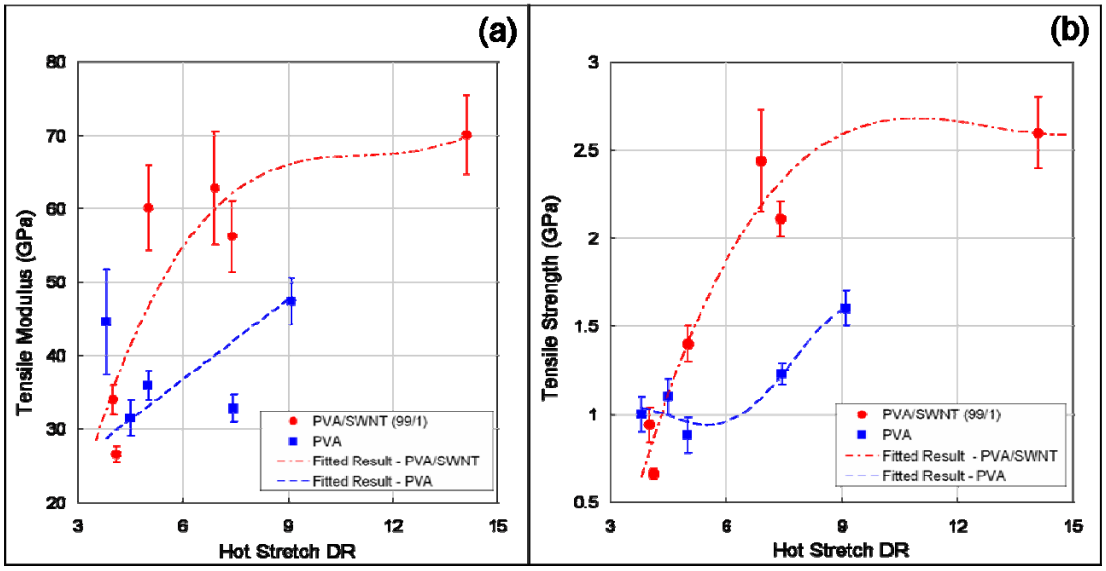

Figure 5.16. Plots for (a) tensile modulus of PVA (B4) and PVA/SWNT (A4) fibers, and (b) tensile strength of B4 and A4 fibers as a function of hot-stretch draw ratio.

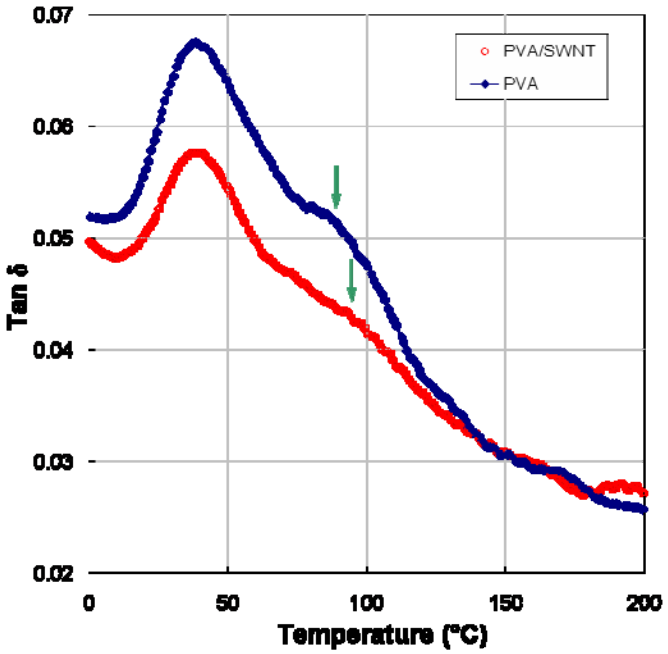

Figure 5.17. Tan δ versus temperature for PVA (B4) and PVA/SWNT (A4) fibers. Arrows indicate T_g transition.

Table 5.7. PVA and PVA/SWNT gel-spun fiber property data compared to current commercially produced high-performance fibers.

Fiber	Strength (GPa)	Modulus (GPa)	Elongation-to-Break (%)	Energy of Fracture (J/g)
PVA (B4) *(average value)*	1.6	47	6.5	40
PVA (B4) *(best value)*	(1.8)	(50)	(5.2)	(46)
PVA/SWNT (A4) *(average value)*	2.6	71	6.2	58
PVA/SWNT (A4) *(best value)*	(2.8)	(78)	(5.1)	(65)
Kevlar® 49 (DuPont)	3	124	2.4	25-30
Zylon® HM (Toyoba)	5.8	270	2.5	46

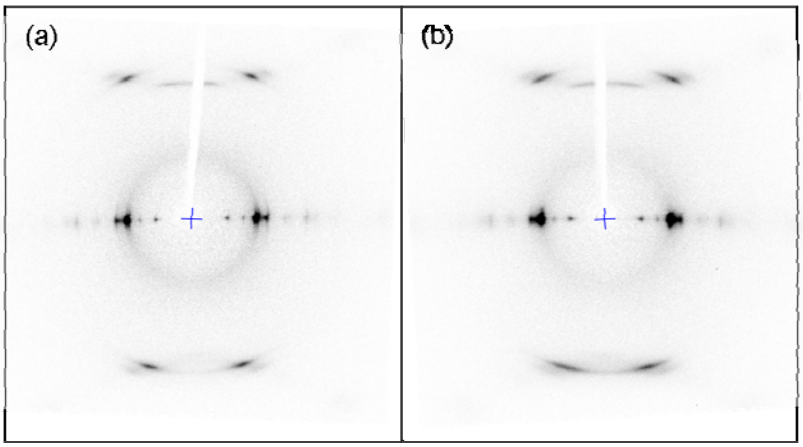

Figure 5.18. Wide-angle X-ray diffraction patterns for best PVA (B4) and PVA/SWNT (A4) fibers spun in gelation study.

Polarized G-band intensity data were also used to determine the orientation of the SWNT in the composite fiber. Polarized G-band data as a function of Ψ is shown in Figure 5.19. The global (average) alignment of SWNT in the fiber was determined using a previously described method [208], where the G-band intensity is taken into account at various Ψ. Herman's orientation factor, f of SWNT was 0.84. This suggests that the total alignment of SWNT is not very high. From polarized Raman spectra at various fiber orientation angles (Figure 5.20) the I_{0°/I_{90° ratio for the PVA/SWNT fiber was determined to be 106. The effective Young's modulus and strength was also determined for the best fibers in this study using equations 5.3 and 5.4 and found to be 2.79 TPa and 110 GPa respectively. As mentioned earlier, these values suggest excellent reinforcement of the PVA by SWNT at low weight concentrations, and exceptional load transfer between the SWNT and PVA matrix.

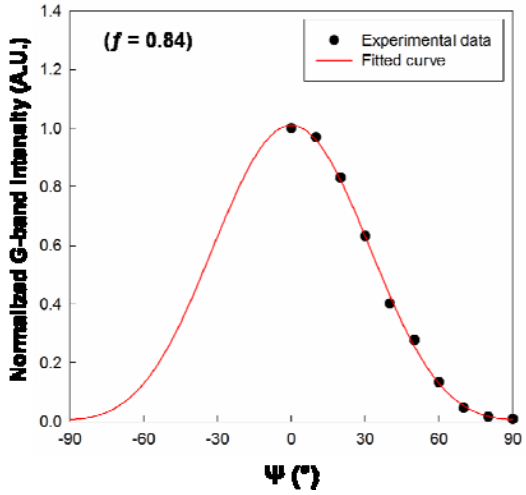

Figure 5.19. Polarized Raman G-band intensity profile as a function of fiber orientation angle, Ψ for PVA/SWNT (A4) fiber.

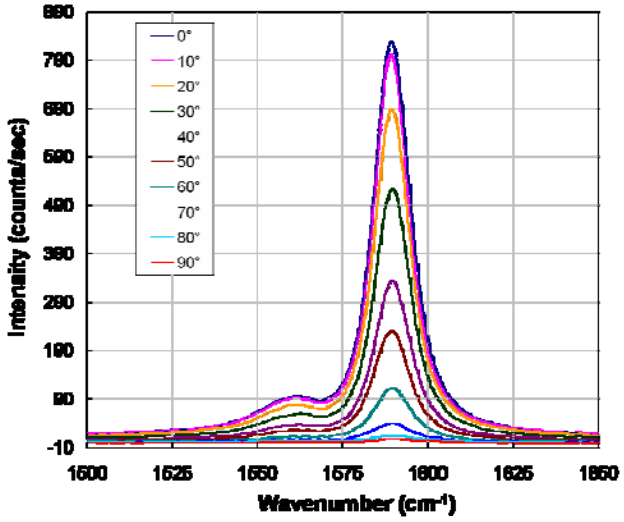

Figure 5.20. Polarized Raman spectra of G-band plotted as a function of fiber orientation angle, Ψ for PVA/SWNT (A4) fiber.

Fibers were placed in DMSO at various temperatures to observe the solvent resistance of the PVA (B4) versus PVA/SWNT (A4) fibers. Figure 5.21 shows the optical micrographs for the fibers treated in DMSO. At room temperature (25 °C) there seems to be no significant difference between the two fibers. However, at 60 °C the PVA fiber is completely fibrillated, while the PVA/SWNT fiber is mostly intact and shows

some regions of swelling. High magnification of the swollen region shows that the fiber is fibrillated in theses regions. At ~ 85 °C (also the dissolution temperature) the PVA fiber is completely dissolved and no fragments could be recovered. The PVA/SWNT fibers are mostly swollen and fibrillated, however there are still some regions of the fiber still intact. Figure 5.22 shows the PVA/SWNT partially swollen fiber in the wet state – the fiber still shows birefringence even in the swollen regions.

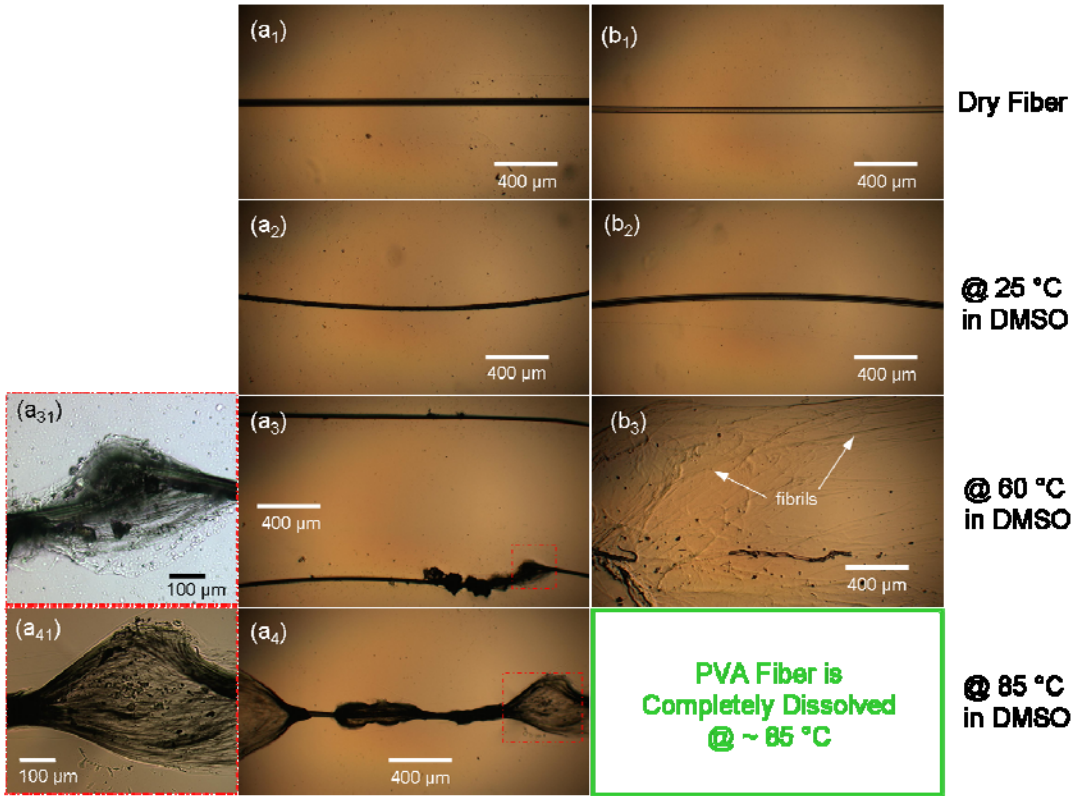

Figure 5.21. Optical micrographs of dried (a) PVA/SWNT (A4) and (b) PVA (B4) fibers after being treated in DMSO at various temperatures.

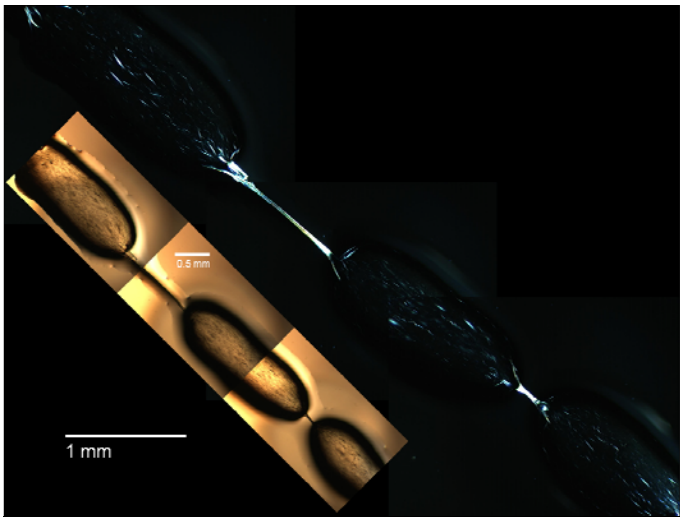

Figure 5.22. Polarized optical micrograph of a partially swollen PVA/SWNT Fiber (A4) treated in DMSO at 85 °C showing retained birefringence. Inset shows the bright-field image.

Figure 5.23 shows SEM of PVA and PVA/SWNT fibers treated in DMSO at 60 °C. PVA/SWNT (Figure 5.23a) fibers are still somewhat intact despite the bubble regions due to swelling, while PVA fibers (Figure 5.23b) are fibrillated and the diameter is reduced due to dissolution of PVA. Regions of the PVA fiber are also completely destroyed and show film-like character (Figure 5.23b_2). Figure 5.24 shows SWNT bundles covered by PVA as the fibers begins to fibrillate in the DMSO.

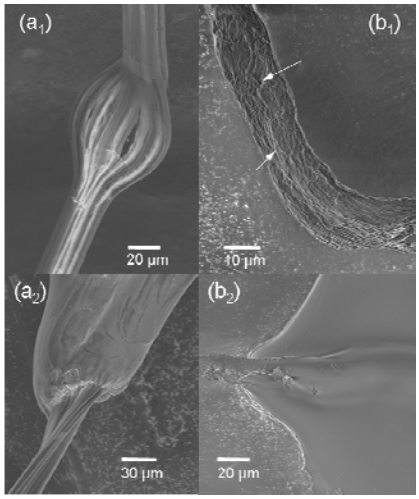

Figure 5.23. Scanning electron micrographs of (a) PVA/SWNT (A4), and (b) PVA fiber treated in DMSO at 60 °C.

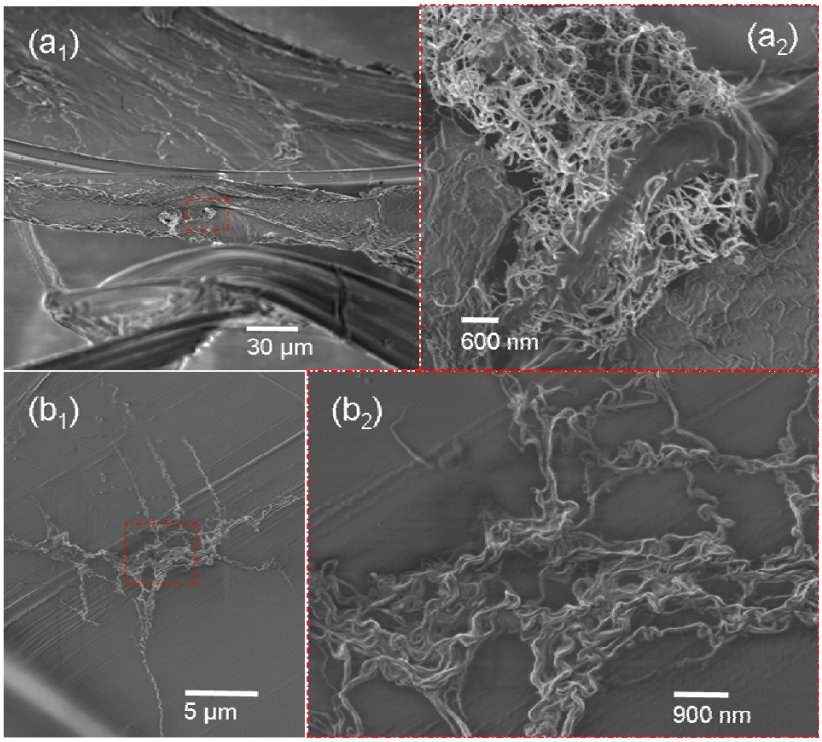

Figure 5.24. Scanning electron micrographs of PVA/SWNT fiber treated in DMSO at 85 °C exposing the SWNT bundles covered by PVA. (a_1) shows swollen area of PVA/SWNT fibers and at high magnification (a_2) shows that the SWNT bundles are entangled. (b_1) shows an area of fibrillation in the fibers and at high magnification (b_2) SWNT are covered by PVA.

Both wet and dry shrinkage data was obtained for the PVA and PVA/SWNT fibers (Figures 5.25 and 5.26). For wet shrinkage tests the fibers were immersed in H_2O and maintained at various temperatures for 30 minutes. The fiber length was measured before and after immersion and percent shrinkage was calculated. This test was repeated 5 times for each fiber, and wet shrinkage data is given in Figure 5.25. The average shrinkage values for PVA and PVA/SWNT fibers in boiling H_2O are 46 and 14 % respectively. PVA/SWNT fibers show a 70 % improvement in the shrinkage properties over PVA fibers. Best values for PVA/SWNT fibers in boiling H_2O show only a 5 % overall shrinkage. The addition of SWNT in the PVA fiber significantly reduces the

movement of the PVA molecules and greatly improves the hydrolytic stability of the fiber.

The mechanical properties of both PVA and PVA/SWNT fiber treated in H_2O at 100 °C was measured and compared to the original fiber properties (Tables 5.8 and 5.9). Fibers boiled in H_2O were in one case restricted and in another unrestricted. In the first case both restricted PVA and PVA/SWNT fibers showed a reduction in fiber diameter, tensile strength, modulus, and toughness properties (Table 5.8). PVA fiber retained 68.7 and 64.8 % of their tensile strength and modulus properties respectively, while PVA/SWNT fibers retained 69.2 and 71.9 % respectively. In the second case for both unrestricted PVA and PVA/SWNT fibers show an increase in diameter but a reduction in tensile strength and modulus properties (Table 5.8). PVA fibers showed a dramatic increase in elongation and toughness properties of 658.4 and 190.5 % respectively. However, PVA/SWNT fibers only displayed a 7.7 and 37.9 % increase in elongation and toughness properties. Stress-strain curves for both original and boiled (unrestricted) PVA and PVA/SWNT fibers are shown in Figure 5.27. Figure 5.28 shows the optical micrographs for the fibers treated in H_2O.

Thermo-mechanical measurements were also performed on these fibers to assess thermal shrinkage. Fibers were heated at a rate of 5 °C/min to a maximum temperature of 200 °C at a stress of 1.6 MPa. The change in length was monitored for each fiber as a function of temperature (Figure 5.26). At 200 °C the thermal shrinkage for PVA, and PVA/SWNT fibers is 2.2 % and 1.8 % respectively. This amounts to a reduction of 18 % in thermal shrinkage for PVA/SWNT fibers as compared to PVA. Based on the TMA curves a transition can clearly be seen for both the PVA and PVA/SWNT fibers near the

T_g for PVA (~77 °C). PVA/SWNT fibers show a broad transition, while PVA fiber shows a sharp transition. The onset of thermal shrinkage near T_g in the fibers may initially occur in the amorphous regions since the chain have more freedom to move. This data suggests that even in the amorphous regions SWNT act as a barricade to PVA chain mobility.

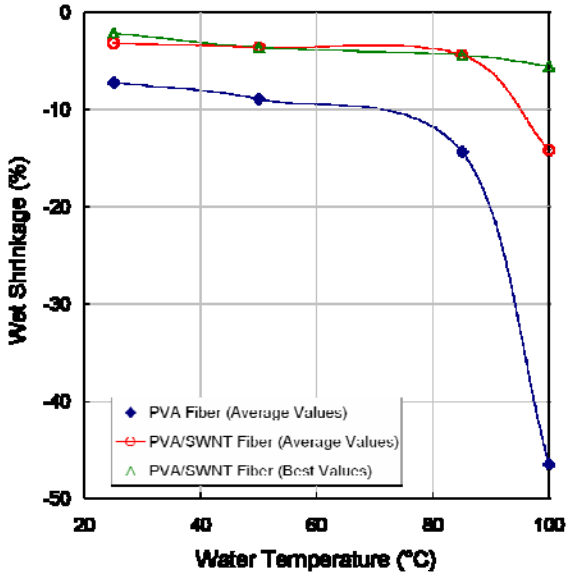

Figure 5.25. Wet Shrinkage data for PVA and PVA/SWNT (99/1) fibers kept for 30 minutes in water at various temperatures.

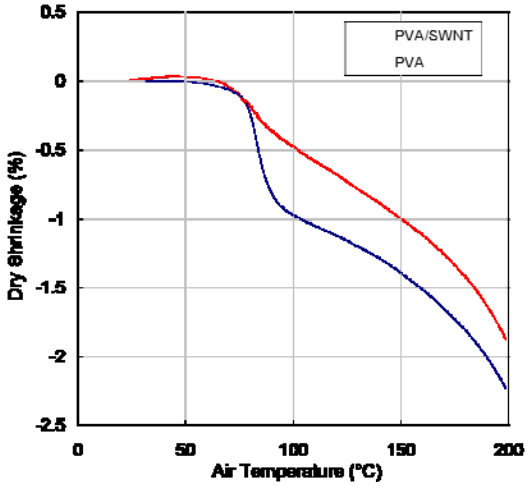

Figure 5.26. Dry Shrinkage for PVA and PVA/SWNT (99/1) fibers obtained by heating the samples in air to 200 °C at 5 °C/min in the TMA.

Table 5.8. Mechanical properties of PVA and PVA/SWNT fibers before and after boiling in water (data is given for both restricted and unrestricted fibers during boiling).

Sample	PVA/SWNT			PVA		
	Original	**Boiled – H_2O (Restricted)**	**Boiled – H_2O (Free)**	**Original**	**Boiled – H_2O (Restricted)**	**Boiled – H_2O (Free)**
Diameter (μm)†	22.6	19.9	25.5	25.1	21.3	36.3
Tensile Strength (GPa)	2.6 ± 0.21	1.8 ± 0.2	0.9 ± 0.1	1.6 ± 0.13	1.1 ± 0.2	0.57 ± 0.1
Modulus (GPa)	70.8 ± 5.4	50.9 ± 4.4	17.3 ± 10.36	47.4 ± 3.2	30.7 ± 8.02	15.5 ± 4.2
Elongation (%)	6.2 ± 0.72	4.7 ± 0.4	6.68 ± 1.3	6.5 ± 1.4	6.6 ± 1.5	49.3 ± 11.1
Toughness (J/g)	58.4 ± 6.8	31.8 ± 4.2	22.2 ± 2.8	40.1 ± 5.9	26.5 ± 6.0	156.5 ± 52.6

† Effective fiber diameter was calculated using a weight method, where the weight of a specific length of fiber was divided by the fiber density (determined experimentally from crystallinity measurements – PVA amorphous density (ρ_a) and crystalline density (ρ_c) are 1.269 and 1.345 g/cm^3 respectively). The volume is evaluated from the previous calculation, and a circular cross-section is assumed to determine the fiber diameter. For tensile test measurements a circular diameter is also assumed to calculate cross-sectional area.

Table 5.9. Retention in fiber properties after boiling in water.

Properties	PVA		PVA/SWNT	
	Boiled – H_2O (Restricted)	**Boiled – H_2O (Free)**	**Boiled – H_2O (Restricted)**	**Boiled – H_2O (Free)**
Tensile Strength	68.7 %	35.6 %	69.2 %	34.6 %
Modulus	64.8 %	32.7	71.9 %	24.4 %
Elongation	1.5 % ↑	658.4 % ↑	24.1 % ↓	7.7 % ↑
Toughness	66 %	190.5 %	54.4 %	37.9 %

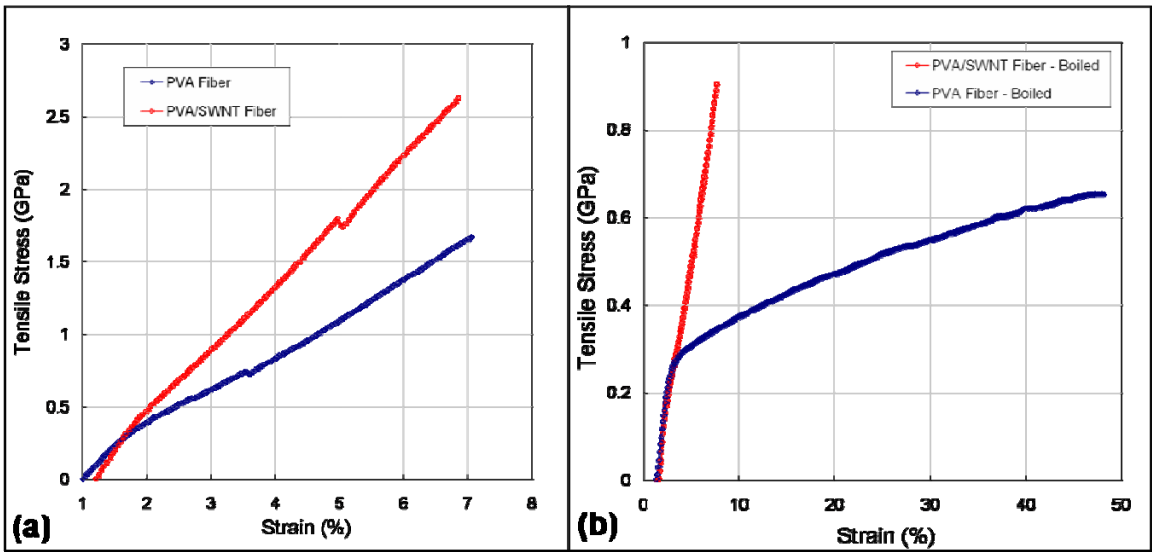

Figure 5.27. Stress-strain curves for (a) original and (b) boiled in water (unrestricted) PVA/SWNT (A4) and PVA (B4) fibers.

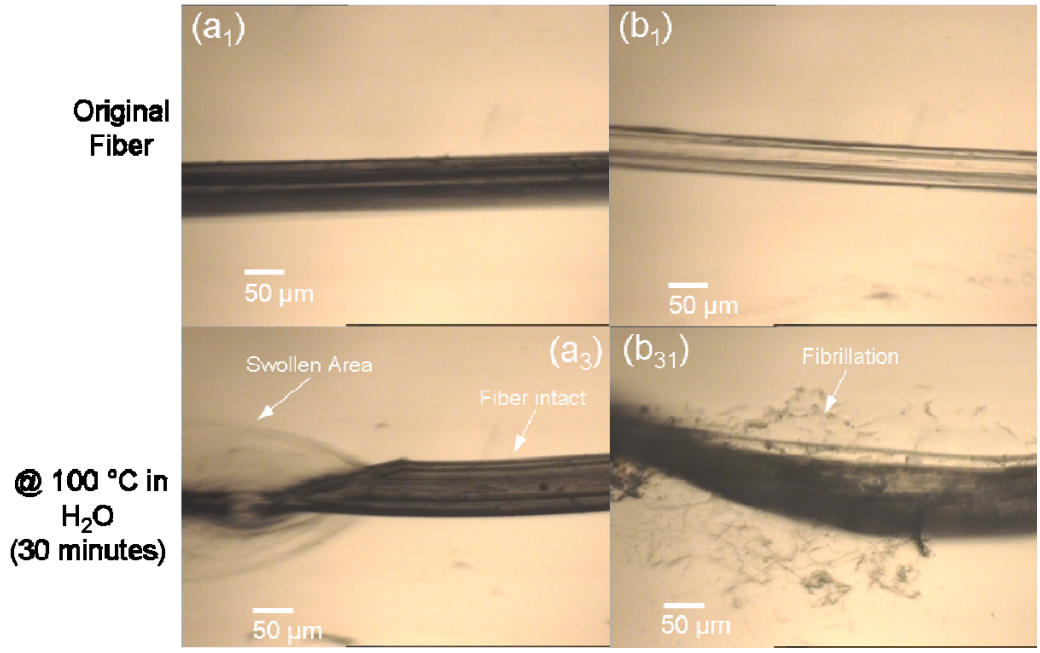

Figure 5.28. Optical micrographs of (a) PVA/SWNT (A4) and (b) PVA (B4) fibers treated in H_2O at 100 °C for 30 minutes.

Creep as well as stress relaxation test were also performed on both PVA and PVA/SWNT fibers. During creep tests, the instantaneous elastic response after deformation is higher in the PVA/SWNT fiber than the PVA fiber (Figure 5.29a). The

stress values chosen of these tests is within the elastic region of the stress-strain curve. Creep test were also performed on the fibers at the same stress (246 MPa) (Figure 5.29b), and the irreversible recovery is slightly lower for the PVA fibers. SWNT may prevent the movement of PVA molecules during recovery. Stress relaxation tests show that after deformation the stress in both PVA (strain 2 %) and PVA/SWNT (strain 1.68 %) fiber only decreases slightly then remains relatively constant (Figure 5.30a). Low strain values are chosen no that relaxation tests occur in the linear viscoelastic region of the stress-strain curve for each fiber (there is no permanent deformation in the fiber). This suggests that the polymer is not able to flow. SWNT provide additional reinforcement in the fiber, therefore the PVA/SWNT fiber can maintain higher stress over the same time period. Figure 5.30b shows the stress relaxation at the same strain of 2 % and again the PVA/SWNT fiber is able to maintain higher stress over the same time period as compared to the PVA fiber.

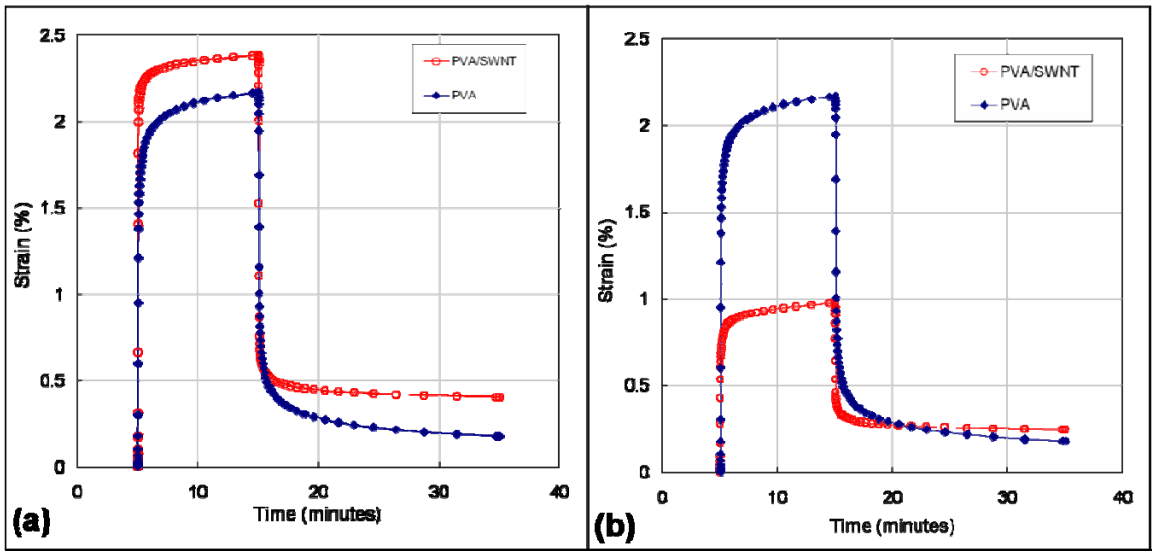

Figure 5.29. Creep behavior at 30 °C in air for both PVA/SWNT (A4) and PVA (B4) fibers showing (a) A4 and B4 fibers displaced at a stress of 400 and 246 MPa (15 % of the breaking stress) respectively, and (b) A4 and B4 are displace by the same stress of 246 MPa.

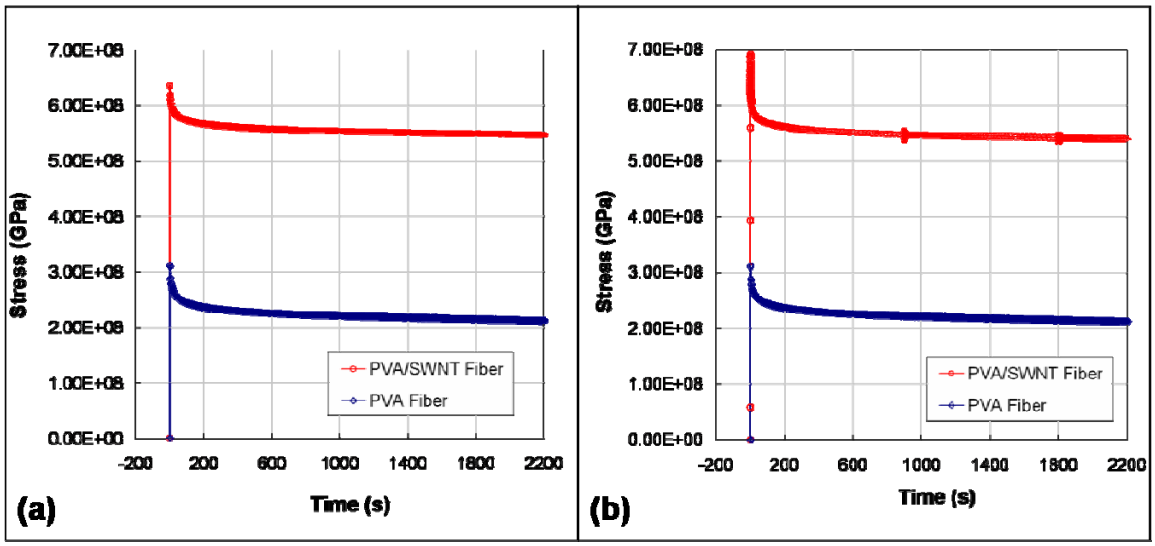

Figure 5.30. Stress Relaxation behavior for both PVA (B4) and PVA/SWNT (A4) (99/1) fibers at (a) 2 % and 1.68 % strain respectively and (b) the same strain of 2 %.

SEM studies on the fibers show that the PVA and PVA/SWNT fibers are ribbon-like (Figure 5.31 and 5.32). Fibrils and kinks can be seen near the fractured surface as well as along the fiber length for PVA/SWNT fibers (Figure 5.32b). For PVA fibers fibrillation and kinking behavior was not observed for fractured fibers. Fractured PVA fibers do not show this fibrillation behavior. In this gel-spinning process PVA and PVA/SWNT fibers have been drawn to high draw ratios. X-ray diffraction of the gel-spun fibers reveals very high PVA orientation in the PVA/SWNT fiber (Table 5.4). Crystal size data is listed in Table 5.5. PVA/SWNT fibers were fibrillated by boiling in DMSO to obtained thin sections of the fiber that could be imaged by HR-TEM. HR-TEM observation of the PVA/SWNT fibers show the presence of exfoliated SWNT in the PVA fiber, and the PVA forms a thick coating on SWNT (Figure 5.33), and in some cases PVA coating is so thick although present SWNT cannot be readily imaged (Figure 5.34). HR-TEM also show that the PVA molecules in this thick coating are well-crystallized in the interfacial region of PVA and SWNT, and lattice fringes are clearly visible with

spacing around 0.39 nm (Figure 5.33 and 5.34). The PVA lattice is found to exist along the length of the SWNT.

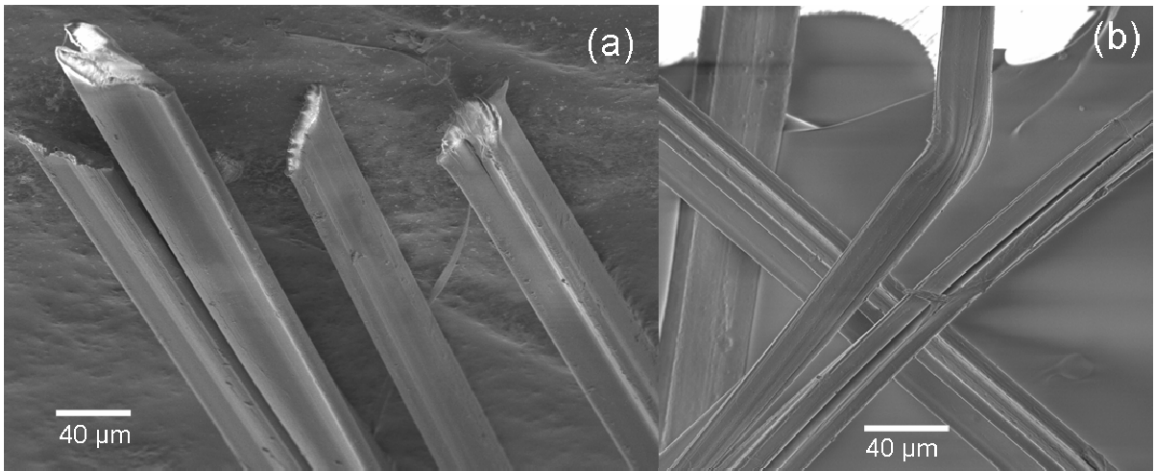

Figure 5.31. Scanning electron micrograph of PVA fiber (B4) (a) showing cut end and (b) showing fiber along length.

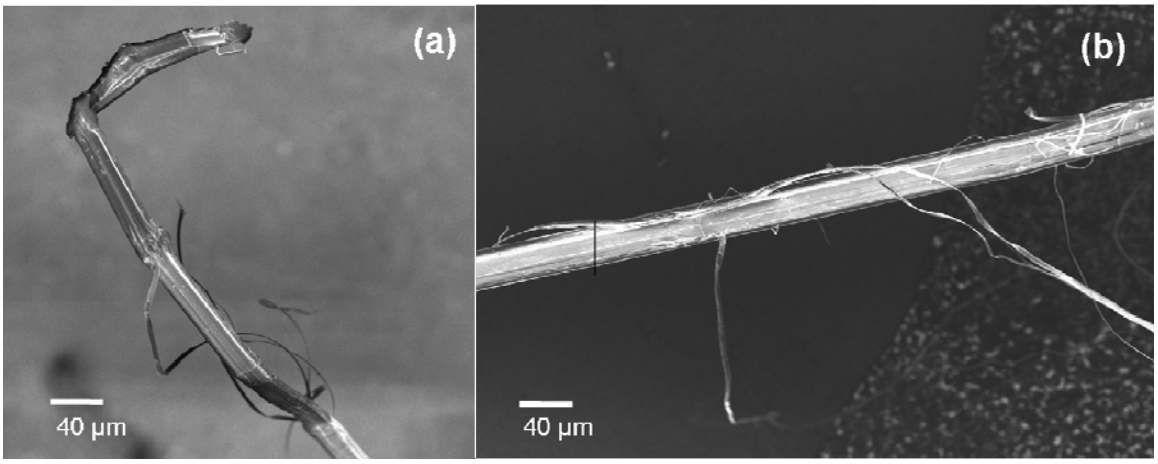

Figure 5.32. Scanning electron micrograph of (a) PVA/SWNT fiber showing fracture end, fibrillation, and kinks in the fibers, and (b) fibrillation further along the length of the fractured PVA/SWNT fiber.

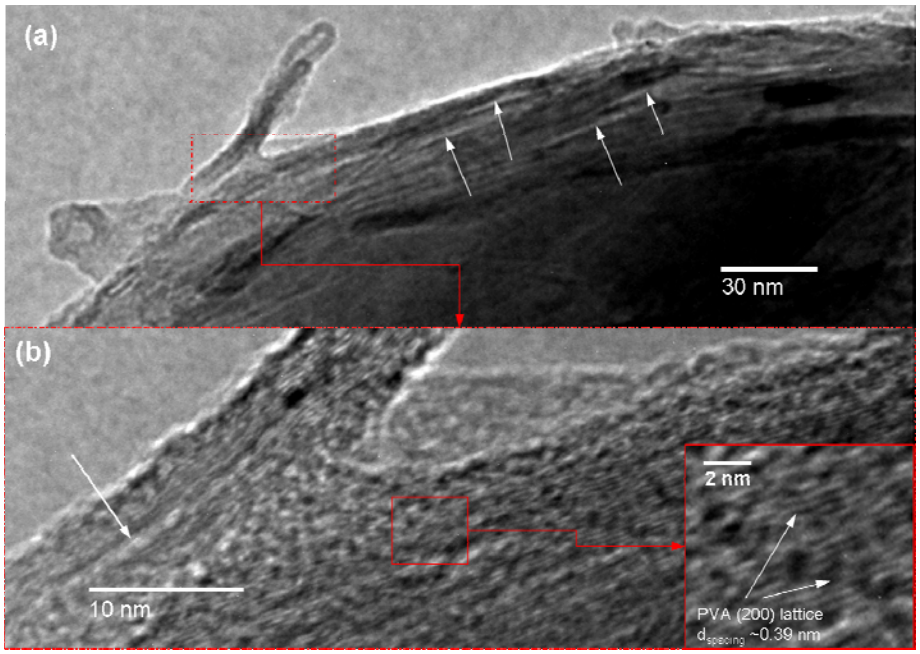

Figure 5.33. High-resolution TEM images of (a) edge of fibrillated PVA/SWNT (99/1) gel-spun fiber showing the presence of SWNT (white arrows) in the PVA matrix, and (b) higher magnification of boxed region in (a) showing the PVA lattice along the SWNT surface (Inset shows magnified PVA lattice image $d_{spacing}$ ~ 0.39 nm).

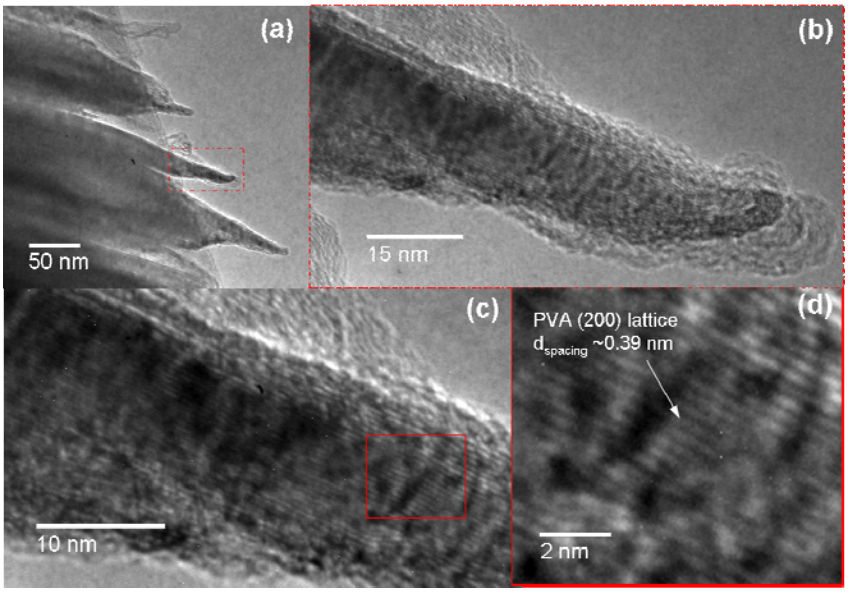

Figure 5.34. High-resolution TEM images of (a) edge of fibrillated PVA/SWNT (99/1) gel-spun fiber showing the presence of SWNT covered by PVA, (b) higher magnification of boxed region in (a) showing the PVA heavily coated on SWNT and SWNT is not visible, (c) higher magnification of (b) showing PVA lattice along the SWNT direction, and (d) magnified image of PVA lattice image $d_{spacing}$ ~ 0.39 nm. It is presumed that the SWNT is buried in the fibril.

5.4. Conclusions

By using gel-spinning, PVA, PVA/SWNT, and PVA/MWNT fibers were processed with high draw ratios. As-spun draw ratio is affected by spin-bath temperature and gelation time. PVA/SWNT had significantly higher draw ratio than control PVA fibers. Modulus and tensile strength increase in PVA/SWNT fibers of 35 % and 40 % respectively even for low PVA orientation and crystallinity indicate that SWNT is an effective reinforcement agent for PVA. Raman spectroscopy data show high SWNT alignment in the fiber where the I_{0°/I_{90° ratio is as high as 100.

In the draw ratio optimization study, spin-bath/gelation temperature is found to significantly affect the drawability of the PVA and PVA/SWNT fibers. PVA/SWNT fiber show freezing behavior at higher temperatures than expected and may be due to temperature dependent phase separation of the DMSO/H_2O solvent mixture in the PVA/SWNT dispersion. Maximum as-spun draw ratios of 36.4 at -7 °C and 24.7 at -28 °C are achieved for the PVA and PVA/SWNT gel fibers. After heat drawing, draw ratios of 85 and 136 are achieved for PVA and PVA/SWNT fibers respectively. Mechanical properties of these fibers are lower than the fibers with lower draw ratio. Low alignment of the polymer chain may be attributed to polymer chain mechanics, where polymer chain elongational deformation in the flow field is competing with chain relaxation time, and consequently chains do not orient even though high extension rates are applied.

The affect of coagulation time on the fiber properties and spinning process was also observed. Under the conditions used in this study, long coagulation time for PVA and PVA/SWNT fiber resulted in reduced drawability. Mechanical properties of these fibers also decrease with increasing coagulation time. Residual weight of solvent in coagulated fibers was determined using TGA and found to decrease with increasing coagulation time.

Gelation studies of PVA and PVA/SWNT fibers at -78 °C over different periods of time show an increase in the mechanical properties as gelation time is increased. For PVA fibers the tensile strength and modulus increased from 0.5 to 1.6 GPa and from 30 to 47 GPa respectively. For PVA/SWNT fibers, the tensile strength and modulus increased from 0.5 to 2.6 GPa and from 25 to 70 GPa respectively. Raman spectroscopy data show high SWNT alignment in the fiber where the $I_{0^\circ} / I_{90^\circ}$ ratio is 106. DMA data shows an increase in the T_g for PVA/SWNT fibers as compared to PVA fibers from 86 °C to 93 °C. PVA fiber treated in DMSO at 60 °C is completely fibrillated, while PVA/SWNT fibers are mostly intact under these conditions. At 85 °C the PVA fiber is completely dissolved in DMSO, whole PVA fiber was swollen but did not dissolve. This data implies that the PVA/SWNT fiber is inhomogeneous and has higher solvent stability as compared to the PVA fiber.

Wet shrinkage data shows that SWNT significant by increases the hydrolytic stability of the PVA fiber, where shrinkage in water is reduced by ~ 70 %. PVA and PVA/SWNT fibers were treated in H_2O under both restricted and unrestricted conditions. The mechanical properties of the treated fibers reduced as compared to the original fibers and this reduction is higher for the unrestricted fiber. For the H_2O treated unrestricted PVA fibers, the toughness increased from 40.1 for untreated fiber to 156.5 J/g for the H_2O treated fiber. Optical micrographs of PVA and PVA/SWNT fibers treated in water at 100 °C for 30 minutes show that the PVA fiber is swollen and fibrillated, while the PVA/SWNT fiber is mostly intact and is swollen in some regions. SEM of the PVA and PVA/SWNT fibers provide evidence that the fibers are ribbon-like, and PVA/SWNT fibers fibrillate and kinked when fractured during tensile tests. HR-TEM studies show that PVA coats SWNT in the composites and the PVA (200) lattice can be imaged in HR-TEM.

CHAPTER 6

CONCLUSIONS AND RECOMMENDATIONS

6.1. Conclusions

The key conclusions of this work are:

6.1.1. Chapter 2

- High molecular weight PVA is not able to sustain orientation without shearing of the solutions. Self-assembled fibers in these solutions are isotropic and semi-crystalline crystallinity is ~48%.
- In the presence of SWNT, PVA molecules subjected to shear will align along the surface of the SWNT. Once shearing is discontinued the alignment of the PVA chains is not lost and remains templated by the SWNT. The aligned PVA molecules on the SWNT surface in-turn template subsequent PVA molecules to form crystalline fibrillar structures.
- These fibrillar structures align with one another to form macroscopic fibers which are ribbon-like. The aligned fibrils form various regular patterns. These fibrillar structures are observed in both PVA and PVA/SWNT fibers.
- Crystallization in PVA/SWNT fibers is ~ 84 % based on X-ray diffraction. X-ray diffraction also shows evidence for changes in the packing of PVA chain within the crystal structure. The (200) peak is most predominant as opposed to the (101) peaks which is expected.
- HR-TEM studies of these fibrils show that fibrils are highly crystalline and stable to the electron beam. Lattice images for PVA in the PVA/SWNT fibril samples can be readily attained and PVA molecules are aligned parallel to the SWNT surface.

6.1.2. Chapter 3

PVA single crystals can be grown at various growth temperatures and display a range of morphologies, crystal perfection, and irradiation stability. In all crystals grown in this work the crystal structure is consistent with Bunn's unit cell for PVA [146].

- At 25 °C PVA growth times range from 9 to 14 months. The individual crystals are diamond-shaped but agglomerate into thin films made of many crystals. Electron diffraction show only *(h0l)* reflection when the beam is perpendicular to crystal surface reveal that PVA chains are parallel to the crystal lamellar and in the fold conformation. Single crystals show a high degree of crystal perfection and up to eight orders of *(h0l)* reflections can be observed in the electron diffraction patterns. Extra spacing's present in the diffraction pattern correspond to further evidence of high degree of PVA crystal perfection. Single crystals show strong electron irradiation resistance at beam strengths of 100 kV and even at beam strengths up to 400 kV, where diffracting power lasts for ~10 minutes and 4 minutes respectively.
- At 50 °C PVA single crystal precipitate from dilute solutions in ~ 13 days, and the crystals are individual diamond-shaped platelets with a significant amount of crystal lamellar thickening. At longer growth times (weeks) PVA polygonal single crystals grow at 50 °C. Crystal perfection of 50 °C crystals is lower than 25 °C crystals and only 3 orders of *(h0l)* reflections are observed. Extra spots are either very weak or non-existent. At 100 kV the diffracting power of 50 °C crystals degrades after 100 seconds and is completely gone after ~10 minutes. After six months of growth time PVA rod crystals were formed which exhibited twinning.
- At 60 °C show hexagonal-shape morphology displaying predominant [100] and [101] growth facets. At 60 °C crystals remain thin and do not show evidence of significant lamellar thickening as compared to the 50 °C crystals even after long

growth times. However, lateral dimensions reach over 100 μm is some directions and the shape of the crystal change to a rounded quadrilateral. Electron diffraction of 60 °C crystals is similar to the 25 °C crystals show a high degree of crystal perfection and irradiation resistance. Diffracting power at 100 kV does not change even after 20 minutes and could be imaged readily at beam strengths of 400 kV.

6.1.3. Chapter 4

- PVA single crystals are grown in PVA/SWNT solutions at 25 °C over long growth times of several months. To yield *aloe plant* structures, where the *aloe leaves* are PVA single crystals templated by SWNT. PVA molecules are aligned along SWNT surface by epitaxial means.
- PVA leaf crystals are up to 200 nm thick near the root and taper off at the crystal tip, and related to the convergence of lamellar layers nucleated at the root. The thickness of the PVA leaf crystal at its base is therefore dictated by the PVA-SWNT template length protruding out of its root.
- A new crystal structure for PVA is formed and confirmed by both X-ray and electron diffraction patterns, and FT-IR confirms that although this crystal structure differs, chemically this material is identical to PVA that crystallizes in the form of Bunn's unit cell when not templated by SWNT.
- The thick stacking of individual lamellar prolongs the life of the crystal in the presence of the electron beam. Up to five orders of reflections can be observed in diffraction patterns taken under minimal illumination conditions in the electron microscope. PVA lattice images and moiré fringes can be obtained at beam strengths of 400 kV at $\times$500,000 magnifications.

- Hexagonal crystal structures of PVA form at long growth times and at elevated temperatures.

6.1.4. Chapter 5

- PVA and PVA/SWNT fibers were made by gel-spinning exhibit high draw ratio. Fiber as-spun draw ratio is mostly affected by spin-bath temperature. PVA/SWNT had significantly higher draw ratio than control PVA fibers. The overall PVA orientation was lower then control PVA fibers. SWNT needle-like morphology may play a role in better fiber drawability. Modulus and tensile strength increase in PVA/SWNT fibers of 35 % and 40 % respectively even for lower PVA orientation and crystallinity indicate that SWNT is an effective reinforcement agent for PVA.
- Draw ratio optimization studies found spin-bath temperature significantly affects the drawability of the PVA and PVA/SWNT fiber. PVA/SWNT fiber show freezing behavior at -25 °C, while PVA fibers freeze at -45 °C this may be due to temperature dependent phase separation in the PVA/SWNT dispersion. High draw ratios of 85 and 136 are achieved for PVA and PVA/SWNT fibers respectively. Mechanical properties and PVA orientation of these fibers are lower than the fibers with lower draw ratio. Low alignment of the polymer chain may be attributed to polymer chain mechanics, where polymer chain elongational deformation in the flow field is competing with chain relaxation time. The conditions $\dot{\varepsilon}_{ii}\, t >> 1$ and $\dot{\varepsilon}_{ii}\, \tau > 1$ for chain orientation is not satisfied, consequently chains do not orient even though high extension rates are applied.
- Long coagulation time for PVA and PVA/SWNT fiber resulted in reduced drawability and subsequently the orientation and mechanical properties.

- Gelation studies of PVA and PVA/SWNT fibers at -78 °C over different periods of time show an increase in the mechanical properties as gelation time is increased. For PVA fibers the tensile strength and modulus increased from 0.5 to 1.6 GPa and from 30 to 47 GPa respectively. For PVA/SWNT fibers the tensile strength and modulus increased from 0.5 to 2.6 GPa and from 25 to 70 GPa respectively. Wet shrinkage data shows that SWNT significant by increases the hydrolytic stability of the PVA fiber, where shrinkage in water is reduced by ~ 70 %. For the H_2O treated unrestricted PVA fibers, the toughness increased from 40.1 for untreated fiber to 156.5 J/g for the H_2O treated fiber.

6.2. Recommendations

This study has yielded many valuable discoveries and contributions to the field of polymer crystallization and in particular the crystallization of polymers in the presence of SWNT. The needle-like morphology and nanoscopic dimensions of SWNT is a nucleating material unlike any previously available in the field of crystallization. This opens a new arena for the study of polymer crystallization. This work simply scratches the surface of possibilities that can be done in this area. Future recommendations to further the work performed in this dissertation are listed below.

- The mechanism for the formation of fibrillar crystal nuclei in PVA/SWNT fibrillar crystal is not clear and needs further investigation.
- Electron beam irradiation resistance and its relation the chain arrangement of PVA in single crystals with differing morphology still remain unsolved.
- Further work is needed to clearly determine the new crystal structure templated by SWNT in PVA/SWNT single crystal. Also, detailed nucleation studies on SWNT templated crystal growth requires further study.

- The mechanism for the formation of large and well organized crystalline PVA domains in the gel at low temperature is not clear. Therefore more studies are need to investigate this phenomena and may be extended to other gel forming polymer systems.
- Physical interfacial interaction between the polymer and SWNT is only one form. Therefore, interfacial morphological studies may be extended to other polymer/CNT systems involving different types of nanotubes, as well as chemical interactions between the polymer and CNT.

APPENDIX A

HIGH-RESOLUTION TRANSMISSION ELECTRON MICROSCOPY AND ELECTRON RADIATION RESISTANCE STUDIES OF POLYMER/SINGLE-WALL CARBON NANOTUBE COMPOSITES

A.1. Introduction

For composite materials good interfacial interaction is necessary to achieve load transfer between the polymer and filler material. Many efforts have been made to modify the interfacial interaction between CNT and its surrounding polymer matrix. Chemical modification of the CNT surface to introduce functional groups has been performed to either create chemical bonding between the polymer matrix and CNT; or to create physical crosslink's between the functional groups and the polymer chains thereby increasing interfacial interaction. Improving load transfer between the filler and matrix has been shown to lead to improvements in the mechanical properties of the composite. For this reason, studying the interface and interphase in the composite can provide information about how well the matrix and fillers interact.

For polymer-nanocomposites one of the best ways to study interfacial morphology is by electron microscopy. Electron microscopy of polymeric materials has always been a challenging problem since these materials are highly radiation sensitive. Microscopists must use specific sample preparation techniques, and careful experimental measures to obtain good images and diffraction patterns in the electron microscope. Some polymer systems show higher resistance to electron irradiation, and some studies have correlated the thermal stability of the polymer with its critical electron beam dose [209, 210]. These studies show that a polymer with a low melting or degradation

temperature will consequently have low critical dose meaning that the electron microscope conditions must be carefully controlled to obtain meaningful information. Many of the typical polymers used in fiber production and specifically in this study fall into this low melting temperature range. To minimize this problem either conductive coatings are applied to the polymer, or the polymer morphology is etched onto a conductive material. However, these methods reduce the ability to obtain detailed HR-TEM images. The addition of SWNT to the polymer matrix may provide a new route for electron microscopy imaging of polymers. The physical interaction between different polymers and SWNT at the interface and polymer irradiation in the presence of SWNT are studied using HR-TEM is summarized here.

A.2. Experimental

A.2.1. Sample Preparation

Polymer/CNT films samples were first disintegrated in their respective solvents into large pieces. These film pieces are continuous cycled in fresh solvent in order to further disintegrate the film into thin sections. These thin sections are collected using a loop (Electron Microscopy Sciences, cat. # 70944) and placed on the TEM grids. The grids were dried in air before observation in the microscope. Polymer/CNT fibers are disintegrated into fibrils by boiling fibers in their respective solvents. Fibers were boiled for 1 to 12 hours depending on how long the fibers took to completely disintegrate. These thin fibers are collected using a loop and placed onto holey carbon coated TEM grids which are subsequently dried for analysis. Polymer/CNT dispersions were diluted to between 50 and 100 times the original concentration. Several droplets (3-5) of the diluted solutions are placed on TEM grids, and grids are dried for observation.

A.2.2. Sample Characterization

Transmission electron microscopy (TEM) experiments were performed using a Hitachi HF-2000 Field Emission Gun transmission electron microscope operated at 200 kV. TEM samples were prepared on 300-mesh holey carbon coated copper grids manufactured by Electron Microscopy Sciences, Hatfield, PA, USA (cat. # HC300-Cu). Polymer/CNT films, fibers, and dispersions were all observed by high-resolution TEM (HR-TEM). To minimize polymer irradiation in the electron microscope, the electron beam illumination was kept very low (the sample was just visible) while stigmation, aperture alignment, and focus adjustments were made. Beam illumination was increased only to capture images of the specimen. Photographs were taken by digital camera and exposure time was only one to two seconds. Once the beam illumination was increased the sample features (lattice) were lost to the beam irradiation instantaneously for neat polymer samples, and after approximately 1-4 minutes for polymer/CNT composites.

A.3. Results and Discussion

For the polymer/SWNT composites studied here the SWNT are not functionalized. Although the throughout the growth and purification process there may be some degree of disorder/defects in the walls of the SWNT [51, 52, 211, 212], they are typically minimal and relative degree of disorder can be detected by Raman spectroscopy [54, 213, 214]. In this work the Raman spectra show a very low degree of disorder/defects in the SWNT materials used. For this reason, a large amount of functionalization on the walls in not expected, therefore chemical interaction between the polymer and SWNT is minimal. The predominant interaction between the polymer and SWNT in these composites is physical van der Waals interactions.

A.3.1. HR-TEM Observation of Polymer/SWNT Composites

PAN/SWNT films were observed using HR-TEM. These films were prepared by solution casting, and first disintegrated in hot DMF then further diluted to make TEM samples. HR-TEM observations show that SWNT bundles are still covered generously by PAN polymer even after disintegration (Figure A.1). The DMF although it is a good solvent for PAN is not able to remove the PAN coating surrounding the SWNT. This is strong evidence for the strong physical interaction between PAN and SWNT. PAN lattice images with spacing's of 0.54 nm are observed nearer to the SWNT surface. Lattice spacing's observed for the PAN is consistent with (110) d-spacing's. Further away from the SWNT surface the polymer structure is not so stable, therefore lattice images cannot be obtained and the polymer molecules undergoes a *burning* effect for the electron beam. These observations indicate the ability of SWNT to template long-chain PAN crystallization (Figure A.1).

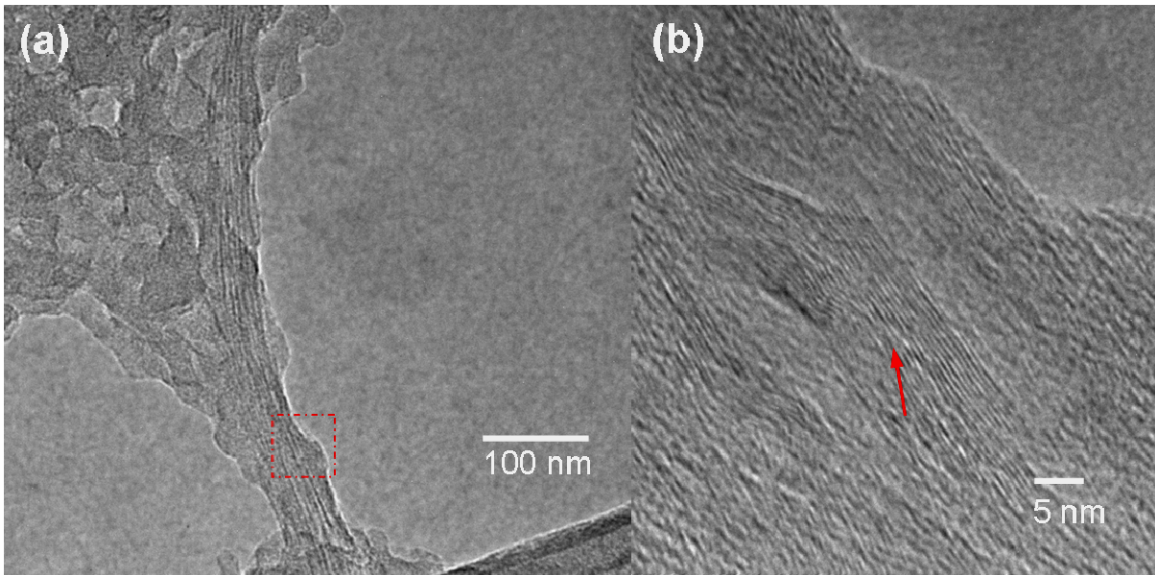

Figure A.1. High-resolution TEM images of (a) PAN/SWNT disintegrated film showing PAN still heavily coated on SWNT bundles, and (b) at higher magnification of boxed region in (a) the presence of PAN crystal lattice indicated by red arrow (lattice fringe spacing ~0.54 nm).

PAN/SWNT (1wt %) fibers processed by gel-spinning technique. In this gel-spinning process PAN and PAN/SWNT fibers can and have been drawn to much higher extensions than the conventionally spun fibers [71, 215]. X-ray diffraction of the gel-spun fibers reveal very high PAN orientation [71]. PAN/SWNT fibers were also characterized by dynamic mechanical analysis (DMA) and shown to have good load transferability of interfacial interaction between PAN and SWNT. Both PAN and PAN/SWNT fibers were fibrillated in boiling DMF to obtained thin sections of the fiber that could be imaged by HR-TEM. HR-TEM observation of the PAN/SWNT fibers show the presence of exfoliated SWNT in the PAN fiber, and the PAN forms a thick coating on SWNT (Figure A.2). HR-TEM also show that the PAN molecules in this thick coating are well-crystallized in the interfacial region of PAN and SWNT, and lattice fringes are clearly visible with spacing around 0.54 nm (Figure A.3). The PAN lattice is found to exist along the entire length of the SWNT. Control PAN fibers were prepared and imaged under the same conditions. It was found that without the presence of SWNT any PAN crystal structure was immediately destroyed by electron irradiation. For this reason, lattice images could not be obtained.

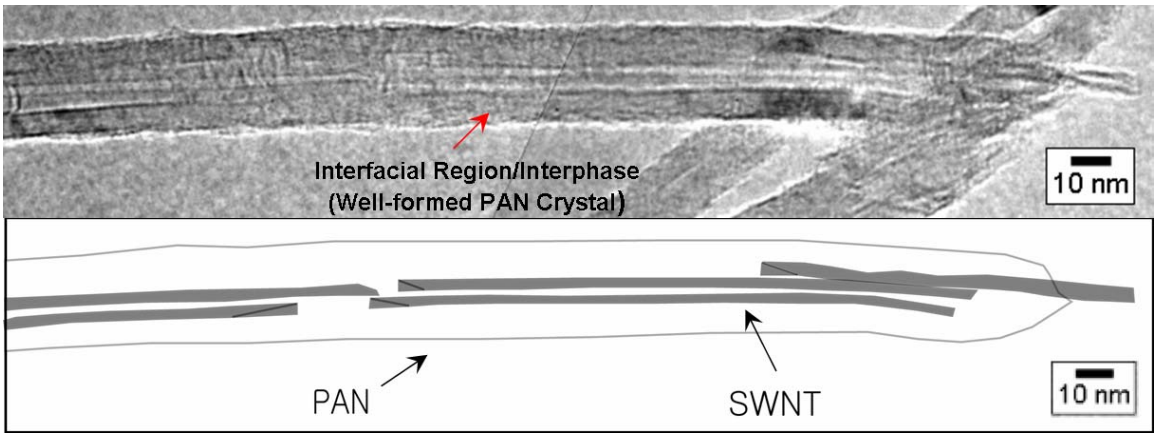

Figure A.2. High-resolution TEM image of PAN/SWNT fiber showing a well-formed crystalline interphase of PAN on SWNT.

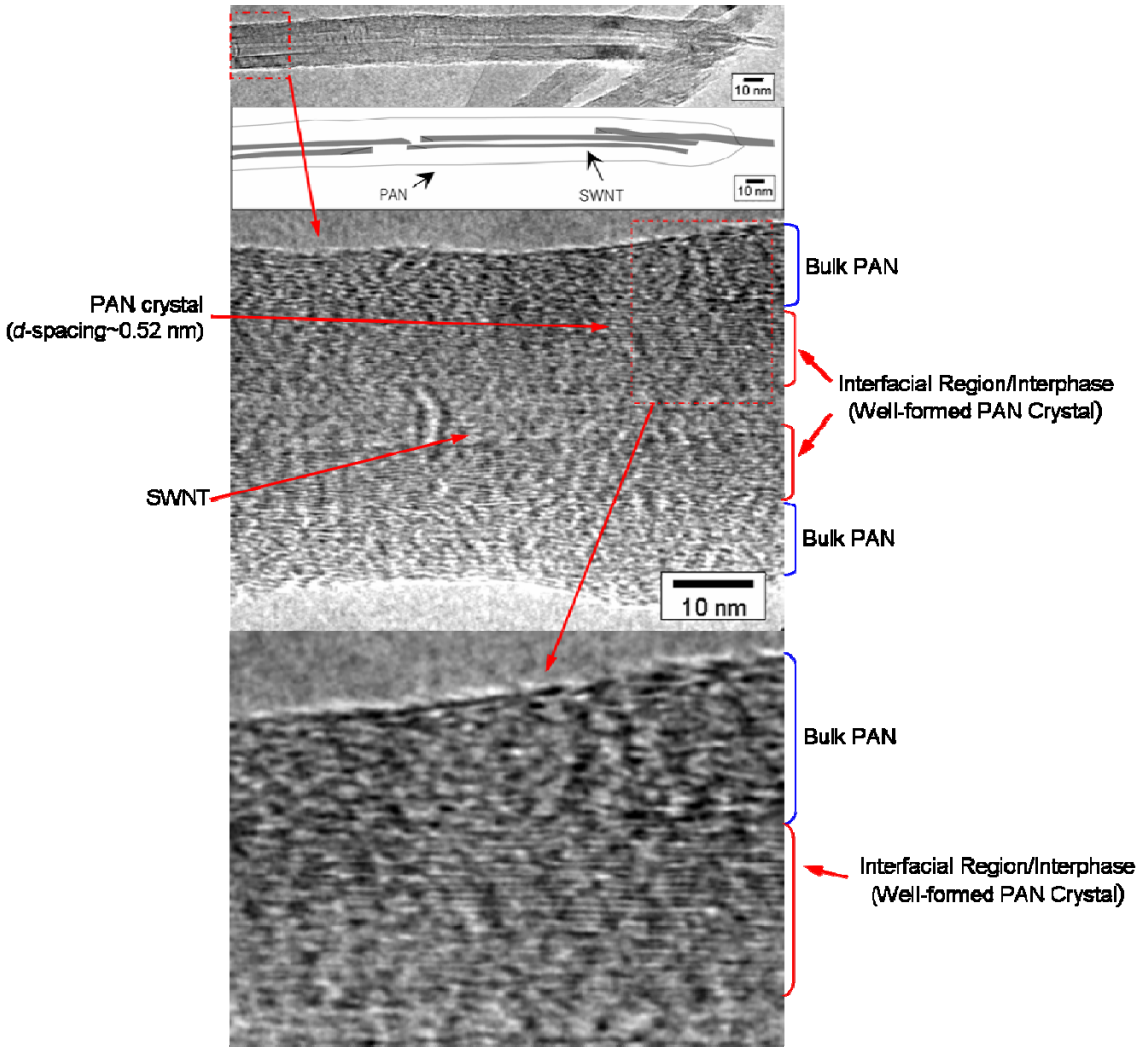

Figure A.3. High-resolution TEM images and their schematics of PAN/SWNT (99/1) fiber of draw ratio 51.

PMMA/SWNT composite films were prepared for HR-TEM studies by cycling the films repeatedly through toluene to remove excess PMMA and the PMMA not strongly interacting with the SWNT. HR-TEM observations show that the SWNT appear nearly clean and free of polymer (Figure A.4). In some regions where the SWNT bundles are highly entangled there appears to be trapped PMMA. Images of individual SWNT show what appear to be small amounts of PMMA still loosely wrapped on the SWNT indicating that there is no strong interaction between PMMA and SWNT. PMMA is an amorphous polymer system therefore no crystal formations can occur near the

SWNT surface. Although it cannot be generalized to all polymer systems, in this study the physical interaction between the polymer and SWNT is significantly enhanced by the crystallization of the polymer near the SWNT surface.

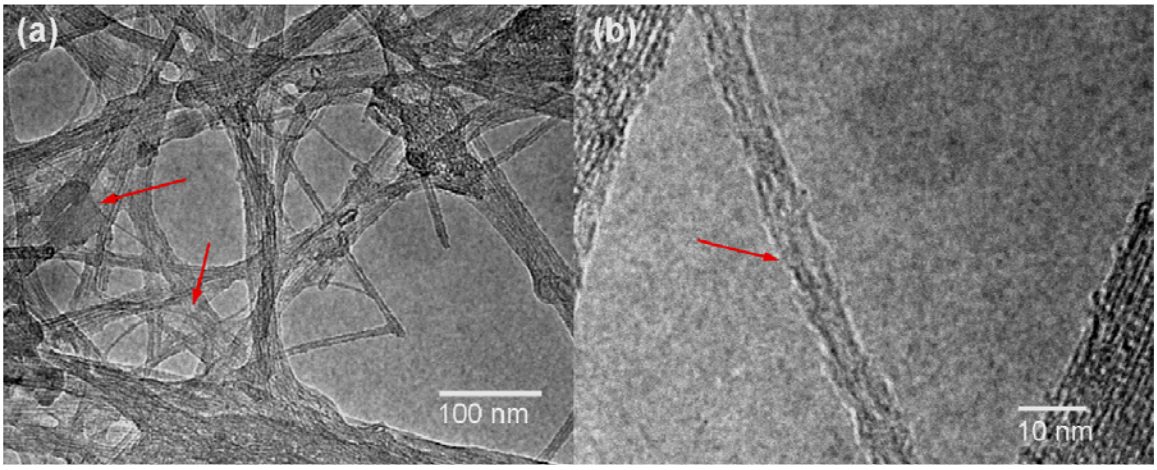

Figure A.4. High-resolution TEM images for PMMA/SWNT disintegrated film showing (a) SWNT to have little or no PMMA coating (red arrows indicate PMMA trapped between entangled SWNT bundles). (b) Higher magnification image showing the presence of a small amount of PMMA near the SWNT surface (indicated by red arrow).

A.3.2. Electron Microscopy Image Stability in Polymer/SWNT Composites

The destruction of the polymer lattice in the electron microscope otherwise known as the *burning* effect of the polymer is caused by electron irradiation due to the lack of electron transport in the non-conductive polymer. Given that the electrons interact inelastically with the polymer crystal structure, this electron accumulation will cause large amounts of lattice vibrations in the polymer crystalline structure, and is a major contribution to its destruction (Figure A.5). Since the polymer provide little to no pathway for charge and heat transport of electrons, the electrons will accumulate (Figure A.6). The heating effects of the electron beam have also been noted to contribute to beam damage in some polymer systems. To reduce this problem a coating method is typically employed, where the polymer sample is coated with a conductive material like carbon or some metal. Since this conductive coating can now provide a pathway for

electron transport the polymer is protected. The downside is that the high-resolution images cannot be obtained since these features will likely be covered by this conductive coating.

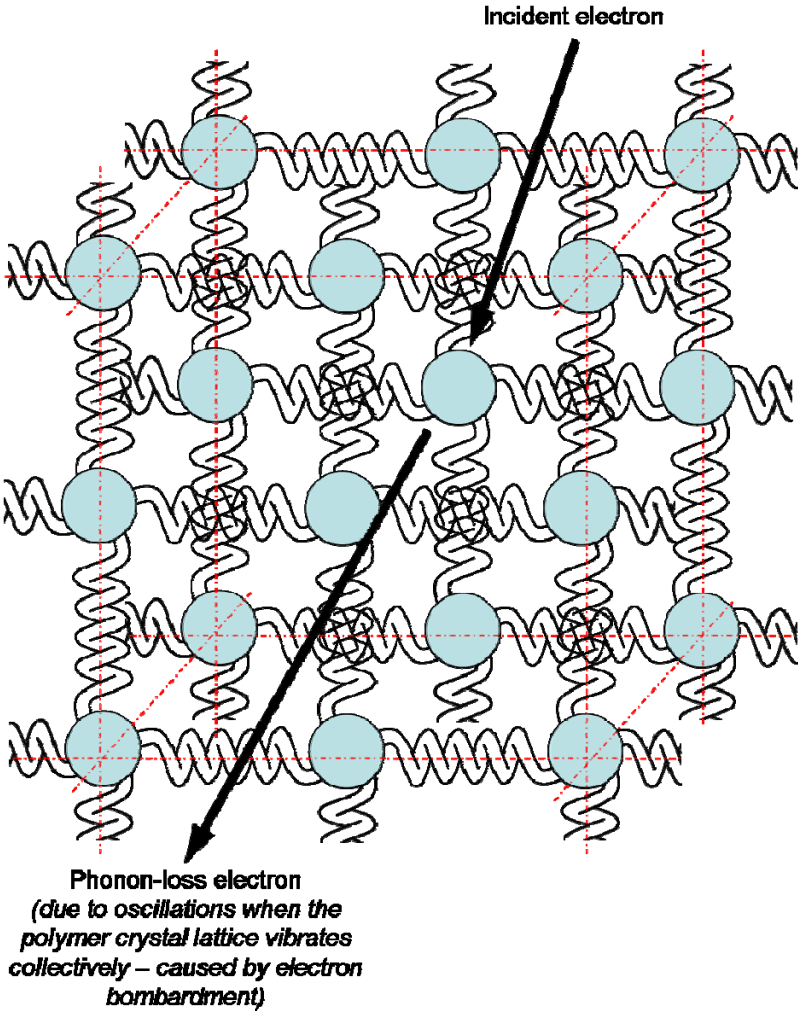

Figure A.5. Schematic of polymer crystal spring lattice and the phonon loss that occur due to the bombardment of electrons from the incident beam.

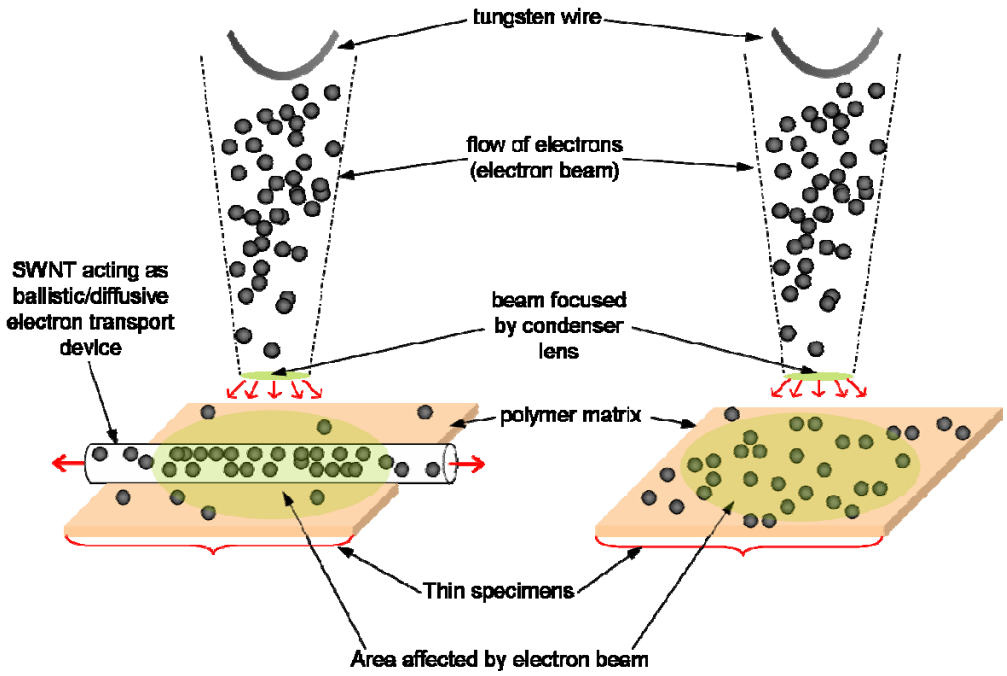

Figure A.6. Schematic of interaction of the incident electron beam in with the polymer matrix with and without the presence of SWNT.

Although the morphology of the interfacial region for each polymer composite studied in this chapter differs depending on the polymer system and composite preparation technique, all composite samples show increased irradiation resistance due to the presence of SWNT. The transport of electrons in both SWNT and MWNT has been shown to be either ballistic or diffusive depending on the type of nanotube and the experimental setup [216-221]. The SWNT, metallic or semi-conductive are orders of magnitude more conductive then the polymer. The interfacial region in the polymer/SWNT composites consists of a nonconductive polymer coating surrounding the conductive SWNT. The presence of SWNT acts as a channel which provides a path for electrons to flow (Figure A.6). This greatly reduces the accumulation of electron in the non-conductive polymer coating which ultimately leads to an overall increase in irradiation resistance. As evidence in this work, high-resolution images can be obtained readily at beam strengths of 200 kV and ×500,000 magnifications.

A.4. Conclusions

Initial observation by HR-TEM of several polymer/SWNT composites reveal that the polymer crystal morphology near the polymer-SWNT interface may play an important role in the overall polymer-SWNT interaction. SWNT are shown to promote crystal formation in the interphase for semi-crystalline PAN in both film and fiber cases. For the amorphous polymer system PMMA where no crystalline interphase is found, there appears to be no strong interaction between the polymer and SWNT. SWNT act as electron transport devices throughout the polymer/SWNT composites and this prolongs the irradiation lifetime of the polymer. Under these conditions, high-resolution lattices images for semi-crystalline PAN can be obtained at beam strengths of 200 kV and up to ×500,000 magnifications.

APPENDIX B

HIGH TEMPERATURE POLYETHYLENE *KEBAB* GROWTH ON SWNT IN NON-SOLVENT N, N DIMETHYLFORMAMIDE/POLYETHYLENE/SWNT SYSTEMS

B.1. Introduction

Heterogeneous polymer crystallization in the presence of graphitic materials has been reported on for some time. Oriented spherulite growth of polypropylene on graphite fibers was reported [178] when polypropylene was melt crystallized in the presence of these fibers. The graphitic layer provided many nucleating sites which led to spherulite growth that was tightly packed forcing the spherulites to grow uniaxially from the surface, and this led to crystallites where the polymer molecules were more or less parallel to the surface. This type of crystallization was termed *transcrystallization*. Poly(etherketoneketone), poly(etheretherketone), poly(phenylenesulfide), and nylon 6,6 have all been shown to transcrystallize on the surface of carbon fibers [222, 223]. Several polymers including poly(tetrahydrofuran), poly(oxacyclobutane), and poly(ethylene oxide) have been shown to form epitaxial layers on graphite during polymerization [181, 182]. Polyethylene melt crystallized in the presence of highly oriented pyrolytic graphite also show that the polyethylene chain-ordering during crystal growth is influenced by the graphite surface [224, 225]. As mentioned in Chapter 1, the discovery of CNT has opened a new class of nucleating agent for the study of polymer crystallization.

Studying polymer crystallization in the presence CNT has been a good route for understanding polymer-CNT interaction. Good polymer-SWNT interaction SWNT has led to the improvement of the radiation stability of the polymer [71, 159] and this is very important for studying polymer crystal morphology in the electron microscope. Understanding the nanoscale interactions between the polymer and CNT is also important for processing composite materials, where interfacial interaction directly affects the composite properties [71, 81, 141, 226, 227]. This chapter studies the ability of polyethylene to crystallize in the presence of SWNT in a poor-solvent at high temperatures.

B.2. Experimental

Unpurified single-wall carbon nanotube (SWNT) (manufactured by Carbon Nanotechnologies Inc. Lot #: R0231, with 35 wt% metal catalyst impurities) was dispersed in N,N-dimethylformamide (DMF) (Sigma-Aldrich, Cat. #: 319937, Lot #: 05735DE) by sonication in a bath sonicator (model #: 3510K-MT, output frequency: 42 kHz ± 6 %) for 24 h at concentration of 15 mg/100 ml and 4mg/100 ml to achieved different levels of SWNT dispersion quality. Linear low density polyethylene (LLDPE) (Huntsman Polymers Corporation, the Lot #: A304HLL1039, Type#: L7501, MFI = 6.6 g/10 min), high density polyethylene (HDPE) (Sigma-Aldrich, Cat. #: 547999, MFI = 2.2 g/10 min), low molecular weight polyethylene (LMWPE) (Aldrich, Cas. #: 9002-88-4, batch # 06107LD, M_w = 4000), and paraffin wax (Sigma-Aldrich, Cas. # 8002-74-2, batch # 18519MD, m_p 73-80 °C) were added to the SWNT dispersions at a ratio of 100 mg of polyethylene: 20 ml SWNT/DMF dispersion in a glass jars with caps. The

mixtures were heated to the boiling point of DMF (~153 °C) for 30 minutes, and in *scenario I* stirred constantly using a magnetic stir while *scenario II* involved no stirring. These mixtures were subsequently cooled to room temperature (25 °C) before samples were prepared for analysis.

Ultra-Purified SWNT (obtained from Carbon Nanotechnologies Inc., Lot #: P-0247, <2 wt% metal impurity) were dispersed in (DMF) at a concentration of 4 mg/100 ml by sonication in a bath sonicator for 24 h at 55 °C. Polymers from the same batches mention above, LLDPE, HDPE, LMWPE, and paraffin wax were subsequently added to the SWNT/DMF dispersions at a ratio of 100 mg LLDPE/HDPE:20 ml DMF to obtain separate mixtures. These mixtures were heated to the boiling point of DMF (~153 ºC) for 4 h and subsequently cooled to room temperature for sample preparation.

B.2.1. Sample Characterization

Transmission electron microscope (TEM) sample were prepared by placing a 1-2 droplets of solutions onto Lacey carbon coated TEM grids (Electron Microscopy Sciences, Cat. #: HC200-Cu) using a Loop (Electron Microscopy Sciences, Cat. #: 70944). High-resolution TEM (HR-TEM) was performed using both JEOL 4000EX electron microscope (accelerating voltage 400 kV) and Hitachi HF-2000 Field Emission Gun electron microscope (accelerating voltage 200 kV). Scanning electron microscopy (SEM) was carried out on LEO 1530 thermally assisted field emission microscope (operating voltage ranging from 10-20 kV) on samples sputtered coated with gold, and Zeiss Ultra60 microscope (operating voltage ranging from 1-5 kV) on uncoated samples. Wide-angle X-ray scattering (WAXS) was done using a Rigaku Micro Max 002 X-ray

generator operated at 45 kV and 0.66 mA and equipped with R-axis VI++ WAXS/SAXS detector.

B.3. Results and Discussion

B.3.1. Solubility of Polyethylene in DMF

B.3.1.1. High Density Polyethylene in DMF

DMF has been shown to be a poor solvent for polyethylene (PE) therefore dissolution is not expected. PE pellets/particles boiled in DMF (153 ºC) (Figure B.1), could be recovered once the solution was cooled to room temperature (25 ºC). In a controlled experiment 100 mg of high density polyethylene (HDPE) was boiled in DMF at 153 ºC for a period of 72 h and the weight of the particles were measured before and after boiling (boiled particles were dried in vacuum). The weight change was small and found to be only ~1 mg of PE dissolved in 100 ml of DMF. To verify whether or not the weight change was real, several grams of HDPE were boiled 100 ml DMF for the same amount of time. After cooling to room temperature, the undissolved HDPE pellets were removed and a significant amount of precipitated material could be seen in the DMF (Figure B.1c). This precipitated material was dried and analyzed by DSC and X-ray.

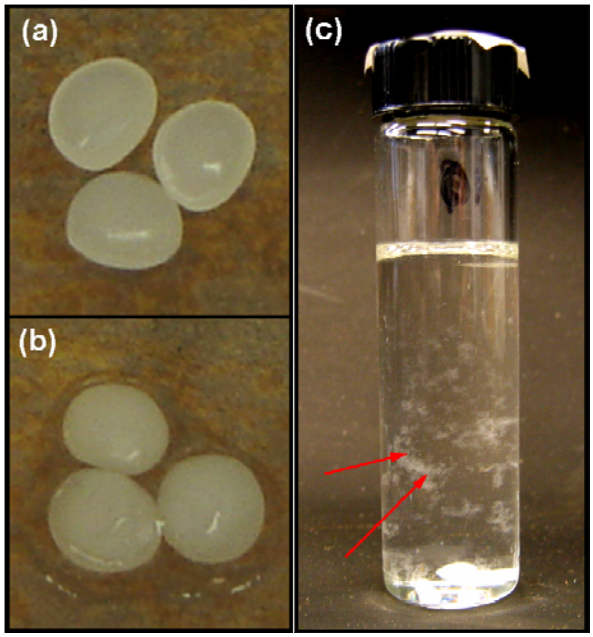

Figure B.1. Photographs of (a) HDPE pellets obtained from manufacturer, (b) HDPE pellets after being boiled in DMF, and (c) dissolved and precipitated HDPE in DMF.

From X-ray diffraction the two major [110] and [200] PE peaks could be identified showing the precipitated materials was in fact PE (Figure B.2). DSC was performed on the dissolved and precipitated HDPE from DMF, undissolved HDPE from DMF, as well as HDPE dissolved and precipitated from xylene. X-ray diffraction of these materials show both (110) and (200) predominant peaks in the intensity versus 2θ profiles (Figure B.3). The DSC curves for the undissolved HDPE from DMF and HDPE dissolved in xylene both show similar curves for melting and crystallization (Figure B.4). However, DSC curves for the PE dissolved and precipitated from DMF show a significant decrease in the melting and crystallization temperatures (Figure B.4 – green curve). These DSC results provide evidence a lower molecular weight PE material is able to be dissolved in boiling DMF.

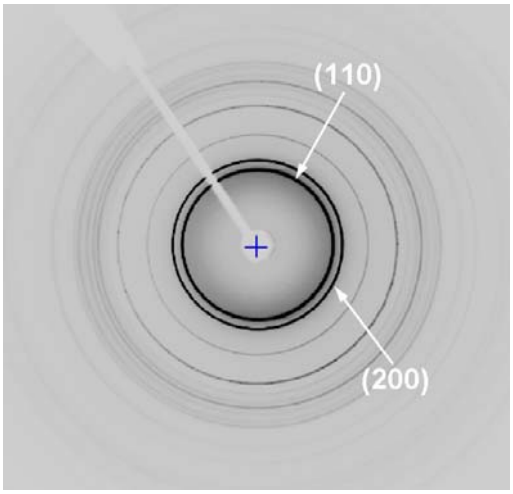

Figure B.2. Wide-angle X-ray diffraction pattern of HDPE precipitated material removed from DMF.

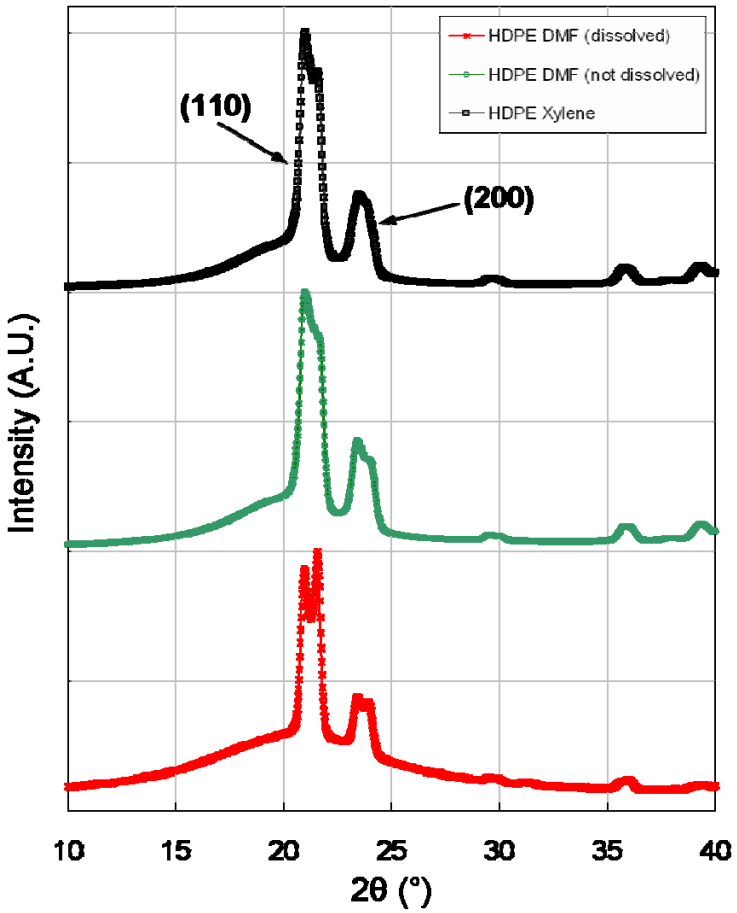

Figure B.3. Wide-angle X-ray integrated scans for HDPE dissolved in DMF (red), HDPE that did not dissolve (green), and HDPE dissolved in xylene (black).

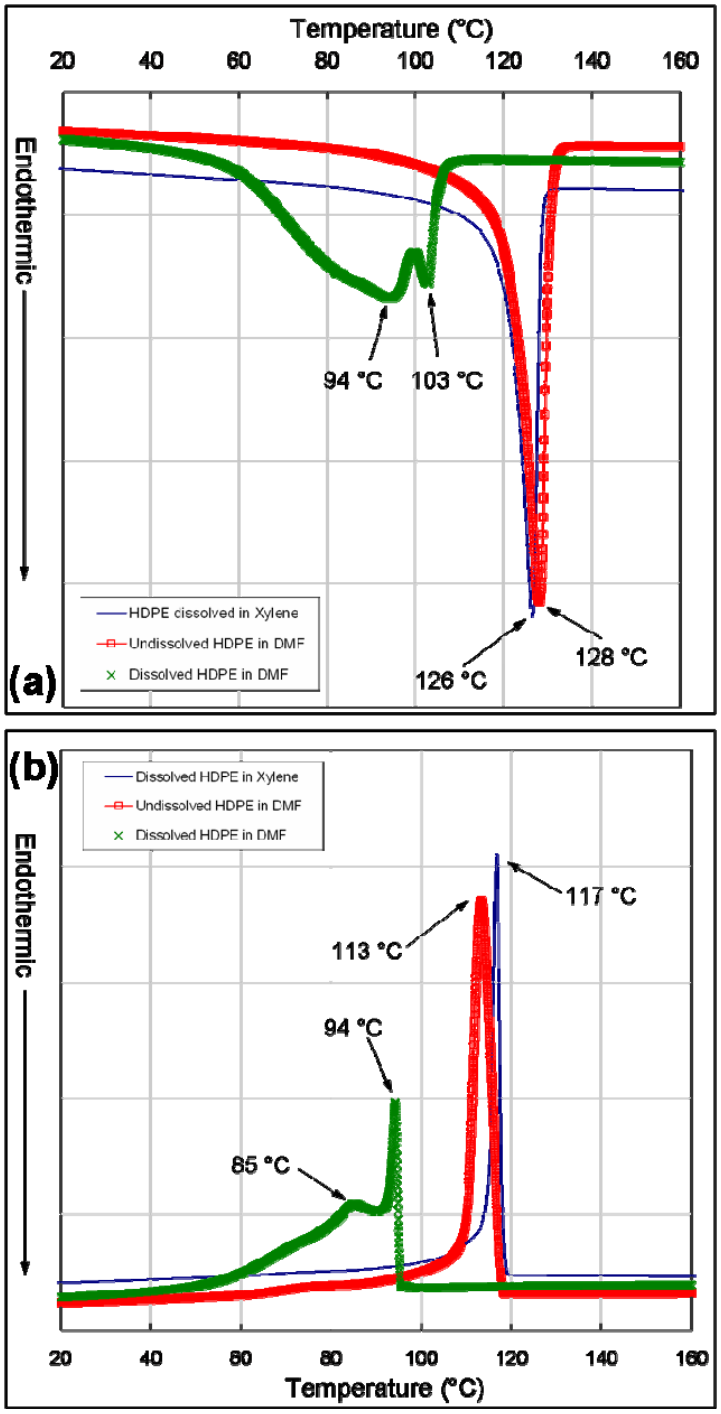

Figure B.4. Differential scanning calorimetry curves showing (a) 1st melting curves for HDPE dissolved in DMF (green), undissolved HDPE (red) and HDPE dissolved in xylene (blue), and (b) cooling curve for HDPE dissolved in DMF (green), undissolved HDPE (red) and HDPE dissolved in xylene (blue).

B.3.1.2. Paraffin Wax and Low Molecular Weight Polyethylene in DMF

Based on the previous results the dissolution of both paraffin wax and low molecular weight PE (LMWPE) ($M_w \sim 4000$) in DMF were studied. In both cases up to ~400 mg of wax and LMWPE could be dissolved in 100 ml of boiling DMF. When compared to the DSC curves for the HDPE dissolved in DMF, the DSC curves for paraffin wax lower melting and crystallization peaks (Figure B.5), while for LMWPE the DSC curves have very similar melting and crystallization peak shapes and temperatures (Figure B.5). This study shows that while DMF is a poor solvent for PE it is possible to dissolve PE with $M_w < 4000$. The crystallization behavior of this low molecular weight PE material is subsequently studied in the presence of unpurified and purified SWNT.

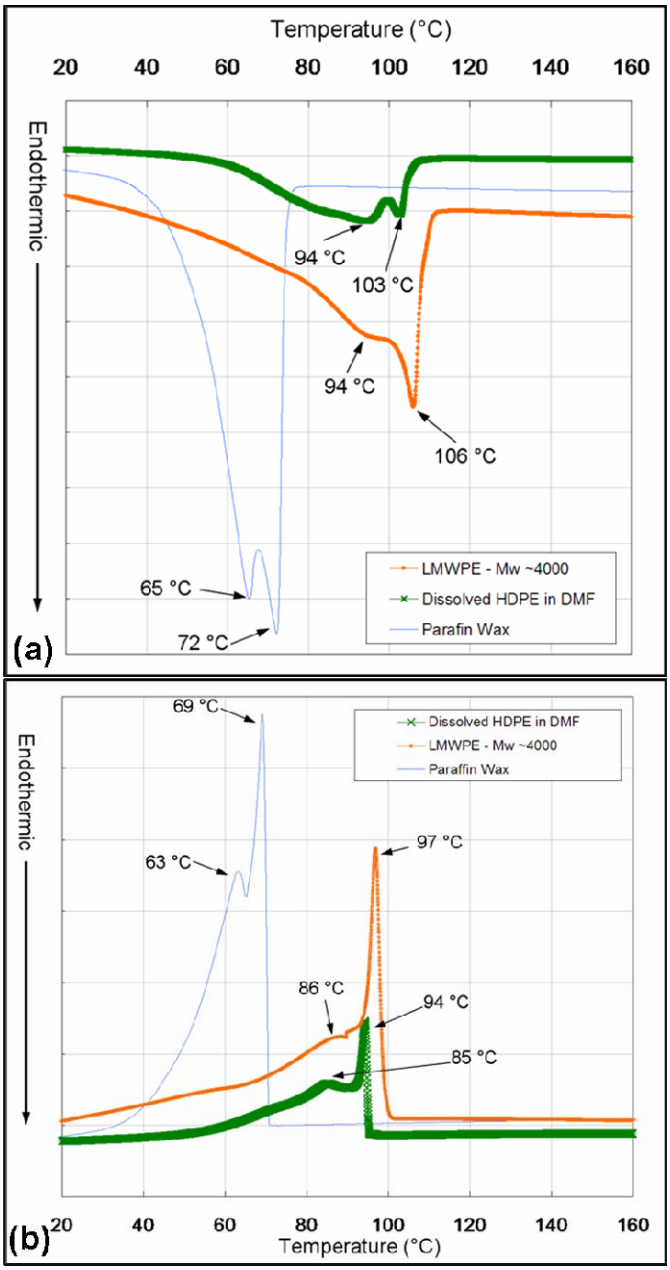

Figure B.5. Differential scanning calorimetry curves showing (a) 1st melting curves for HDPE dissolved in DMF (green), LMWPE (orange) and paraffin wax (light blue), and (b) cooling curve for HDPE dissolved in DMF (green), LMWPE (orange) and paraffin wax (light blue).

B.3.2. Unpurified SWNT (~35 wt% metal impurity) and PE in DMF

To vary the chain structure of the PE both linear low density polyethylene (LLDPE), HDPE, and LMWPE were used. LLDPE chains contain a significant amount

of short branching, while HDPE/LMWPE only has very few branches along the chain. High-resolution transmission electron microscope (HR-TEM) images of the raw SWNT material used in this study show the presence of a large amount of metal nanoparticles and large bundle size of ~ 26 nm (Figure B.6).

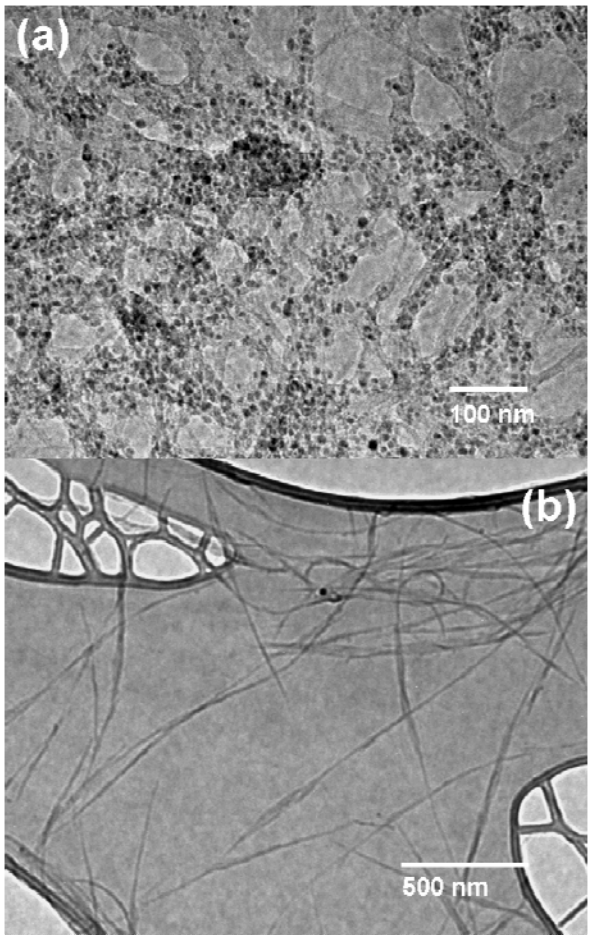

Figure B.6. High-resolution TEM micrographs of (a) SWNT (35 wt % metallic impurity), and (b) SWNT (2 wt % metallic impurity).

B.3.2.1. LLDPE and Unpurified SWNT in DMF

Scanning electron microscope (SEM) analysis of the SWNT bundle size in the SWNT materials after being boiled in the presence of LLDPE shows diameter variation from region to region in the sample. In some places the diameter of SWNT bundles is

around ~26 nm revealing no LLDPE wrapping (Figure B.6 and B.7a), while in other regions the SWNT bundle size increases to ~50 nm (Figure B.7b). In these thicker regions scanning electron microscope (SEM) was used to focus an electron beam at operating voltage of 20 kV onto one large SWNT bundle (Figure B.8) for 10 minutes, after this time period an LLDPE shell is burned off exposing the SWNT bundle (Figure B.8b). This shows that the low molecular weight LLDPE dissolved in DMF is able to form a generous coating on the SWNT bundle surface.

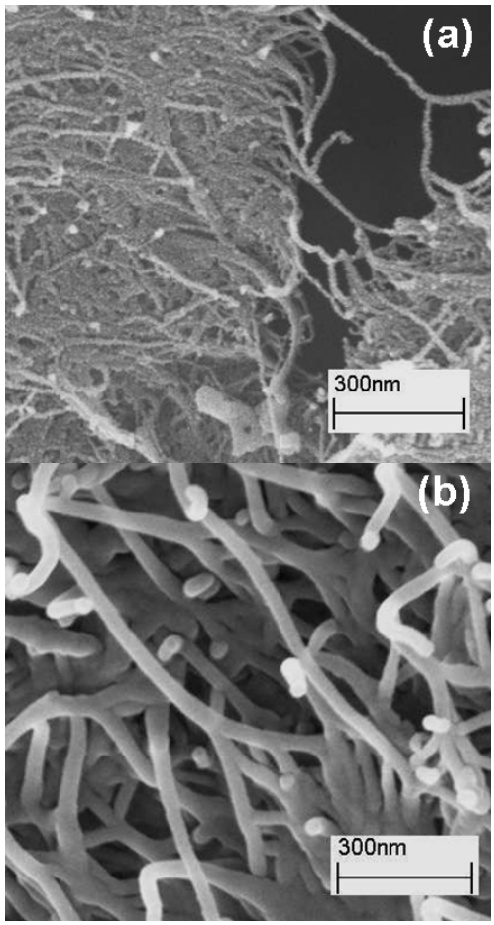

Figure B.7. Scanning electron micrographs of (a) SWNT (35 wt% metallic impurity) powder, and (b) Impure SWNT after boiling in LLDPE showing significantly large bundle size.

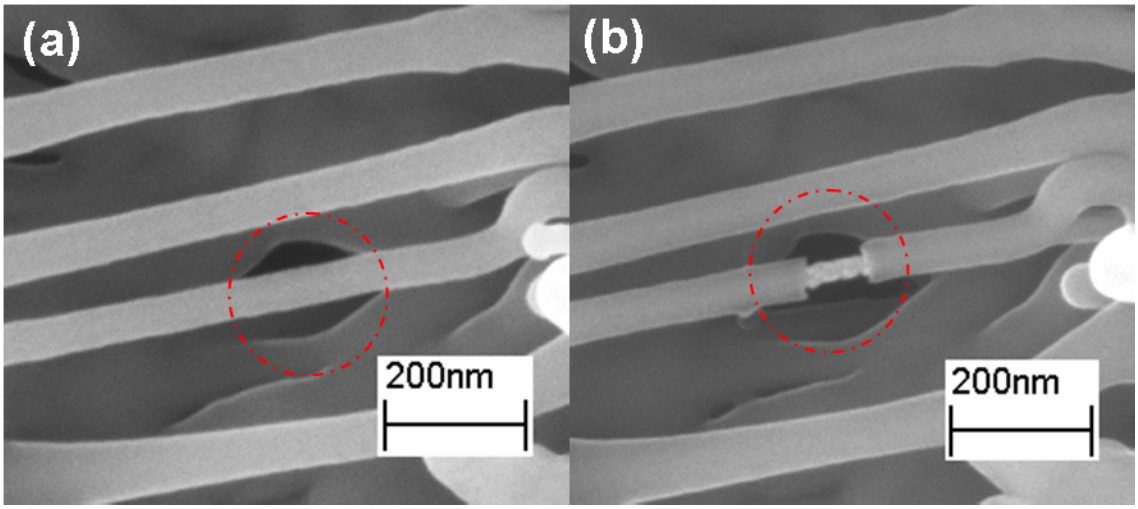

Figure B.8. Scanning electron micrograph of (a) SWNT (35 wt % metallic impurity) coated with LLDPE before electron beam damage, and (b) after beam damage at 20 kV where LLDPE coating was removed.

Although polyethylene has been shown to have weak radiation resistance [11], crystalline PE has been shown to survive for some time at higher operating voltages (80 kV) in the electron microscope[228]. In this work, the destruction of LLDPE coating on SWNT at significantly lower voltages over a similar time period indicated that LLDPE coating consists of more amorphous rather than crystalline regions. SWNT bundles are also observed to protrude from the LLDPE particle (Figure B.9), and the diameter of these SWNT bundles is also around ~50 nm, which indicates LLDPE wrapping of the SWNT bundle. No observation of polyethylene *kebab* growth was observed in these samples. This type of crystal growth has been observed in other studies where PE has been crystallized in the presence of SWNT [100].

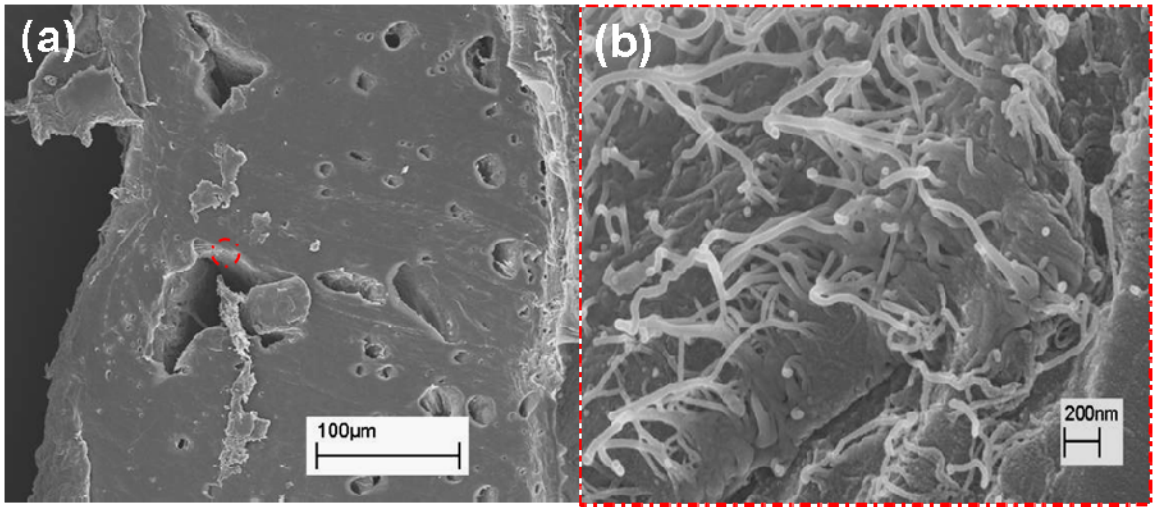

Figure B.9. Scanning electron micrograph of (a) surface of LLDPE pellet after being boiled in DMF, and (b) higher magnification showing SWNT (35 wt% metallic impurity) bundles embedded in the pellet.

B.3.2.2. HDPE/LMWPE and Unpurified SWNT in DMF

SWNT boiled in the presence of HDPE and LMWPE were dried and examined using HR-TEM. PE *kebabs* were found to only grow on the cleaner portion of the unpurified SWNT (Figure B.10). There was no evidence from microscopy observations that HDPE formed a *shish* coating over the SWNT bundles before *kebab* growth occurred. The presence of metal nanoparticles on the SWNT surface leads to a prevention of crystallization of PE. Previous studies of PE *kebab* growth on SWNT have speculated of an epitaxial interaction between SWNT and PE which promote chain folding on the SWNT surface to initiate *kebab* growth [100, 101]. The existence of metal nanoparticles on the SWNT surface prevents this epitaxial PE chain-graphite interaction therefore; PE *kebabs* do not grow in the presence of metal nanoparticles.

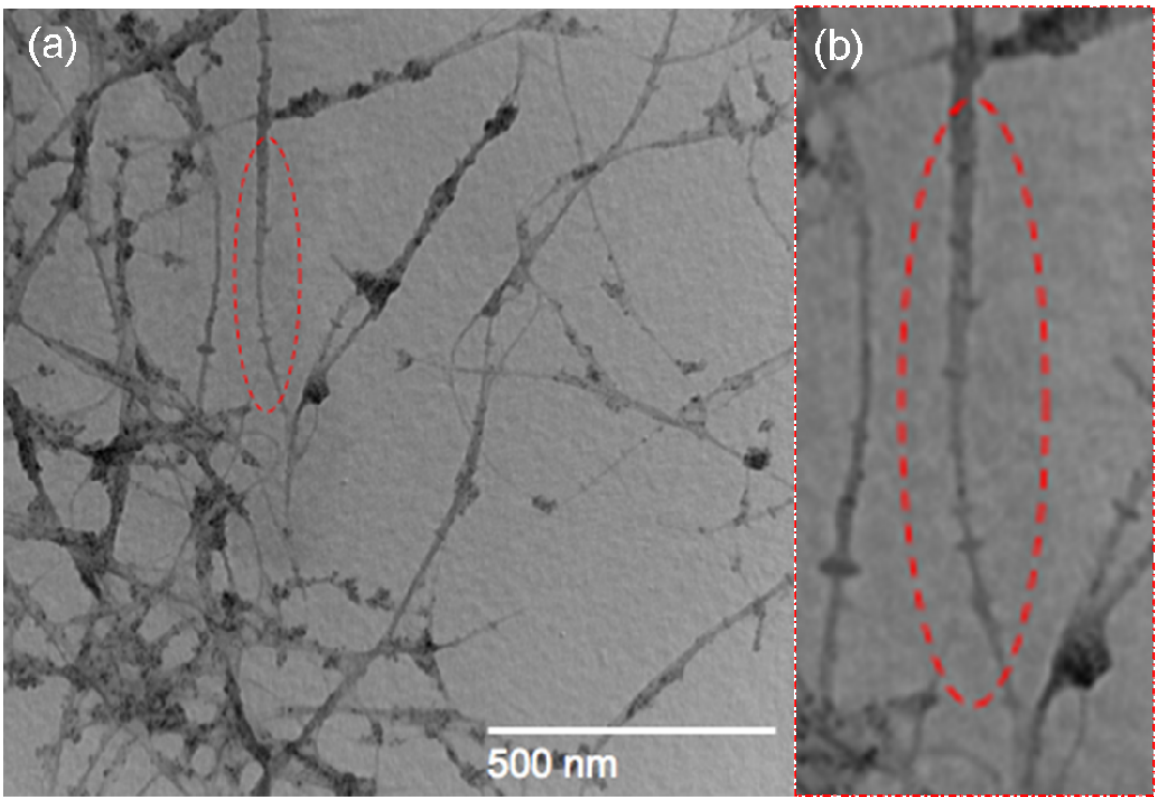

Figure B.10. (a) High-resolution TEM bright field image of LMWPE *kebab* growth on SWNT *shish*. (b) higher-magnification showing the *kebabs* only grows in cleaner portion of the SWNT (35 wt% metallic impurity).

B.3.3. Purified SWNT (~2 wt% metal impurity) and PE in DMF

B.3.3.1. LLDPE and Purified SWNT in DMF

HR-TEM analysis of LLDPE/SWNT samples show that on a small amount of SWNT bundles the formation of LLDPE crystalline kebabs were found with an average lamellar thickness of 9.5 ± 1 nm (Figure B.11). The inherent chain structure of LLDPE is such that there is a significant amount of short branches along the main chain, and for this reason crystallinity is reduced due to the increase in branching density. Studies on branched polyethylene and LLDPE crystallization have shown that the increase in branching density reduced crystallization [229]. The use of purified SWNT in this experiment led to significant reduction of metal nanoparticles in the sample. Therefore,

LLDPE was able to have better interaction with the surface of SWNT bundles. SWNT was able to nucleate and template the crystal growth of LLDPE *kebabs*.

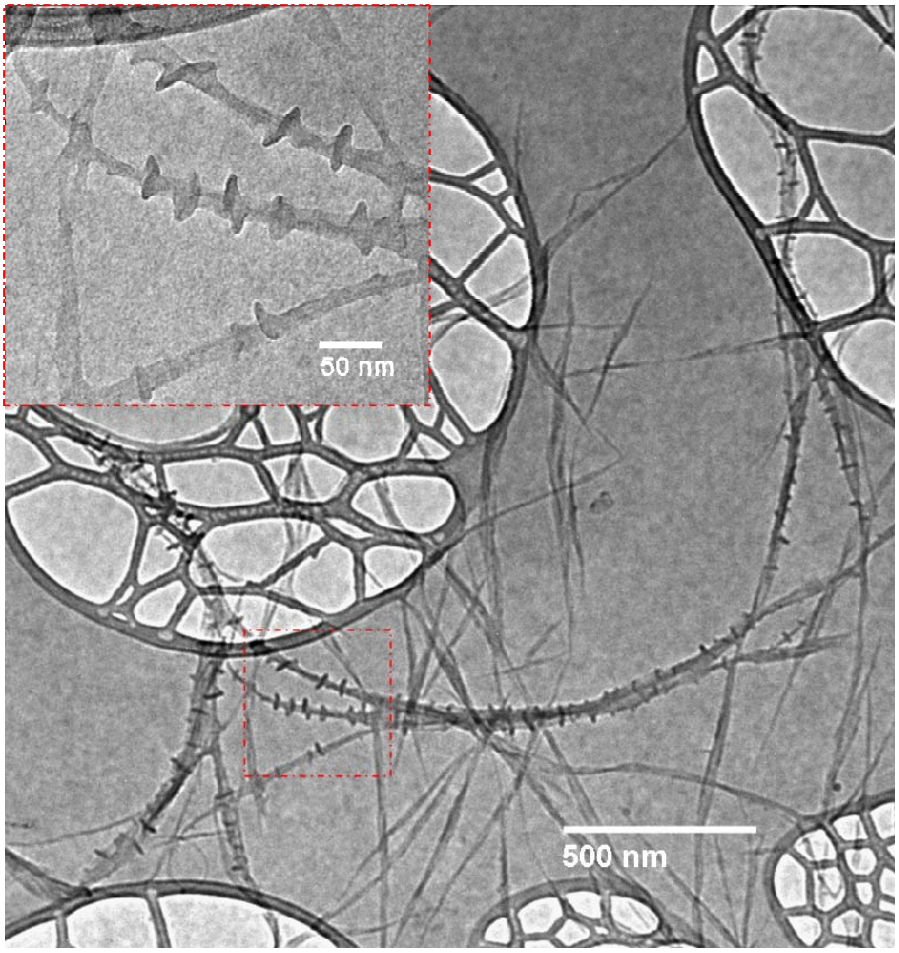

Figure B.11. High-resolution TEM bright field image of LLDPE *kebab* growth on SWNT *shish*. Inset: higher-magnification showing the *kebabs* on the SWNT (2 wt% metallic impurity).

B.3.3.2. HDPE/LMWPE and Purified SWNT in DMF

HR-TEM analysis of samples prepared by boiling HDPE pellets in SWNT/DMF dispersions show that much more SWNT bundles are covered by HDPE *kebabs* (Figure B.12) as compared to the LLDPE samples. On smaller diameter SWNT bundles ≤ 20 nm the kebab growth completely surrounds the bundle (Figure B.12b), but for larger SWNT

bundles >30 nm there are some regions where kebab growth is initiated at different sides of the bundle (Figure B.12c). Average kebab lamellar thickness is ~11 nm. The kebab disc diameter also varied for both LLDPE and HDPE samples from 35 nm to 150 nm, and this may be due to different crystal growth rates in the solution.

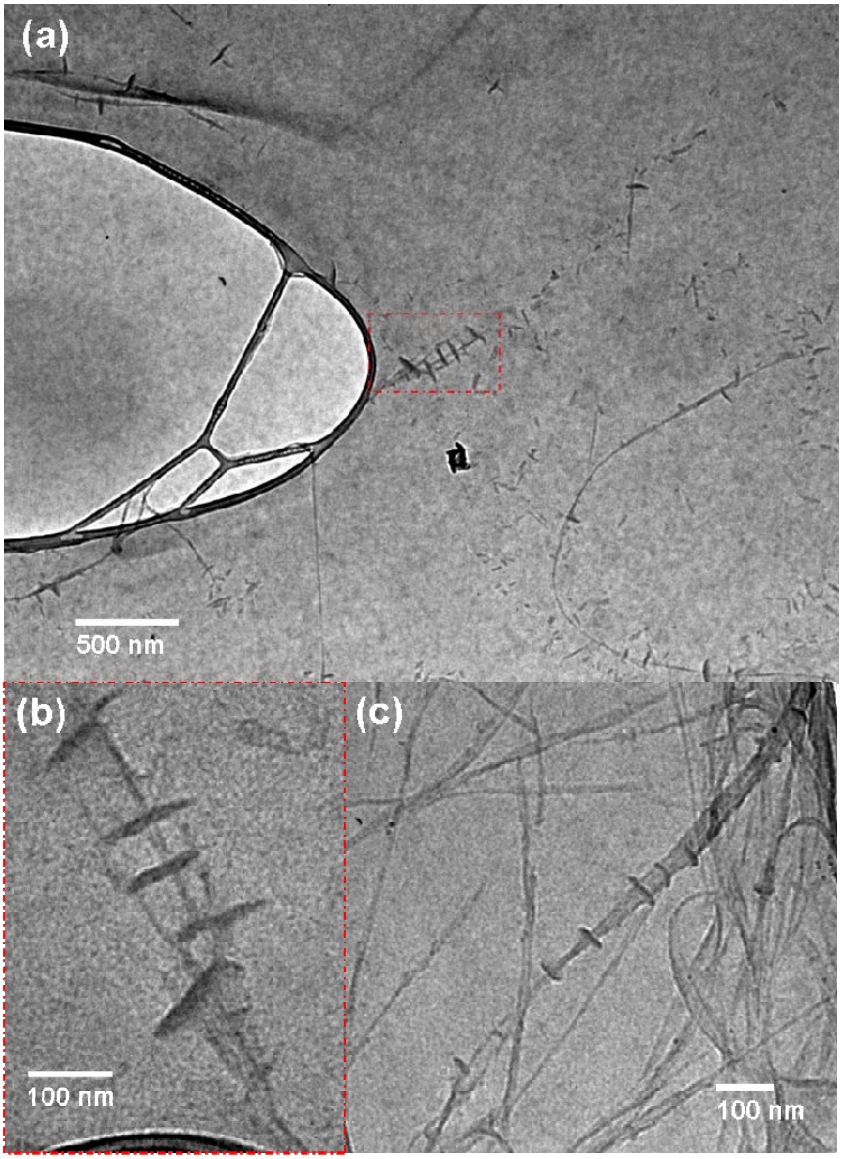

Figure B.12. High-resolution TEM bright-field image of (a) HDPE *kebab* growth on SWNT *shish*, (b) higher-magnification showing the *kebabs* on the SWNT (2 wt% metallic impurity), and (c) *kebab* growth initiating on the sides of SWNT large bundles.

SEM analysis was also performed to examine the morphology of the HDPE kebabs on SWNT bundles. Both HR-TEM and SEM studies show the periodicity of *kebab* growth on SWNT *shish* is somewhat random (Figure B.13). For SWNT bundles that are completely covered by kebabs the periodicity between kebabs is ~ 80 nm for both LLDPE and HDPE sample. For SWNT bundles with minimal kebab coverage the kebab growth is much more random and spread out. Although DMF is a poor solvent for polyethylene and a much higher crystallization temperature (~153 ºC) was used as compared to previous studies where HDPE has been crystallized in the presence of CNT [100, 101], this work shows that both LLDPE and HDPE still able to crystallize. This DMF boiling temperature must exceed the T_θ for both LLDPE and HDPE in DMF since both polymer are able to interact with SWNT and form crystals.

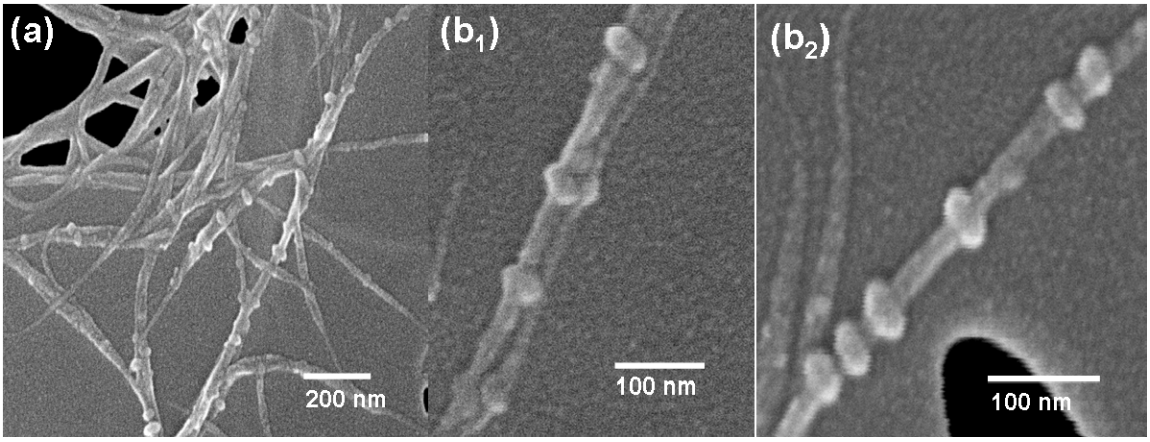

Figure B.13. Scanning electron micrographs of (a) HDPE *kebab* growth on SWNT (2 wt% metallic impurity), and (b) and (c) higher-magnification of *kebab* growth.

B.4. Conclusions

Although DMF is a poor solvent for PE, X-ray and DSC evidence confirm that low molecular weight (M_w ~ 4000) can be dissolved in boiling DMF (~ 153 ºC).

LLDPE does not crystallize in the presence of unpurified SWNT, but forms an amorphous coating on the bundles. The presence of metallic nanoparticles decrease the interaction between LLDPE and SWNT, and this coating could be easily removed by *burning* using an electron beam at a low operation voltage of 20 kV. Crystallization of HDPE on the surface of SWNT is hindered by the presence of the metallic nanoparticles, and HDPE kebab growth could be found in regions of the SWNT bundles where no nanoparticles were present. For purified SWNT low molecular weight compounds for both LLDPE and HDPE were both able to crystallize into *kebabs* on SWNT shish in this poor solvent DMF at a high T_c ~ 153 ºC. For smaller SWNT bundles the PE kebabs completely surround the bundles, however for larger bundles polyethylene kebabs growth from the sides of the bundle. Average *kebab* lamellar thickness was for LLDPE and HDPE kebabs crystals were 9.5 nm and 11 nm respectively. For HDPE/SWNT/DMF mixtures as compared to LLDPE/SWNT/DMF mixtures more *kebab* covered SWNT are present, and this may be due to the ability of HDPE to crystallize more readily than LLDPE because of less branching. Overall *kebab* growth is limited by the small amount of low molecular weight LLDPE and HDPE dissolved in DMF.

APPENDIX C

CRYSTALLIZATION IN PVA AND PVA/SWNT GEL FILMS

C.1. Experimental

Atactic poly(vinyl alcohol) (PVA) (from Kuraray Co. Ltd. Tokyo, Japan; lot # 636837, DP: 18,000, and 98.4 % hydrolyzed) was dissolved in an 80:20 volume ratio of dimethyl sulfoxide (DMSO), and distilled water respectively in a 400 ml beaker equipped with a magnetic stir bar and heated to temperatures between 85 to 90 °C to obtain a 3 wt% PVA solution (80 ml DMSO, 20 ml water, and 3.4 g PVA). SWNT (obtained from CNI, Houston, TX, USA, lot# P-0247) (0.4 mg/ml) dispersions were obtained in DMSO by sonicating using a Branson 3520 bath sonicator (frequency 42 kHz, power 100 W) at a concentration of 33 mg/80 ml DMSO for 24 h at 40 °C. To obtain a PVA/SWNT dispersion, 3.4 g of PVA was dissolved into the SWNT/ DMSO dispersions at 85 to 90 °C and distilled water was added to obtain PVA:SWNT weight ratio of 99:1. The mixtures were stirred with an overhead Caframo high-shear mechanical stirrer (model# BDC1850) at a shear speed of 300 RPM continuously for 48 h or until an optically homogeneous dispersion was obtained.

Gel films were made by pouring a PVA solution and PVA/SWNT dispersion into glass crystallization dishes, and immediately immersing these dishes into a methanol bath maintained at -78 °C to form a gel film. The films were kept immersed for a 24 h period before drying in a vacuum oven at 60 °C for 72 h. Films were also prepared by solution casting, where PVA solutions and PVA/SWNT dispersions were poured into Teflon® dishes and dried in a vacuum oven at 60 °C for two weeks. In both cases the dried films were used for further analysis.

C.1.1. Sample Characterization

Wide-angle X-ray scattering was done on the Rigaku Micro Max 002 X-ray generator operated at 45 kV and 0.66 mA and equipped with R-axis VI++ detector. Crystallinity from wide-angle X-ray diffraction were determined using the software MDI Jade 6.1. AreaMax software was used for background subtraction and integration. The area due to the crystalline and amorphous contribution of the polymer was determined by peak fitting analysis. Differential scanning calorimetry (DSC) measurements were performed on Q-100 DSC (manufactured by TA Instruments, New Castle, DE, USA). Digital photographs were taken using a DSC-F88 Cyber-shot digital camera (manufactured by Sony)

C.2. Results and Discussion

As mentioned in Chapter 5 the tensile strength and modulus increase as gelation time is increased in the fiber spinning process. To understand why the increase is observed the gelation of PVA/DMSO/H_2O solutions and PVA/SWNT/DMSO/H_2O dispersions is studied as a function of time. Droplets of PVA/SWNT/DMSO/H_2O dispersion were sandwiched between two glass slides and immersed in methanol kept at -78 °C for 1, 5, 10, and 25 s (Figure C.1). The droplets show ice formation immediately after being immersed in the methanol, however icing occurs much more quickly than gelation (i.e. fully formed gel film). A fully gelled film could not be removed from between the glass slides until the gelation time of at least exceeded 10s. Therefore, longer gelation time seems to lead to more uniform gel formation throughout the film and this may also be true for gel fibers. Time elapsed photographs of this freezing process show that total gelation occurs over time (Figure C.1).

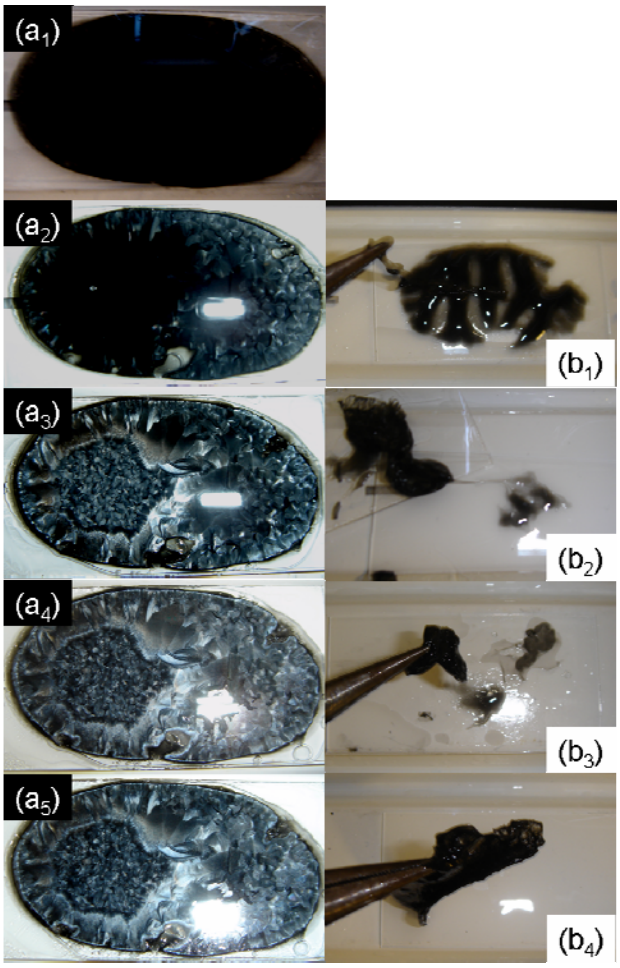

Figure C.1. Digital photographs of (a_1 to a_5) PVA/SWNT solution compressed between two glass slides after being immersed in methanol at -78 °C for 0, 1, 5, 10, and 20 seconds respectively. Digital photographs of PVA/SWNT gel films after immersion into methanol where the top gals slide has been removed showing (b_1) after one second the PVA/SWNT material is still liquid like, (b_2) after five seconds and incomplete gel film has formed some PVA/SWNT material is still liquid like, (b_3) after 10 seconds the film is still not fully gelled, and (b_4) after 20 seconds a fully gelled film could be removed from the glass slide leaving no residue.

DSC studies were performed on both PVA and PVA/SWNT films dried in vacuum at 60 °C and undried films. DSC analysis of PVA and PVA/SWNT gel films show a sharp peak at ~ 225 to 228 °C (Figure C.2). Crystallinity was measured using the enthalpy of melting, for this peak. The theoretical enthalpy for 100 % crystalline PVA is 138.6 J/g of repeating unit [157, 230]. Crystallinty for PVA and PVA/SWNT films was

average over three DSC runs and was 66 and 65 % respectively. Upon cooling the films recrystallize and the second heating curves show a melting peak of ~ 216 °C (Figure C.3). This implies that the crystals formed during gelation at -78 °C versus the crystal form during melting and recrystallization melts at a much higher temperature exhibiting a higher degree of crystal perfection. The T_g transition is also much more suppressed in the 1st heating curve than it is in the 2nd providing further evidence of crystal perfection (Figure C.2). Solution cast PVA and PVA/SWNT films were also prepared for comparison. DSC studies of these films show that crystallinity in dried films for PVA and PVA/SWNT films is only ~30 % which is comparable to other studies in the literature for PVA and PVA/CNT films [110, 230] prepared in a similar manner. DSC results for both PVA and PVA/SWNT gel and solution cast films can be found in Table C.1. This is significantly lower than the crystallinity for the gel films. The 1st crystal melting peak is also ~20 °C lower for the solution cast films as compared to the gel. This studies shows that gelation has a significant influence on crystal structure development for PVA.

Table C.1. Crystal size and DSC data determined for PVA and PVA/SWNT gel and solution cast films.

		PVA Films		**PVA/SWNT (99/1) Films**	
	(hkl)	**Gel Film**	**Cast Film**	**Gel Film**	**Cast Film**
Crystal Size (nm)	(101)	13	10	14	10
	(200)	10	9	10	9
	(111)	9	9	9	9
ΔH_m **(J/g)**		91.5	41.3	89.6	43.3
T_m **(°C)**		227	206	226	200
Crystallinity* (%)		66	30	65	31

**Crystallinity measured by differential scanning calorimetry (DSC).*

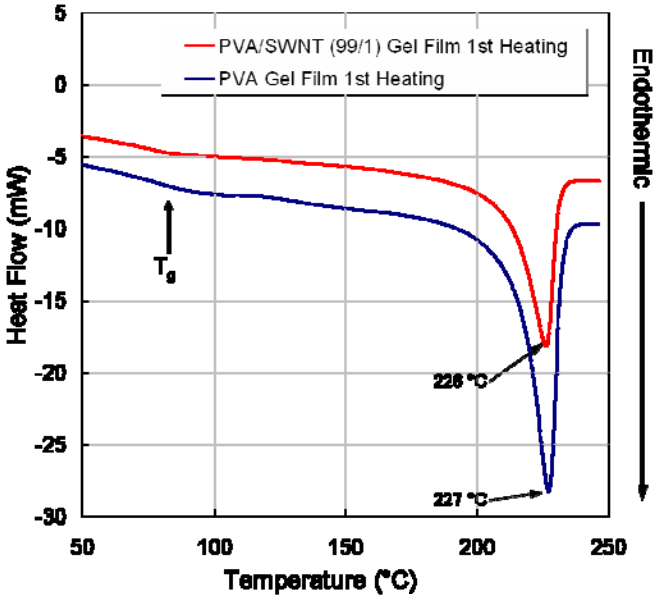

Figure C.2. 1st heating DSC curves for PVA (blue) and PVA/SWNT (red) dried gel films showing suppression in the T_g transition and T_m at approximately ~227 and 226 °C respectively.

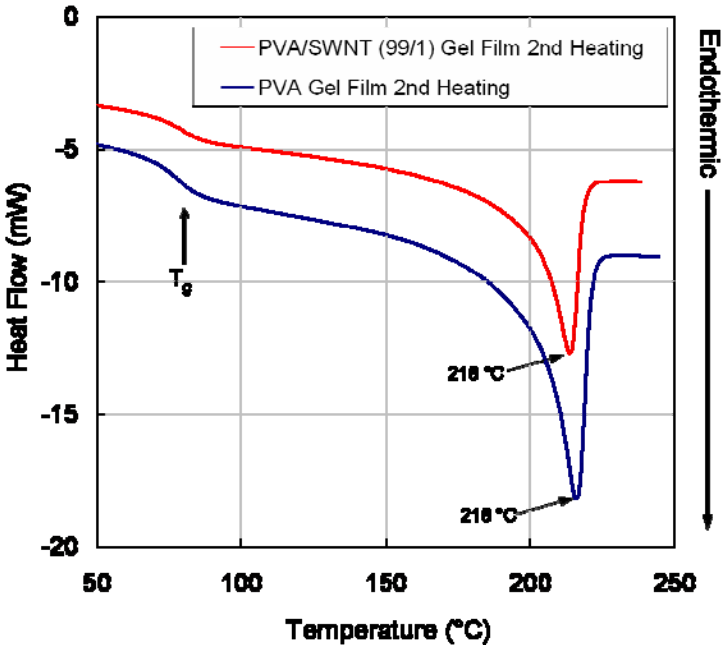

Figure C.3. 2nd heating DSC curves for PVA (blue) and PVA/SWNT (red) dried gel films showing a pronounced T_g transition and T_m at approximately ~216 °C.

X-ray studies for both solution cast and gel films are consistent with DSC data. The diffraction patterns show sharp crystalline rings for the gel films and broader diffused rings for solution cast films (Figure C.4). For the gel-films diffraction spots are also present in the diffraction patterns suggesting the formation of large crystalline domains in the films (Figure C.5). The comparison of crystal size and crystallinity data for both solution cast and gel films are summarized in Table C.1. Diffraction profiles for PVA/SWNT gel and solution cast films also show weak peak positions consistent with those described in Chapter 4 for the SWNT templated PVA crystal growth (Figure C.6). This suggests that SWNT can also template some amount of PVA crystal growth in the bulk films. Both DSC and X-ray studies on these PVA and PVA/SWNT gel films provide some understanding of how crystal formation may take place in the PVA and PVA/SWNT gel fiber and why longer gelation of the fibers lead to an increase in mechanical properties.

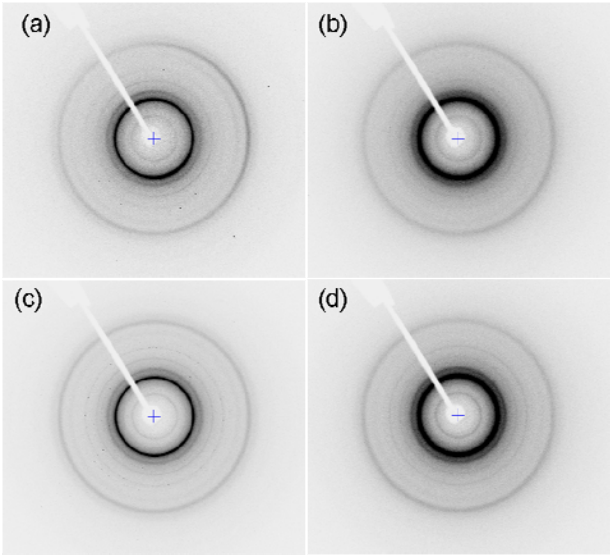

Figure C.4. Wide-angle X-ray diffraction patterns for (a) PVA gel film, (b) PVA solution cast film, (c) PVA/SWNT gel film, and (d) PVA/SWNT solution cast film.

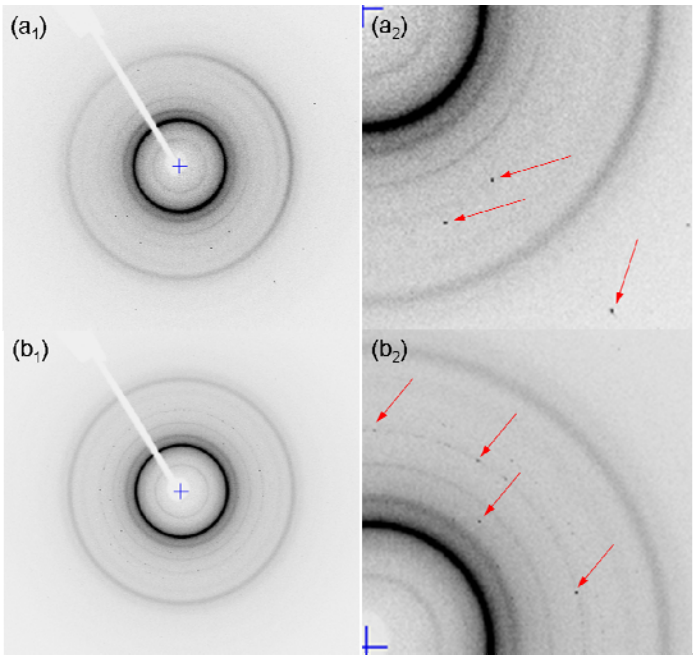

Figure C.5. Wide-angle X-ray diffraction patterns for (a_1) PVA gel film, (a_2) magnified portion of (a_1) showing diffraction spots associated with large crystal formation, (b_1) PVA/SWNT gel film, and (b_2) magnified portion of (b_1) showing diffraction spots associated with large crystal formation.

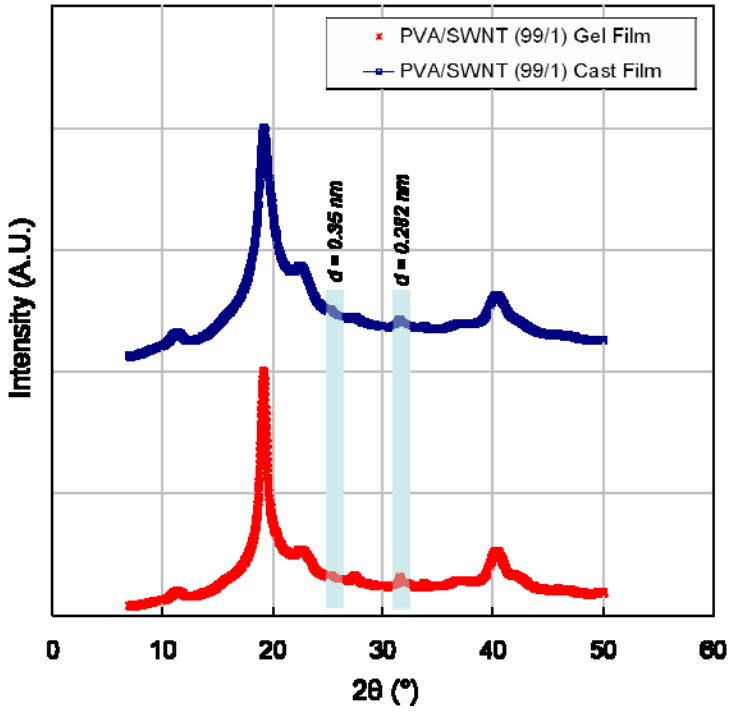

Figure C.6. Integrated 2θ scans for PVA/SWNT gel film and PVA/SWNT solution cast films showing weak diffraction peaks associated with SWNT templated crystal growth.

DSC studies on gel films show a large increase in crystallinity as compared to solution cast film. PVA gel-formed crystals exhibit a melting temperature ~10 °C higher than heat induced crystallization. Gel fibers may exhibit this same phenomenon. PVA and PVA/SWNT films show the formation of large crystalline domains even at low gelation temperatures. There is also evidence of SWNT templated crystal growth.

REFERENCES

1. Bragg, W., *X-ray and Crystal Structure*, Glaskow: University Press, (1914).

2. Staudinger, H., H. Johner, and R. Signer, *The polymeric formaldehyde, a model of cellulose.* Zeitschrift Fur Physikalische Chemie--Stochiometrie Und Verwandtschaftslehre. **126**(5/6): p. 425-448, (1927).

3. Carothers, W.H., *Polymers and polyfunctionality.* Transactions of the Faraday Society. **32**(1): p. 0039-0053, (1936).

4. Passey, R.D., L. Dmochowski, W.T. Astbury, and R. Reed, *Electron Microscope Studies Of Normal And Malignant Tissues Of High-Breast-Cancer And Low-Breast-Cancer Strains Of Mice.* Nature. **160**(4069): p. 565-565, (1947).

5. Ruska, E., *The Development of the Electron-Microscope and of Electron-Microscopy.* Reviews of Modern Physics. **59**(3): p. 627-638, (1987).

6. Till, P.H., *The Growth of Single Crystals of Linear Polyethylene.* Journal of Polymer Science. **24**(106): p. 301-306, (1957).

7. Mott, N.F., *Theory of Crystals Growth.* Nature. **165**(4191): p. 295-297, (1950).

8. Jaccodine, R., *Observations Of Spiral Growth Steps In Ethylene Polymer.* Nature. **176**(4476): p. 305-306, (1955).

9. Bassett, D.C., F.C. Frank, and A. Keller, *Evidence For Distinct Sectors In Polymer Single Crystals.* Nature. **184**(4689): p. 810-811, (1959).

10. Flory, P.J., *Principles of Polymer Chemistry*, Ithaca: Cornell University Press, (1953).

11. Geil, P.H., *Polymer Single Crystals*. Polymer Reviews, ed. H.F. Mark and E.H. Immergut. Vol. 5, New York: John Wiley & Sons. 560, (1963).

12. Sharples, A., *Introduction to Polymer Crystallization*, New York: Martin's Press, (1966).

13. Mandelkern, L., *The Crystalline State*, in *Physical Properties of Polymers* American Chemical Society: Washington D.C. p. 145-200, (1993).

14. Hoffman, J.D. and R.L. Miller, *Kinetics of Crystallization from the Melt and Chain Folding in Polyethylene Fractions Revisited: Theory and Experiment.* Polymer. **38**(13): p. 3151-3212, (1997).

15. Bassett, D.C. and A.M. Hodge, *On The Morphology Of Melt-Crystallized Polyethylene .1. Lamellar Profiles.* Proceedings of the Royal Society of London Series a-Mathematical Physical and Engineering Sciences. **377**(1768): p. 25-&, (1981).

16. Bassett, D.C., A.M. Hodge, and R.H. Olley, *Lamellar Morphologies In Melt-Crystallized Polyethylene.* Faraday Discussions. p. 218-+, (1979).

17. Bassett, D.C., R.H. Olley, and I.A.M.A. Raheil, *On Isolated Lamellae of Melt-Crystallized Polyethylene.* Polymer. **29**: p. 1539-1543, (1988).

18. Bassett, D.C. and A.S. Vaughan, *On The Lamellar Morphology Of Melt-Crystallized Isotactic Polystyrene.* Polymer. **26**(5): p. 717-725, (1985).

19. Toda, A. and A. Keller, *Growth of Polyethylene Single-Crystals From the Melt - Morphology.* Colloid and Polymer Science. **271**(4): p. 328-342, (1993).

20. Strocks, K.H., Journal of the American Chemical Society. **60**: p. 1753, (1938).

21. Dawson, I.M. and V. Vand, *Observation Of Spiral Growth-Steps In Normal-Paraffin Single Crystals In The Electron Microscope.* Nature. **167**(4247): p. 476-476, (1951).

22. Geil, P.H., *Nylon Single Crystals.* Journal of Polymer Science. **44**(144): p. 449-458, (1960).

23. Badami, D.V. and P.H. Harris, *Nylon 66 Single Crystals.* Journal of Polymer Science. **41**(138): p. 540-541, (1959).

24. Holland, V.F., S.B. Mitchell, W.L. Hunter, and P.H. Lindenmeyer, *Crystal Structure and Morphology of Polyacrylonitrile in Dilute Solution.* Journal of Polymer Science. **62**: p. 145-151, (1962).

25. Pennings, A.J., *Lamellar And Fibrillar Crystallization Of Polymers.* Makromolekulare Chemie-Macromolecular Chemistry and Physics. p. 99-142, (1979).

26. Hoffman, J.D., *Formation of Polmer Fibrils by Flow-Induced Crystallization.* Polymer. **20**(9): p. 1071-1077, (1979).

27. Matsuzaw.S, Yanagisa.H, and K. Yamaura, *Stress-Induced Crystallization Of Poly(vinyl alcohol) From Its Aqueous-Solution Under Steady-State Flow.* Kolloid-Zeitschrift and Zeitschrift Fur Polymere. **250**(1): p. 20-&, (1972).

28. Pennings, A.J. and A.M. Kiel, *Fractionation of Polymers by Crystallization from Solution, III. On the Morphology of Fibrillar Polyethylene Crystals Grown in Solution.* Kolloid-Zeitschrift und Zeitschrift fur Polymere. **205**(2): p. 160-162, (1965).

29. Pennings, A.J., Vanderma.Jm, and H.C. Booij, *Hydrodynamically Induced Crystallization Of Polymers From Solution .2. Effect Of Secondary Flow.* Kolloid-Zeitschrift and Zeitschrift Fur Polymere. **236**(2): p. 99-&, (1970).

30. Pennings, A.J., Zwijnenb.A, and R. Lageveen, *Longitudinal Growth Of Polymer Crystals From Solutions Subjected To Single Shear-Flow.* Kolloid-Zeitschrift and Zeitschrift Fur Polymere. **251**(7): p. 500-501, (1973).

31. Wikjord, A.G. and R.S. Manley, *Hydrodynamically Induced Crystallization of Isotactic Polystyrene.* Canadian Journal of Chemistry. **47**(4): p. 703-&, (1969).

32. Smith, P. and P.J. Lemstra, *Ultra-High-Strength Polyethylene Filaments By Solution Spinning-Drawing.* Journal of Materials Science. **15**(2): p. 505-514, (1980).

33. Smith, P. and P.J. Lemstra, *Tensile-Strength Of Highly Oriented Polyethylene.* Journal of Polymer Science Part B-Polymer Physics. **19**(6): p. 1007-1009, (1981).

34. Smith, P., P.J. Lemstra, B. Kalb, and A.J. Pennings, *Ultrahigh-Strength Polyethylene Filaments By Solution Spinning And Hot Drawing.* Polymer Bulletin. **1**(11): p. 733-736, (1979).

35. Pennings, A.J., Vanderma.Jm, and A.M. Kiel, *Hydrodynamically Induced Crystallization Of Polymers From Solution .3. Morphology.* Kolloid-Zeitschrift and Zeitschrift Fur Polymere. **237**(2): p. 336-&, (1970).

36. Keller, A., A. Keller, and R. Engleman, *Electron Microscope-Electron Diffraction Investigations Of The Crystalline Texture Of Polyamides.* Journal of Polymer Science. **36**(130): p. 361-387, (1959).

37. Iijima, S., *Helical Microtubules Of Graphitic Carbon.* Nature. **354**(6348): p. 56-58, (1991).

38. Iijima, S. and T. Ichihashi, *Single-Shell Carbon Nanotubes Of 1-nm Diameter.* Nature. **363**(6430): p. 603-605, (1993).

39. Futaba, D.N., K. Hata, T. Namai, T. Yamada, K. Mizuno, Y. Hayamizu, M. Yumura, and S. Iijima, *84% Catalyst activity of water-assisted growth of single walled carbon nanotube forest characterization by a statistical and macroscopic approach.* Journal of Physical Chemistry B. **110**(15): p. 8035-8038, (2006).

40. Murakami, Y., S. Chiashi, Y. Miyauchi, M.H. Hu, M. Ogura, T. Okubo, and S. Maruyama, *Growth of vertically aligned single-walled carbon nanotube films on quartz substrates and their optical anisotropy.* Chemical Physics Letters. **385**(3-4): p. 298-303, (2004).

41. Thess, A., R. Lee, P. Nikolaev, H.J. Dai, P. Petit, J. Robert, C.H. Xu, Y.H. Lee, S.G. Kim, A.G. Rinzler, D.T. Colbert, G.E. Scuseria, D. Tomanek, J.E. Fischer, and R.E. Smalley, *Crystalline ropes of metallic carbon nanotubes.* Science. **273**(5274): p. 483-487, (1996).

42. Journet, C., W.K. Maser, P. Bernier, A. Loiseau, M.L. delaChapelle, S. Lefrant, P. Deniard, R. Lee, and J.E. Fischer, *Large-scale production of single-walled carbon nanotubes by the electric-arc technique.* Nature. **388**(6644): p. 756-758, (1997).

43. Cassell, A.M., J.A. Raymakers, J. Kong, and H.J. Dai, *Large scale CVD synthesis of single-walled carbon nanotubes.* Journal of Physical Chemistry B. **103**(31): p. 6484-6492, (1999).

44. Kong, J., A.M. Cassell, and H.J. Dai, *Chemical vapor deposition of methane for single-walled carbon nanotubes.* Chemical Physics Letters. **292**(4-6): p. 567-574, (1998).

45. Kong, J., H.T. Soh, A.M. Cassell, C.F. Quate, and H.J. Dai, *Synthesis of individual single-walled carbon nanotubes on patterned silicon wafers.* Nature. **395**(6705): p. 878-881, (1998).

46. Nikolaev, P., M.J. Bronikowski, R.K. Bradley, F. Rohmund, D.T. Colbert, K.A. Smith, and R.E. Smalley, *Gas-phase catalytic growth of single-walled carbon nanotubes from carbon monoxide.* Chemical Physics Letters. **313**(1-2): p. 91-97, (1999).

47. Colomer, J.F., C. Stephan, S. Lefrant, G. Van Tendeloo, I. Willems, Z. Konya, A. Fonseca, C. Laurent, and J.B. Nagy, *Large-scale synthesis of single-wall carbon nanotubes by catalytic chemical vapor deposition (CCVD) method.* Chemical Physics Letters. **317**(1-2): p. 83-89, (2000).

48. Bronikowski, M.J., P.A. Willis, D.T. Colbert, K.A. Smith, and R.E. Smalley, *Gas-phase production of carbon single-walled nanotubes from carbon monoxide via the HiPco process: A parametric study.* Journal of Vacuum Science & Technology a-Vacuum Surfaces and Films. **19**(4): p. 1800-1805, (2001).

49. Hu, S., M. Tsuji, and F. Horii, *Phase structure of poly(vinyl alcohol) single crystals as revealed by solid stae ^{13}C N.M.R. spectroscopy.* Polymer. **35**: p. 2516-2522, (1994).

50. Nagasawa, S., M. Yudasaka, K. Hirahara, T. Ichihashi, and S. Iijima, *Effect of oxidation on single-wall carbon nanotubes.* Chemical Physics Letters. **328**(4-6): p. 374-380, (2000).

51. Chiang, I.W., B.E. Brinson, A.Y. Huang, P.A. Willis, M.J. Bronikowski, J.L. Margrave, R.E. Smalley, and R.H. Hauge, *Purification and characterization of single-wall carbon nanotubes (SWNTs) obtained from the gas-phase decomposition of CO (HiPco process).* Journal of Physical Chemistry B. **105**(35): p. 8297-8301, (2001).

52. Dillon, A.C., T. Gennett, K.M. Jones, J.L. Alleman, P.A. Parilla, and M.J. Heben, *A simple and complete purification of single-walled carbon nanotube materials.* Advanced Materials. **11**(16): p. 1354-1358, (1999).

53. Bandow, S., S. Asaka, Y. Saito, A.M. Rao, L. Grigorian, E. Richter, and P.C. Eklund, *Effect of the growth temperature on the diameter distribution and chirality of single-wall carbon nanotubes.* Physical Review Letters. **80**(17): p. 3779-3782, (1998).

54. Dresselhaus, M.S. and P.C. Eklund, *Phonons in carbon nanotubes.* Advances in Physics. **49**(6): p. 705-814, (2000).

55. O'Connell, M.J., S.M. Bachilo, C.B. Huffman, V.C. Moore, M.S. Strano, E.H. Haroz, K.L. Rialon, P.J. Boul, W.H. Noon, C. Kittrell, J.P. Ma, R.H. Hauge, R.B. Weisman, and R.E. Smalley, *Band gap fluorescence from individual single-walled carbon nanotubes.* Science. **297**(5581): p. 593-596, (2002).

56. Reich, S., C. Thomsen, and P. Ordejon, *Electronic band structure of isolated and bundled carbon nanotubes.* Physical Review B. **65**(15), (2002).

57. Wang, Z.L. and C. Hui, *Electron Micrsocopy of Nanotubes*: Klumer Academic Publishers, (2003).

58. Colomer, J.F., L. Henrard, P. Launois, G. Van Tendeloo, A.A. Lucas, and P. Lambin, *Interpretation of electron diffraction from carbon nanotube bundles presenting precise helicity.* Physical Review B. **70**(7), (2004).

59. Koziol, K., M. Shaffer, and A. Windle, *Three-dimensional internal order in multiwalled carbon nanotubes grown by chemical vapor deposition.* Advanced Materials. **17**(6): p. 760-+, (2005).

60. Williams, K.A., P.T.M. Veenhuizen, B.G. de la Torre, R. Eritja, and C. Dekker, *Nanotechnology - Carbon nanotubes with DNA recognition.* Nature. **420**(6917): p. 761-761, (2002).

61. Baker, S.E., W. Cai, T.L. Lasseter, K.P. Weidkamp, and R.J. Hamers, *Covalently bonded adducts of deoxyribonucleic acid (DNA) oligonucleotides with single-wall carbon nanotubes: Synthesis and hybridization.* Nano Letters. **2**(12): p. 1413-1417, (2002).

62. Gao, G.H., T. Cagin, and W.A. Goddard, *Energetics, structure, mechanical and vibrational properties of single-walled carbon nanotubes.* Nanotechnology. **9**(3): p. 184-191, (1998).

63. Lu, J.P., *Elastic properties of carbon nanotubes and nanoropes.* Physical Review Letters. **79**(7): p. 1297-1300, (1997).

64. Popov, V.N., V.E. Van Doren, and M. Balkanski, *Elastic properties of crystals of single-walled carbon nanotubes.* Solid State Communications. **114**(7): p. 395-399, (2000).

65. Liu, T. and S. Kumar, *Effect of Orientation on the Modulus of SWNT Films and Fibers.* Nano Letters. **3**(5): p. 647-650, (2003).

66. Salvetat, J.P., G.A.D. Briggs, J.M. Bonard, R.R. Bacsa, A.J. Kulik, T. Stockli, N.A. Burnham, and L. Forro, *Elastic and shear moduli of single-walled carbon nanotube ropes.* Physical Review Letters. **82**(5): p. 944-947, (1999).

67. Deheer, W.A., W.S. Bacsa, A. Chatelain, T. Gerfin, R. Humphreybaker, L. Forro, and D. Ugarte, *Aligned Carbon Nanotube Films - Production And Optical And Electronic-Properties.* Science. **268**(5212): p. 845-847, (1995).

68. [cited; Available from: http://www.cnanotech.com/,

69. Sreekumar, T.V., T. Liu, B.G. Min, H. Guo, S. Kumar, R.H. Hauge, and R.E. Smalley, *Polyacrylonitrile Single-Walled Carbon Nanotube Composite Fibers.* Advanced Materials. **16**(1): p. 58-61, (2004).

70. Kumar, S., T.D. Dang, F.E. Arnold, A.R. Bhattacharyya, B.G. Min, X. Zhang, R.A. Vaia, C. Park, W.W. Adams, R.H. Hauge, R.E. Smalley, S. Ramesh, and P.A. Willis, *Synthesis, Structure, and Properties of PBO/SWNT Composites.* Macromolecules. **35**(24): p. 9039-9043, (2003).

71. Chae, H.G., M.L. Minus, and S. Kumar, *Oriented and exfoliated single wall carbon nanotubes in polyacrylonitrile.* Polymer. **47**(10): p. 3494-3504, (2006).

72. Chen, J., M.A. Hamon, H. Hu, Y.S. Chen, A.M. Rao, P.C. Eklund, and R.C. Haddon, *Solution properties of single-walled carbon nanotubes.* Science. **282**(5386): p. 95-98, (1998).

73. Strano, M.S., C.A. Dyke, M.L. Usrey, P.W. Barone, M.J. Allen, H.W. Shan, C. Kittrell, R.H. Hauge, J.M. Tour, and R.E. Smalley, *Electronic structure control of single-walled carbon nanotube functionalization.* Science. **301**(5639): p. 1519-1522, (2003).

74. Goux-Capes, L., A. Filoramo, D. Cote, J.P. Bourgoin, and J.N. Patillon, *Coupling carbon nanotubes through DNA linker using a biological recognition complex.* Physica Status Solidi a-Applications and Materials Science. **203**(6): p. 1132-1136, (2006).

75. Paiva, M.C., B. Zhou, K.A.S. Fernando, Y. Lin, J.M. Kennedy, and Y.P. Sun, *Mechanical and Morphological Characterization of Polymer-Carbon Nanocomposites from Functionalized Carbon Nanotubes.* Carbon. **42**: p. 2849-2854, (2004).

76. Lin, Y., B. Zhou, K.A.S. Fernando, P. Liu, L.F. Allard, and Y.P. Sun, *Polymeric carbon nanocomposites from carbon nanotubes functionalized with matrix polymer.* Macromolecules. **36**(19): p. 7199-7204, (2003).

77. Wang, H., W. Zhou, D.L. Ho, K.I. Winey, J.E. Fischer, C.J. Glinka, and E.K. Hobbie, *Dispersing single-walled carbon nanotubes with surfactants: A small angle neutron scattering study.* Nano Letters. **4**(9): p. 1789-1793, (2004).

78. Islam, M.F., E. Rojas, D.M. Bergey, A.T. Johnson, and A.G. Yodh, *High weight fraction surfactant solubilization of single-wall carbon nanotubes in water.* Nano Letters. **3**(2): p. 269-273, (2003).

79. Moore, V.C., M.S. Strano, E.H. Haroz, R.H. Hauge, R.E. Smalley, J. Schmidt, and Y. Talmon, *Individually suspended single-walled carbon nanotubes in various surfactants.* Nano Letters. **3**(10): p. 1379-1382, (2003).

80. Vigolo, B., A. Penicaud, C. Coulon, C. Sauder, R. Pailler, C. Journet, P. Bernier, and P. Poulin, *Macroscopic fibers and ribbons of oriented carbon nanotubes.* Science. **290**(5495): p. 1331-1334, (2000).

81. Zhang, X., T. Liu, T.V. Sreekumar, S. Kumar, V.C. Moore, R.H. Hauge, and R.E. Smalley, *Poly(vinyl alcohol)/SWNT Composite Film.* Nano Letters. **3**(9): p. 1285-1288, (2003).

82. Bhattacharyya, S., J.P. Salvetat, and M.L. Saboungi, *Reinforcement of semicrystalline polymers with collagen-modified single walled carbon nanotubes.* Applied Physics Letters. **88**(23), (2006).

83. Richard, C., F. Balavoine, P. Schultz, T.W. Ebbesen, and C. Mioskowski, *Supramolecular self-assembly of lipid derivatives on carbon nanotubes.* Science. **300**(5620): p. 775-778, (2003).

84. Fukushima, T., A. Kosaka, Y. Ishimura, T. Yamamoto, T. Takigawa, N. Ishii, and T. Aida, *Molecular Ordering of Organic Molten Salts Triggering by Single-Walled Carbon Nanotubes* Science. **300**(5628): p. 2072-2074, (2003).

85. Liu, L.Q., A.H. Barber, S. Nuriel, and H.D. Wagner, *Mechanical properties of functionalized single-walled carbon-nanotube/poly(vinyl alcohol) nanocomposites.* Advanced Functional Materials. **15**(6): p. 975-980, (2005).

86. Rozhin, A.G., Y. Sakaibara, H. Kataura, S. Matsuzaki, K. Ishida, Y. Achiba, and M. Tokumoto, *Anisotropic Saturable Adsorption of Single-Wall Carbon nanotubes Aligned in Polyvinyl Alcohol.* Chemical Physics Letters. **405**: p. 288-293, (2005).

87. Ryan, K.P., M. Cadek, A. Drury, M. Ruether, W.J. Blau, and J.N. Coleman, *Carbon nanotube nucleated polymer crystallization.* Fullerenes Nanotubes and Carbon Nanostructures. **13**: p. 431-434, (2005).

88. Zhang, X., T. Liu, T.V. Sreekumar, S. Kumar, X. Hu, and K. Smith, *Gel Spinning of PVA/SWNT Composite Fiber.* Polymer. **45**: p. 8801-8807, (2004).

89. Dalton, A.B., S. Collins, E. Munoz, J.M. Razal, V.H. Ebron, J.P. Ferraris, J.N. Coleman, B.G. Kim, and R.H. Baughman, *Super-Tough Carbon-Nanotube Fibres.* Nature. **423**(6941): p. 703, (2003).

90. Miaudet, P., S. Badaire, M. Maugey, A. Derre, V. Pichot, P. Launois, P. Poulin, and C. Zakri, *Hot-drawing of single and multiwall carbon nanotube fibers for high toughness and alignment.* Nano Letters. **5**(11): p. 2212-2215, (2005).

91. Probst, O., E.M. Moore, D.E. Resasco, and B.P. Grady, *Nucleation of Polyvinyl Alcohol Crystallization by Single-Walled Carbon Nanotubes.* Polymer. **45**: p. 4437-4443, (2004).

92. Coleman, J.N., W.J. Blau, A.B. Dalton, E. Munoz, S. Collins, B.G. Kim, J. Razal, M. Selvidge, G. Vieiro, and R.H. Baughman, *Improving the Mechanical Properties of Single-Walled Carbon Nanotube Sheets by Intercalation of Polymer Adhesives.* Applied Physics Letters. **82**(11): p. 1682-1684, (2003).

93. Neimark, A.V., S. Ruetsch, K.G. Kornev, and P.I. Ravikovitch, *Hierarchical pore structure and wetting properties of single-wall carbon nanotube fibers.* Nano Letters. **3**(3): p. 419-423, (2003).

94. Tzavalas, S., V. Drakonakis, D.E. Mouzakis, D. Fischer, and V.G. Gregoriou, *Effect of carboxy-functionalized multiwall nanotubes (MWNT-COOH) on the crystallization and chain conformations of poly(ethylene terephthalate) PET in PET-MWNT nanocomposites.* Macromolecules. **39**(26): p. 9150-9156, (2006).

95. Wu, T.M. and E.C. Chen, *Crystallization behavior of poly(epsilon-caprolactone)/multiwalled carbon nanotube composites.* Journal of Polymer Science Part B-Polymer Physics. **44**(3): p. 598-606, (2006).

96. Ryan, K.P., S.M. Lipson, A. Drury, M. Cadek, M. Ruether, S.M. O'Flaherty, V. Barron, B. McCarthy, H.J. Byrne, W.J. Blau, and J.N. Coleman, *Carbon-nanotube nucleated crystallinity in a conjugated polymer based composite.* Chemical Physics Letters. **391**(4-6): p. 329-333, (2004).

97. Zeng, H.L., C. Gao, Y.P. Wang, P.C.P. Watts, H. Kong, X.W. Cui, and D.Y. Yan, *In situ polymerization approach to multiwalled carbon nanotubes-reinforced nylon 1010 composites: Mechanical properties and crystallization behavior.* Polymer. **47**(1): p. 113-122, (2006).

98. Dondero, W.E. and R.E. Gorga, *Morphological and mechanical properties of carbon nanotube/polymer composites via melt compounding.* Journal of Polymer Science Part B-Polymer Physics. **44**(5): p. 864-878, (2006).

99. Bhattacharyya, A.R., T.V. Sreekumar, T. Liu, S. Kumar, L.M. Ericson, R.H. Hauge, and R.E. Smalley, *Crystallization and Orientation Studies in Polypropylene/Single Wall Carbon Nanotube Composite.* Polymer. **44**: p. 2373-2377, (2003).

100. Li, C.Y., L. Li, W. Cai, S.L. Kodjie, and K.K. Tenneti, *Nanohybrid Shish-Kebabs: Periodically Functionalized Carbon Nanotubes.* Advanced Materials. **17**: p. 1198-1202, (2005).

101. Li, L.Y., Y. Yang, G.L. Yang, X.M. Chen, B.S. Hsiao, B. Chu, J.E. Spanier, and C.Y. Li, *Patterning polyethylene oligomers on carbon nanotubes using physical vapor deposition.* Nano Letters. **6**(5): p. 1007-1012, (2006).

102. Mitchell, C.A. and R. Krishnamoorti, *Non-isothermal crystallization of in situ polymerized poly(epsilon-caprolactone) functionalized-SWNT nanocomposites.* Polymer. **46**(20): p. 8796-8804, (2005).

103. Ryan, K.P., S.M. Lipson, A. Drury, M. Cadek, M. Ruether, S.M. O'Flaherty, V. Barron, B. McCarthy, H.J. Byrne, W.J. Blau, and J.N. Coleman, *Carbon-Nanotube Nucleated Crystallinity in a Conjugated Polymer Based Composite.* Chemical Physics Letters. **391**: p. 329-333, (2004).

104. Yudin, V.E., V.M. Svetlichnyi, A.N. Shumakov, D.G. Letenko, A.Y. Feldman, and G. Marom, *The nucleating effect of carbon nanotubes on crystallinity in R-BAPB-type thermoplastic polyimide.* Macromolecular Rapid Communications. **26**(11): p. 885-888, (2005).

105. Hsu, W.K., W.Z. Li, Y.Q. Zhu, N. Grobert, M. Terrones, H. Terrones, N. Yao, J.P. Zhang, S. Firth, R.J.H. Clark, A.K. Cheetham, J.P. Hare, H.W. Kroto, and D.R.M. Walton, *KCl crystallization within the space between carbon nanotube walls.* Chemical Physics Letters. **317**(1-2): p. 77-82, (2000).

106. Leelapornpisit, W., M.-T. Ton-That, F. Perrin-Sarazin, K.C. Cole, J. Denault, and B. Simard, *Effect of Carbon Nanotubes on the Crystallization and Properties of Polypropylene.* Journal of Polymer Science: Part B: Polymer Physics. **43**: p. 2445-2453, (2005).

107. Minus, M.L. and S. Kumar, *Shear induced poly(vinyl alcohol)/single wall carbon nanotube composite fiber formation in solution.* Abstracts of Papers of the American Chemical Society. **229**: p. U1116-U1116, (2005).

108. Minus, M.L. and S. Kumar, *Single wall carbon nanotube templated crystallization and orientation of poly(vinyl alcohol).* Abstracts of Papers of the American Chemical Society. **231**, (2006).

109. Cadek, M., J.N. Coleman, V. Barron, K. Hedicke, and W.J. Blau, *Morphological and mechanical properties of carbon-nanotube-reinforced semicrystalline and amorphous polymer composites.* Applied Physics Letters. **81**(27): p. 5123-5125, (2002).

110. Ryan, K.P., M. Cadek, V. Nicolosi, S. Walker, M. Ruether, A. Fonseca, J.B. Nagy, W.J. Blau, and J.N. Coleman, *Multiwalled Carbon Nanotube Nucleated Crystallization and Reinforcement in Poly(vinyl alcohol) Composites.* Synthetic Metals. **156**: p. 332-335, (2006).

111. Kumar, S., H. Doshi, M. Srinivasarao, J.O. Park, and D.A. Schiraldi, *Fibers from Polypropylene/Nano Carbon Fiber Composites.* Polymer. **43**: p. 1701-1703, (2002).

112. Haggenmueller, R., J.E. Fischer, and K.I. Winey, *Single Wall Carbon Nanotube/Polyethylene Nanocomposites: Nucleating and Templating Polyethylene Crystallites.* Macromolecules. **39**(8): p. 2964-2971, (2006).

113. Zhang, Q., D.R. Lippits, and S. Rasogi, *Dispersion and Rheological Aspects od SWNTs in Ultrahigh Molecular Weight Polyethylene.* Macromolecules. **39**(2): p. 658-666, (2006).

114. Coleman, J.N., M. Cadek, R. Blake, V. Nicolosi, K.P. Ryan, C. Belton, A. Fonseca, J.B. Nagy, Y.K. Gun'ko, and W.J. Blau, *High-performance nanotube-reinforced plastics: Understanding the mechanism of strength increase.* Advanced Functional Materials. **14**(8): p. 791-798, (2004).

115. Zhou, W., P.A. Heiney, H. Fan, R.E. Smalley, and J.E. Fischer, *Single-Walled Carbon Nanotube-Templated Crystallization of H_2SO_4: Direct Evidence of Protonation.* Journal of the American Chemical Society. **127**(6): p. 1640-1641, (2005).

116. Balavoine, F., P. Schultz, C. Richard, V. Mallouh, T.W. Ebbesen, and C. Mioskowski, *Helical Crystallization of Protiens on Carbon Nanotubes: A First Step Towards the Development of New Biosensors.* Andewandte Chemie International Edition. **38**(13/14): p. 1912-1915, (1999).

117. Garcia-Gutierrez, M.C., A. Nogales, D.R. Rueda, C. Domingo, J.V. Garcia-Ramos, G. Broza, Z. Roslaniec, K. Schulte, R.J. Davies, and T.A. Ezquerra, *Templating of crystallization and shear-induced self-assembly of single-wall carbon nanotubes in a polymer-nanocomposite.* Polymer. **47**(1): p. 341-345, (2006).

118. Anand, K.A., U.S. Agarwal, and R. Joseph, *Carbon nanotubes induced crystallization of poly(ethylene terephthalate).* Polymer. **47**(11): p. 3976-3980, (2006).

119. Chawla, K.K., *Composite Materials Science and Engineering*, New York: Springer-Verlag, (1998).

120. Schoene, C. and E. Scala, *Multiple Necking Phenomena In Metal Composites.* Metallurgical Transactions. **1**(12): p. 3466-&, (1970).

121. Vennett, R.M., S.M. Wolf, and A.P. Levitt, *Multiple Necking of Tungsten Fibers in a Brass-Tungsten Composite.* Metallurgical Transactions. **1**(6): p. 1569, (1970).

122. Drzal, L.T., M.J. Rich, and P.F. Lloyd, *Adhesion Of Graphite Fibers To Epoxy Matrices .1. The Role Of Fiber Surface-Treatment.* Journal of Adhesion. **16**(1): p. 1-30, (1983).

123. Biro, D.A., G. Pleizier, and Y. Deslandes, *Application Of The Microbond Technique .3. Effects Of Plasma Treatment On The Ultra-High Modulus Polyehtylene Fiber Epoxy Interface.* Journal of Materials Science Letters. **11**(10): p. 698-701, (1992).

124. Brown, J.R., P.J.C. Chappell, and Z. Mathys, *Plasma Surface Modification Of Advanced Organic Fibers .2. Effects On The Mechanical, Fracture And Ballistic Properties Of Extended-Chain Polyethylene Epoxy Composites.* Journal of Materials Science. **27**(12): p. 3167-3172, (1992).

125. Ehrburger, P. and J.B. Donnet, *Interface in Composite-Materials.* Philosophical Transactions of the Royal Society of London Series A-Mathematical Physical and Engineering Sciences. **294**(1411): p. 495, (1980).

126. Drzal, L.T., M.J. Rich, M.F. Koenig, and P.F. Lloyd, *Adhesion of Graphite Fibers to Epoxy Matrices .2. The Effect of Fiber Finish.* Journal of Adhesion. **16**(2): p. 133-152, (1983).

127. Donnet, J.B. and R.C. Bansal, *Carbon Fibers*, New York: Marcel Dekker, (1984).

128. Clark, K.K., N.J. Wadworth, and W. Watt, *Carbon Fibres, Their Place in Modern Technology*, London: The Plastics Institute, (1974).

129. Jangehud, I., A.M. Serrano, R.K. Eby, and M.A. Meador. in *Proceedings of the 21st Biennial Conference on Carbon*. Buffalo, New York, (1993).

130. Sharma, P., W. Miao, A. Giri, and S. Raghunathan, *Nanomaterials: Manufacturing, Processing, and Applications*, in *Dekker Encyclopedia of Nanoscience and Nanotechnology* Marcel Dekker: New York, (2004).

131. Liu, L.M., Z.N. Qi, and X.G. Zhu, *Studies on nylon 6 clay nanocomposites by melt-intercalation process.* Journal of Applied Polymer Science. **71**(7): p. 1133-1138, (1999).

132. Jiao, S., M.L. Jenkins, and R.W. Davidge, *Interfacial fracture energy-mechanical behaviour relationship in Al2O3/SiC and Al2O3/TiN nanocomposites.* Acta Materialia. **45**(1): p. 149-156, (1997).

133. Luna-Xavier, J.L., A. Guyot, and E. Bourgeat-Lami, *Synthesis and characterization of silica/poly (methyl methacrylate) nanocomposite latex particles through emulsion polymerization using a cationic azo initiator.* Journal of Colloid and Interface Science. **250**(1): p. 82-92, (2002).

134. Wypych, F. and K.G. Satyanarayana, *Functionalization of single layers and nanofibers: a new strategy to produce polymer nanocomposites with optimized properties.* Journal of Colloid and Interface Science. **285**(2): p. 532-543, (2005).

135. Barber, A.H., S.R. Cohen, S. Kenig, and H.D. Wagner, *Interfacial fracture energy measurements for multi-walled carbon nanotubes pulled from a polymer matrix.* Composites Science and Technology. **64**(15): p. 2283-2289, (2004).

136. Namilae, S. and N. Chandra, *Multiscale model to study the effect of interfaces in carbon nanotube-based composites.* Journal of Engineering Materials and Technology-Transactions of the Asme. **127**(2): p. 222-232, (2005).

137. Ding, W., A. Eitan, F.T. Fisher, X. Chen, D.A. Dikin, R. Andrews, L.C. Brinson, L.S. Schadler, and R.S. Ruoff, *Direct observation of polymer sheathing in carbon nanotube-polycarbonate composites.* Nano Letters. **3**(11): p. 1593-1597, (2003).

138. Sandler, J., G. Broza, M. Nolte, K. Schulte, Y.M. Lam, and M.S.P. Shaffer, *Crystallization of Carbon Nanotube and Nanofiber Polypropylene Composites.* Journal of Macromolecular Science Part B. **42**(3&4): p. 479-488, (2003).

139. Eitan, A., K. Jiang, D. Dukes, R. Andrews, and L.S. Schadler, *Surface Modification of Mutiwalled Carbon Nanotubes: Toward the Tailoring of the Interface in Polymer Composites.* Chemisry of Materials. **15**: p. 3198-3201, (2003).

140. Cooper, C.A., S.R. Cohen, A.H. Barber, and H.D. Wagner, *Detachment of nanotubes from a polymer matrix.* Applied Physics Letters. **81**(20): p. 3873-3875, (2002).

141. Qian, D., E.C. Dickey, R. Andrews, and T. Rantell, *Load transfer and deformation mechanisms in carbon nanotube-polystyrene composites.* Applied Physics Letters. **76**(20): p. 2868-2870, (2000).

142. Assender, H.E. and A.H. Windle, *Crystallinity in Poly(vinyl alcohol). A. An X-ray Diffraction Study of Atatic PVOH.* Polymer. **39**(18): p. 4295-4305, (1998).

143. Cha, W.I., S.H. Hyon, and Y. Ikada, *Gel Spinning of Poly(vinyl alcohol) from Dimethyl Sulfoxide/Water Mixture.* Journal of Polymer Science Part B-Polymer Physics. **32**(2): p. 297-304, (1994).

144. Cullity, B.D. and S.R. Stock, *Elements of X-ray Diffraction*. 3rd Edition ed, New Jersey: Prentice Hall, (2001).

145. Wilchinsky, Z.W., *Measurement of Orientation in Polypropylene Film.* Journal of Applied Physics. **31**(11): p. 1969-1972, (1960).

146. Bunn, C.W., *Crystal Strucutre of Poly(vinyl Alcohol).* Nature. **161**(4102): p. 929-930, (1948).

147. Klug, H.P. and L.E. Alexander, *X-ray Diffraction Proedures For Polycrystalline and Amorphous Materials*, New York: John Wiley & Sons Inc. 716, (1954).

148. Wang, Z.L. and Z.C. Kang, *Functional and Smart Materials Structure Evolution and Structure Analysis*, New York: Plenum Press, (1998).

149. Valentini, L., J. Biagiotti, M.A. Lopez-Manchado, S. Santucci, and J.M. Kenny, *Effects of carbon nanotubes on the crystallization behavior of polypropylene.* Polymer Engineering and Science. **44**(2): p. 303-311, (2004).

150. Sakurada, I., T. Ito, and K. Nakamae, *Elastic Moduli of the Crystal Lattices of Polymers.* Journal of Polymer Science Part C. **15**: p. 75-91, (1966).

151. Sakurada, I., *Polyvinyl Alcohol Fibers*, New York: Marcel Dekker Inc., (1985).

152. Yamamoto, T., O. Sangen, and K. Mikiharu, *Poly(vinyl alcohol) (High Molecular Weight)*, in *Polymeric Materials Encyclopedia*, J.C. Salamone, Editor, CRC Press: Boca Raton. p. 6991-6998, (1996).

153. Kenny, J.F. and V.F. Holland, *Crystallization and Dissolution Temperatures of Poly(vinyl alcohol) Crystal Lamellae.* Journal of Polymer Science Part A-1. **4**: p. 699-706, (1966).

154. Tsuboi, K. and T. Mochizuki, *Single Crystals of Polyvinyl Alcohol.* Polymer Letters. **1**: p. 531-534, (1963).

155. Harris, H.E., J.F. Kenny, G.W. Willcockson, R. Chiang, and H.N. Friedlander, *Structure-Property Relationships of Poly(vinyl Alcohol). II. The Influence of Molecular Regularity on the Crystallization-Dissolution Temperature Relationships of Poly(vinyl Alcohol).* Journal of Polymer Science: Part A-1. **4**: p. 665-677, (1966).

156. Tsuboi, K., T. Mochizuki, and M. Matsumoto, *Polyvinylalcohol Single Crystals.* Journal of Electron Microscopy. **12**(2): p. 123-124, (1963).

157. Peppas, N.A. and P.J. Hansen, *Crystallization Kinetics of Poly(vinyl-alcohol).* Journal of Applied Polymer Science. **27**(12): p. 4787-4797, (1982).

158. Laudise, R.A., *The Growth Of Single Crystals*. Solid State Physical Electronics Series, ed. N. Holonyak, Englewood Cliffs: Prentice-Hall, Inc., (1970).

159. Minus, M.L., H.G. Chae, and S. Kumar, *Single Wall Carbon Nanotube Templated Oriented Crystallization of Poly(vinly alcohol).* Polymer. **47**(11): p. 3705-3710, (2006).

160. Reneker, D.H. and P.H. Geil, *Morphology of Polymer Single Crystals.* Journal of Applied Physics. **31**(11): p. 1916-1925, (1960).

161. Pinsker, Z.G., *Electron Diffraction*, London: Butterworths Scientific Publications. 441, (1953).

162. Keller, A., *A Note On Single Crystals In Polymers - Evidence For A Folded Chain Configuration.* Philosophical Magazine. **2**(21): p. 1171-&, (1957).

163. Agar, A.W., F.C. Frank, and A. Keller, *Electron Microscope Oberservations of Moire Patterns in Single Crystals of Polyethylene*, in *Growth and Prefection of Crystals - Proceedings of a International Conference on Crystal Growth*, R.H. Doremus, B.W. Roberts, and D. Turnbull, Editors Chapman & Hall Limited: New York. p. 568-578, (1958).

164. Agar, A.W., F.C. Frank, and A. Keller, *Crystallinity Effects In The Electron Microscopy Of Polyethylene.* Philosophical Magazine. **4**(37): p. 32-55, (1959).

165. Tsuji, M., S.K. Roy, and R.S. Manley, *Direct Lattice Imaging In Single-Crystals Of Isotactic Polystyrene.* Polymer. **25**(11): p. 1573-1576, (1984).

166. Revol, J.F. and R. Manley, *Lattice Imaging in Polyethylene Single Crystals.* Journal of Materials Science Letters. **5**: p. 249-251, (1986).

167. Shimamura, K., N. Michiaki, T. Ikeda, T. Uchida, and H. Manabu, *Fractionation and Crystal Morphology of Rigid Polymer, Poly(p-Phenylene Benzobisthiazole).* Journal of Macromolecular Science Part B. **43**(5): p. 1015-1024, (2004).

168. Shimamura, K., J.R. Minter, and E.L. Thomas, *Lattice Imaging of High Modulus Poly(p-Phenylene Benzobisthiazole) Fibres.* Journal of Materials Science Letters. **2**: p. 54-58, (1983).

169. Tsuji, M., *Electron Microscopy*, in *Comprehensive Polymer Science: The Synthesis, Characterization, Reactions & Applications of Polymers*, G. Allen and J.C. Bevington, Editors Pergamon Press: New York, (1989).

170. Tsuji, M., S. Isoda, M. Ohara, A. Kawaguchi, and K. Katayama, *Direct Imaging of Molecular Chains in a Poly(p-Xylylene) Single Crystal.* Polymer. **23**(11): p. 1568-1574, (1982).

171. Adams, W.W., S. Kumar, D.C. Martin, and K. Shimamura, *Lattice Imaging of Poly(p-Phenylene Benzobisoxazole) Fibre.* Polymer Communications. **30**: p. 285-287, (1989).

172. Schlesinger, W. and H.M. Leeper, *Gutta .1. Single Crystals Of Alpha-Gutta.* Journal of Polymer Science. **11**(3): p. 203-213, (1953).

173. Khoury, F. and F.J. Padden, *On The Growth Habits Of Twinned Crystals Of Polyehtylene.* Journal of Polymer Science. **47**(0149): p. 455-468, (1960).

174. Burbank, R.D., *Molecular Structure in Crystal Aggregates of Linear Polyethylene.* Bell Systems Technical Journal. **39**: p. 1627, (1960).

175. Chatterjee, A.M., F.P. Price, and S. Newman, *Heterogenoeus Nucleation Of Crystallization Of High Polymers From Melt .1. Substrate-Induced Morphologies.* Journal of Polymer Science Part B-Polymer Physics. **13**(12): p. 2369-2383, (1975).

176. Chatterjee, A.M., F.P. Price, and S. Newman, *Heterogenoeus Nucleation Of Crystallization Of High Polymers From Melt .2. Aspects Of Transcrystallinity And Nucleation Density.* Journal of Polymer Science Part B-Polymer Physics. **13**(12): p. 2385-2390, (1975).

177. Chatterjee, A.M., F.P. Price, and S. Newman, *Heterogenoeus Nucleation Of Crystallization Of High Polymers From Melt .3. Nucleation Kinetics And Interfacial Energies.* Journal of Polymer Science Part B-Polymer Physics. **13**(12): p. 2391-2400, (1975).

178. Hobbs, S.Y., *Row Nucleation Of Isotactic Polypropylene On Graphite Fibers.* Nature-Physical Science. **234**(44): p. 12-&, (1971).

179. Wang, C. and C.R. Liu, *Transcrystallization of polypropylene on carbon fibres.* Polymer. **38**(18): p. 4715-4718, (1997).

180. Sano, M., M.O. Sandberg, and S. Yoshimura, *Polymerization-Induced Epitaxy of Polypeptides on Graphite Studied by Scanning Tunneling Microscopy.* Langmuir. **10**(10): p. 3815-3819, (1994).

181. Sano, M., D.Y. Sasaki, and T. Kunitake, *Structural Study of Polyehters on Graphite by Scanning Tunneling Microscopy. Polymerization-Induced Epitaxy.* Macromolecules. **25**(25): p. 6961-6969, (1992).

182. Sano, M., D.Y. Sasaki, and T. Kunitake, *Polymerization-Induced Epitaxy: Scanning Tunneling Microscopy of a Hydrogen-Bonded Sheet of Polyamide on Graphite.* Science. **258**: p. 441-443, (1992).

183. Wittman, J.C. and B. Lotz, *Epitaxial Crystallization of Polymers on Organic and Polymeric Substrates.* Progess in Polymer Science. **15**: p. 909-948, (1990).

184. Hoffman, J.D., *Regime III Crystallization in Melt-Crystallized Polymers: The Variable Cluster Model of Chain Folding.* Polymer. **24**: p. 3-26, (1983).

185. Mooney, R.C.L., *An x-ray study of the structure of polyvinyl alcohol.* Journal of the American Chemical Society. **63**: p. 2828-2832, (1941).

186. Sakurada, I., *FASERN AUS POLYVINYLALKOHOL.* Kolloid-Zeitschrift and Zeitschrift Fur Polymere. **139**(3): p. 155-163, (1954).

187. Sakurada, I., K. Fuchino, and N. Okada, Bulletin - Institute for Chemical Research - Kyoto University. **23**: p. 78, (1950).

188. Mochizuki, T., Journal of the Chemical Society Japan. **81**: p. 6, (1960).

189. Colvin, B.G., *Crystal-Structure Of Polyvinyl-Alcohol.* Nature. **248**(5451): p. 756-759, (1974).

190. Kunugi, T., *Poly(vinyl alcohol) Fibers - High Modulus; by Vibrating Zone-Drawing*, in *Polymeric Materials Encyclopedia*, J.C. Salamone, Editor, CRC Press: Boca Raton. p. 7010-7013, (1996).

191. Yamura, K., *Poly(vinyl alcohol) - High Strength and High Modulus*, in *Polymeric Materials Encyclopedia*, J.C. Salamone, Editor, CRC Press: Boca Raton. p. 6998-7002, (1996).

192. Hull, D. and T.W. Clyne, *An Introducution to Composite Materials*. 2nd ed. Cambridge Solid State Science Series, New York: Cambridge University Press, (1996).

193. Wang, Z., P. Ciselli, and T. Peijs, *The extraordinary reinforcing efficiency of single-walled carbon nanotubes in oriented poly(vinyl alcohol) tapes.* Nanotechnology. **18**(45), (2007).

194. Kudin, K.N., G.E. Scuseria, and B.I. Yakobson, *C2F, BN, and C nanoshell elasticity from ab initio computations.* Physical Review B. **64**(23), (2001).

195. Yakobson, B.I., C.J. Brabec, and J. Bernholc, *Nanomechanics of carbon tubes: Instabilities beyond linear response.* Physical Review Letters. **76**(14): p. 2511-2514, (1996).

196. Zhou, X., H. Chen, J.J. Zhou, and Z.C. Ou-Yang, *The structure relaxation of carbon nanotube.* Physica B. **304**(1-4): p. 86-90, (2001).

197. Tu, Z.C. and Z. Ou-Yang, *Single-walled and multiwalled carbon nanotubes viewed as elastic tubes with the effective Young's moduli dependent on layer number.* Physical Review B. **65**(23), (2002).

198. Treacy, M.M.J., T.W. Ebbesen, and J.M. Gibson, *Exceptionally high Young's modulus observed for individual carbon nanotubes.* Nature. **381**(6584): p. 678-680, (1996).

199. Wong, E.W., P.E. Sheehan, and C.M. Lieber, *Nanobeam mechanics: Elasticity, strength, and toughness of nanorods and nanotubes.* Science. **277**(5334): p. 1971-1975, (1997).

200. Yamaura, K., T. Katoh, K. Koezuka, M. Iwaseya, and L. Dai, *Spinning of the Solutions of Poly(vinyl alcohol)/NaCl/H_2O Systems and Their Fiber Properties.* Journal of Materials Science. **39**: p. 1609-1614, (2004).

201. Suzuki, M., T. Tanigami, S. Matsuzawa, and K. Yamaura, *Influence of Molecular Weight and Syndiotacticity on the Structure of High-Performance Poly(vinyl alcohol) Fibers Prepared by Gel Spinning.* Journal of Applied Polymer Science. **86**: p. 1970-1977, (2002).

202. Hyon, S.H., W.I. Cha, and I. Yoshito, *Poly(vinyl alcohol) Fiber*, in *Polymeric Materials Encyclopedia*, J.C. Salamone, Editor, CRC Press: Boca Raton. p. 7003-7010, (1996).

203. Rasmussen, D.H. and A.P. MacKenzie, *Phase Diagram for the System Water-Dimethylsulphoxide.* Nature. **220**: p. 1315-1317, (1968).

204. Yamaura, K. and R. Kumakura, *Gel Spinning of Partially Saponificated Poly(vinly alcohol).* Journal of Polymer Science. **77**: p. 2872-2876, (2000).

205. Hoogsteen, W., R.J. van der Hooft, A.R. Postema, G. ten Brinke, and A.J. Pennings, *Gel Spun Polyethylene Fibres.* Journal of Materials Science. **23**(5): p. 3459-3466, (1988).

206. Roukema, M., *High-Speed Spinning of Ultra-High Molecular Weight Polyethylene Fibres*, in *Mathematics and Natural Sciences*, University of Groningen: Nederlands. p. 206, (1991).

207. Smook, J. and A.J. Pennings, *Elastic Flow Instabilties and Shish-Kebab Formation During Gel-Spinning of Ultra-High Molecular Weight Polyethylene.* Journal of Materials Science. **19**: p. 31-43, (1984).

208. Liu, T. and S. Kumar, *Quantitative Characterization of SWNT Orientation by Polarized Raman Spectroscopy.* Chemical Physics Letters. **378**: p. 257-262, (2003).

209. Kumar, S. and W.W. Adams, *Electron Beam Damage in High Temperature Polymers.* Polymer. **31**: p. 15-19, (1990).

210. Martin, D.C., J.H. Chen, J.Y. Yang, L.F. Drummy, and C. Kubel, *High resolution electron microscopy of ordered polymers and organic molecular crystals: Recent developments and future possibilities.* Journal of Polymer Science Part B-Polymer Physics. **43**(14): p. 1749-1778, (2005).

211. Rinzler, A.G., J. Liu, H. Dai, P. Nikolaev, C.B. Huffman, F.J. Rodriguez-Macias, P.J. Boul, A.H. Lu, D. Heymann, D.T. Colbert, R.S. Lee, J.E. Fischer, A.M. Rao, P.C. Eklund, and R.E. Smalley, *Large-scale purification of single-wall carbon nanotubes: process, product, and characterization.* Applied Physics a-Materials Science & Processing. **67**(1): p. 29-37, (1998).

212. Hashimoto, A., K. Suenaga, A. Gloter, K. Urita, and S. Iijima, *Direct evidence for atomic defects in graphene layers.* Nature. **430**(7002): p. 870-873, (2004).

213. Rao, A.M., E. Richter, S. Bandow, B. Chase, P.C. Eklund, K.A. Williams, S. Fang, K.R. Subbaswamy, M. Menon, A. Thess, R.E. Smalley, G. Dresselhaus, and M.S. Dresselhaus, *Diameter-selective Raman scattering from vibrational modes in carbon nanotubes.* Science. **275**(5297): p. 187-191, (1997).

214. Eklund, P.C., J.M. Holden, and R.A. Jishi, *Vibrational-Modes Of Carbon Nanotubes - Spectroscopy And Theory.* Carbon. **33**(7): p. 959-972, (1995).

215. Chae, H.G., T.V. Sreekumar, T. Uchida, and S. Kumar, *A Comparison of Reinforcement Efficiency of various Types of Carbon Nanotube in Polyacrylonitrile Fiber.* Polymer. **46**: p. 10925-10935, (2005).

216. Mann, D., A. Javey, J. Kong, Q. Wang, and H.J. Dai, *Ballistic transport in metallic nanotubes with reliable Pd ohmic contacts.* Nano Letters. **3**(11): p. 1541-1544, (2003).

217. Frank, S., P. Poncharal, Z.L. Wang, and W.A. de Heer, *Carbon nanotube quantum resistors.* Science. **280**(5370): p. 1744-1746, (1998).

218. Poncharal, P., C. Berger, Y. Yi, Z.L. Wang, and W.A. de Heer, *Room temperature ballistic conduction in carbon nanotubes.* Journal of Physical Chemistry B. **106**(47): p. 12104-12118, (2002).

219. Bachtold, A., M.S. Fuhrer, S. Plyasunov, M. Forero, E.H. Anderson, A. Zettl, and P.L. McEuen, *Scanned probe microscopy of electronic transport in carbon nanotubes.* Physical Review Letters. **84**(26): p. 6082-6085, (2000).

220. Martel, R., T. Schmidt, H.R. Shea, T. Hertel, and P. Avouris, *Single- and multi-wall carbon nanotube field-effect transistors.* Applied Physics Letters. **73**(17): p. 2447-2449, (1998).

221. Yang, D.J., S.G. Wang, Q. Zhang, P.J. Sellin, and G. Chen, *Thermal and electrical transport in multi-walled carbon nanotubes.* Physics Letters A. **329**(3): p. 207-213, (2004).

222. Chen, E.J.H. and B.S. Hsiao, *The Effects Of Transcrystalline Interphase In Advanced Polymer Composites.* Polymer Engineering and Science. **32**(4): p. 280-286, (1992).

223. Klein, N. and G. Marom, *Transcrystallinity In Nylon-66 Composites And Its Influence On Thermal Expansivity.* Composites. **25**(7): p. 706-710, (1994).

224. Tracz, A., J.K. Jeszka, I. Kucinska, J.P. Chapel, G. Boiteux, and M. Kryszewski, *Influence of the crystallization conditions on the morphology of the contact layer of polyethylene crystallized on graphite: Atomic force microscopy studies.* Journal of Applied Polymer Science. **86**(6): p. 1329-1336, (2002).

225. Magonov, S.N., N.A. Yerina, Y.K. Godovsky, and D.H. Reneker, *Annealing and recrystallization of single crystals of polyethylene on graphite: An atomic force microscopy study.* Journal of Macromolecular Science Part B-Physics. **45**(2): p. 169-194, (2006).

226. Schadler, L.S., S.C. Giannaris, and P.M. Ajayan, *Load transfer in carbon nanotube epoxy composites.* Applied Physics Letters. **73**(26): p. 3842-3844, (1998).

227. Kumar, S., H. Doshi, M. Srinivasarao, J.O. Park, and D.A. Schiraldi, *Fibers from polypropylene/nano carbon fiber composites.* Polymer. **43**(5): p. 1701-1703, (2002).

228. Burbank, R., *Molecular Structure in Crystal Aggregates of Linear Polyethylene.* The Bell System Technical Journal. **39**: p. 361, (1960).

229. Wilfong, D.L. and G.W. Knight, *Crystallization Mechanisms for LLDPE and its Fractions.* Journal of Polymer Science: Part B: Polymer Physics. **28**(6): p. 861-870, (1990).

230. Ryan, K.P., M. Cadek, V. Nicolosi, D. Blond, M. Ruether, G. Armstrong, H. Swan, A. Fonseca, J.B. Nagy, W.K. Maser, W.J. Blau, and J.N. Coleman, *Carbon nanotubes for reinforcement of plastics? A case study with poly(vinyl alcohol).* Composites Science and Technology. **67**(7-8): p. 1640-1649, (2007).